MODELLING OF FINES MIGRATION MECHANISMS IN HIGH PERMEABILITY SANDS – IMPACT ON RESERVOIR PERFORMANCE

SAID AL-MUFARJI

A thesis submitted in partial fulfilment of the
requirements of
The Robert Gordon University
for the degree of Master of Philosophy

This research programme was carried out
in collaboration with the Shell UK Ltd

April 2009

DEDICATION

I dedicate this work to the All Mighty ALLAH, my parents, my family and my teachers.

ACKNOWLEDGEMENTS

Praise be to ALLAH, The Most Beneficent, The Most Merciful

The author would like to express his sincere gratitude and appreciation to Professor M. B. Oyeneyin, of the School of Engineering, The Robert Gordon University, for technical guidance and support in numerous ways. Professor Oyeneyin's contribution to defining and clarifying the research work, have helped to put this thesis in its final shape.

The author is greatly indebted to Dr. S. Jihan, Lecturer in the School of Engineering, RGU, for many hours devoted to technical advices, moral support throughout this study and overall guidance.

The author wishes to express his sincere thanks to Mr. William Townsley of Shell UK Limited, for his assistance and help with the collaboration agreement between Shell and RGU permitting the utilisation of Shell software packages for reservoir performance predictions.

Special thanks go to the Chairman of MB Petroleum Services Mr. Mohammed Barwani, and to the Managing Director, MB Petroleum Services Mr. Hafidh Al Busaidi for time allocation, support and moral encouragements which were crucial in the completion of the write-up of this thesis.

Also sincere gratitude goes to all Fluent Inc. staff for their help in setting up the Computational Fluid Dynamics (CFD) package especially at the initial stage of this research programme.

Thanks are also due to Dr. A. Lamki, Deputy Managing Director of the Petroleum Development Oman (PDO) and to Dr. Redha Backer, Human Resources Superintendent,

PDO, for the support and time allocation which were essential for the completion of this research.

Special thanks go to Mr Henry Brekelman of Shell UK for the administrative help. Many thanks to all friends and colleagues in the School of Engineering especially Dr. Assem Al-Hajj, Dr. O. Mahtot, Dr. Siddique and Mr. K. Al-Saadi, for their encouragement and support. The author expresses sincere gratitude to Shell UK and PDO for the research sponsorship. Finally, the author would like to express his appreciation to his family for standing by him all these years, especially to his dear wife Salima Al Ghazi whose understanding, patience and encouragement were very instrumental during the undertaking of this thought-provoking and laborious research work.

Abstract

Today the oil and gas industry suffers significant production losses due to fines migrations in high permeability sandstone formations or sand packs. During drilling, production or injection, fines migration continues to cause formation impairment resulting in oil and gas inflow reductions or injectivity resistance. The problem is further enhanced in mature reservoirs where increased water ingress and multiphase production aggravate the fines mobilisation. Proper fines management can optimise productivity, injectivity, safeguard facilities and reduce well maintenance cost. Today‘s core flood tests as part of risk assessment limit tests to single phase or at best two-phase oil/water flow. Meanwhile existing reservoir simulators have no facilities to analyse solid particles impact on productivity and injectivity.

This research work presents the unique technique adopted to analyse fines migration mechanisms in a true multiphase environment. The methodologies adopted include studies of fines particle impacts on pressure drawdowns in several sensitivities of rock permeability, water cut, multiphase flow, liquid flow, porosity, fines grain size, and the rest of relevant rock and fluid properties performed using an appropriate Computational Fluid Dynamics (CFD) simulator. The resultant drawdown pressures were then used to back-calculate corresponding particle-damaged permeabilities using a conventional field approach. From the results obtained, detailed mapping of prevailing pore blocking mechanisms and corresponding permeability impairment profiles are presented as functions of operating conditions. The technique integrates the CFD and 3-D reservoir simulation concepts to define and quantify the effects of different operating conditions on discretised reservoir blocks. Among the major research outcomes are two developed particle-damaged absolute

permeability models for multiphase and liquid flow conditions involving fines migration in porous media. The models were tested and validated using ten examples of field data with acceptable error margins in the majority of the cases.

Contributions to knowledge include: i) new analysis of particle impact in multiphase and liquid flows, ii) integration of CFD with 3-dimensional reservoir simulator and iii) the developed particle-damaged models.

Areas where more study is required include: a) dry gas CFD simulation, b) use of real rock (thin-section) pore structure scans as the computational mesh and c) adapting the application to EOR (enhanced oil recovery) operations such as steam injection, miscible fluid injection and others. These are highlighted as suggestions for further work to improve effectiveness of the developed advances towards better fines migration management. The research work is concluded with recommendations (supported by flow efficiency case studies) on contemporary innovations in fines management.

Table of Contents

Dedication ii
Acknowledgement iii
Abstract v
Table of Contents vii
Table of Figures x
Nomenclature xiii

CHAPTER 1 1

INTRODUCTION 10
1.1 BACKGROUND 1
1.2 OBJECTIVES 2
1.3 APPROACH 5
1.4 CONTRIBUTIONS TO KNOWLEDGE 6
1.5 ARRANGEMENT OF THESIS 10

CHAPTER 2 13

REVIEW OF RESERVOIR FINES MIGRATION STUDIES AND PARTICLE INTRUSION 13
2.1 FINES DEFINITIONS AND MEASUREMENTS 13
2.2 DEFINITION OF PERMEABILITY 18
2.2.1 Permeability Damage due to Fines Movement 21
2.3 FINES MIGRATION 22
2.3.1 Fines Migration During Well Operations 24
2.3.2 Critical Flow Rates Causing Fines Movement 28
2.4 FINES INTRUSION FROM WELLBORE INTO THE RESERVOIR 32
2.5 REVIEW OF PORE DIAMETER DETERMINATION 34
2.5.1 Determination of Pore Blocking Damage Mechanisms 37
2.5.2 Review of Jamming Ratio: Concept of Pore Plugging 38
2.5.3 Review of Uncertainties of Jamming Ratios 39
2.5.4 Review Of Formation Damage Caused by Various Factors 41
2.5.5 Reservoir Formation Damage due to Fluids Injection 42
2.5.6 Impact of Particles on Water Injection Rate in Horizontal Wells 43
2.6 CAUSES OF FORMATION DAMAGE OBSERVED IN THE OIL AND GAS INDUSTRY 49
2.7 FINES/ SAND MANAGEMENT PRACTICES IN THE OIL AND GAS INDUSTRY 52
2.8 RESEARCH WORK IN THE OIL AND GAS INDUSTRY 58
2.8.1 Relationship between Sand Prediction and Formation Damage Prediction 64
2.9 CORE LABORATORY ANALYSIS AND RESERVOIR SIMULATION LIMITATIONS 65
2.91 Reservoir Permeability Determination Using Well Inflow Analysis 67
2.10 THE NEED FOR COMPUTATIONAL FLUID DYNAMICS (CFD) SIMULATIONS 69
2.11 FIELD PRACTICES USED IN THE VALIDATIONS OF THE DEVELOPED MODELS 71
2.11.1 Drawdown Pressure Theory Used in Validating Developed Model 73
2.11.2 Build-Up Pressure Analysis Used in Validating Developed Model 74
2.11.3 Horizontal Wells Analyses Used in the Permeability Models Validations 77

CHAPTER 3 81

CFD MODELLING OF FINES FLOW IN MULTIPHASE FLUIDS 81
3.1 INTRODUCTION 81
3.1.1 Method Used in Carrying Out the CFD Simulations 82
3.1.2 Modelling Approach 82
3.1.3 Computational Fluid Dynamics (CFD) Package 83
3.1.4 Program Structure 85
3.1.5 Objectives of the Fines Analysis Program 87
3.2 EXPERIMENTAL ANALYSIS OF THE MODEL STRUCTURE 88

3.2.1 Initial Set-up: Grid Mesh Model Design ... *88*
3.2.2 Boundary Conditions ... *91*
3.2.3 CFD Data Trends Prediction Using MATLAB Software ... *92*
3.3 Simulations Process and Data Acquisition ... 93
3.4 Fines Interaction with the Porous Media ... 99
3.4.1 Particles Frictional Viscosity and Fluid Molecular Viscosity ... *105*
3.5 Reservoir scale analyses ... 108
3.5.1 Study Of Liquid Carrying 10-200µm Fines Through A 1000 mD Rock. ... *109*
3.5.2 Effect of 10 microns Fines Migration In Liquid Flow ... *109*
3.5.3 Impacts of 200 µm Fines on Liquid Flow Through 1000mD Rock ... *112*
3.5.4 Multiphase Flow Mobilising 10-200µm Fines Through 1000 mD rock. ... *115*
3.5.5 Comparison of 10 µm Fines Impacts on Multiphase and in Liquid flow ... *115*
3.6 Results of the Simulations ... 118
3.6.1 Impacts of 200 µm Fines on Δp in Multiphase and Liquid Flow. ... *120*
3.6.2 Impacts of 50- 150 µm fines on pressure in multiphase and liquid media ... *123*
3.6.3 Studies of 10 – 200 µm fines flow in Multiphase and liquid in 2000 mD rock ... *128*
3.6.4 Effect of 10 microns Fines Migration in Liquid Flow in a 2000 mD model ... *128*
3.6.5 Multiphase analysis of 10 microns Fines Migration in a 2000mD rock ... *131*
3.7 Results Discussions ... 135

CHAPTER 4 ... 146

PORE BLOCKING MECHANISMS FROM FINES MIGRATIONS AND SOLID INTRUSIONS ... 146
4.1 Introduction ... 146
4.2 Pore Plugging Analysis in Multiphase and Liquid Flows. ... 146
4.3 Use of CFD Pressure Drops to Calculate Corresponding Permeabilities ... 151

CHAPTER 5 ... 159

PARTICLE-DAMAGED PERMEABILITY MODELS DEVELOPMENT ... 159
5.1 Introduction ... 159
5.1.1 The Need for Damaged Permeability Models in the Reservoir Studies ... *161*
5.2 Particle-Damaged Permeability Model Development Strategy ... 162
5.2.1 Summary of the 4 permeability model development scenarios ... *162*
5.3 Analysis of Particle-damaged Permeability in Liquid through 1000 mD Rock ... 178
5.3.1 Particle-Damaged Permeability Model Development in Liquid Scenario ... *181*
5.4 Damaged Permeability Model Development: Multiphase Scenario ... 190
5.5 Reservoir Simulator Which Analyzed the Damaged Permeability Models ... 194

CHAPTER 6 ... 200

TESTING AND VALIDATION OF THE DEVELOPED PERMEABILITY MODELS ... *200*
6.1 Introduction ... 200
6.1.1 Testing the Developed Liquid Permeability Model at Various Scenarios ... *200*
6.1.2: Testing the Damaged Permeability Multiphase Model at Various Scenarios ... *205*
6.2 First Validation Using Field's Liquid Build-Up Pressure Survey ... 209
6.2.1 Second Validation Using Field Build-up Pressure Survey ... *214*
6.2.2 Third Validation Using Field Build-up Pressure Survey ... *218*
6.2.3 Fourth Validation Using Field Drawdown Pressure Survey ... *222*
6.2.4 Fifth Validation Using Field Pressure Fall-off Survey ... *227*
6.2.5 Sixth Validation Using Gas Wells Pressure Build-up Survey Analysis ... *231*
6.2.6 Seventh Validation Using Gas Well's Pressure Build-up Survey Analysis ... *234*
6.2.7 Eighth Validation Using Gas Well's Pressure Build-up Survey ... *237*
6.2.8 Gas Well Production Analysis ... *241*
6.2.9 Second Gas Well Production Analysis ... *243*
6.2.10 Ninth Validation Using Horizontal Well Productivity Analysis ... *245*
6.2.11 Tenth Model Validation Using Field Vertical Well (SDD-36 (b)) ... *251*

CHAPTER 7 ... 258

DISCUSSIONS, CONCLUSIONS AND RECOMMENDATIONS *258*
7.1 Discussions *258*
7.2 Conclusions *262*
7.2.1 Damaged Permeability Models Development for 1000 mD Rock *262*
7.3 Recommendations *271*

CHAPTER 8 ..... **273**

SUGGESTIONS FOR FURTHER WORK *273*

REFERENCES **275**

APPENDIX A-1: FLUENT'S CFD COMMERCIAL APPLICATIONS IN VARIOUS INDUSTRIES 282
A-1.1 Applications in the Oil & Gas industry *282*
A-1.2 FLUENT'S CFD APPLICATIONS IN OTHER INDUSTRIES 283
APPENDIX A-2: SUMMARY OF MORES FEATURES 284
APPENDIX A-3: COLLABORATION ESTABLISHMENT 287
APPENDIX A-4: MATLAB SOFTWARE USED IN TRENDS MATCHING 288
APPENDIX A-5: SIMULATION RESULTS OF CRUDE AND FINES FLOW AT EACH WATER CUT 292
APPENDIX A-6: PRESSURES IN MULTIPHASE AND LIQUID DUE TO FINES FLOWING THROUGH 1000MD ROCK . 293
Appendix A-6.1: Multiphase-liquid pressure drops due to particles through 2D rock *295*
APPENDIX A-7: PARTICLE-DAMAGED PERMEABILITY MODEL IN LIQUID FLOW 296
Appendix A-7.1: Damaged permeability model in multiphase, 1000 mD rock *297*

Table of Figures

Figure 1.1: A simple well diagram showing particles control measures at reservoir 4
Figure 1.2: Modeling Steps of Fines Migration in Multiphase High Permeability Sands 9
Figure 2.1 : Images of kaolinite, illite-smectite fines and measuring devices 15
Figure 2.2: Fines particles at different scales: illite and feldspar 17
Figure 2.3: Core sample measurement of permeability 19
Figure 2.4: Equation used to determine permeability in Darcy unit 20
Figure 2.5: Fines particles plugging pore spaces during migration 23
Figure 2.6: Conditions for particles deposition or passage through pore structures 26
Figure 2.7: Migrated fines of different origin found in a PDO's well Barik-12 27
Figure 2.8: Formation damages according to Barkman and Davidson (60) 47
Figure 2.9: PDO's South Oman oil production affected by sand particles. 56
Figure 2.10: Types of sand control measures in Oman to minimise sand/fines impact. 57
Figure 2.11: Thick wall cylinder test layout 60
Figure 2.12: Thick-walled cylinder technique used in determining sand influx zone 61
Figure 2.13: Principles of reservoir fluid flow fundamentals 68
Figure 2.14: Reservoir behaviour during a pressure drawdown (production) test 74
Figure 2.15 Reservoir behaviour during a pressure build-up test 75
Figure 2.16: Inflow pattern formed around a horizontal well 78
Figure 3.1: The CFD Program Structure 86
Figure 3.2: Computational grid cells model 89
Figure 3.3:Crude (oil, gas and 20%water) simulated speeds across porous medium. 94
Figure 3.4: Hydrocarbon Liquid Velocities at Various % Water Cut 96
Figure 3.5: Average crude velocity per fines particle grain size 97
Figure 3.6: Fines (sand) simulated speed across modelled porous medium 99
Figure 3.7: Pressure drop profile distribution across the computational grid. 107
Figure 3.8: Liquid velocity changes during 10 μm fines particle mobilisation 109
Figure 3.9: Velocity changes when 10 μm fines (sand) was flowing in a liquid medium 110
Figure 3.10: Pressure changes when 10 μm fines in hydrocarbon liquid flow was simulated. 111
Figure 3.11: Liquid velocity profile when 200 μm fines mobilisation was simulated. 112
Figure 3.12: Particle velocity profiles when 200 μm fines was flowing in a liquid medium. 113
Figure 3.13: Pressure contours when 200μm fines was simulated in liquid flow. 114
Figure 3.14: Multiphase (crude) velocity changes when 10 μm fines mobilisation was simulated 116
Figure 3.15: Sand velocity profiles when 10 μm fines was flowing in a multiphase flow. 117
Figure 3.16: Pressure profiles when 10 μm fines flow in a multiphase fluid was simulated. 118
Figure 3.17: Pressure drop comparison in multiphase and liquid flowing 10μm fines 119
Figure 3.18: Multiphase velocity changes during 200 μm fines grains mobilisation 120
Figure 3.19: Velocity vectors of 200 μm fines grains flow in a multiphase medium 121
Figure 3.20: Pressure profiles during 200μm fines mobilisation in a multiphase flow. 122
Figure 3.21: Multiphase and liquid pressure drops during 200 μm fines flow. 123
Figure 3.22: Multiphase and liquid pressure drops during 50 μm particles flow. 124
Figure 3.23: Multiphase and liquid pressure drops during 100 μm fines flow. 124
Figure 3.24: Multiphase and liquid pressure drops during 150 μm particles flow. 125
Figure 3.25: Liquid velocities during 10 μm particles flow simulation through 2000 mD rock 129
Figure 3.26: Velocities when 10 μm fines (sand) was simulated in liquid through 2000 mD rock 130
Figure 3.27: Pressure profiles results of 10 μm fines in liquid flow through 2000 mD drainage 131
Figure 3.28: Multiphase crude velocities during 10 μm particles flow through 2000 mD rock 133
Figure 3.29: 10 μm fines velocities through a 2000 mD drainage in a multiphase medium 134
Figure 3.30: Pressure profiles of 10 μm particles in multiphase flow through 2D drainage 135
Figure 3.31: Multiphase-liquid pressure drops during 10 μm fines flow in a 2000mD rock. 138
Figure 3.32: Pressure drops comparison in multiphase and liquid flows in 2000 mD and 1000 mD scenarios. 139
Figure 3. 33: Multiphase and liquid pressure drops when 50 μm fines flow was simulated in 2 D rock 140

Figure 3. 34: Impacts of 50 μm grain on Δp in multiphase and liquid flow: 2000 mD and 1000 mD scenarios 140
Figure 3. 35: Multiphase and liquid pressure drops due to 100 μm particles flow in 2000mD rock. 141
Figure 3.36: Comparison of multiphase and liquid pressure drops due to 100 μm fines flow in 2D and 1D rocks 141
Figure 3. 37: Multiphase and liquid pressure drops during 150 μm fines flow in a 2000 mD drainage. 142
Figure 3.38: Comparison in multiphase and liquid pressure drops when 150 μm fines flow in 2D and 1D rocks 142
Figure 3. 39: Multiphase and liquid pressure drops due to 200μm fines flow in a 2000mD model. 143
Figure 3. 40: Comparison of multiphase and liquid pressure drops due to 200 μm fines flow in 2D and 1D rocks 143
Figure 4.1: CFD generated pressure declines in multiphase and liquid flowing 10μm fines 152
Figure 4.2: Permeability profiles in multiphase and liquid flowing 10μm fines 152
Figure 5.1: Particle size impacts on drawdown pressure in a 1000 mD drainage 164
Figure 5.2: Particle size impact on permeability in a liquid scenario 165
Figure 5.3: Log-log scale of particle size impact on permeability in a liquid scenario 166
Figure 5.4: Particles impacts on drawdown pressures in a 1000mD multiphase drainage 167
Figure 5.5: Particle size effects on permeability in multiphase scenario 168
Figure 5.6: Log-log scale of particle size effects on permeability in multiphase scenario 169
Figure 5.7: Particle size impacts on drawdown pressure in a 2000 mD liquid drainage 170
Figure 5.8: Particle size impacts on drawdown pressure in a 2000mD multiphase drainage 171
Figure 5.9: Particle size impacts on permeability in liquid scenario 172
Figure 5.10: Log-log scale of particle size impact on permeability in a liquid scenario 173
Figure 5.11: Particle size effects on permeability in multiphase scenario 174
Figure 5.12: Log-log scale of particle size impacts on permeabilities in a multiphase scenario 175
Figure 5.13: Comparison of particle size impact on permeability in liquid and multiphase 176
Figure 5.14: Comparison of particle size impact on permeability in liquid and multiphase 177
Figure 5.15: Damaged permeability matching. Effects of 10 μm grain on permeability 178
Figure 5.16: Matching of impacts of 10μm grain size on drawdown pressure 179
Figure 5.17: Matching impact of 50 microns grains on permeability 180
Figure 5.18: Drawdown pressure matching. Impact of 50 μm grain size 181
Figure 5.19: Permeability matching of CFD simulated trends in a 1000 mD liquid scenario 182
Figure 5.20: Model generated damaged permeability profiles of non-simulated grain sizes 185
Figure 5.21: Effective oil and water permeabilities and corresponding relative permeabilities (113) 186
Figure 5.22: Relative permeabilities of oil and water 189
Figure 5.23: Effective permeabilities of oil and water 190
Figure 5.24: CFD based permeability profiles matching in a 1000mD multiphase scenario. 191
Figure 5.25: Model generated damaged permeability profiles of non-simulated grain sizes 193
Figure 5.26: How a static geological (permeability) model can be imported into MoReS (117) 197
Figure 6.1: Comparison between developed model‘s and CFD results in the liquid medium 203
Figure 6.2: Comparison of developed model results and CFD results in multiphase medium 207
Figure 6.3: Pressure build-up test analysis 211
Figure 6.4: Model‘s permeability profile based on all pressure build-up data vs. survey result 214
Figure 6.5: Pressure build-up survey analysis using field practices 216
Figure 6.6: Model‘s permeability profile based on pressure build-up data 218
Figure 6.7: Conventional pressure build-up survey field practice analysis 220
Figure 6.8: Model‘s permeability profile based on pressure build-up data 222
Figure 6.9: Conventional drawdown analysis using logarithm of production time 224
Figure 6.10: Drawdown analysis using production time 225
Figure 6.11: Model‘s permeability profile based on pressure drawdown data 227
Figure 6.12: Water injection well pressure fall-off survey analysis 229
Figure 6.13: Model permeability profile of a water injection well 230
Figure 6.16: Pressure build-up survey analysis of a dry gas well 232
Figure 6.15: Multiphase Model‘s permeabilities based on gas pressure build-up data 233
Figure 6.16: Pressure build-up analysis of a dry gas producing well 235
Figure 6.17: Model‘s permeability profile based on all gas pressure build-up data 236

Figure 6.18: Pressure build-up analysis of a gas producing well 239
Figure 6.19: Model permeability profile based on gas pressure build-up data 241
Figure 6.20: Stabilized test analysis to obtain coordinates for AOFP calculations 243
Figure 6.21: Coordinate determination for AOFP analysis 245
Figure 6.22: Measured drawdown pressure and model generated profile 250
Figure 6.23: Field measured permeability vs. model's distribution of permeabilities 251
Figure 6.24: Field measured permeability vs. model's distribution of permeabilities 255
Figure 7.1: Model matching CFD Damaged Permeability profiles in a 1000 mD liquid scenario 263
Figure 7.2: Model generated damaged permeability profiles of non-simulated grain sizes 264
Figure 7.3: Matching CFD damaged permeability profiles in a 1000mD multiphase scenario 265
Figure 7.4: Multiphase model generated damaged permeabilities of un-simulated grain sizes 266
Figure 7.5: Model validation results using real field pressure survey data 267
Figure 7.6: Model validation results using real field pressure survey data 268
Figure A.1: Fitting 10 μm, 1000 mD liquid scenario CFD results using MATLAB 289
Figure A.2: Parabola regression matching of 10 μm fines grain and various sensitivities 291

Nomenclature

The following table contains symbols used in this thesis. Symbols having more than one meaning or those which are relevant to only a specific section are defined in the appropriate sections in the text.

Symbol		Definition
a	=	A constant
$\boldsymbol{a}$	=	Large half-axis of the drainage ellipsoid formed by a horizontal well (ft)
a_1, a_2, a_3	=	Constants that apply over several ranges of R_e
A	=	Area of pore (in^2)
AOFP	=	Absolute open-flow potential or maximum gas flow rate (MMScf/d)
b	=	Constant accounting for mechanical stability of filter cake
B_g	=	Gas formation volume factor (res bbl/STB)
B_o	=	Oil formation volume factor, (res bbl/STB).
B_w	=	Water formation volume factor (res bbl/STB)
C	=	Dynamic fluid loss coefficient ($in^3/in^2\text{-}hr^{1/2}$)
CFD	=	Computational fluid dynamics
C_t	=	Total reservoir compressibility (1/psi)
C_{2i}	=	Inertial resistance factor (m^{-1})
D	=	Perforation /or completion interval thickness, (ft)
D_F	=	Fines grain mean diameter size (μm)
D_G	=	Gravel mean diameter (μm)
D_P	=	Pore mean diameter size (μm)
$\frac{d_p}{d_r}$	=	Transient pressure gradient (psi/ft)
e_w	=	Coefficient of restitution for particle-wall collisions (dimensionless)
EGP	=	External gravel pack
ESS	=	Expandable sand screen
F	=	Average pore length (ft) multiplied by a tortuosity factor
F_D		Drag force
g_x		Gravitational acceleration in horizontal (x) direction
h	=	Reservoir (Pay zone) thickness (ft)
I	=	Inlet cell type
IGP	=	Internal gravel pack
J_h	=	Horizontal productivity index (b/d)/(psi)
J_v	=	Vertical productivity index (b/d)/(psi)
k	=	Formation absolute permeability, (md)
k_g	=	Gas permeability (mD)
k_h	=	Horizontal permeability, (md)

K = Constant, characteristic of fluid
$k_i(D_G,\chi_i)$ = Damaged permeability at i^{th} length of the drainage length as a function of G_F (md)
k_o = Oil effective permeability (md)
k_{ro} = Relative oil permeability (md)
k_{rw} = Relative water permeability (md)
k_v = Vertical permeability, (md)
k_w = Water effective permeability (md)
k_x = Horizontal permeability (md)
k_z = Vertical/ z-direction permeability (md)
L = Live cell type
L = Length of the ellipsoid (ft)
L_x = Width of drainage boundary (ft)
L_y = Length of drainage boundary (ft)
LN = Natural logarithm
L_p = Liquid phase
M = Number of grid blocks along the horizontal side.
m = Slope of the graph of Pressure vs. Log time ratio, in pressure test analysis (psi/log cycle)
M_p = Multiphase.
n = Total number of layers perforated
Np = Total production volume (stb)
O = Outlet cell type
$\bar{p}$ = Average pressure within the drainage volume (psi)
P = Porous cell type
PDL = Pre-drilled liner
p_e = (Far-field) external reservoir pressure (psi)
pe = Extrapolated pressure in the pressure test curve to $\log\{(t+\Delta t)/\Delta t\}= 1$ (psig)
Pi = Initial reservoir pressure (psi)
PIF = Productivity improvement factor
p_{wf} = Flowing well pressure (psi)
P_{wp} = Expected near-wellbore pore pressure (psi).
pws = Shut-in well pressure (psia)
q = Liquid production rate (bbl/d)
q_g = Gas flow rate, (stb/d) (converted from MMscf/d)
q_h = Horizontal liquid flow rate (bbl/d)
q_v = Vertical liquid flow rate (bbl/d)
q_w = Water injection/ invasion rate (bbl/d).
q_{wc} = Critical/maximum oil rate above which water coning happens (STB/d)
r = Radius distance from wellbore (ft)
r_e = External drainage radius (ft)
r_{eh} = Effective radius based on acre spacing (ft)
r_i = Radius of grid (ft)
r_p = Radius of penetration or depth of mud filtrate (in)
r_w = Wellbore radius (ft)
r_v = Ratio of V_w to V_s
R_e Reynolds number
S = Mechanical skin and un-stimulated filter cake damage skin (unitless)

S = Saturation (always expressed as a fraction of the pore volume)
S_g = Gas saturation (fraction)
S_{gr} = Residual gas saturation to water (fraction)
S.L. = Slotted liner
S_o = Oil saturation (fraction)
S_{or} = Residual oil saturation to water (fraction)
S_w = Water saturation (fraction)
S_{wc} = Connate (or irreducible) water saturation (fraction)
S_{wi} = Initial water saturations (fraction)
T = Absolute temperature ($^{\circ}$R)
t = Exposure time (hr)
t = Total production time before the well was shut-in (hr)
Tsc = Temperature at standard condition = 520 $^{\circ}$R
tp = Production time (hrs)
TWC = Thick-walled cylinder strength (bar), (1bar=14.5 psi).
$\vec{u}_{s,w}$ = Solids velocity at the wall
V_s = Volume of solids (in^3)
V_w = Volume of continuous phase (in^3)
W = Wall cell type
wc = Water cut
WWS = Wire-wrapped screen
Z = Gas compressibility (deviation) factor (fraction)

Greek Symbols

α_S = Solids volume fraction (fraction)
$\alpha_{S,\max}$ = Solids volume fraction at the packing limit (fraction)
χ_i = i^{th} length of the drainage area (ft)
$\frac{\partial p}{\partial x_i}$ Pressure drop through the medium at each i^{th} distance (Pa/m)
ΔP_{dd} = Drawdown pressure applied near the wellbore (psi).
ΔP_{de} = Field wide depletion pressure (psi)
$\Delta P\ (D_G, \chi_i)$ = Pressure drawdown as function of fines grain size and ith drainage length (psi).
ΔP = Pressure drop or drawdown pressure (psi)
$\Delta p/\Delta \delta$ = Change in pressure with drainage distance (psi/ft)
Δt = Pressure build-up time or shut-in time fraction (hrs)
ϕ = Grid block average porosity (fraction)
Φ = Porosity (fraction)
η = Hydraulic diffusivity (md)/[psi(cp)]
η_p = Number of pores per cubic centimetre (N/in^3).
I_{ani} = Permeability anisotropy (unitless)
κ = Air permeability (md).
λ_ρ = Pore mean diameter (μm)

INTRODUCTION

1.1 Background

Today the oil and gas industry suffers significant production losses due to impairment of unconsolidated sandstone reservoirs caused by fine sand particles (fines) migration within the reservoir zones as well as particles injected into producing zones. Effective management of fines particles in hydrocarbon fields today requires careful studies of multiphase liquid-particles mixture flow characteristics through porous media. The studies should incorporate several sensitivities and scenarios to mimic complex flow mechanisms occurring in pore structures. Appropriate sand/ fines management could help not only in enhancing oil and gas production, but also in preserving well integrity by minimising fines flow accumulation which may affect well completion devices in high production rate wells. This research work demonstrates proven processes which can be used to selectively model solid fines particles migration flowing with multiphase hydrocarbon fluid mixture through reservoir pore structures. Hence the approach, unlike core laboratory analysis is not limited to fluid types such as hydrocarbon gas flow effects. Unfortunately, the ongoing core lab experiments and fluid flow analysis do not involve injection of hydrocarbon gas for safety reasons. The core lab methodology also does not incorporate continuous multiple sensitivities analysis of fines grain size and various fines concentrations in oil, gas, water and particle flow mixture. Furthermore, the results obtained from core plugs analysis are not always representative of the entire reservoir drainage area despite the fact that the data is scaled-up to reservoir size, and used in field development activities. This research‘s objectives as outlined below, are to conduct extensive studies and employ novel approaches tested and validated using field data in order to minimise the uncertainties existing today in the oil and gas industry.

1.2 Objectives

The main objectives of this research are summarised as follows:

(a) To study the characteristics of (gas free) liquid mixture of oil, water and fines particles flow into and within a porous medium and then determine flow impacts due to several sensitivities of reservoir properties.

(b) To study characteristics of multiphase complex mixture (gas, liquid hydrocarbon and fines particles) flow within and into a porous medium and then determine hydrocarbon multiphase effects (due to gas presence) and induced fines pore blocking mechanisms at several scenarios of reservoir properties.

(c) To determine reservoir permeability reduction due to solid particles dictated by multiphase (gas presence) and liquid (gas free) flow media.

(d) To develop particle-damaged permeability models in both multiphase and liquid scenarios.

Thus the main focus is to analyze fines migration characteristics through different pore structures and then simulate various conditions that have impact on the migration mechanisms. The key objective therefore is to offer the oil and gas industry the best available means of managing fluid production from wells having fines influx tendency which applies to the majority of wells in all high permeability sandstone reservoirs. In high permeability (> 500 milli Darcy (mD)) sandstone reservoirs, 60% to 70% of the wells have fines related problems (1).

Table 1.1: Size limits of soil in the USDA soil textural classification system

Name of soil separate	Diameter limit (mm)	Diameter limits (microns)
Very coarse sand	2.00 - 1.00	2000 - 1000
Coarse sand	1.00 - 0.50	1000 - 500
Medium sand	0.50 - 0.25	500 - 250
Fine sand	0.25 - 0.10	250 -100
Very fine sand	0.10 - 0.05	100 - 50

As explained in chapter 2, several fines definitions exist; some investigators (2) refer to fines as fine-grained sand particles having grain sizes of less than 62 microns referring to the silt and clay while others (3) consider fines grains sizes of up to 250 microns. In this research fines are fine-grained sand particles having various grain sizes ranging from 10 to 200 μm in some cases including the silt and clay group having less grain size than Brown‘s analysis given in table 1.1.

Fines are made of loose solid materials composed of silt group of particles mixed with clay minerals existing in hydrocarbon reservoirs (4, 5) and very fine sand. The silt group includes silica, feldspar, mica, calcite, dolomite, siderite and chloride particles; whereas the clay minerals include kaolinite, illite, chlorite, smectite and other types of clay called mixed-layer clays (5)..

Today the oil and gas industry tries sub-optimally to manage fine sand through a sand control strategy which includes use of mechanical devices such as: internal gravel packs (IGP), external gravel packs (EGP), wire-wrapped screens (WWS), pre-drilled liners (PDL), meshrite (premium screen), slotted liners (SL), expandable sand screens (ESS) and so forth.

Based on field observations the more the fines production is restricted the more the reduction of reservoir production capacity; hence in order to obtain production rate increases, the current industry strategy allows fines production which depending on conditions explained later in this research, cause pore blockage and thus tend to affect production. Figure 1.1 is a simple horizontal well layout showing well components including 4 ½" wire-wrapped screens which are used for particles control usually of up to 200 μm grain size. In high permeability sandstone reservoirs, hydrocarbon fluids and particles flow together.

To minimise particles impact on production, well equipment and surface facilities, sand particles control devices such as WWS, ESS, PDL, SL etc. are installed right at the reservoir level.

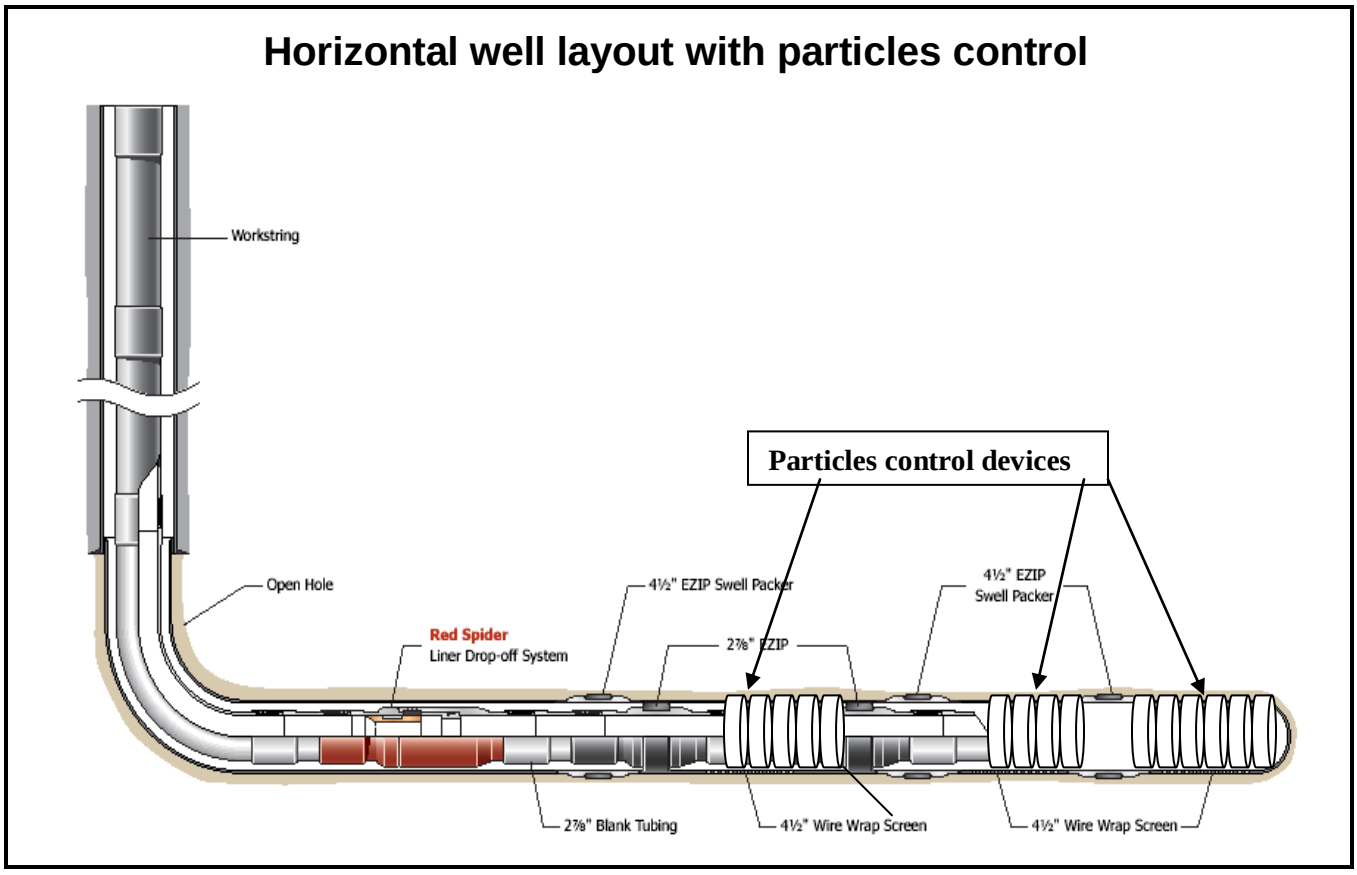

Figure 1.1: A simple well diagram showing particles control measures at reservoir

This study is intended to improve the industry‘s strategy as explained in this thesis. The research approach is summarised in section 1.3.

1.3 Approach

The research initially involved studies of existing investigations on the subject carried out by various researchers who addressed the topics differently using several approaches ranging from analytical, empirical, experimental to numerical modelling. Reviews of those studies are given in chapter 2. In general, analytical and empirical approaches tend to use published correlations that compute various formation damage mechanisms such as conditions causing shallow invasions, deep invasions, external cake formation, internal bridging and other formation damages explained in chapter 2. Experimental approaches refer mainly to core sample and formation plug sample analyses. Several core analyses are discussed in chapter 2. Numerical modelling of fines migration mechanisms is not widespread. As explained in the next chapter, even today‘s leading 3D reservoir simulators do not cater for particle analysis due to limitations the industry faces in granular flow modelling.

Having identified limitations in each of the methodologies used, a very comprehensive investigation was employed which involved application of two independent simulation packages, a computational fluid dynamic (CFD) for multiphase and solid particles mixture flow analysis in a porous medium and a 3-dimensional reservoir performance prediction simulator. Both simulators have been used in the oil and gas industry, as explained in Appendix A-1 in case of the CFD coded by Fluent Inc; and in appendix A-2 in case of Shell International‘s MoReS (Modular Reservoir Simulator).

The steps in the investigation can be summarised as follows:

(a) Using Fluent Inc.'s CFD program, hydrocarbon multiphase fluids with particles of various grain sizes in microns were simulated in a modelled porous medium to determine pressure distributions as a result of fines impact to pore structures. The same analysis was repeated without hydrocarbon gas and the differences were noted. Then comparison was made between the two analyses. The process was carried out in high permeability sandstone's conditions of 1000 mD and was repeated in 2000 mD involving rock and fluid sensitivities explained in chapters 2, 3 and 4.

(b) Reservoir permeability reduction as a function of time was then determined from the corresponding damaged reservoir pressure distribution.

Pore blocking mechanisms which are functions of several factors such as grain size, pore size, reservoir indices, flow rate, fluid type, viscosity, water cut, permeability, porosity, drawdown pressure and others which are elaborated in the next chapter, were then determined. Furthermore, damaged-permeability profile models were developed. The models were then incorporated in one of the most advanced 3-dimensional Modular Reservoir Simulator (MoReS) at the collaborating establishment (Shell UK Ltd) to perform comprehensive reservoir performance studies as per the agreement in appendix A-3.

With this modelling package, multiple sensitivity scenarios were carried out to test the setup using conventional field data.

1.4 Contributions to Knowledge

This research work has resulted in several additions to the existing knowledge of fines migrations and their impacts to production performance, including:

Development of comprehensive fines migration models which can predict damaged permeability decline profiles across the entire drainage area in both multiphase and

liquid granular flows. The models take into account all rock and fluid properties. As such this research work developed a detailed analysis of particle flow impact in a complex hydrocarbon multiphase flow mixture in a porous medium to study hydrocarbon and fines movements. Currently this analysis cannot be performed in core labs and does not exist in contemporary reservoir simulators used in the oil and gas industry.

Fully fledged multiphase fines migration analysis at multiple sensitivities of rock and fluid properties to hydrocarbon reservoir scale. Today, neither experimental work nor numerical reservoir simulators have such a unique capability. Also no existing reservoir simulators have solid particle (granular) analysis capability.

Integration of CFD and reservoir simulation packages. Procedures and methodologies of how to create an integrated particle analyzing software package which incorporates a fines flow simulator into a hydrocarbon reservoir performance prediction simulator were developed. So far no such attempt has been reported elsewhere.

The output of the above contributions have significantly added new knowledge on fines migration and its effects on hydrocarbon production. As a result, better oil prediction method as well as improved fines control measures can be achieved to enhance hydrocarbon production. Therefore the research minimised significant limitations currently faced by conventional core-flood laboratory analyses, numerical reservoir simulations and empirical methods. As such it is now possible:

i) To effectively analyse hydrocarbon gas impact in a flowing mixture of solid particles and multiphase fluid; then to be able to predict damaged permeability decline profiles across the reservoir.

ii) To determine fines particles impact on pressure distribution through the entire porous medium, then analyse particle-damaged permeability distribution across the entire drainage area.

iii) To perform more effective granular multiphase flow production and predictions using the integrated CFD / 3-dimensional simulation package capable of analysing flow at reservoir conditions.

iv) To predict possible pore plugging mechanisms for several scenarios of reservoir conditions as explained in chapter 4.

These contributions to knowledge are among the major breakthroughs of this research work in that they demonstrate and provide means of quantifying lateral variations in reservoir particle-damaged permeabilities across the sand body and how to incorporate them into a numerical simulator, a fact which is normally not accounted for in the oil industry today as fines-affected reservoir simulators so far do not exist.

Figure 1.2 displays the research‘s fundamental focus on the complex fines particles migration in a multiphase flow. The figure emphasises the message that since fines sand particles co-exist with hydrocarbon fluids (oil, gas and water), reservoir simulations must include rigorous solid particle analysis and that core labs need provisions for extensive hydrocarbon gas analyses simulating insitu conditions. Similarly, the resultant particle-damaged permeability should be mapped across the entire reservoir model and not input in reservoir simulators as constant values or simple linear distributions.

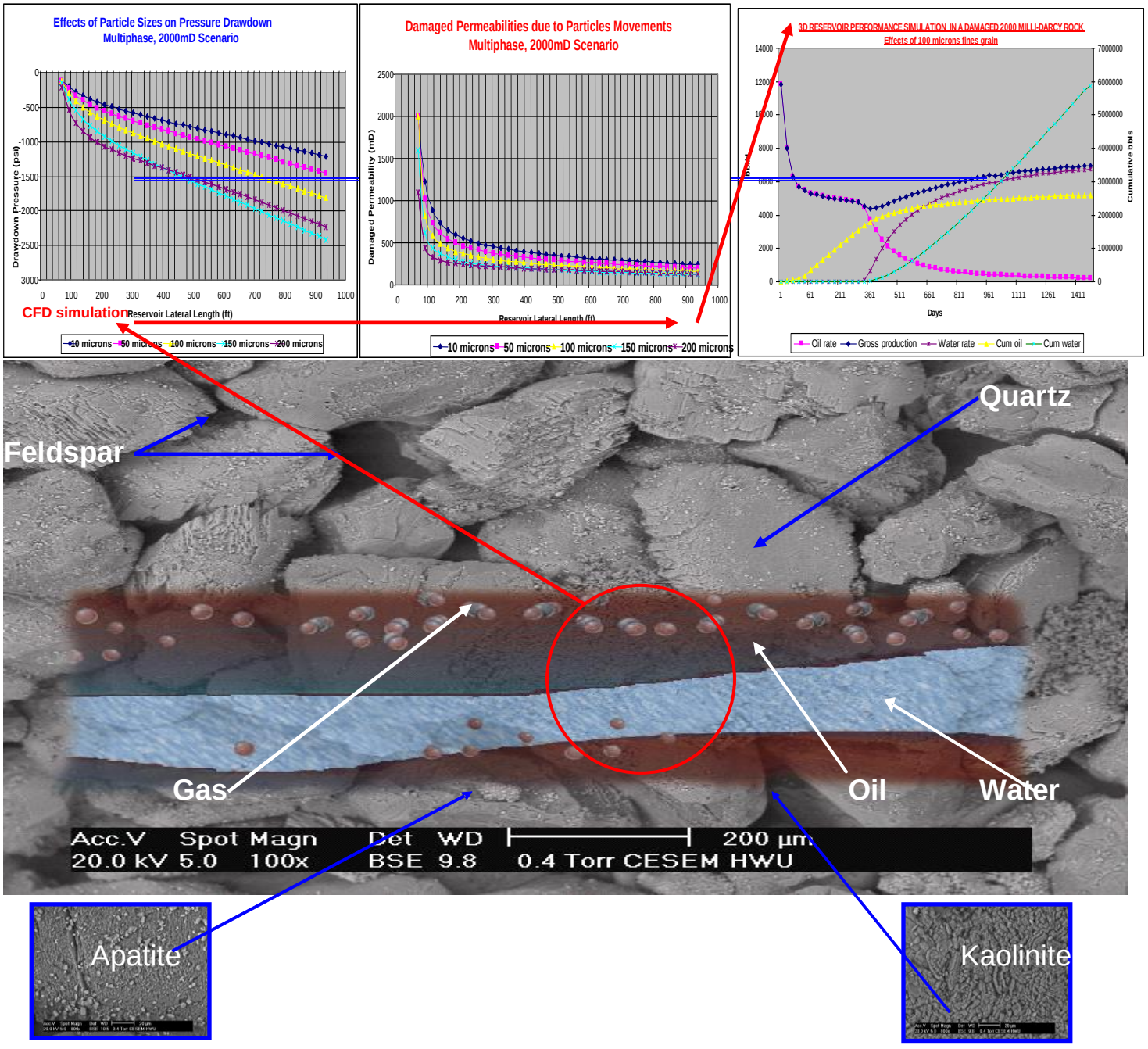

Figure 1.2: Modeling Steps of Fines Migration in Multiphase High Permeability Sands

Figure 1.2 summarizes important modelling steps of fines migration and its impact on hydrocarbon production prediction. A complex mixture of hydrocarbon liquid, gas and fines

particles (kaolinote, apetite, quartz, etc.) flow together in reservoir pores. In the figure the red circle is a small cluster of pore spaces example through which a mixture of hydrocarbon oil, water, gas and particle sizes or part of the mixture may pass (depending on conditions explained in the next chapters). Simulations of liquid and solid particles flow mixture carried out to identify impact of grain size on the flow in terms of drawdown pressure are explained in chapter 3. The resultant drawdown pressures were then graphically analysed as shown at the top left side of figure 1.2. It is a graph of drawdown pressures per fines grain size simulated by the CFD reflecting multiphase scenario comprised of 10 – 200 microns fines particles flowing with oil, gas and water through a 2000 mD reservoir model‘s pores. The drawdown pressures were then used to calculate corresponding reservoir absolute permeability using the Darcy equation and other conventional correlations explained in chapters 2 and 4. In the process, two particle-damaged permeability models were developed; multiphase model and liquid model. An example of the multiphase particle-damaged model‘s result is given on the top middle graph in figure 1.2, whereas the right hand side graph is a reservoir simulation result showing production prediction in a 100 micron particle size scenario.

1.5 Arrangement of Thesis

Chapter 1 provides research‘s introduction, objectives, approach and contributions to knowledge. Extensive reviews and discussions of fines migration mechanisms within the reservoir and solid particle intrusion from the wellbore fluids (drilling fluid, water injection, workover fluid and completion fluid) into the reservoir are given in chapter 2. Literature reviews of several investigations on the same subject by different researchers are also included in the chapter which then discusses current field practices used in fines and sand management. It elaborates on the need to carry out an in depth and accurate analysis of fines impact on multiphase hydrocarbon

flow using a comprehensive modelling approach which can analyse most of the reservoir properties transcending current limitations. The chapter finally introduces a Computational Fluid Dynamics (CFD) package which can be used to analyse the impacts of particles on fluid flow. Chapter 3 introduces theories of CFD modelling; then explains the software package used in the research and the reasons for selecting it. It describes the basic functions, architecture, suitability of the package for this research work as well as specific areas of application. The chapter provides explanations on interaction between solid particles and porous media in a setup reflecting hydrocarbon drainage characteristics. Boundary conditions and essential granular flow modelling requirements are elaborated in the chapter. It explains steps which were taken in performing several simulations at various scenarios and sensitivities. Results are summarised graphically and in tabular form.

Chapter 4 covers the concept of pore blocking mechanisms due to fines migrations and solid intrusions using results obtained from the CFD simulations. Pore plugging studies carried out in multiphase and liquid granular flows and the resultant corresponding pore plugging mechanisms are explained in the chapter. As pore plugging studies involve fines diameter, pore diameter, porosity and permeability, in this chapter results of all sensitivities carried out in chapter 3 were used in the pore plugging analyses.

Chapter 5 is about particle-damaged permeability model development using results from chapters 3 and 4. The damaged permeabilities were back-calculated from the CFD-generated drawdown pressure profiles. The approach takes into consideration the effects of fines particles of various sizes (10-200 microns) across the entire reservoir at numerous variable sensitivities in multiphase, liquid, rock and fluid conditions. Gas was analysed as part of the multiphase fluid

mixture comprising oil, water and gas. Two models covering all different particle sizes in both liquid and multiphase scenarios were developed.

The models are based on the nature of hydrocarbon production at the reservoir level. The reservoir can be a gas saturated (multiphase) or a non-saturated one (liquid only). The model applicable in liquid scenario is different from the multiphase model. The later is much more complex due to presence of hydrocarbon gas which involves approaches completely different from the liquid analyses. Gas being mixed with liquid, the multiphase analysis is not possible to be used for liquid only as the relative permeability determination of each fluid present in a mixture is dependant on saturation of each fluid in the mixture. Relative permeability concept is presented in chapter 5.

The chapter also shows how the models can be used into a 3-D modular reservoir simulator (MoReS) to predict reservoir production performance. As such MoReS general description is provided in the chapter.

Chapter 6 discusses testing and validations of the developed models. Initially the developed models tests against non-simulated grain sizes are demonstrated. Then validations of the developed models using actual field practices and well data are demonstrated along with resultant error percentages. Chapter 7 covers results discussions, research conclusions and recommendations whereas chapter 8 provides suggestions for further work.

Chapter 2

REVIEW OF RESERVOIR FINES MIGRATION STUDIES AND PARTICLE INTRUSION

In order to have a clear understanding of existing technologies and how they evolved to current status, literature surveys of related major studies and field practices were carried out and are presented in this chapter starting from fines definition, fines migration aspects, critical rates, solid particles intrusion through the wellbore into the reservoir to fines migration prediction methods.

2.1 Fines Definitions and Measurements

Different researchers referred to in this chapter investigated the nature of fines which exist in unconsolidated hydrocarbon sandstone reservoirs. Fines are fine-grained sand particles having various grain sizes in some cases even up to 200 microns are referred to as fine sands (3) as per Brown‘s analysis given in table 1.1.

Fines are made of loose solid materials composed of silt group of particles mixed with clay minerals existing in hydrocarbon reservoirs according to Colmenares et al (4). The silt group includes silica, feldspar, mica, calcite, dolomite, siderite and chloride particles; whereas the clay minerals include kaolinite, illite, chlorite, smectite and mixed-layer clays as explained by Civans (5).

.

Fines are produced "in situ" or due to field operations and are free to migrate through the reservoir pore structures along with multiphase flowing fluids which include oil, water and hydrocarbon gas depending on reservoir fluid and rock properties. Swelling between the particle layers happens because of absorbed water due to the cation exchange chemical reaction (6). This process is affected by ionic strength of the introduced fluid, temperature, electrical conductivity and the pH of the fluid. Kaolinites are usually attached loosely to the surfaces of the rock pores and are released into aqueous fluids by the interaction between different fluids (7, 8). Figure 2.1 shows fines images of illite-smectite, kaolinite and smectite clay.

The very fine (< 60 μm) silt and clay particles from core samples, are commonly measured using Scanning Electron Microscope (SEM), CAT scanning, Back-Scattered Electron (BSE) and X-Ray Diffraction (XRD) devices (8). However there are other methods which are used in the core laboratories to measure fines properties. These include: (a) X-Ray Fraction (XRF) (b) Cryogenic SEM and (c) Thin section analysis.

Figure 2.1 shows the two major measuring devices commonly used in core laboratories to study fines characteristics, Scanning Electron Microscope (SEM) and CAT scanning.

Figure 2.1 : Images of kaolinite, illite-smectite fines and measuring devices

In a laboratory analysis conducted by Byrne et al (9), smectites are reported to contain large amount of sodium ions which cause the mineral to absorb water and swell to several times the original volume in the presence of fresh water. Smectite is a 2:1 type of clay composed of

two tetrahedral and one octahedral layer bound together by weak interactive forces. Smectites and mixed-layer clays are referred to as swelling clays (9). The swelling of smectites on pore surfaces reduces the porosity and permeability of the formation. Smectites can also be released from pore surfaces and migrate during the swelling process. Figure 2.2 depicts two measurement scales of fines particles, the 100μm scale shows a mixture of illite and feldspar fines particles called illitised feldspars (IF) and pure feldspar (F) particles. The 500μm scale illustrates variations in fines grain sizes (9). The figure also shows details of clay mineral fines called illite.

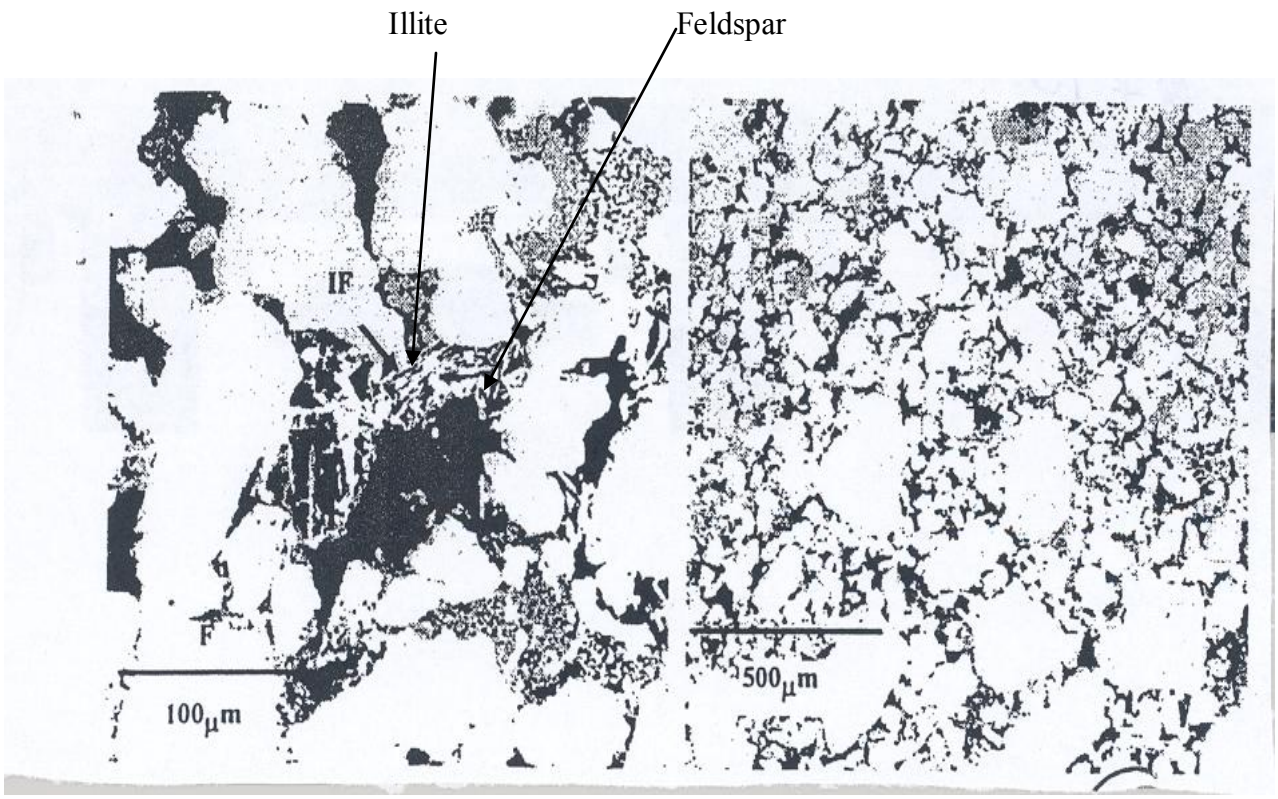

Figure 2.2: Fines particles at different scales: illite and feldspar

Based on the analysis of fines particles, it has been reported by Recham (10) that illite (a hydrous mica) can also swell when it co-exists with smectite as the analysis showed that illite like smectite, is a typical example of a 2:1 type of fines. It has several crystal structures and sometimes forms an irregular fibrous network (figure 2.2) in a pore space, reducing the capacity of fluid flow. The analysis concluded that pore damage in water-sensitive sandstone formations is predominately caused by fines particles. These include clay minerals which usually occur as loose pore-filling or pore-lining aggregates in the formation.

Since this research work focuses on fines migration in high permeability sands, it is important to understand what is meant by permeability.

2.2 Definition of Permeability

Permeability is the ability of a rock to transmit fluids, and is commonly measured in Darcies or milliDarcies (mD). Formations that transmit fluids readily, such as sandstones, are described as permeable and tend to have many, well-connected pores. Impermeable formations, such as shales and siltstones, tend to be finer grained or of a mixed grain size, with smaller, fewer, or less interconnected pores. Figure 2.3 shows how permeability of a core sample is measured (11). Although field practice use mD as a permeability unit, Darcy (D) is an SI unit of permeability.

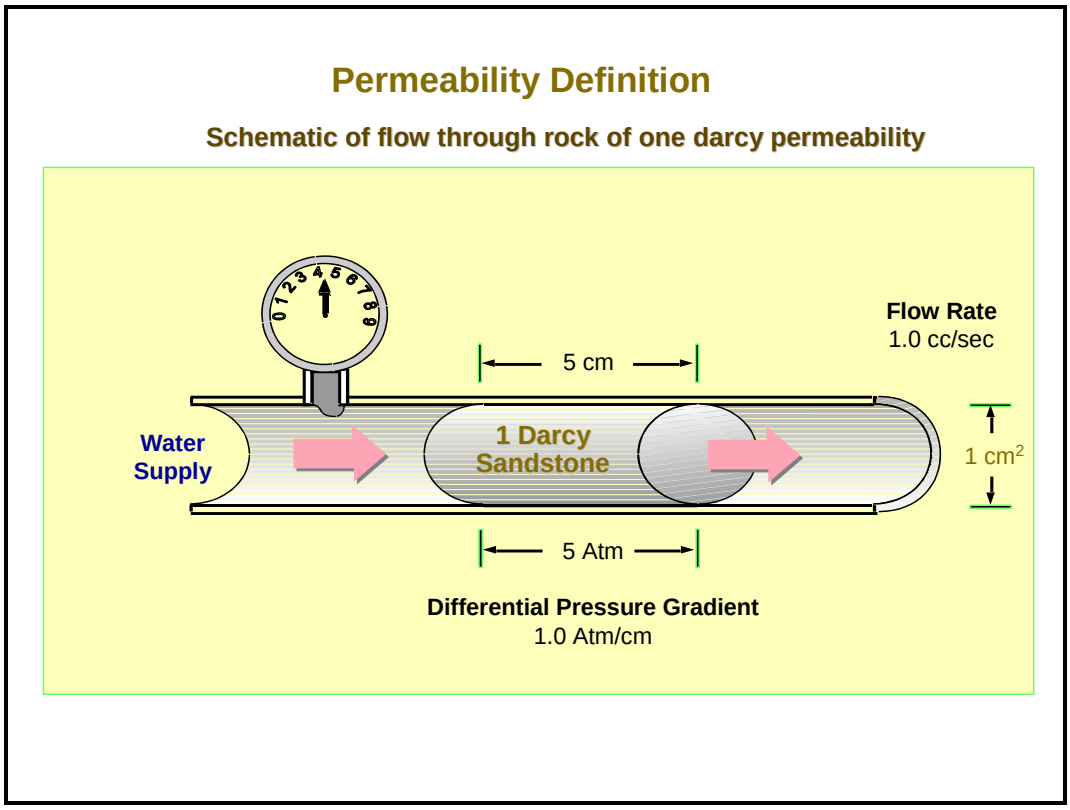

Figure 2.3: Core sample measurement of permeability

A Darcy is a permeability measure and is derived from the flow rate q in a porous medium as shown in figure 2.4. Hence refering to figures 2.3 and 2.4, one Darcy permeability is obtained when water having viscosity of 1 cP is flowing through a core sample having a cross sectional area of 1 cm^2 at a flow rate 1 cm^3 /sec, across which a differential pressure gradient of 1 atmosphere per cm length is generated.

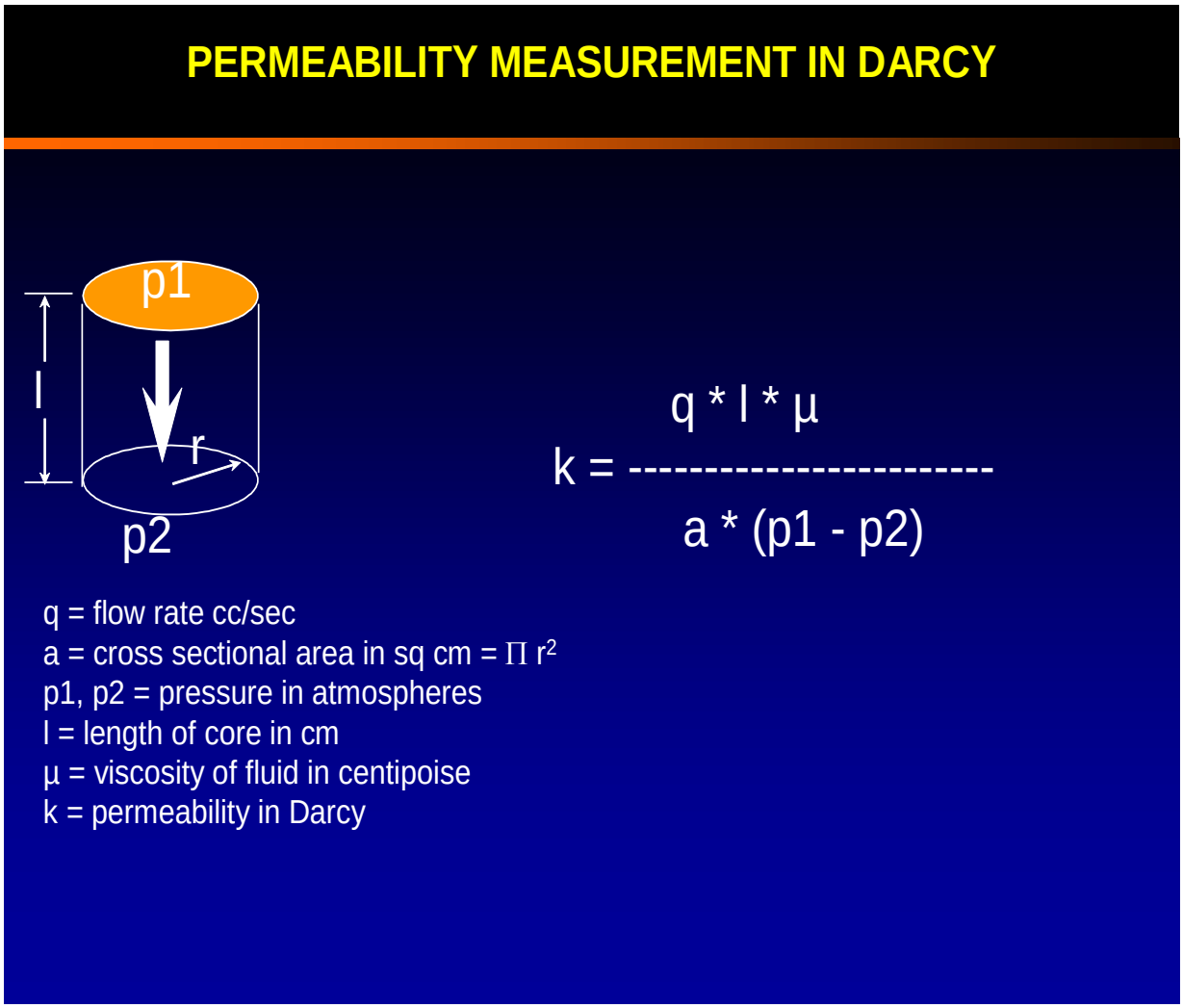

Figure 2.4: Equation used to determine permeability in Darcy unit

There are three different types of permeabilities which are measured in the oil and gas industry. Absolute permeability is the measurement of the permeability when a single fluid, or single phase is present in the rock.

Effective permeability is the ability to preferentially flow or transmit a particular fluid through a rock when other immiscible fluids are present in the reservoir (for example, effective permeability of gas in a gas-water reservoir). The relative saturations of the fluids as well as the nature of the reservoir, affect the effective permeability.

Relative permeability is the ratio of effective permeability of a particular fluid at a particular saturation to absolute permeability of that fluid at total saturation. If a single fluid is present in a rock, its relative permeability is the measured absolute permeability. Calculation of relative permeability allows for comparison of the different abilities of fluids to flow in the presence of each other, since the presence of more than one fluid may inhibit or increase the mixture flow. In other words flow rate of the mixture of oil and water due to oil-water emulsion and resultant mixture viscosity will be less compared to water flow rate on its own. If gas is added in the oil-water mixture, the resultant flow rate will increase.

Porosity which is a percentage or fraction of void to bulk volume of the rock, has a direct relation with permeability since pore spaces which determine fluid capacity if unobstructed will result in high permeability. Sandstone reservoir porosities range between 25% and 45% (11). Hence porous medium if obstructed say with fines particles, will result in a reduction in permeability. Permeability reduction due to particles movement is explained in section 2.2.1.

2.2.1 Permeability Damage due to Fines Movement

Following the permeability definition given above, permeability damage, or restriction to flow through natural flow paths in the reservoir, can be grouped into three types. These are absolute permeability damage, relative permeability reductions, and viscosity effects which are explained in this section. Absolute permeability damage is a result of particulate material occupying all or a portion of the formation pore spaces. This damage reduces the permeability and must be removed or bypassed to overcome its effect. Relative permeability changes or reductions often result in reduced permeability to the desired producing fluid. This change in relative permeability can occur due to the change in rock wettability (from an oil wetting to a water wetting) and/ or by the change in fluid saturations. These changes can occur when fluids

are pumped or circulated into the well for example during a workover, stimulation, logging or any activity requiring a well entry. Viscosity effect is referred to fluid emulsion rate increase on increased fluid viscosity in the reservoir formation fluids. The effect or impact to the fluids is reduction in fluid flow rates. Viscosity increase happens when emulsion causing fluids such as polymers which are more viscous than the reservoir fluids, are pumped into the well. They can result in restricted flow rates.

In addition, there are two more permeability related damages which are found in the literature. These are rate sensitive or non-Darcy skin effect and stress sensitivity, i.e., near wellbore drilling effects due to increased effective wellbore stresses and pressure drawdown during production. These were not considered as they are not within the scope of this research work.

2.3 Fines Migration

Fines migration is defined as the movement of fines particles which include clay, quartz particles or similar materials within the reservoir formation due to drag forces during fluid flow. The physical fines migration process is related to the motion of the particles and involves hydrodynamic forces which get stronger as the particle size increases (12). It happens when the fines particles which are loosely adhered to the pore wall surfaces are mobilized by dragging forces of flowing fluid (12). Hence fines are physically dislodged and carried by the fluid through the micro capillary pore structures of irregular internal diameters. Fines migration may result from an unconsolidated or inherently unstable formation, or from use of an incompatible treatment fluid that liberates fines particles. These particles which get mobilized during the fines migration process, should be removed to avoid near-wellbore pore damage. The reason being, within the hydrocarbon reservoir, a complex mixture of oil, gas, water and fines particles flow or migrate together through pore structures which should not be obstructed by

particles. Figure 2.5 shows Scanning Electron Microscope (SEM) images of kaolinite and mixed-layer clay particles plugging the pore spaces. Many reservoirs contain significant amount of potentially mobile fines. The images are of core (13) with partially degraded rock grains. The clay particles shown in the figure are surrounding pore sizes greater than 60 μm. Fines can be mobilised mechanically (fluid flow velocity) or chemically (pH change, salinity reduction, deflocculant invasion), however the mobilization impact on production is often worse after water flow increase.

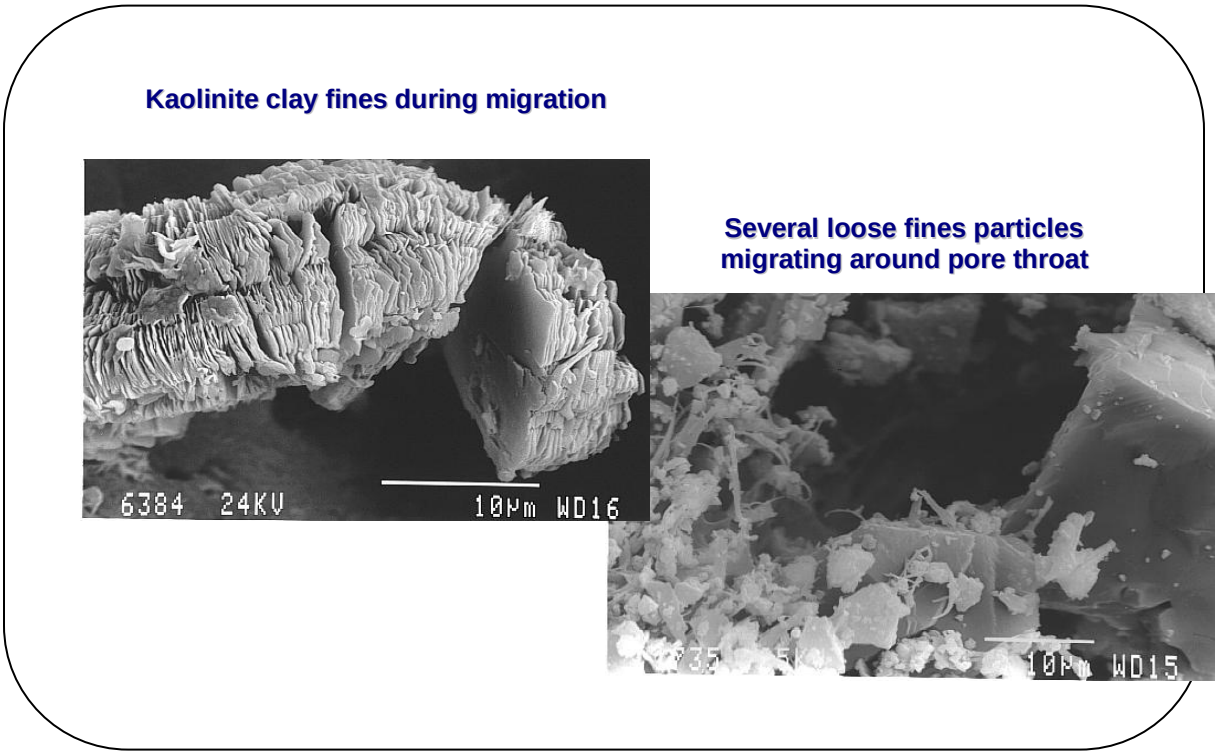

Figure 2.5: Fines particles plugging pore spaces during migration

The concept of fines mobilisation has been described by several investigators (13, 14, 15 and 16) based on a combination of experimental work, analytical approaches and numerical modelling. According to them, in order for fines migration to occur, physical activities and/or

chemical reactions in reservoirs must take place. This research work focuses mainly on the physical nature of fines migration and solid intrusion activities. Much of the related physical fines migration studies such as the work of Vasques et al (15), were conducted in core laboratories. Their studies which included fines mobilisation, concluded that fines migration usually occur as a result of mechanical dislodgement of fines particles loosely adhering to pore walls by flowing fluids. Such a process is considered to happen as a result of hydrodynamic flow turbulence (viscous drag) through the porous media which was observed during several core tests (15). The mechanical dislodgement action which depended on the ratio of pore diameter to grain size, was found to be affected by the viscosity and the fluid flow rate according to other core tests conducted at high flow rates (15).

2.3.1 Fines Migration During Well Operations

Formation fines can migrate during production and workover operations. During workover or completion operations, fines migration can take place due to changes in water salinity since the workover fluid‘s salinity will chemically impact the reservoir fluid‘s salinity. During production of hydrocarbon fluids, fines can migrate either when a critical flow rate (explained in section 2.3.2) is reached, or when water breakthrough into the hydrocarbon mixture occurs since the advent of water production instigates fines migration (16). In all cases, the outcome was pore plugging which resulted in permeability reduction which in turn caused pressure decline hence production impairment.

Figure 2.6 is a schematic which shows conditions causing particle depositions and/or plugging in pore spaces (17). Depending on the jamming ratio (the ratio of mean pore size to mean fines grain size) explained in sections 2.5.2 and 2.5.3, the particles may either migrate along the flow paths until they reach the wellbore, or accumulate due to factors explained in

those sections or get captured in pore throat constrictions. When particles cannot penetrate pore spaces, they accumulate and either form pore bridging, surface deposition or preferentially block the pore (size exclusion phenomena), as shown in figure 2.6. Suspended fines particles adhered to pore walls will reduce pore diameter, and subsequent pore blocking will happen as particles continue to accumulate (surface deposition). If the grains are much smaller than the pore throat diameter, they may migrate through easily hence no impact on pore size reduction; however, at very low velocities, the grain particles may get deposited (smooth deposition) due to gravitational forces. If some of the fines particles are larger than the pore throat size, then while the smaller can pass through, it takes one such large grain to plug the pore diameter stopping other particles from passing through (size exclusion). As a result of pore plugging, reservoir formation damage occurs which means reduction of permeability around a wellbore which is referred to as a ―skin factor" from which additional pressure drop created by the formation damage or impairment to the base permeability can be calculated.

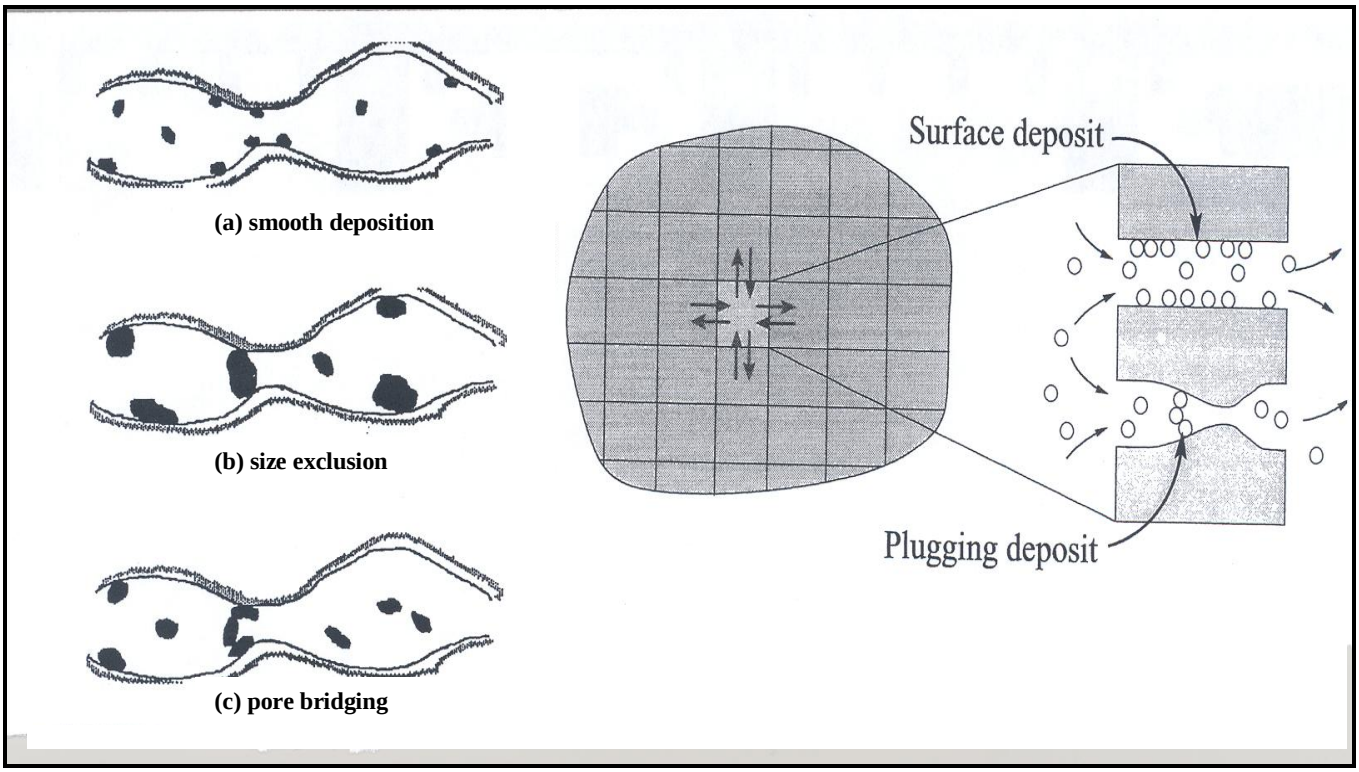

Figure 2.6: Conditions for particles deposition or passage through pore structures

Figure 2.6 diagrammatically shows situations which may or may not allow fines or solid particles to: (a) pass through pores, (b) get deposited in the pore throat structures and/or (c) plug pore spaces. Figure 2.7 depicts migrated fines particles and their impact on the reservoir production rates based on the PDO's Barik field core study (18). According to the study, low gravity solid concentrations, though may contain particle sizes smaller than pore throat diameter they may build-up at the pore constriction causing other particles to accumulate behind them (pore filling) especially at low fluid velocity and or high viscosity (< 20 m/hr velocity, >10 cP viscosity respectively). The study was conducted on a core sample recovered from a depth of 2768.7 m in June 2006. Types of fines analysed were: potassium Feldspar (F), Plagioclase (P), Clay fines (C) and Quartz (Q). While the upper image shows

particles magnification of 170x with a corresponding 20 μm scale, the lower image shows comparatively higher magnification of 550x with a corresponding 200 μm scale.

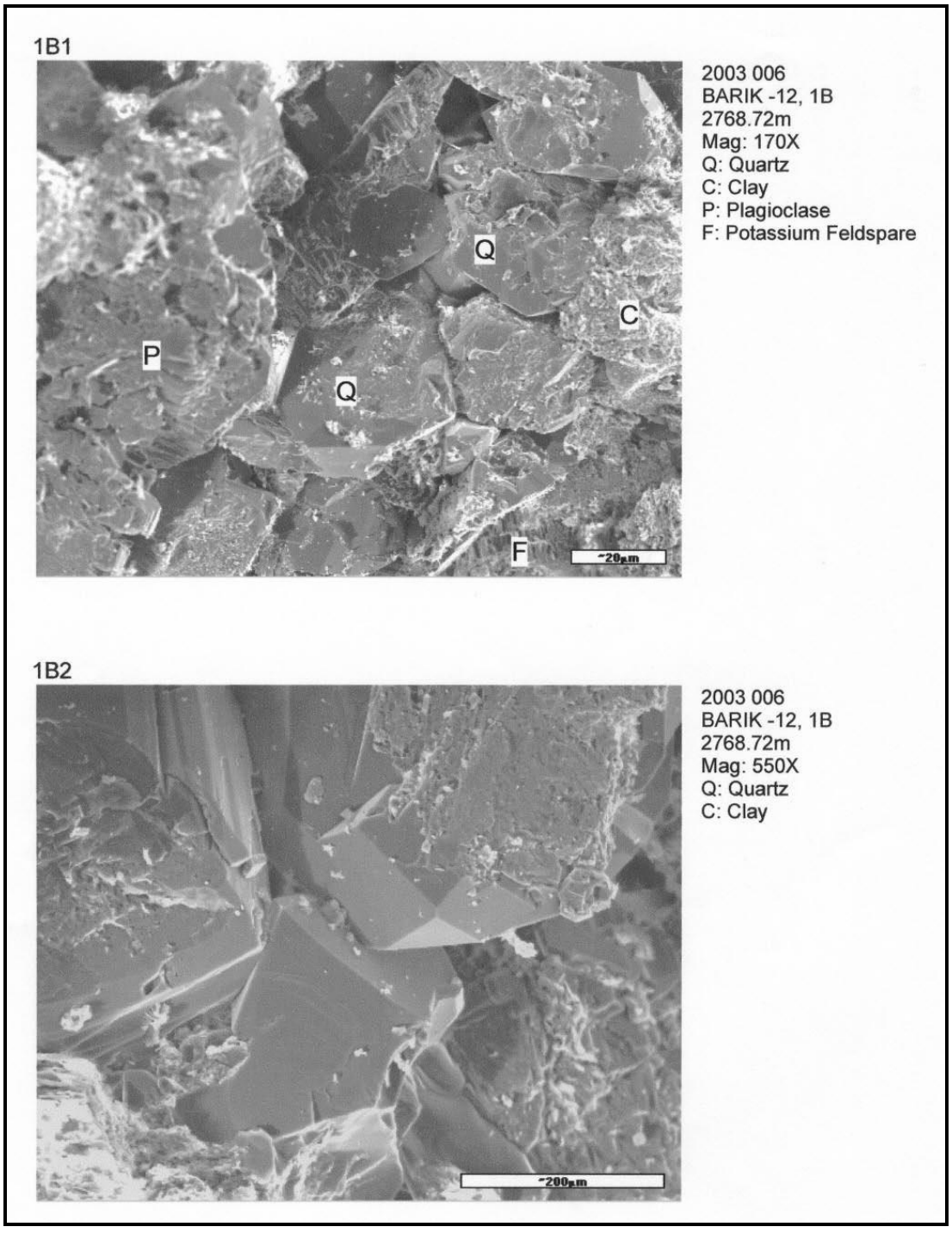

Figure 2.7: Migrated fines of different origin found in a PDO's well Barik-12

Fines migration studies on different rock wettability by Poynton et al, Recham and Schechter (19, 20, and 21), indicated that fines can also migrate in the non-wetting phase based on several core analyses which concluded that pore damage is associated with fines migration through water phase in an oil-wet pore structure surfaces of the rock pores. In those studies, kaolinites fines particles in the process were found to be released into aqueous fluids by fluid-fluid interaction which can take place in both wetting and non-wetting phases regardless of drilling mud type used. So in both mud types; oil-based mud (OBM) and water-based mud (WBM), fines migration occurs and causes pore structural damage. Very recently, this concept was thoroughly studied by Wagner et al (22) who reported success in applying a reversible oil-based reservoir-drilling fluid (RDF) the filter-cake of which reversed wettability from oil-wet to water-wet when exposed to an acidic fluid having disolved particles.

2.3.2 Critical Flow Rates Causing Fines Movement

Critical flow rate is the fluid flow rate above which fines influx may be mobilised along the fluid. Critical rates which depend on fines concentration in the fluid, have been analysed by Rahman, Arshad and Chen (23). According to them, the critical velocity of kaolinite suspension for particle concentration of 1000 ppm, is 0.28 cm/s (0.009 ft/s), and that a decrease in well performance occurs either due to high production flow rates (>10,000 b/d) depending on production duration, or fines swelling caused by water salinity related problems. However according to them, impacts of fines migration due to high injection or hydrocarbon production rates are more than the water salinity effect.

Since the onset of water production tends to dislodge and mobilise fines (16), water critical flow rates tend to be used as guidelines. Excessive water production (either due to water

influx from a water layer into an oil layer (–water coning") or injection water breakthrough from a nearby injector, will accelerate fines and sand mobilization in unconsolidated sandstone formations. According to Nguyen et al (24), –Production of large volumes of water, coupled with production of formation sand and fines from oil and gas wells, often curtail the reservoir potential production of hydrocarbon. It is therefore highly desirable to decrease the volume of water and mitigate the solids produced from producing wells". Water coning which results in excessive water cut production, is instigated by exceeding a critical production rate which several investigators tried to quantify. Smith et al (25) reported Meyer and Garder's studies on the critical oil rate at which water coning or excessive water production and hence particles movement acceleration could occur. From the studies, equation 2.3 may be used as a guide to determine the critical production rate at which a well can produce excessive water which will accelerate sand and fines particles production.

$$q_{wc} = \frac{0.001535(\rho_w - \rho_o)(k)(h^2 - D^2)}{\left\{\mu_o B_o \ln\left(\frac{r_e}{r_w}\right)\right\}} \quad \text{----------(2.3)}$$

Where:

q_{wc} = critical/maximum oil rate above which water coning happens (STB/d)

ρ_w = water density, lb/ft^3

ρ_o = oil density, lb/ft^3

k = formation permeability, mD

h = pay zone thickness, ft

D = perforation/completion interval thickness, ft

μ_o = viscosity of oil, cP

B_o = oil formation volume factor, Res bbl/STB

r_e = external drainage radius, ft

r_w =wellbore radius, ft

According to Van Everdingen et al (26), Barenblat and Entoy (27) as well as Geilikman et al (28), a solid particle is subjected to transient pressure gradient d_p/d_r when it is mobilised by hydrocarbon fluids during production. When a well choke is opened up (beaned-up) periodically it induces transient pressure gradient which causes reservoir damage even in wells with sand control measures. Based on their studies, d_p/d_r can be quantified and is expressed as follows:

$$\frac{d_p}{d_r} \approx \frac{(p_e - p_{wf})(t)}{\left\{\ln\left(\frac{\sqrt{a\eta t}}{r}\right)\right\}(r)} \quad \text{..... (2.4)}$$

Where:

$\frac{d_p}{d_r}$ is transient pressure gradient

pe is (far-field) external reservoir pressure

p_{wf} is flowing wellbore pressure

t is time

r is radius distance from wellbore

a is a constant and can be taken as 2.25 according to (28).

η the hydraulic diffusivity.

As far as field practices are concerned, most oil and gas operating companies tend to use historical observations and analyse them to maintain production rates at which minimal fines particles and/or sand production occurs. These companies include BP, Shell International, Marathon and Total. As a result local companies which are affiliated with those international

companies also follow similar guidelines (29, 30, 31, 32). Until 1998, Shell Operating companies worldwide had never confidently decided on critical gross production rates beyond which unacceptable fines/sand production may occur. Instead, they all set production limits based on observed produced fines/sand per crude volume produced. Hence "maximum allowable particles rate" in lb/ft^3 or in pptb (pounds per thousand barrels) from oil wells or in pounds per million standard cubic feet (lb/MMscf) from gas wells were established in at least six different companies located in different countries (Holland, UK, Nigeria, Oman, Malaysia and Brunei) mainly based on production history performance. For example, in Shell UK Limited, ranges of maximum gross production rates were defined for each maximum tolerable produced sand rate. The fewer the solid particles the well produced, the more total gross production was allowed from that well. As an example, for a well producing about 30 pptb of sand per day, less than 5000 barrel/day (b/d) was the gross liquid production limit set for it, meanwhile for a well producing about 10 pptb per day sand, 5000 – 15000 b/d was the allowable fluid production (30). Finally more than 15000 b/d was acceptable if a well produced sand at about 5 pptb per day or less. Other operating companies adapted a policy of progressive increase in hydrocarbon production rate as long as low to medium sand concentrations in the order of <1 lb/ft^3 is produced. This is especially the case in wells without sand control measures depending on surface facilities' robustness and the production strategy set in each company. In Shell International operations, subject to reservoir particle sizes, drawdown pressure and reservoir radius, the safe drawdown pressure range is considered to be between 500 psi and 1000 psi (33).

It is important to note that, in the oil and gas industry, reasonable care is usually taken in increasing the production rate of a well. The reason for this is that at certain critical

production rates, water influx and hence reservoir particles production are likely to take place. Hence beaning up wells (increasing production by opening the choke further) is a procedure which is carried out in accordance to production strategies defined in hydrocarbon and sand /fines particles management. This is based on the fact that transient pressure gradients generated with rapid production increase could mobilize fines and could damage the reservoir formation due to excessive drawdown pressure which may result. Recently, a new approach was developed in the Southern North Sea gas fields analysis which involved most of field's produced particles data to better manage sand issues which are associated with fines influx. According to McPhee et al (34), "It couples sand failure prediction, methodical and structured sand control selection (including consideration of production performance, longevity and risks) with novel solids lifting and erosion assessment models to better quantify the risk…"

The following is a review of wellbore particle injection impact on pore structures which resulted in pore plugging and thereby reduced production rates.

2.4 Fines Intrusion From Wellbore Into The Reservoir

From the wellbore, solid particle penetration or intrusion into the reservoir formation especially during water injection, drilling fluid circulation, completion fluid circulation, hydraulic fracturing, acid stimulation or workover operations can plug pore spaces and thereby impair the formation if particle size control through proper filtration is not carried out (35). Hence both injectivity as well as productivity could be affected since solid particle intrusion is a major cause of pore blocking. Damage types referred to as "external filter-cake", "internal cake" or "shallow/deep invasion" depend on the disolved solid's grain sizes used in the operation and other factors such as injection pressure, pore size and fluid viscosity (36). If proper pore size

distribution analysis is not done or is not used in selecting injected particle sizes along with the dissolving mechanism to achieve a particular objective, then the solid particles may cause reservoir impairment which will affect not only injectivity but also productivity of reservoir fluids. Such effects depend on several factors explained in this chapter in addition to jamming ratio impacts. The impact on production is dependent on pore size through which fluid and particle mixture flow. The higher the ratio the more the fluid will pass through. Jamming ratios and their impact on hydrocarbon production are explained in sections 2.5.2 and 2.5.3.

Injecting fluid into the well tends to result in particle accumulation not only at the wellbore sandface but also possibly into the reservoir vicinity and may cause injectivity reduction subject to the conditions explained below. The layer caused by particle accumulation is referred to as ‗skin' and causes resistance to liquid flow through it whether from the well into the reservoir in the case of fluid injection or from the reservoir into the wellbore in the case of fluid production. As a result, the well is considered to be suffering formation damage as explained in section 2.5.1.

In some cases, however, there could be a requirement to formulate an external filter-cake during the drilling or completion phase with an objective of keeping the borehole stable for installation and/or removal of drill-strings or completion tubulars. Thereafter attempts can be made to clean out the impermeable filter-cake before production/injection starts. In other cases an objective could be to achieve under-balance conditions needed to allow reservoir fluid to flow into the well. For example, if an under-balanced perforation is required, solids should be designed to penetrate pores, meanwhile hydrostatic pressure will be kept less than the reservoir pressure at the perforated interval.

2.5 Review of Pore Diameter Determination

Several techniques have been used to characterize pore structure as explained below. One of these techniques is Mercury intrusion porosimetry which is often used to characterize the pore structure. This technique is commonly used to measure pore size distributions. The theory of mercury porosimetry is based on the physical principle that a non-reactive, non-wetting liquid will not penetrate pores until sufficient pressure is applied to force its entrance. In this technique mercury is forced into pores under pressure and intrusion volume and pressure are measured (34). However, this technique detects only the pore volume and diameters of continuous and blind pores. None of the other torturous characteristics are measurable. Also, mercury intrusion requires very high pressures, which may significantly distort the pore structures of the core sample. Mercury used in this technique is harmful to one‘s health and pollutes the environment (35). Another well-known technique is Liquid Extrusion Technique. In this technique, a liquid whose surface free energy is lower than that of the gas is used to fill the pores of the sample. Because of the reduction in the free energy of the system the pores are filled spontaneously. A non-reacting gas is employed to force the liquid out of the pores. The gas can displace the liquid in a pore, provided work done by gas is equal to the increase in surface free energy required for the replacement of the low free energy

sample-liquid surface by the high free energy sample –gas surface (35). Both methods suffer from disadvantages. For instance, with liquid extruction only a mean pore diameter or a surface area can be measured and the method is only suitable when the porosity is high. With mercury intrusion it is possible to obtain a pore size distribution assuming that the pore space is composed of tubular structures with a cylindrical shape. However, in real core sample this

assumption is violated since the pores of a sandstone plug will have irregular shapes. This effect causes a bias in the pore size distributions as obtained with mercury porosimetry. With mercury porosimetry it is also not possible to find out what the real shape of the pores is. Numerically, pore diameter quantifications have been carried out by a few researchers (36, 37, 38, 39) who studied fines migration, pore plugging predictions and pore plugging damage mechanisms.

Dullien's analysis (36) showed that pore diameter depends on the square root of the ratio of permeability (κ) and porosity. According to him as per equation 2.5, pore mean diameter can be calculated as follows:

$$\lambda_\rho = \sqrt{\frac{\kappa * 32}{\phi}} \quad \text{..... (2.5)}$$

Where:
ϕ = grid block average porosity (fraction)

λ_ρ = Pore diameter (μm)

Blake and Kozeny (37), arrived at a different conclusion as far as pore diameter is concerned. According to them, it is a function of particle diameter D_F and porosity. Hence Blake-Kozeny's correlarion is as follows:

$$\lambda_\rho = \frac{D_F * \phi}{(3 * (1 - \phi))} \quad \text{..... (2.6)}$$

Where:

D_F = Mean fines particle grain size (μm)

Coberly (38) concluded that pore size simply depends on particle diameter divided by 6.5. Hence according to him:

$$\lambda_\rho = \frac{D_F}{6.5} \quad \text{..... (2.7)}$$

As explained in section 2.5.2, knowledge of pore size to fines size ratio $\frac{\lambda_\rho}{D_F}$ (jamming ratio) is important in analysing pore damage mechanism potential. Hence in each case, it is essential to determine possible mean pore diameter.

Kozeny (39) earlier considered that pore diameter λ_ρ is a square root of permeability to air (in mD). Hence $\lambda_\rho = \sqrt{\kappa}$. But the equation was later modified by Carman (40) as $\lambda_\rho = 0.95\sqrt{\kappa}$ which was later considered obsolete as it was found by Cargnel and Luzardo (41) not to be reliable enough. As an example, pore diameter (λ_ρ) determined by the Carman-Kozeny equation (which was later declared obsolete), was found to be over estimating the real value when it was validated by Cargnel and Luzardo (41) against a porous element whose permeability was 950 mD. When the porous element was measured using a Scanning Electron Microscope, the resultant pore diameter was 10µm. Applying the Carman-Kozeny equation, pore size was found to be 29.3µm which is almost 3 times more than the measured value. Hence the formula was found to be over estimating. However, Cargnel and Luzardo accept the Carman-Kozeny equation as a rule of thumb if the permeability to air is replaced with permeability to liquid which is always smaller. Furthermore in 1989, Pautz and Crocker (42) comparing the capillary pressure method with the modified equation concluded that mean pore diameter is not close or equal to the square root of permeability and that the jamming ratio is not a good indicator of permeability reduction.

2.5.1 Determination of Pore Blocking Damage Mechanisms

Pore damage determination based on comparison between fines grains diameters and pore size were established by researchers who defined damage mechanism using correlations (43, 44) which are summarized as follows:

If ($D_F > (0.33 * D_P)$),"Instant bridging/ external filter cake"----------(2.8)

If (($0.1 * D_P$)< D_F <($0.33 * D_P$)),"Invasion & deposition" ---------- (2.9)

If ($1/7 * D_P < D_F < 1/3\ D_P$), "Invasion & Internal filter-cake formation" ---------- (2.10)

If ($D_F < 1/7 * D_P$), "There is no formation damage expected" ---------- (2.11)

Where:

D_F = Fines grain size (μm)

D_P = Pore diameter (μm)

ϕ = grid block average porosity (fraction)

Furthermore, pore blocking damage mechanisms were determined based on other published correlations by several other researchers (45, 46, 47, 48). Although the criteria are similar to those used for the gravel packs and particles, in this case they are referring to fines particles and pore sizes. The correlations are summarised as follows:

If (D_P / D_F) >15, "no interaction",---------- (2.12)

If ($10 < D_P / D_F < 15$), "Pore filling",---------- (2.13)

If ($6.5 < D_P / D_F < 10$), "Internal bridging/single pore blocking",---------- (2.14)

If ($5 < D_P / D_F < 6.5$), "Shallow internal bridging",----------(2.15)

If ($D_P / D_F < 5$), "External cake/ no invasion"---------- (2.16)

If ($D_F > (0.33 * D_P)$),"Instant bridging", ---------- (2.17)

If (($0.1 * D_P$)< D_F <($0.33 * D_P$)),"Invasion & deposition") ---------- (2.18)

2.5.2 Review of Jamming Ratio: Concept of Pore Plugging

Based on the studies carried out by Oyeneyin et al (45) involving gravel-sizing for effective sand control design and evaluation, a summary of ways of determining pore plugging mechanisms is given in table 2.2.

Table 2.2: Pore plug mechanisms based on jamming ratios

If $(D_G/D_F) > 15$	then the state of "No interaction" will occur.
If $(10<D_G/D_F<15)$	then a state of "Pore filling" is possible.
If $(6.5< D_G/D_F <10)$	then "Internal bridging" may occur.
If $(5< D_G/D_F <6.5)$	then "Shallow internal bridging" may happen.
If $(D_G/D_F <5)$	then "External/ no invasion" may happen.
If $(D_F> 0.33\ D_P)$	then "Instant bridging" should be expected.
If $(0.1\ D_P <D_F<0.33\ D_P)$	then "Invasion & deposition" is likely to happen.

Where:

D_G = Gravel mean diameter

D_F = Fines mean grain size

D_P = Pore mean diameter

Tables 2.3 and 2.4 are examples of how to determine pore plugging mechanisms in various gravel pack sizes and various fines particle grain sizes based on the principles reported in (45, 46, 47).

Table 2.3 : Pore Plugging Mechanisms of 50µm fines and various gravel packs

Gravel type	Gravel mean-size (millimetres)	Gravel mean-size (inches)	D_G/D_F	Possible Pore blocking Mechanism
#12/20	1.13	0.044	22.6	No interaction
#20/40	0.584	0.023	11.68	Pore filling
#30/50	0.464	0.018	9.28	Internal bridging
#40/60	0.332	0.013	6.64	Internal bridging
#50/70	0.26	0.010	5.2	shallow internal bridging

Table 2.4: Pore Plugging Mechanisms in #20/40 (0.584mm) gravel D_G due to various fines sizes

Fines size (microns)	Fines size D_F (mm)	D_G/D_F	Possible Pore blocking Mechanism
30	0.03	19.47	No interaction
50	0.05	11.68	Pore filling
80	0.08	7.30	Internal bridging/single pore blocking
100	0.1	5.84	Shallow internal bridging
120	0.12	4.87	External / no invasion

2.5.3 Review of Uncertainties of Jamming Ratios

Jamming ratio is based on the ratio of mean pore diameter to mean fines diameter (D_P/D_F). It has been pointed out by several researchers that the jamming ratio analysis is quite subjective. Example of conditions for fluid passage identified by several investigators can be

summarised as follow: Abrams (49) presented the following empirical criteria for permeability impairment due to suspended solid particles:

a) If $D_F > D_P/3$, particles can bridge pores immediately and form external filter-cake

b) If $D_P/7 < D_F < D_P/3$ particles can invade the formation and form internal filter-cake.

c) If $D_F < D_P/7$ there is no formation damage expected.

Other researchers such as Velzen and Leerlooijer (50) having analysed the above jamming ratio criteria, found them to be not satisfactory. According to them, particle grain size of $1/3^{rd}$ of D_P is too large since even less than that was found to be causing instant bridging. They suggested that the ratio should be between $1/4^{th}$ and $1/3^{rd}$ of D_P. Other investigators such as Pautz and Crocker (51) considered $1/5^{th}$ whereas Zhang et al (52) suggested $1/8^{th}$ of D_P as a minimum grain size if particles are to penetrate pores. Hence it should be clear that the jamming ratios (D_P/D_F) are just indicative of particles possibility of entering estimated pore diameter. Correlations used to estimate pore diameter (explained in section 2.5) are also subjective as they have been compared with laboratory analyses and were found either over estimating or underestimating the measured pore sizes. Uncertainties on formation damage mechanism identifications exist, since different jamming ratio criteria based on different correlations are used. Table 2.5 summarises the criteria used. Mathematical expressions of the four correlations in table 2.5 are given in section 2.5.

Table 2.5: Pore Plugging Damage Mechanisms based on jamming ratios

Correlation	If $\frac{D_P}{D_F} \geq$	Damage Mechanism
Coberly	6.5	External cake/Shallow internal bridging
Blake-Kozeny	4.5	External cake/No invasion
Dullien	3.3	External cake/No invasion
Carman-Kozeny	1.0	External cake/No invasion

2.5.4 Review Of Formation Damage Caused by Various Factors

Formation damage near and around the reservoir section open to the wellbore may happen if one of the following or a combination of them occur:

i) Injecting liquids with solid particles which have diameters greater than or similar to or slightly less than formation pores. The size ratios and their uncertainties are discussed in sections 2.5.2 and 2.5.3.

ii) If the injected fluid is incompatible with the reservoir fluids, it is likely to result in solid precipitates which will affect the injectivity by plugging formation pores.

iii) If bacterial growth develops (both aerobic and anaerobic), it will form an impermeable layer, and hence injection rate reduction will result.

The following are rock and fluid properties which are directly related to formation damage. If they get affected and their properties changed by the drilling process or water injection process, formation damage is likely to occur:

mechanical properties of formation,

pore stress magnitude and orientation,

pore pressure,

porosity—primary and secondary,

permeability,

formation fluids,

formation temperature,

formation mineralogy.

The mechanical properties, pore stress magnitude and orientation all relate to wellbore stability and may dictate drilling and well completion requirements to maintain a stable hole and well control, especially in highly deviated and horizontal wells. Significant overbalance pressure can cause fluid invasion and damage. In some cases, these formation imparement may also indicate that wells could be drilled underbalanced, possibly preventing considerable formation damage while drilling (thus possibly eliminating the need for acidizing after initial production). Additionally, pore pressure is important since it helps in restricting fluid invasion and assists in removing damage if it has occurred. Porosity and permeability are the most significant formation properties as far as production rates are concerned; hence formation damage will be a result of their damage.

As stated in clause ii) in this section, incompatibility between injected fluids and reservoir formation fluids tends to result in solid precipitates if appropriate conditions of reservoir temperature, pressure and mineralogy prevail.

2.5.5 Reservoir Formation Damage due to Fluids Injection

Studies carried out by Economides et al (53), suggest that drilling mud particle damage is estimated to penetrate reservoir formation layer a length ranging between 1" and 12" (1ft) whereas drill filtrate goes further and can penetrate up to 6ft of formation. According to them, the filtrate could have reached further but as initial filtrate builds up, it slowly prevents subsequent filtrates and becomes logged or saturated decreasing further filtrate invasion.

Based on studies carried out by Patchett et al (54), solid particle intrusion and mud filtrate can cause pore bridging if particle sizes are $1/3^{rd}$ to $1/7^{th}$ of the pore throat or larger. According to them, damaged absolute permeability studies revealed that mud filtrate invasion resulted in 10-90% permeability reductions. Determination of the extent of permeability damage (k_d) was carried out in 2001 by Karacan et al, (55). They found out that, k_d was a function of and is proportional to average pore diameter, pore area and number of pores per cubic inch. Hence:

$$k_d \cong f\left\{F\int_0^{\infty} A^2\eta_p(A)dA\right\} \text{ ----------(2.19)}$$

Where:

F = Average pore diameter (in) multiplied by a tortuosity factor

A = Area of pore (in^2)

η_p = Number of pores per cubic inches (N/in^3).

k_d = Damaged absolute permeability (unit depends on proportionality constant)

According to Millhone's studies (56), to avoid formation damage, it is recommended to inject completion fluid particles of < 2 μm in the order of 2ppm or less.

2.5.6 Impact of Particles on Water Injection Rate in Horizontal Wells

Studies carried out by Suryanarayana et al (57) showed that both horizontal and vertical permeabilities have direct impact on injection rate. According to them, the directional permeabilities (k_x, k_z) values are critical in the study of horizontal well injection or production and are directly affected by injected particles. The studies revealed a method of calculating water injection invasion rate given in equation 2.20. Based on equation 2.20, the larger the

permeability, the higher the injection rate in barrel per day (b/d) (57). The reservoir model in this case is divided into grids where M is the total number of grids in the model.

$$q_w = \sum_{i}^{M} \frac{2\pi\Delta h_i \sqrt{k_x k_z k_{rw}}}{\{\mu_w \ B_w \ \}\ln\left(\frac{r_i}{r_w}\right) + S} \{p_i - p_{wf}\} \text{ ----------(2.20)}$$

Where:

q_w = water injection/ invasion rate (b/d).

M = the number of grids in the reservoir model.

S = skin factor

r_i = radius of grid (ft)

r_w = wellbore radius (ft)

B_w = water formation volume factor (res bbl/STB)

μ_w = water viscocity (cP)

k_x = horizontal permeability (md)

k_z = vertical/ z-direction permeability (md)

k_{rw} = relative water permeability (dimensionless)

Δh = reservoir thickness (ft)

pi = injection pressure (psi)

p_{wf} = bottom hole pressure (psi)

As explained in section 2.5.3, extra care needs to be taken so that ideal particle sizes can be selected and properly disolved in the injection fluid in order to avoid the creation of impermeable layers which are detrimental to the injection process. The reason being, formation of filter-cake for example during drilling, is associated with filtrate loss of the drilling fluid escaping into the borehole formation leaving solids (clays etc.) behind. With

time the solids will build-up on the wellbore surface depending on particle size circulation velocity and pore diameters. As elaborated in sections 2.5.2, 2.5.3 and 2.5.4, if the pore size distribution is much larger than the solid particles in the fluid mixture, a deeper invasion of fluid and particles can occur in permeable zones. Otherwise, if particle sizes are larger than pore sizes deposition of fine solids on the wellbore face will take place. As the invasion increases, the thickness of the filter cake also increases until a strong impermeable filter-cake layer is formed which will prevent further invasion of liquid. Although during drilling the filter cake or mud cake is required to strengthen the wellbore surface thereby preventing the formation caving-in, however, there is a great chance of causing formation damage of various degrees depending on filtrate invasion depth and the size of grain particles penetrated into the pay zone. Temporary removable shallow invasion may be favoured if the well is completed with an IGP (internal gravel pack) to minimise fines and sand blocking the gravel pack. Deeper invasion is always detrimental as it will prevent hydrocarbon fluid movement from the reservoir to the wellbore or vice versa. In the case of water injection, like in workover fluid circulation, if proper pore size distribution analysis is not done to determine optimal solid particle sizes, formation damage caused by particle invasion is likely to occur. The depth of invasion of solid particles from the wellbore into the formation is dependent on the distribution and size of formation pores, pore structure, injection rate, viscosity, shape and size of the particles (58). Favourable ratios of pore size to particle size are discussed in sections 2.5.2, 2.5.3 and 2.5.4. Hence fluid movement from the wellbore into the formation is restricted by pore diameter and particle size injected, and in the worst case even injectivity can be prevented although the filtrate can penetrate further. Studies carried out by

Economides et al (59), showed that depth of mud filtrate invasion with time can be calculated as follows:

$$r_p = \sqrt{(r_w^{\,2}) + (2r_w/\phi)(2C\sqrt{t}) + 360byt)} \quad \text{----------(2.21)}$$

Where:

r_p = radius of penetration or depth of mud filtrate (in)

r_w = well-bore radius (in)

ϕ = porosity (fraction)

C = dynamic fluid loss coefficient ($in^3/in^2\text{-}hr^{1/2}$)

t = exposure time (hr)

b = constant accounting for mechanical stability of the filter cake (cm^3/cm^2).

y = mud filtrate shear rate at the wall (sec^{-1})

Equation 2.21 does not account for particles size though it accounts for porosity. In this case only the dynamic fluid loss coefficient (C) is associated with jamming ratios. Studies on formation damage mechanisms by Barkman and Davidson (60) indicate that there are four types of wellbore induced formation damage:

a) Wellbore narrowing or external filter-cake formation, b) Particle invasion or internal filter-cake formation, c) Wellbore fill-up, and d) Perforation plugging

These damage mechanisms are summarised in Figure 2.8. The white section in the figure is the wellbore which ideally should be unobstructed to maximise fluid injection volume. The black bar denotes a layer of solid particles accumulation invading the reservoir denoted by light green zone. Depending on the size of the suspended solid particle sizes versus the reservoir‘s pore sizes through which liquid and particles are injected, the particles may or may not penetrate. Hence they may or not get accumulated outside the reservoir at wellbore face despite fluid penetration through the reservoir. This phenomena is called filter-cake formation on the face of the wellbore which will reduce or narrow wellbore space as shown

in part (a) of the figure 2.8. If the solid particles were smaller than pore sizes, the particles could have penetrated or invaded the reservoir resulting in internal filter cake and pore bridging as shown in part (b) of the figure. Part (c) shows gravitational effect on solid accumulation at the bottom of the well normally caused by low injection rate and / or much bigger solid particle sizes compared with pore sizes. In this case the well will be filled up with particles. Part (d) shows a perforation done by an explosive to allow reservoir hydrocarbon fluid to flow from the reservoir into the wellbore. Since perforation is done while the wellbore is filled with fluid mixed with some solid particles, the particles can be forced to pass and accumulate deeper into the reservoir resulting in plugging some of the reservoir pores if the perforation process is done in an over-balanced pressure condition.

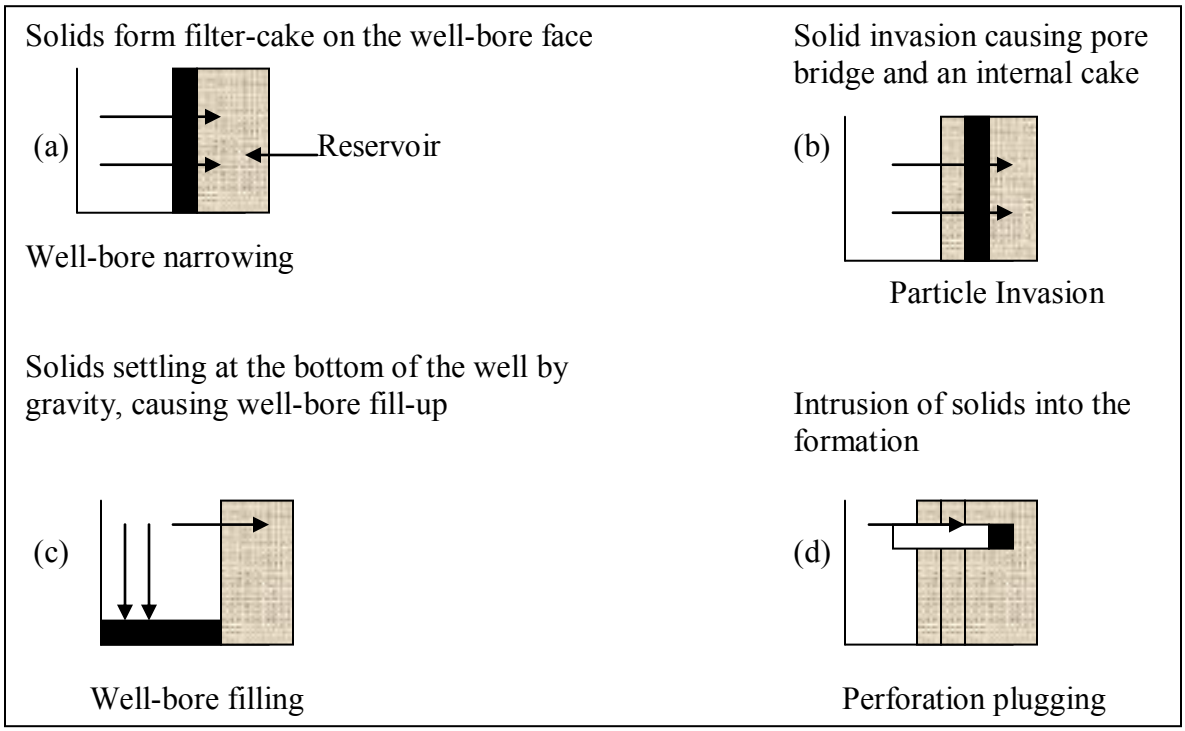

Figure 2.8: Formation damages according to Barkman and Davidson (60)

Review of fines migration and its impact on reservoir fluid flow, suggests that there are opposing conclusions as far as particle penetration through pores and particle pore blockage are concerned. For example, studies by Gruesbeck and Collins (61) concluded that fines entrainment is directly proportional to the flow rate. However, this concept was disproved by

Wojtanowicz et al (62) who claimed that fines particles release is not a linear function of velocity. Rather it depends on two factors: i) the mechanism with which the fines particles are released and deposited, as well as ii) the available quantity of suspended particles ready to be mobilised.

Donaldson and Baker (63) stated that there are three factors which cause gradual stoppage of particles that initially entered large pore spaces. The factors are: i) sedimentation, ii) direct interception and iii) surface deposition. According to them, plugging of pores is a result of the combination of internal blockage of pores and filter-cake build-up. They appear to support the claim that particle release is directly proportional to the velocity of the fluid.

Particle filtration tests were carried out by Vetter et al (64) who concluded that any particle size can cause formation damage. According to them particle grain sizes as small as 0.05 microns (μm) to 7 μm can result in formation damage. Depending on velocity, the smaller particles (sub-microns) can cause gradual permeability decline while they penetrate deeper into the formation. In this case, depth of penetration is directly proportional to the fluid velocity.

The studies suggest that, the bigger particles result in rapid permeability decline and do not penetrate deeper into the formation. The authors also state that, although the particles causing external cake usually cannot invade the formation deeply, such an invading process causes extremely severe formation damage near the wellbore.

Studies carried out by Oyeneyin et al (65) identified the following pore blocking damage mechanisms:

(i) Gradual pore blocking mechanism

(ii) Single pore blocking mechanism

(iii) Internal cake formation

(iv) State of no clog (No invasion)

(v) Process of self filtration (Internal filter cake)

(vi) State of clog (Gradual Invasion).

Details of how to determine each of the mechanisms are given in sections 2.5.1-2.5.3.

2.6 Causes of Formation Damage Observed in the Oil and Gas Industry

Most hydrocarbon unconsolidated sandstone fields happen to suffer fines particles production problems depending on how the production is managed. Though it is a common problem, causes happen to differ from one field to another. For example, the major root causes of formation damage identified in a West Coalinga (California) field according to studies carried out by Tague (66) are summarised as follows:

1. Fines migration occurs due to the presence of uncemented, or weakly cemented clay particles.
2. Extremely fine grain sized sand particles entry usually takes place due to the unconsolidated and poorly sorted nature of particle sizes mobilised by the reservoir fluids.
3. Clay swelling of smectites and migration of illite clays tend to happen upon contact with fresh water. Both smectites and illite clays are naturally occurring particles in sandstone (clastic) reservoirs.

While those are typical to the West Coalinga field, studies carried out in Shell International operated oil fields (67) concluded that the use of slotted liners in Nigeria, Malaysia, Oman and Brunei created several unique forms of potential formation damage. According to the studies the first potential source of formation damage identified as clay swelling was caused

by the fresh water foam used in drilling. Hence it was concluded that, if the foam quality is not monitored or closely controlled, there is likelihood that fresh water could be pumped into the producing interval leading to clay swelling and clay migration hence pore space constriction as well as liner slot plugging.

Several reports (68, 69, 70) demonstrate that sand and fines migration can lead to rapid production declines from wells completed with slotted liners, pre-drilled liners and wire-wrapped screens, due to the ability of the sand and fines to act as plugging agents which tend to reduce reservoir fluid inflow into the well. In addition to sand and fines migration, compositional analysis of the produced water was identified as another probable source of formation damage particularly when mixed with injected water of different composition resulting in precipitates such as calcium carbonate scale and/or barium sulphate scale which is most difficult to remove (70). Iron sulphides and other corrosion related products are also considered a possible source of formation damage due to the presence of hydrogen sulphide (71). All of these formation damage causes are sometimes classified as primary plugging agents that are capable of reducing reservoir fluid flow in the near wellbore region through narrow openings of sand control measures such as slots of the liners. In the near wellbore region, several other potential forms of formation damage were identified including wettability alteration and emulsions. These were considered likely especially in hydrocarbon fields having high asphaltene content of the oil.

One of the major causes of fines particles accumulation is a high production rate through partially perforated (limited completed) reservoir interval which may result in high flow velocities, promoting mechanical dislodgment of formation fines (71). Once fines have been detached from the pore walls they migrate and clog at pore throats impairing permeability

and thus reduce well productivity. This behaviour is evidenced by a decline in both flowing tubing head pressure and production rate with time. In the case of artificially lifted wells, especially using electrical submersible pumping (ESP) systems, if this situation is not corrected or prevented, the drop in production inflow may lead to insufficient intake pressure rendering inefficient operation of the pump and consequently a premature pump failure is likely to happen (72).

Reports from the oil and gas industry‘s major companies (73) agree on the types of well operational activities which induce formation damage or impairment. According to them, the activities that reduce well inflow and injectivity potentials can occur during the following phases of a well‘s life cycle:

Drilling: Reservoir formation damage or impairment is caused primarily by the ingress of solids in the drilling fluids into pore structures which tend to be blocked due to uncontrolled solids particle size in the absence of proper filtration. Also damage tends to occur due to bit crushing of the formation during drilling operations. In addition in some cases due to incompatibility of the drilling fluid with the formation fluid, solid precipitates are formed which clog formation pores thereby affecting injectivity and productivity.

Completion: Reservoir formation impairment can also be caused by the fluids and solids circulated in the well during completion operations. Excessive solid and filtrates not only impair formation pores which cause inflow or injectivity reductions but also plug completions components including sand control equipment such as wire–wrapped screens, gravel packs, pre-packed screens, expandable screens, pre-drilled liners and slotted liners depending on the amount, concentration and size of solid particles injected in the completion

fluids versus slot sizes or flow space available in the sand control measure. However, what goes into the pores does not plug screens when it flows out.

Water flooding: pore structure impairment caused by particulates in the injection water or by incompatibility of the injection water with the formation fluids has been observed via reductions in injectivity indices. To avoid or minimise injection reduction, proper procedure is required to filter out all particles which may plug pore spaces. Solid intrusions and their impact to pore spaces were elaborated in section 2.4.

2.7 Fines/ Sand Management Practices in the Oil and Gas Industry

Having analysed produced solid particle management processes in many exploration and production (E&P) companies such as Shell, Petroleum Development Oman, SPDC, Total, Daleel Petroleum, Petrogas, Exxon Mobile, BP, Amoco and a few others (74, 75, 76, 77), there are no dedicated practical fines control measures. Rather there are sand control measures which are explained below. The reasons for discussing sand control are three fold:

a) Definition of fines as given in section 2.1 covers particle sizes discussed below which are regarded as fines although other people refer to them as sands.

b) Through the process of controlling coarser grained (sand) particles, the finer particles to some extent get restricted too.

c) Because the industry has observed reduction in flow capacity by further reduction in finer sand particles, so far the fines management strategy allows for fines production to avoid related production deferment due to fines restrictions; hence sand control strategy is part of fines control process.

Today fines and sand managements are carried out differently in different areas. However, many oil field operators attempt to control fines and sand productions by choke adjustments,

drawdown pressure control, water shutoff, downhole sand control installation and by the use of surface installed abrasion resistant particle filters such as ‗desanders' etc.

Since well operations such as production, water injection, acid stimulation, fraccing, scale inhibition and so forth, can instigate fines migration which can cause formation impairment, several attempts and measures are in place to mitigate resultant formation damage.

One of the common practises in managing fines-affected/sand production is called a ‗**bean-down**' approach or choke size reduction to reduce production once solid particles are observed on the surface. Depending on facilities available to monitor sand production, once fines concentrations reach a set threshold amount in lb/ft^3 are detected, based on production operation policies of the company, beaning down (reduction of) production takes place automatically or manually. It should be realised that beaning down production is not a cure for particles influx; it rather reduces particles production which otherwise may not only cause pore blockage, but also may result in abrasive erosion of completion accessories due to corresponding velocity rates depending on reservoir pressure or lifting pump pressures. Particles erosion of completion components or pump internals will eventually affect well integrity as a result not only production will be lost but also may end up in an unsafe operation.

In most cases, ‗bean-down' or drawdown pressure control is carried out by choke size reduction on surface. Some operators use downhole chokes operated from surface near wellheads.

Water shutoff is another effective means of particles influx reduction since the advent of fines influx is accelerated or at least instigated by excessive water production as explained in sections 2.3, 2.3.1, 2.3.2 and 2.4. Hence water shutoff normally reduces fines production.

The challenge is to avoid/ minimize –in situ" water channel and preventing it from percolating through other perforations or other producing layers which previously had been producing less water. In a well having cemented production casing, this may happen either in the absence of a geological barrier (e.g. shale layer) or if cement isolation behind the casing is not adequate. In open-hole completion cases, external casing packers (ECPs) as well as swelling packers are being used in horizontal wells. However, in the majority of artificially lifted wells other than gas-lifted ones, identification of water influx zone is very costly and may not be possible in some cases due to access difficulties while the well is kept on production based on completion type and in some cases completion inclination, size and depth vs. available logging tools. Nowadays use of expensive by-pass tubulars called _Y-tool' in electric submersible pump (ESP) wells permits well entry. Recently operators such as Petroleum Development Oman, started to complete wells with two completion strings in wells lifted using sucker rod (beam) pump. One is used as a well entry tubing while the other is used as a producing tubing. Thus identification of the water zone by itself remains a challenge. Moreover, even when water influx is identified, depending on the geological complexity of the zone, sometimes it may not be possible to shutoff the water zone mechanically or chemically.

As far as **sand control measures** are concerned, almost all downhole sand control measures contribute to major inflow reduction. However, their advantages include sand particles influx minimisation and wellbore containment which are helpful in terms of well productivity, accessibility say for logging, cleaning or any remedial action. The common mechanical sand control equipment includes: expandable sand screens (ESS), wire-wrapped screens (WWS), internal gravel packs (IGP), external gravel packs (EGP), conventional slotted liners (SL),

keystone slotted liners, pre-packed screens, pre-drilled liners (PDL), meshrite (premium screen) and so forth. One example of an area which employs such measures in unconsolidated sandstone reservoirs is PDO (Petroleum Development Oman). Oil production contributions derived from such control measures are shown in figures 2.9 and 2.10 which also show sand control varieties and percentage utilisation of each type in Oman‘s PDO fields (78). These are typical control measures found in many other fields worldwide.

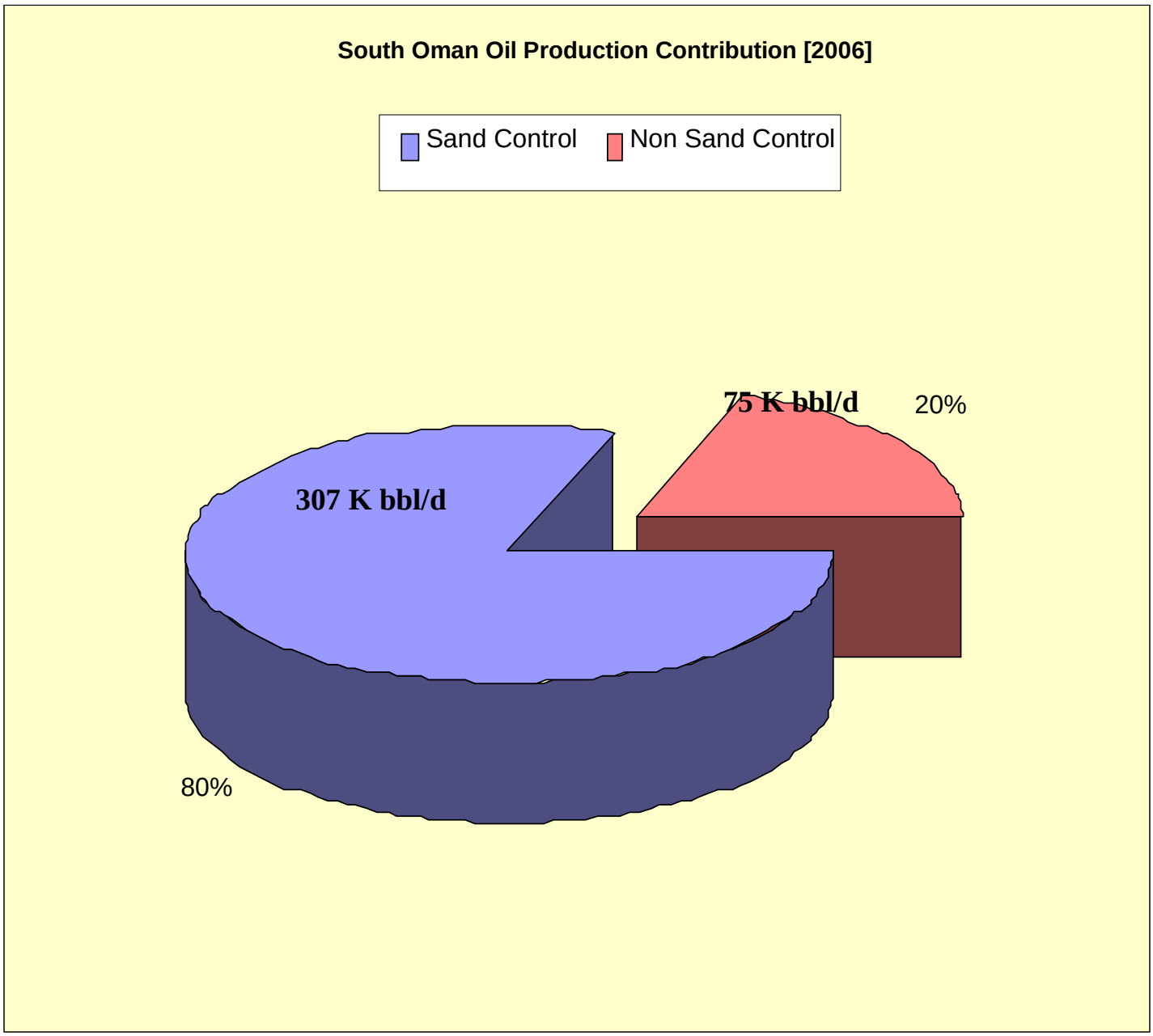

Figure 2.9: PDO's South Oman oil production affected by sand particles.

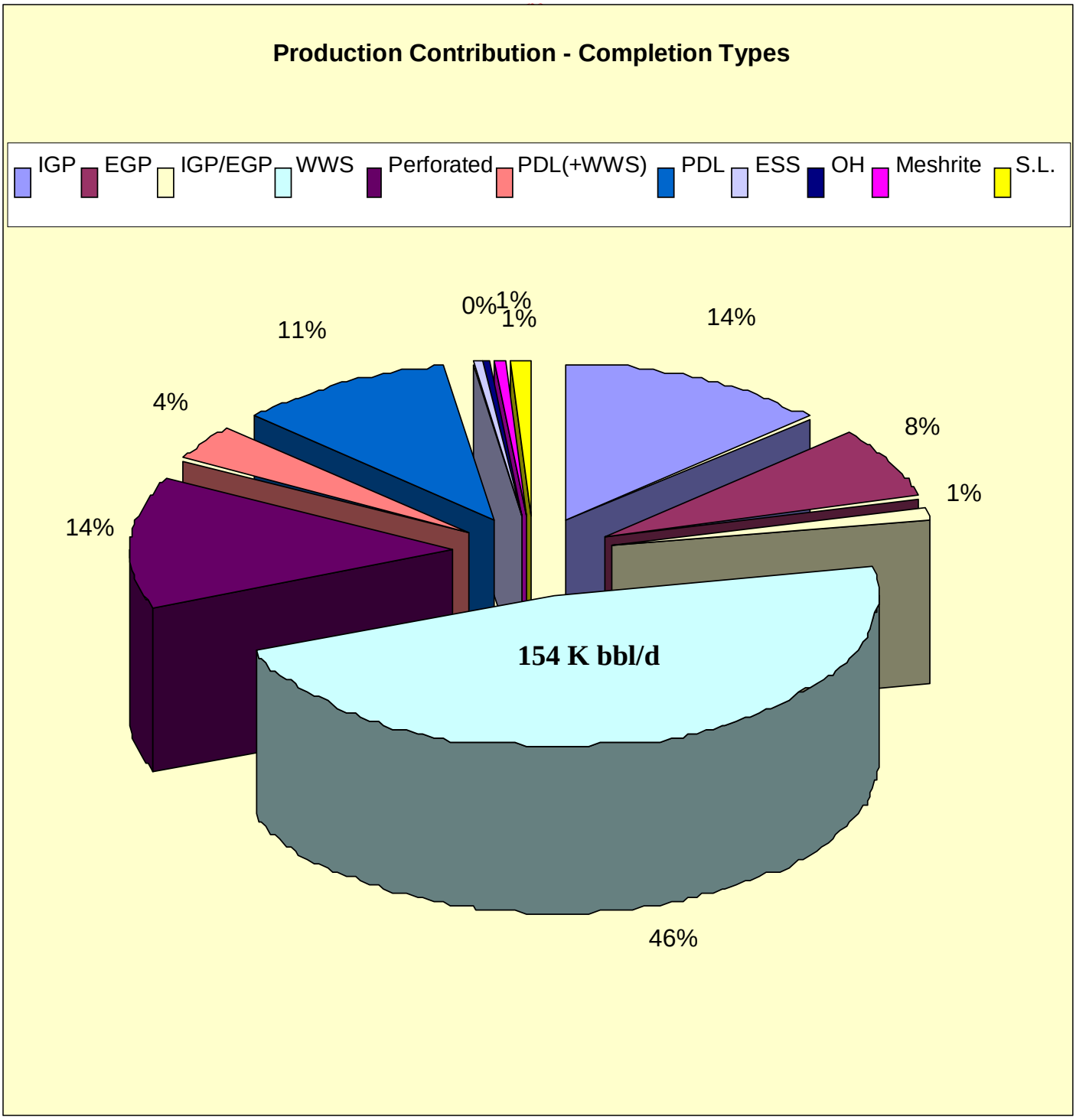

Figure 2.10: Types of sand control measures in Oman to minimise sand/fines impact.

These measures need to be installed during the initial well completion stage, otherwise if installed after that stage, the issue will involve expensive workover costs.

Use of **desanders'** on the surface can help in securing surface facilities integrity against particles erosion. A desander is a vessel which catches sand particles from the wellhead or flow-line and allows evacuation of particle-less flow through its downstream outlet. It requires frequent cleaning depending on the sand influx rate and the unit's size. In an offshore platform environment, space availability can be an issue. Depending on the amount of sand production, the size and design of the desander may vary accordingly. In most cases the more the sand influx, the larger the vessel. However, the desander being a surface unit, neither protects subsurface completion components nor reduces down-hole sand inflow or accumulation. Disposal of the accumulated sand from the device based on environmental regulations is another challenge and a costly activity especially in offshore operations.

2.8 Research Work in the Oil and Gas Industry

Of the little fines migration research undertaken in the industry, only a fraction of the outcomes are practised by hydrocarbon producing companies. One of those, which managed to obtain worldwide recognition and application, despite its known limitations, is the Shell Research Centre's developed sand prediction package called FIST (Fully Integrated Sand Tool) (79). The relationship between sand prediction and fines prediction is given in section 2.8.1.

FIST uses several combined sources of information such as historical failure data, overburden stresses, horizontal forces, spatial interpolation of core data, log data, pore pressures etc. to produce joint probability distribution and to evaluate several sand production patterns as follows:

Per each producing reservoir layer, the probability of sand production risk at particular time is calculated and reported. Advice is given on whether to selectively monitor zones of interest or to carry out preventive measures of the most hazardous areas.

It provides probability distribution of the fraction of particular failed producing interval (out of all intervals analysed) as a function of time using Monte-Carlo simulations. This allows assessments of the relative risk of all failures in different wells thereby decisions can be made on the overall field‘s sand control measures. Monte-Carlo simulation is used to generate probability estimates when a certain number of producing intervals in a group of many intervals may fail before a given time.

FIST analysis is suitable for both oil and gas wells with or without water cut productions. Hence the software package can also be used to analyse some sand layer failure expectations in water producing wells. It is applicable for vertical wells, highly deviated wells, as well as horizontal wells, with open hole or cemented perforated completions.

The Shell‘s research on reservoir sand failure which was used to develop FIST, involved experimental, empirical and numerical approaches. The assumption is that the behaviour of sand particles surrounding perforation tunnels can be simulated using Thick-Walled-Cylinder (TWC) (80) tests on a hollow cylindrical core sample having dimensions of 1” outside diameter by 0.33” inside diameter by 2” length. Figure 2.11 shows how the core sample is positioned in the high pressure cell used for TWC tests. During the test, an external pressure is exerted to the sample using pressurised hydraulic oil via the blue area keeping the inner hollow (white area) at atmospheric pressure. The hydraulic pressure is increased to a fixed rate (say 300 psi/minute) until catastrophic core sample collapse occurs. The pressure at

which this failure happens is called the TWC strength. Catastrophic failure is explained later in this section.

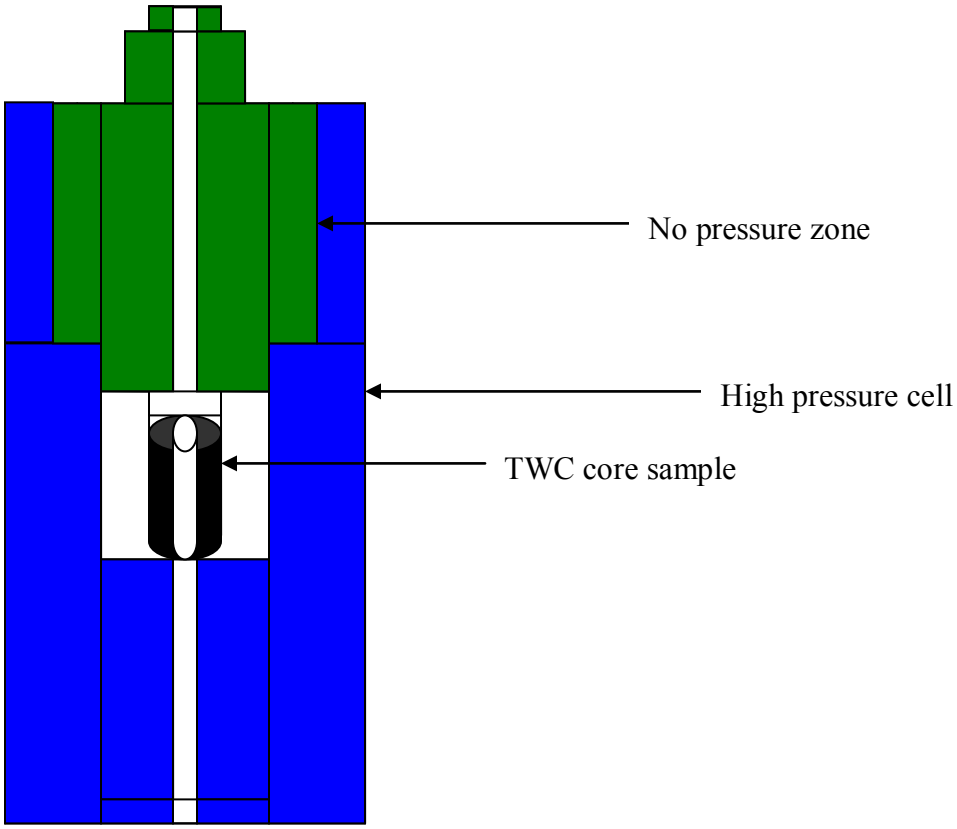

Figure 2.11: Thick wall cylinder test layout

According to this analysis, initial sand influx based on perforation instability is likely to happen when the following conditions occurs:

$\sigma'_{vwf} \geq 1.07\ TWC$ ----------(2.22)

Where:

σ'_{vwf} is expected near-wellbore vertical effective stress at perforation depth (bar).

Note: 1 bar = 14.5 psi.

TWC is thick-walled cylinder strength (bar).

$\sigma'_{vwf} = \sigma_{vf} - Pwf$ ----------(2.23)

Where:

σ_{vf} is expected far-field vertical total stress (bar).

Pwf is expected near-wellbore pore pressure (bar), and is expressed as follows:

$Pwf = Pi - (\Delta P_{de} + \Delta P_{dd}) = Pi - Total\ Drawdown$ ----------(2.24)

Where:

Pi is initial reservoir pressure (bar)

ΔP_{de} is field wide depletion pressure (bar)

ΔP_{dd} is drawdown pressure applied near the wellbore (bar).

Figure 2.12 is a graphical presentation of the analysis:

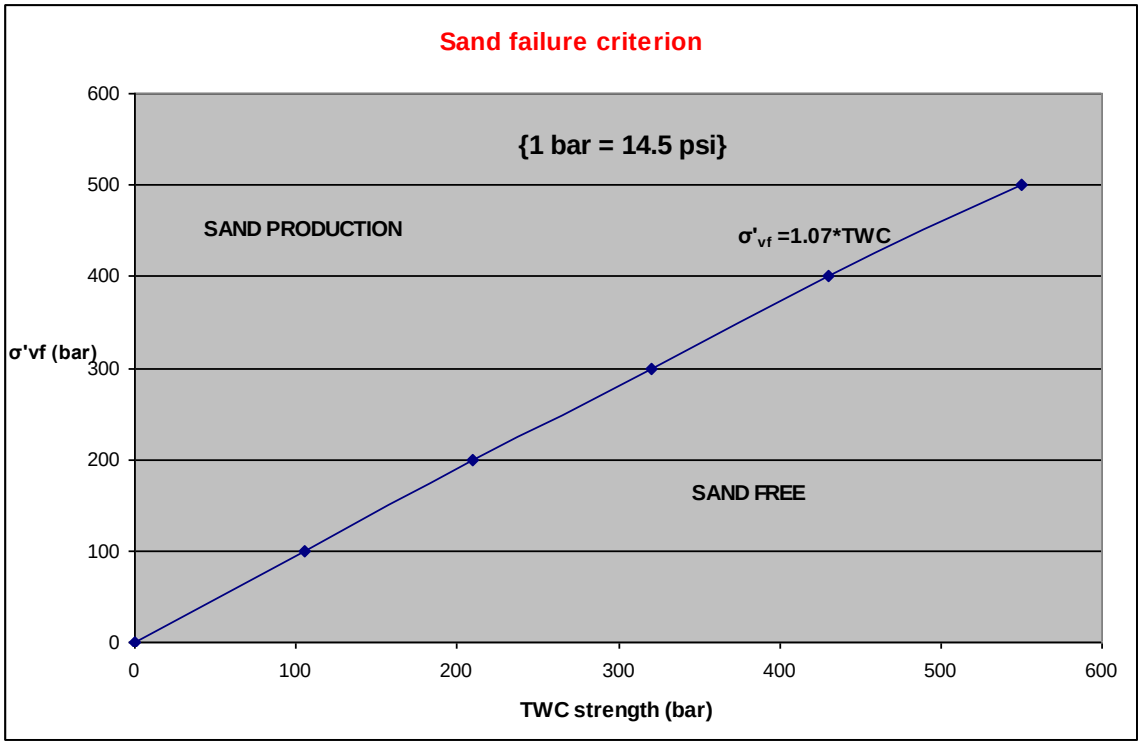

Figure 2.12: Thick-walled cylinder technique used in determining sand influx zone

The main concern about the above criterion is that it is based on a core ~~"t~~hick-wall cylinder" test which may not necessarily represent the vast majority of formations world wide. Also even when a petrophysical approach is taken where logs are used to estimate rock strength,

the measurement is regarded as qualitative and not quantitative. Hence prediction is presented qualitatively as transient sand failure, massive transient failure and catastrophic failure. These are summarised as follows (81):

Initial transient failure is referred to as a situation where the normal circular wellbore starts to take a different shape, elliptical for example. The dominant force is a compressive force. In such a situation, it is still quite possible to adjust production operations so that the risk of producing initial sand is minimised or prevented. Reduction of drawdown pressure or increase in reservoir pressure e.g. by increasing water injection rate in a nearby water injector (if any), may restore well stability and thereby long term sand-free production can be acquired.

Massive transient failure occurs as a follow-up to the initial transient failure and is more sensitive to drawdown as some tensile forces start on the wellbore at the perforated intervals. Even at this stage, the well stability in terms of fines/sand production can be restored especially by reduction in pressure drawdown.

Catastrophic failure is a very rare type of failure but once it happens, the sand will keep on being produced continuously and nothing much can be done except a workover to install sand control measures such as wire wrapped screens, pre-packed screens, gravel packs, slotted liners, expandable screens etc.

The stress calculations are based on many input parameters such as density, porosity, reservoir pressure profile, drawdown pressure profile, inclination, perforation interval and the rest of rock mechanical properties. The prediction involves 50/50 failure probability concept. This is based on the combined probability formula (82), which states that:

$$\text{Combined probability} = 1-(\text{risk of no failure})^{(\text{No. of layers})} \quad \text{----------(2.25)}$$

Or,

$$\sum_{i=1}^{n} \rho_i = [1-(1-\rho_i)^n] \quad \text{----------(2.26)}$$

Where:

ρ_i = Probability of failure of individual layer

n = Total number of layers perforated

The sum of individual failure probabilities in this case will be higher than the individual layer probabilities.

Shell's recent laboratory analysis of sand failure by Van Den Hoek et al (83), confirmed that there is a tendency of increasing sand production in a high effective vertical stress well having exceeded the "thick-walled cylinder" (TWC) stress limit for initial perforation failure. In other words, initial perforation will always cause excessive sand/fines production if the near-wellbore vertical stress (σ'_{vwf}) exceeds the laboratory measured stress using a thick-walled cylinder stress (TWC) system. Based on similar studies by Amory (84), fine/sand mobilisation into the wellbore is expected to commence when $\sigma'_{vwf} \geq 1.07$ (TWC).

The implied reason is that at higher near-wellbore stresses, a large cavity around the wellbore is required for well stabilisation. As a result, wells which have higher near-wellbore stresses (exceeding TWC-limit), are expected to produce large volumes of sand before the well finally cleans up. Hence fully opened choke (beaned-up) in a newly drilled well may produce significant "transient" fines because the bottomhole cavity is being formed instantly. Whereas in an old producing well, a stable bottomhole cavity exists, hence a bean-up is not expected to cause significant sand influx.

2.8.1 Relationship between Sand Prediction and Formation Damage Prediction

Formation damage prediction is referred to particle-damaged permeability prediction. In this research as can be seen in chapter 5, particle size, pressure drop, fluid properties and rock properties were used to develop particle-damaged permeability models. Hence knowledge of particle size in additional to the petrophysical measurements done in FIST analysis provide useful information to predict fines-damaged permeability.

A few researches such as those done by Oyeneyin and Faga indicate possibility of obtaining fines grain sizes distribution using electric logging devices (85-86). According to the reports, formation fines grain size distribution along with geological information on expected minerals can be used to estimate particle hardness. The relationship between the response of the gamma ray tool and grain-size and the relationship between porosity, permeability and texture can be used for grain-size prediction using the pattern recognition capabilities of backpropagation neural networks. The selection of a backpropagation neural network methodology was additionally justified on the basis of its reported superiority over conventional linear and non-linear regression techniques in dealing with complex non-linear relationships such as those existing between petrophysical properties (85 – 86).

Other investigations such as those referred to by Faga (86) indicate that fines grain size determination was demonstrated. According to him, "A network trained using data from the fluvio-deltaic depositional environment of the Brent Group could be applied for prediction in the marine environment of the Statfjord sands which have mean grain-sizes that are higher than those of the Brent by at least 200 microns".

Sand and fines particles dislodgement from the formation are then expected to take place at conditions causing formation failure. The magnitude of that can be minimal, moderate or

catastrophic. Hence the relationship is in fines particle size and its mineralogical information from which formation hardness can be estimated. Therefore if the type and size of fines along with corresponding reservoir pressure at the zone of interest are identified along with other rock mechanical information, particle-damaged permeability can be calculated as explained in chapters 4 and 5.

2.9 Core Laboratory Analysis and Reservoir Simulation Limitations

Sand particle analyses are usually carried out in the oil and gas industry‘s core laboratories using specialized core analysis laboratories (SCAL) techniques. Common core plug sample scales vary; however in most cases the usual size is about 2.5” length and 1” diameter size. It is important to note that in most cases, only dead liquid (without gas) is used in the experiments due to safety precautions while working in a confined space. The liquid used is often brine (salty water particularly mixed with 3 % KCl (potassium chloride) solution). The Reason being that is the usual type of liquid mixture circulated into the well during and after well completion as well as during a work-over operation. Confining pressure of up to 500 psi is used to test core plugs with brine or other solvents. Thereafter higher pressures up to 2500 psi are applied in analysing plug permeability based on flow rate and pressure changes.

There are quite a few limitations in core fines analysis. It is important to note that in most high permeability unconsolidated sands, it is very difficult to get proper representative core sample due to difficulties in obtaining a complete (100%) sample recovery. This is besides the problems of core damage often encountered even after partial recovery. It is subject to the nature of the composition of the core which include complex clay particles such as kaolinites, smectites, illites etc. Below is a list of several limitations in the conventional fines/sand analyses used by the oil and gas industry today. Both core laboratory experimental work as

well as leading commercial reservoir simulators, suffer significant shortcomings such as those listed below. Hence a need to further eliminate uncertainties in the oil and gas industry still prevails. So far the core lab‘s limitations include inability to inject hydrocarbon gas in a confined space (deemed a safety hazard). In addition, although the analyses are limited to core plug scales only, core plug results are nevertheless scaled-up to reservoir size extent and are assumed to represent the entire reservoir extent. This particular procedure poses several uncertainties such as the followings:

i) Representative-ness of the core data in terms of rock properties over the entire reservoir interval. A one foot-long piece of core plug may not represent the entire reservoir layer. Hence core pressure, temperature, permeability, porosity, fluid saturations, particle size and other rock and fluid properties may not be distributed across entire reservoir in the similar manner as in the core sample.

ii) Variations in reservoir geology away from the wellbore at which the core sample was taken. The heterogeneity of the reservoir rock and fluid properties in terms of particle shape, roundness, sorting and combinations of shale and sand along with faults and fractures can not be reproduced from core plug samples.

iii) Many averaging methods and flow models are used, each having its own various uncertainties. Hence errors tend to happen based on uncertainties related to the averaging method used in experiments.

iv) Core data need to undergo regression analysis due to wide spread range of data on permeability vs. porosity semi-log plots. There are a lot of uncertainties in the regression process which may result in measurement errors.

The above assume that the core sample recovery is 100%. Quite often samples recovered are small broken pieces which may not be suitable for the analysis, and yet tend to be used, as such the results could be questionable. Furthermore, there is a tendency that fields from which cores have never been taken, get similar core description analyses based on assumptions that depositional environment is similar if some similarities on permeability/porosity were identified. Hence, not only are results scaled-up to a single well reservoir but they are extended to cover even wider fields where core data may not be available. As far as leading reservoir simulators such as Eclipse, MoReS, Stars, CMG, etc. are concerned, they do not have the capability of carrying out solid fines migration analysis. As such fines are not analysed as part of fluid transmissibility simulation in discretized grid blocks.

2.9.1 Reservoir Permeability Determination Using Well Inflow Analysis

Determination of reservoir permeability at reservoir conditions usually considers pressure drop in the process; being part of the principles of near wellbore well inflow analysis. Figure 2.13 is a schematic of a reservoir and a wellbore showing reservoir fluid mechanics driven by reservoir pressure with a changing reservoir diameter according to well flowing pressure (87).

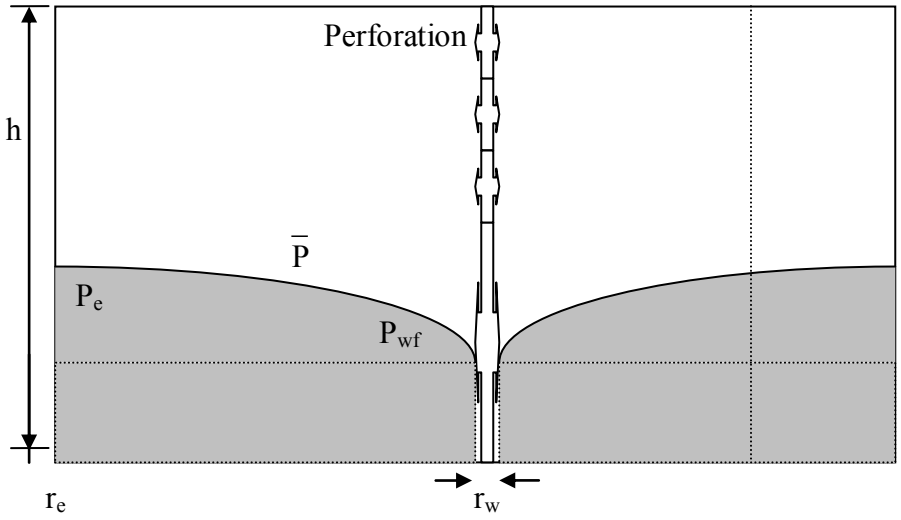

Figure 2.13: Principles of reservoir fluid flow fundamentals

In a radial flow such as that given in figure 2.13, based on fluid flow mechanics, production rate (q) is a function of draw down pressure ($\bar{p} - p_{wf}$). This is from the principles of flow dynamics (86) which are expressed as follows:

$$\int_{pwf}^{p} dp = \frac{q\mu}{2\pi kh} \int_{rw}^{re} \frac{dr}{r} \text{ ----------(2.27)}$$

The above equation is derived from the volume-averaged pressure within the radial cell as follows:

$$\bar{p} = \frac{\int_{r_w}^{r_e} pdV}{\int_{r_w}^{r_e} dV} \text{ ----------(2.28)}$$

Where:

$\bar{p}$ = the average pressure within the drainage volume (psi)

q = production rate (bbl/d)

p_{wf} = flowing well pressure (psi)

μ = viscosity (cP)

r_e = external drainage radius (ft)

r_w = wellbore radius (ft)

k = permeability (md)

h = reservoir thickness (ft)

According to Dake (87), integrating equation 2.27 thereafter including the mechanical skin factor (S), eventually will result in the modified inflow equation expressed in field units (stb/d, psi, mD, ft.) as follows:

$$\bar{p} - p_{wf} = \frac{141.2 q \mu B}{kh}(\ln \frac{r_e}{r_w} - \frac{3}{4} + S) \text{ ----------(2.29)}$$

Where: B is a formation volume factor (res bbl/STB).

From equation 2.29 pressure drops ($\bar{p} - p_{wf}$) of the simulated liquid (oil + water) and multiphase fluids can be used to calculate corresponding permeabilities. Individual phase analysis is demonstrated in chapter 5 section 5.3.1 which provides relative and effective permeability analyses of individual phases (oil, water, etc…). No free gas on its own was simulated, however mixtures of liquid and gas (multiphase) were simulated.

2.10 The Need for Computational Fluid Dynamics (CFD) Simulations

The fines migration studies discussed above identified potential causes of pore damage and types of damage mechanisms but there are no details on how to deal with them at a reservoir scale and how they can be numerically modelled at a reservoir scale; whereas in this research work, as explained in the next chapters, more realistic analyses are proposed to minimise

suboptimal production or injection due to fines migration or solid particles intrusion are proposed. Furthermore, investigations involving laboratory work such as core analyses to determine permeability and other parameters are still being conducted using liquid and in some cases with very minimal gas and not fully fledged multiphase fluids since hydrocarbon gas especially in the absence of liquid cannot safely be analysed in confined spaces at various large volumes. In addition, core lab analysis does not involve various fines particles injection into core samples at different scenarios of grain sizes, water cuts, pressures etc. as discussed in this research work. Having analysed limitations of special core analysis (SCAL) and leading commercial simulators the necessity of reducing existing uncertainties became very clear and was the basis of this research work. As such, as illustrated in this thesis, an integrated solution was developed using an appropriate computational fluid dynamics (CFD) package for fines migration analyses and MoReS for corresponding reservoir performance prediction analysis.

Hence detailed analyses of fines migration were carried out with a main objective of an in depth investigation of the impact of fines in hydrocarbon multiphase fluids as they flow in a porous medium. The studies were done using a computational fluid dynamics (CFD) software package from which corresponding damaged permeabilities were calculated. The damaged permeabilities can be incorporation into a comprehensive reservoir 3-dimensional simulator for reservoir performance predictions as elaborated in chapter 5. The CFD package is amongst the latest and has already been tested elsewhere such as in the aircraft and other industries (Appendix A-1) to analyse hydraulic fluid dynamics. It is a good package in simulating multiphase fluid and granulate particles (such as fines/sand) together flowing in a porous medium.

In undertaking such a comprehensive approach, initially detailed simulations were performed using a modelled porous medium block to identify and analyse even minute effects as presented in the first part of chapter 3. Later on, a reservoir scale model was set-up through which multiple sensitivity scenarios were simulated. Both approaches and their results are presented in chapters 3 to 5.

The results of the CFD analyses including pressure drop simulations, were the basis of damaged permeability distribution determinations. The permeability distributions were further studied involving many scenarios and sensitivities. As a result, two particle-damaged permeability models were developed as explained in chapter 5. The developed models applicable in multiphase and liquid media, can be incorporated into a 3D reservoir simulator such as MoReS which is explained in chapter 5 and Appendix A-2. MoReS was available at the collaborating (Appendix A-3) establishment (Shell UK) to perform comprehensive reservoir performance and prediction studies.

In order to validate the developed particle-damaged permeability models using real field practices, relevant field analyses were reviewed and are explained in section 2.11.

2.11 Field Practices Used in the Validations of the Developed Models

The most commonly used conventional field procedures in determining absolute and effective permeabilities from reservoir pressure drawdown measurements (production test) or from pressure fall-off/ build-up data (shut-in test), are discussed below in sections 2.11.1 and 2.11.2. These transient pressure tests and the CFD simulations carried out in this research all use pressure drop analyses hence the reason for comparing well test outcomes with the developed model results.

Bottomhole pressures of hydrocarbon producing wells, water injection wells, as well as gas wells are normally measured and analysed using well test standard procedures to obtain permeabilities (87, 88) given reservoir thicknesses. In addition, from well tests, it is possible to obtain skin factors, reservoir boundaries (with boundary types), distances to boundaries, faults (if any), radius of investigation, initial reservoir pressure, average reservoir pressure and a few other parameters. While the field's well test practices result in single permeability values (89, 90), the models offer arrays of permeability data across the porous medium. In other words, today a typical well test field practice results in only one single permeability value, while the developed model using the same well test's range of pressure drawdown measurements results in a profile of permeability values across the drainage area.

The following are the conventional well test methods used in oil and gas fields:

1. Drawdown Pressure Surveys
2. Build-up Pressure Surveys
3. Fall-off Pressure Surveys
4. Injection Pressure Surveys
5. Multi-well Pressure Surveys

While the first two are done in hydrocarbon producing wells, the third and the fourth are done in water injecting wells. The last type of well test involves more than one well, and in most cases determines the influence of one well on another (interference test), or alternatively produce and shut-in a well while observing pressure /production responses from offset wells (pulse test). In validating the developed models, a drawdown pressure test, build-up pressure test and fall-off test are presented in chapter 6 since these field practices are used today to determine permeability and involve pressure drawdown data. Hence, while the CFD

process also includes the same type of data, those practices are the most appropriate and relevant ones in validating the developed models compared to any other field practice.

2.11.1 Drawdown Pressure Theory Used in Validating Developed Model

Referring to figure 2.14, several reservoir activities occur during the pressure drawdown test (89, 90). Important activities can be summarized as follows: Initially at t = 0 hour, the pressure is uniform throughout the reservoir. At the beginning of the pressure drawdown at about t = 0.01 hour, only a small region within about 10 ft of the wellbore has shown the effects of the pressure transient. Sometime later, at t =1 hour, the pressure transient has moved into a larger region which could reach up to 100 ft from the wellbore depending on reservoir pressure energy. Still later, at t =100 hours, the pressure transient has moved even further from the wellbore and entered the reservoir dominated region also called infinite pressure acting region. This is the period during which steady state pressure could be achieved if the reservoir pressure and wellbore pressure difference is kept constant. As production continues, the pressure transient continues to move through the reservoir until it reaches all boundaries of the reservoir. In case the reservoir pressure is maintained say with water flood pressure supplement, then the pressure behaviour will be infinite acting till the reservoir pressure reduces.

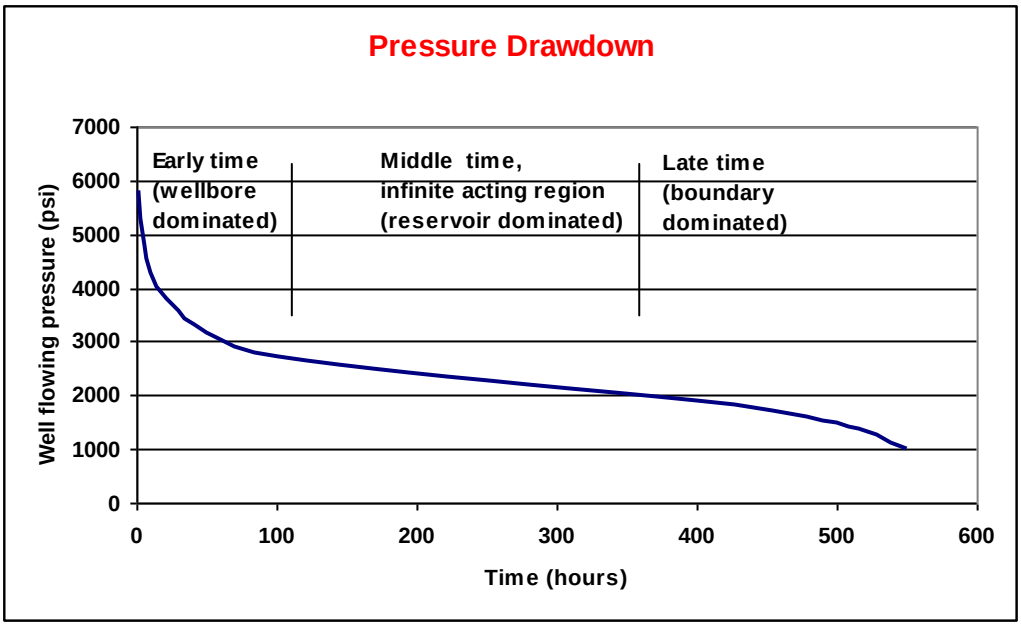

Figure 2.14: Reservoir behaviour during a pressure drawdown (production) test

2.11.2 Build-Up Pressure Analysis Used in Validating Developed Model

Referring to figure 2.15, during a pressure build-up test, at the instant of shut-in, t = 0 hour, the pressure begins to build up in the well (89, 90). However, this rise in pressure does not affect the entire reservoir at once. Soon thereafter, at t = 0.01 hour, the pressure buildup has affected only that part of the reservoir within about 10 ft or so from the wellbore. A pressure gradient still exists in the bulk of the reservoir. This means that fluid continues to flow in most of the reservoir during this early pressure buildup. At t =1 hour, the pressure has built up in a larger area which may reach about 100 ft or so from the wellbore depending on reservoir pressure energy, which is the pressure extent available in the reservoir. As the shut-in period continues, the region within which the pressure has built up grows until the entire reservoir is at uniform pressure.

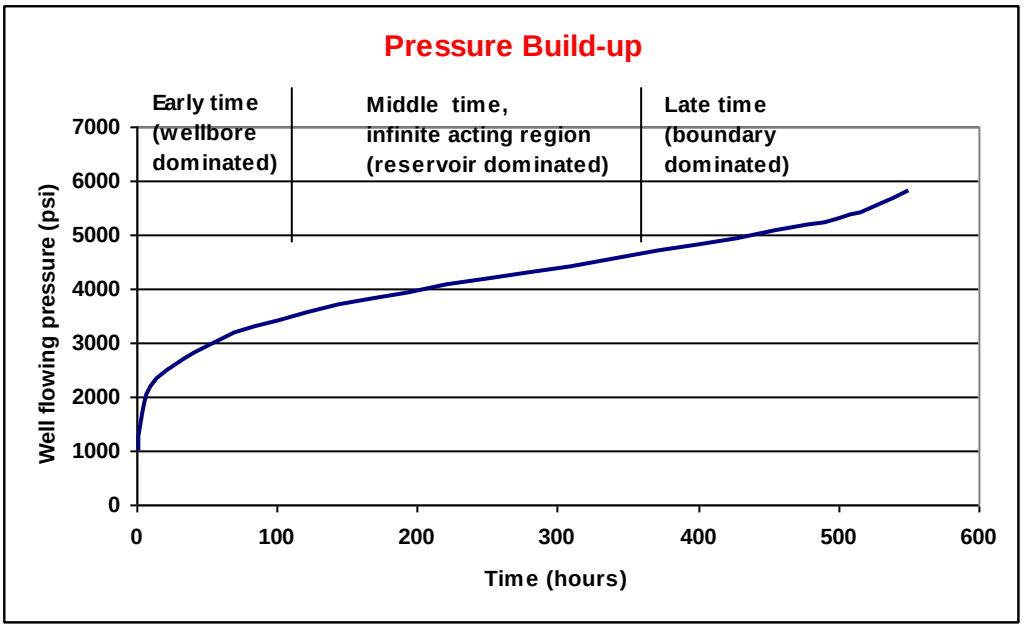

Figure 2.15 Reservoir behaviour during a pressure build-up test

In all these (drawdown, build-up) surveys pressures are recorded continuously with time while the pressure gauge is located near the reservoir inlet to the wellbore with a pressure shut-in tool above the gauge to avoid/ minimise impact of pressure due to liquid flow into the well (wellbore storage effects).

From the pressure and time data, standard pressure drawdown (or fall-off) and pressure build-up analyses can be carried out using pressure vs. log $\left\{\frac{t+\Delta t}{\Delta t}\right\}$ graphical approach. details of these analyses are given in chapter 6. From the graph, ~~"m~~" which is a slope in the graph can be determined, the permeability can be obtained from the following equation:

$$k = \frac{162.6 q \mu B_{oi}}{mh} \quad \text{----------(2.30)}$$

"m' which is the slope of the extrapolated curve in pressure vs. log $\left\{\frac{t+\Delta t}{\Delta t}\right\}$ graph is expressed as follows:

$$m = 162.6 \frac{q\mu B_o}{kh} \quad \text{psi/log.cycle} \text{ ---------- (2.31)}$$

Where:

q = flow rate (bbl/d)

μ = produced fluid viscosity (cP)

B_{oi}= initial oil reservoir formation factor (res bbl/STB)

h = reservoir height (ft)

While the above equations 2.30 and 2.31 are applicable for liquid producing or injecting wells, the conventional pressure build-up equation for gas well is given as follows (91):

$$pe - pws = -162.6\left\{\frac{\left[q_g \mu_g B_g\right]}{\left[k_g h\right]}\right\}\log\left(\frac{t+\Delta t}{\Delta t}\right) \quad \text{.....(2.32)}$$

Where B_g is expressed as follows:

$$B_g = Z\frac{T}{T_{sc}}\frac{P_{sc}}{\left\{\frac{pe+pws}{2}\right\}} \quad \text{.....(2.33)}$$

Where:

pe is extrapolated pressure in the pressure test curve to $\log\left\{\frac{t+\Delta t}{\Delta t}\right\} = 1$ (psi)

Z is gas compressibility (deviation) factor (dimensionless)

pws is shut-in well pressure (psia)

T is absolute temperature ($^{\circ}$R)

B_g is gas formation volume factor (rb/stb)

q_g is gas flow rate, (stb/d) (converted from MMscf/d)

μ_g is gas viscosity (cP)

k_g is gas permeability (mD)

t is total production time before the well was shut-in (hr)

Δt is time interval during which pressure measurement was taken (hr)

h is reservoir thickness (ft)

T_{sc} is standard temperature =520 $^{\circ}$R

P_{sc} is standard pressure = 14.65 psia

2.11.3 Horizontal Wells Analyses Used in the Permeability Models Validations

Validations of the developed permeability models was also carried out for horizontal wells having various horizontal lengths. This section discusses theories of horizontal well pressure analyses which were used to validate the models. Validations are explained in chapter 6. There are many horizontal well production performance analyses but the ones modified after Joshi (92), Babu and Odeh (93) are considered the most practical ones as outlined below. Horizontal well performance analysis is best carried out using the elliptical inflow pattern approach. According to Joshi, Babu and Odeh and others (92, 93), a horizontal well produces an inflow pattern in an elliptical shape as shown in figure 2.6. In the figure, **L** denotes the length of the ellipsoid, and is directly proportional to the half axis, **a** (92, 93).

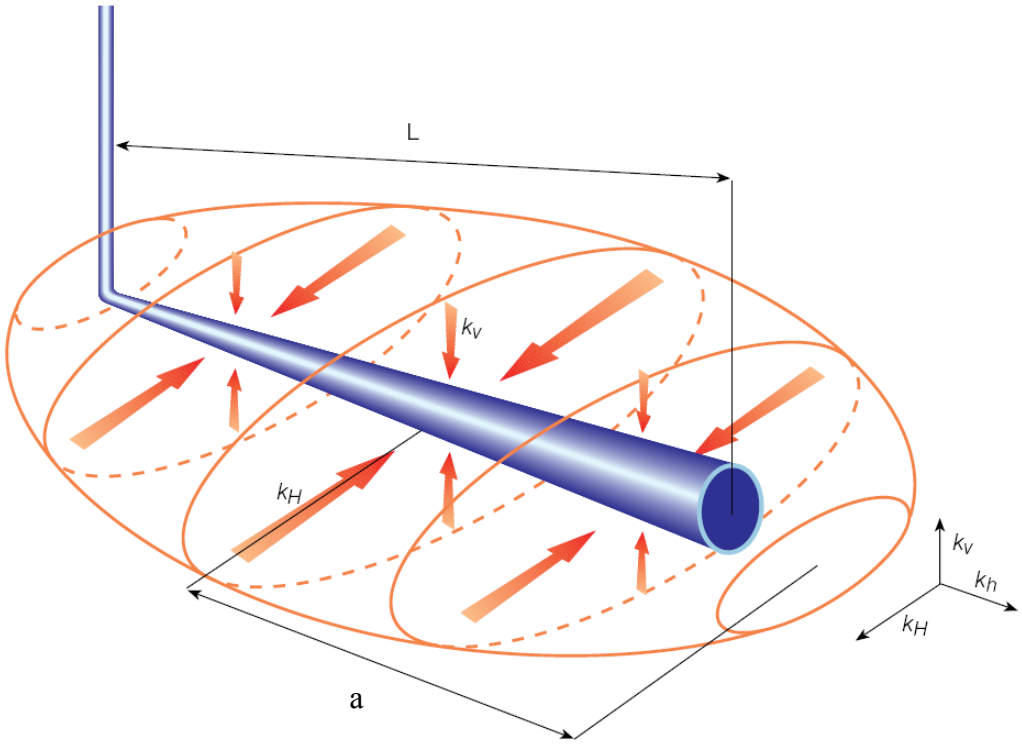

Figure 2.16: Inflow pattern formed around a horizontal well

Flow rate determination in a horizontal well using the horizontal ellipsoid inflow pattern approach in mixed steady-state horizontal plane and pseudo-steady state vertical plane conditions depicted in figure 2.16 is given by equation 2.34 based on recent horizontal reservoir studies (93).

$$q_h = \frac{k_h h(p_i - p_{wf})}{141.2B_o\mu\left\{\left[\ln\left[\frac{a+\sqrt{a^2-\left(\frac{L}{2}\right)^2}}{\frac{L}{2}}\right]\right]+\left(\frac{I_{ani}h}{L}\right)\ln\frac{(I_{ani}h)}{[r_w(I_{ani}+1)]}\right\}} \quad \text{---------- (2.34)}$$

Where $\boldsymbol{I_{ani}}$ is permeability anisotropy and is expressed as follows:

$$I_{ani} = \sqrt{\frac{k_h}{k_v}} \quad \text{---------- (2.35)}$$

and ***a*** which is the major half-axis of the drainage ellipsoid formed by a horizontal well of length **L** is expressed as follows:

$$a = \frac{L}{2}\left\{\sqrt{0.5 + \sqrt{0.25 + \left\{\frac{r_{eh}}{(L/2)}\right\}^4}}\right\} \text{ ----------(2.36)}$$

Where:

k_h = Horizontal permeability (md)

k_v = Vertical permeability (md)

h = Reservoir height (ft)

p_i = Initial reservoir pressure (psi)

p_{wf} = Flowing bottom hole pressure (psi)

μ = Viscosity (cP)

B_o = Oil formation volume factor (res. bbl/STB)

r_w = Wellbore radius size (inches)

r_{eh} = Effective radius based on acre spacing (ft)

q_h = Horizontal flow rate (bbl/d)

L = Length of the ellipsoid (ft).

The equations above were further subdivided to manage multiple scenario analyses involving other sensitivities as explained below. Hence equation (2.34) was partitioned as follows:

$$\alpha = k_h h(P_i - P_{wf}), \text{ ----------(2.37)}$$

$$\beta = 141.2 B_o \mu, \text{----------(2.38)}$$

$$\chi = \ln\left[\frac{a + \sqrt{a^2 - \left(\frac{L}{2}\right)^2}}{\frac{L}{2}}\right], \text{----------(2.39)}$$

$$\delta = \left(\frac{I_{ani}h}{L}\right), \text{----------(2.40)}$$

$$\varepsilon = \ln\left\{\frac{(I_{ani}h)}{[r_w(I_{ani}+1)]}\right\}. \text{----------(2.41)}$$

In other words, the horizontal flow equation 2.34 became:

$$q_h = \frac{\alpha}{\beta\{\chi + (\delta)(\varepsilon)\}} \text{ ----------(2.42)}$$

Chapter 3 provides a unique approach in the study of various combinations of fines particle impacts on multiphase production and fluid injection using the CFD which can perform granular multiphase simulations.

The principle objective of this study is to investigate in a much greater detail the impact of fines in hydrocarbon multiphase fluids as they flow in a porous medium.

Hence the outcome of this research work is expected to some extent to help reduce some of the existing fines related uncertainties the oil and gas industry experiences.

Chapter 3

CFD MODELLING OF FINES FLOW IN MULTIPHASE FLUIDS

3.1 Introduction

Chapter 2 provided an extensive review of previous and ongoing studies on fines migrations within the reservoir and solid particle intrusion from wellbore fluids into the reservoir and their impacts on hydrocarbon production. It also outlined previous and current field practices of fines management in the oil and gas industry. Towards the end, Chapter 2 introduced complex fines migration analysis using a specialised Computational Fluid Dynamics (CFD) approach which is detailed in this chapter.

The main objective of using the CFD for fines analysis is to minimise uncertainties existing in many fines management strategies mentioned in chapter 2. Hence this chapter demonstrates how to simulate the impact of fines particles on reservoir performance reflected by drawdown pressures across the entire modelled porous medium through which hydrocarbon multiphase fluid and solid fines particles flow together. The process in all cases is free from most contemporary limitations mentioned in chapter 2, however it cannot measure permeability directly but the pressure drawdown which it can measure can be used to calculate the corresponding permeabilities as explained in chapter 4.

Results of the CFD simulations were validated using field data through field practices with acceptable outcomes as demonstrated in chapter 6.

Starting with existing experimental limitations, due to safety related issues in handling hydrocarbon gas in a closed environment, solid fines and hydrocarbon gas saturated crude mixtures cannot possibly be analysed in laboratories; whereas this specialised CFD is capable

of simulating granular multiphase flow (solid particles in gas saturated liquid) much more accurately. The CFD used in this study which can handle granular flow, is among the latest coded by Fluent Inc. and has already been tested elsewhere in several industrial works such as the aircraft industry to analyse hydraulic fluid dynamics and other industries as outlined in Appendix A-1. Section 3.1.3 provides various CFD capabilities in analysing several types of multiphase-solid-particle flow. In order to examine the effectiveness of the package, multiphase flow simulation sensitivities were performed across the entire modelled porous medium at several reservoir conditions of temperature, pressure, velocity, water cut, fines quantities and multiple fines grain sizes at reservoir dimensions. Multiphase flow referred to in this thesis includes a flow mixture of hydrocarbon oil, water and gas flowing with fines grains whose sizes range between 10 and 200 μm at different fluid proportions which are explained in the chapter. Fluent multiphase analysis was done using the Eulerian multiphase model (94) explained in sections 3.1.3, 3.2.1 and 3.4.

Results are shown graphically while data used to draw the graphs are given in Appendix A-6. Based on the results which are comparable with actual field observations as illustrated in this chapter and chapters 5 and 6, the CFD modelling was robust.

This chapter is divided into four main parts: (i) Method used in carrying out the CFD simulations, (ii) Experimental analyses of computational models, (iii) Results and (iv) Discussions.

3.1.1 Method Used in Carrying Out the CFD Simulations

3.1.2 Modelling Approach

In undertaking such a modelling process, initially simulations were performed using a porous medium block model to identify and analyse the minute fines effects as they were being

revealed. Later, on a reservoir scale model was set-up through which multiple sensitivity scenarios were simulated. The most important simulation results are the pressure drop profiles across the computational grid. Pressure drop values were downloaded as ‗comma separated variables' (CSV) files into Microsoft Excel software for detailed analysis. The pressure drop (drawdown) data are very critical in the study of reservoir rock and fluid properties especially the permeability which is discussed later in chapter 4. From the CFD simulation results, velocity vectors of fines particles flowing along with crude were measured separately as explained in sections 3.3 and 3.5. This provides the possibility of studying unique characteristics of fines particles flowing in a mixture flow of water, oil and gas. As such, presented in this chapter are individual solid phase and liquid phase characteristics both qualitatively and quantitatively. The CFD results which are presented from section 3.3 to 3.6, were studied to identify and group all fines related effects, factors and sensitivities influencing both multiphase flow and liquid (gas free) flow behaviours. Results discussions start from section 3.7 to the end of the chapter. The simulation results comparison of instantaneous velocities between liquid phase and solid phase is one of the key features which make the investigation more realistic compared to laboratory experimental studies which can not measure so accurately individual solid particles speeds separately although they flow in a multiphase mixture of oil, water and gas while all continuously flow together.

3.1.3 Computational Fluid Dynamics (CFD) Package

CFD is a computer program which can be used for modelling fluid flow, heat transfer and chemical reactions. Significant computational work took place using the Fluent coded numerical package. Modelling multiphase fluid flow with solid particle migration in any known oil /gas field has never been carried out in the systematic methodology presented in

this study. Multiple simulations were carried out using modelled geometrical grid accessible through the graphical user interface (GUI) to numerically model liquid (oil, water), multiphase (oil, water and gas) fluids and fines particle movement through the porous medium model. A wide range of physical models such as Eulerian multiphase model, Laminar and turbulent flow models, Lagrangian trajectory models, thermal effects models and so forth were used in simulating numerous types of granular multiphase fluid flow problems related to oil, gas, water, reservoir rock and solid particles. Details on fines interactions with the porous media are given in section 3.4. The physical models were retrieved via the GUI, from which problem definition, computation and graphical post-processing displays could be viewed. The CFD is capable of handling customised sensitivities such as those mentioned later in this chapter; and can be linked to some computer aided systems.

The numerical model used provides possibility of mesh design flexibility and can solve flow conditions using both structured and unstructured meshes.

The CFD supports 2D and 3D mesh types such as tetrahedral, hexahedral, pyramid, wedge, quadrilateral, as well as triangular and mixed (hybrid) meshes (95). A 2D quadrilateral mesh was used in the analysis because it best fits conventional reservoir simulator‘s mesh structures and computational mesh blocks. Reservoir simulator as explained in chapter 5, used a reservoir black oil model similar to the one used in the CFD analysis.

Both compressible and incompressible fluids can be solved using a pressure-based finite volume method.

The following are the program capabilities related to multiphase fluid flow with solid particles. The CFD used is capable of simulating the following nine scenarios (96). All the

nine capabilities are relevant to the research work presented in this chapter except for scenario number 4 –Free surface flows with complex surface shapes".

Laminar or turbulent flow, using suite of turbulence models available.

Steady state or transient flow.

Any combination of multiphase flow.

Free surface flows with complex surface shapes.

Temperature and composition dependent fluid properties.

Incompressible or compressible flow.

Laminar flow of non-Newtonian fluids.

Flow through porous media including thermal effects of the solid media.

Dispersed second phase of particles /bubbles /droplets including:

- Lagrangian trajectory calculations with stochastic tracking to account for the effects of turbulence.
- Inert heating or cooling of solid particle phase.
- Coupled mass, momentum and heat transfer between the solid particles and liquid phases.

Fines grain particles having grain sizes: 10μm, 50μm, 100μm, 150 μm and 200 μm flowing with hydrocarbon fluid mixture of oil, water and gas through 1000 mD and 2000 mD porous media were simulated. In the CFD, particles interactions with the porous media are explained in section 3.4.

3.1.4 Program Structure

The Fluent CFD package includes the following program structure elements which are explained below in this section.

Solver and post-processor

PrePDF pre-processor

GeoMesh pre-processor

Grid filters.

The basic program structure is shown in Figure 3.1 (97). Referring to figure 3.1,

the solver does mesh generation or mesh import from mesh creating package (e.g. gambit, T-grid etc.) and also does mesh adaptation. It does physical models, boundary conditions, fluid and solid properties definition, performs calculations and does post-processing work. The PDF files are used for viewing and printing using Adobe Acrobat Reader available in both Windows and Unix systems. These files have a .pdf suffix in the filename. PDF files are easier to access and to print compared to postscript files. Pre-PDF is the pre-processor for modelling PDF functions such as calculations of PDF look up tables.

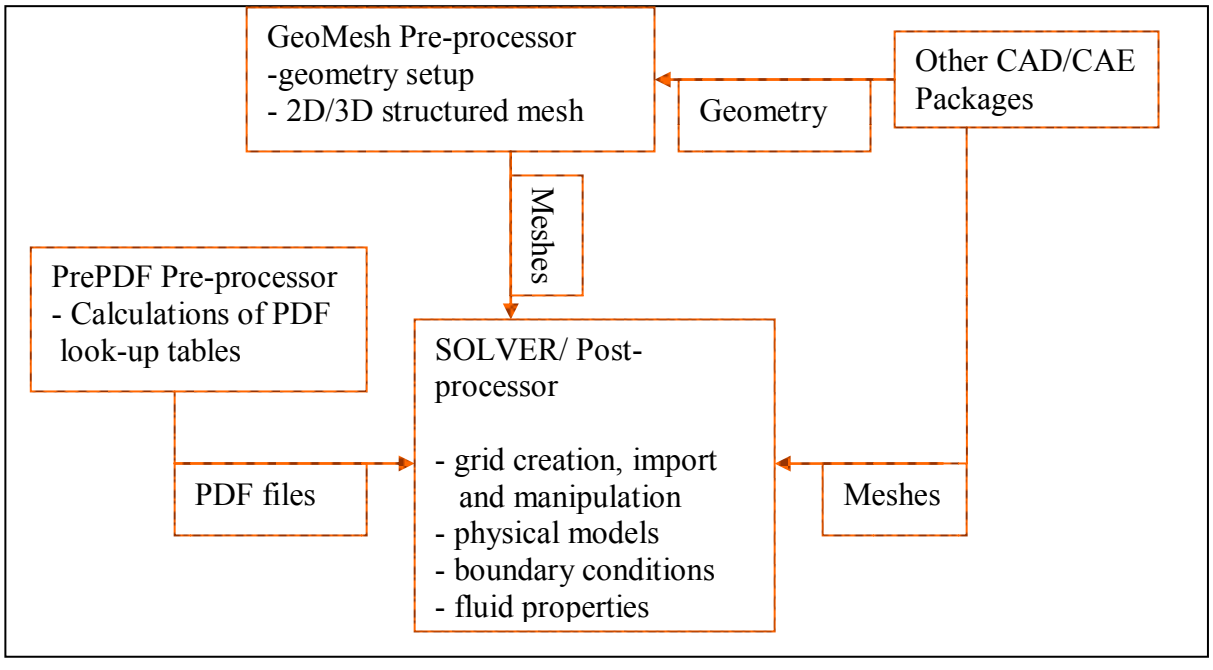

Figure 3.1: The CFD Program Structure

The Fluent solver carries out numerical solutions using a control volume-based finite difference technique to solve problems which require conservation equations for mass, momentum, energy and chemical species such as hydrocarbon gas (98).

Pressure-based finite volume method is used for compressible and incompressible fluids.

The governing equations are discretized on a curvilinear grid to enable computation in complex /irregular geometries. A non-staggered system is used for storage of discrete velocities and pressures. Interpolation is accomplished via a first-order, power-Law scheme or optionally via higher order upwind schemes (98). The equations are solved using algorithms with an iterative line-by-line matrix solver and multi-grid acceleration.

The solver is also a post-processor which has data visualisation capability including graphical animations as well as export facilities for graphics manipulations. Figure 3.1 summarises what the solver and the pre-processors can perform.

While the solver has grid generation utilities for 3D/ Cartesian and cylindrical-polar meshes, it can also import and copy more complex quadrilateral and hexahedral grids created by the pre-processor GeoMesh. Once a grid has been read into the solver, all remaining operations including executing the solution, refining the grid, viewing the results are performed within the post-processor. Setting up of boundary conditions and defining fluid properties are part of pre-processing.

3.1.5 Objectives of the Fines Analysis Program

The main objective is to analyse the impact of fines particles of various sizes on pressure drawdown across the porous media through which particles in a multiphase (oil, gas and water) flow will be simulated using the CFD. Other objectives of the analysis include

investigations on pressure changes due to: grain size effects, water cut effects, porosity effects, viscosity effects and fluid density effects.

3.2 Experimental Analysis of the Model Structure

3.2.1 Initial Set-up: Grid Mesh Model Design

A number of geometries were initially carried out to perform sensitivities on solutions based on mesh size per computational grid. The sensitivities results based on memory availability, computing time and final solution accuracy, determined the final set-up of the geometry of the computational grid model. Table 3.1 shows comparison of different geometries made and corresponding mesh sizes. The numbers of cells penetrated by liquid and fines velocities were taken as the basis of optimal grid model selection.

Table 3.1: Sensitivities on Mesh Sizes and Porous Medium Geometries

Dimensions (cm)			Grid Model		Total cells	Species	Cell type *	Statistics for velocity	
Length	Height	Depth	I cell	J cell				Liquid cells penetrated	Fines cells penetrated
100	100	30	60	45	2700	4	I,L,P,L,O,W,W	1114	1792
100	100	50	50	50	2500	4	I,L,P,L,O,W,W	1204	1797
100	100	40	50	45	2250	4	I,L,P,L,O,W,W	1203	1767

* Cell type: I = Inlet, L = Live, P =Porous, O = Outlet, W = Wall

In table 3.1, the J cells are the cell across the x-axis direction whereas the I cells are along the y-axis direction. The 4 species are components of the multiphase mixture which are oil, water, gas and solid fines particles. Five cell types were used, the inlet cells, outlet cells, wall cells, live cell and porous cell which are outlined below in figure 3.2. As far as number of cells penetrated it is an indication of flow efficiency through the porous medium model. Note that figure 3.2 shows the micro analysis of a small model structure required to study minute

details of simulation outcomes. A reservoir scale analysis is given from section 3.5 to the end of this chapter.

The larger the number of cells penetrated the more efficient the set-up was. The no-flow borders around ends symbolise reservoir bounds above and below which hydrocarbon does not flow.

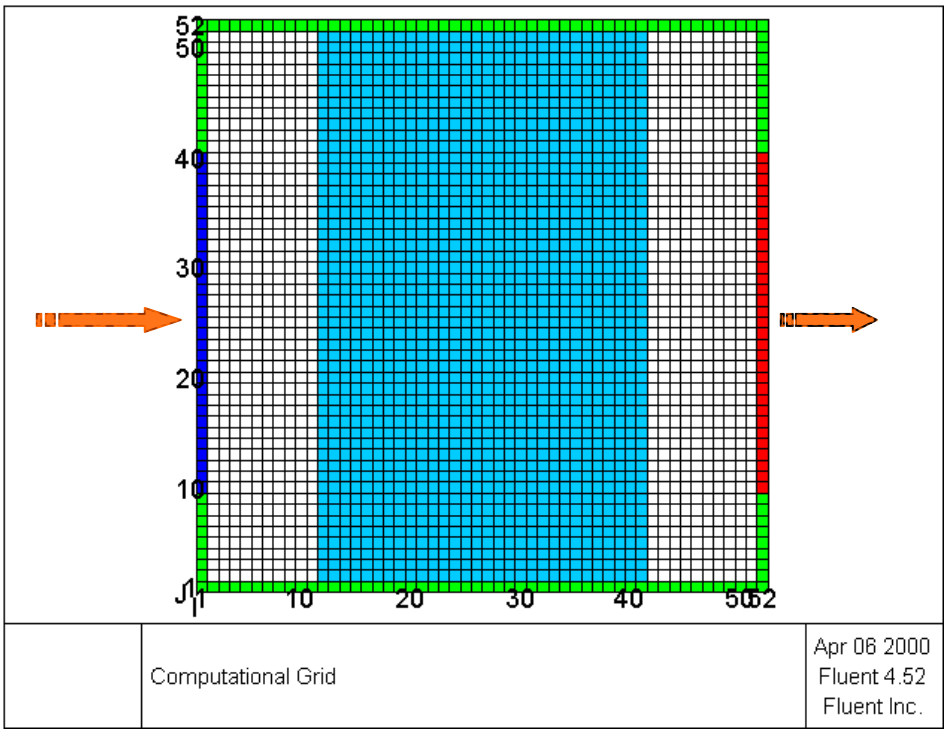

Figure 3.2: Computational grid cells model

Figure 3.2 thus is a computational grid which was modelled to simulate fines effects in multiphase flow in a porous medium in which high permeability sandstone reservoir properties were defined. In the figure, the light blue coloured zone is the porous medium, whereas the white coloured meshed areas are unrestricted flow areas. The dark blue boundary is the flow inlet while the red boundary is the flow exit. The green boundary is a no-flow border. There were other trials which crashed due to memory allocation problems. The optimal model of about 40" (100 cm) by 40" (Figure 3.2) was subdivided into multiple cells.

A total of 2700 cells were modelled of which 2500 were open to flow. Each of these cells was analysed using partial differential equations designed for granular multiphase fluid dynamics (99).

Hence the optimal grid model set-up was found to be the 50 x 50 cell which resulted in the highest numbers of penetrated liquid cells and solid fines cells. The work was carried out using a computational grid block as per Figure 3.2 generated by the solver. It is a meshed block composed of cells with inlet and outlet boundaries between which a porous medium is located.

Advances in Fluent CFD after the work done in 2000, are more on the Eulerian multiphase model which uses separate sets of fluid equations for interpenetrating fluids or phases. The main relevant features of the CFD are similar as far as their use in this research is concerned. Brief description of Fluent CFD advances are in Appendix A-1.

Referring to figure 3.2 (micro model), each side of the porous medium measuring 4" (10.16cm) was modelled to represent conductive fault throw which many reservoirs happen to be bounded with. Hence even effects of free-flow scenarios (conducting faults) were simulated. The macro (reservoir scale) model is given in section 3.5. The fluids simulated were mixtures of hydrocarbon oil, hydrocarbon gas and water which are all together referred to as crude. Flowing with the crude are various fines grain sizes at various concentrations. The porous medium (blue section) whose dimensions are 24 inches (30 cells) by 37 inches (50 cells) was further subdivided to represent all ranges of properties found in multiphase sandstone reservoirs. The medium was modelled such that it contained conventional high permeability clastic reservoir properties of rock and fluids which are elaborated further in the chapter (from section 3.2.2 onwards). The fines grain sizes were chosen based on observed

dimensions as revealed by scanning electron micrograph (SEM) presented in chapter 2. Hence fines grain size range between 10 microns and 200 microns were used. Low gravity fines concentration by volume of water in the mixture in which the water cut was fixed at 22%, ranged from 20% to 50%. Which means for 20%, the total concentration was 20% of 22% i.e. 4.4% only. It should be noted that concentration sensitivity by water cut volume was confined or fixed within the 22% water cut while simulations carried out at different water cuts, the fines concentration was kept at 4.4% of the total fluid volume regardless of water cut percentage. This was done to maintain consistency. In all these and the other sensitivities carried out in this research, the analyses were on resultant pressure drops. Usually, as explained in section 2.3.2, in the oil an gas industry, produced fines particles contents tend to exceed 10gm per 1000 lts. of liquid produced which is 10% solid content by volume. Hence the concentration range simulated is within the observed field production. Table 3.2 lists a range of rock and fluid properties simulated by the CFD.

3.2.2 Boundary Conditions

Table 3.2: Range of Simulated Rock and Fluids Properties

Parameter	**Range**	**Units**
crude density	50 - 64 (800 – 1030kg/m^3)	lb/ft^3
viscosity	1.2 – 10	cP
water cut	0 – 100	%
porosity	25 – 45	%
fines grain sizes	10-200	microns
permeability	1000 - 2000	mD
fines concentration	4.4 - 10	%
gas composition:	78% methane, 21% ethane, 1% propane +.	

Using the graphical user interface, boundary conditions were set-up, with physical property ranges as per Table 3.2.

In order to closely study the trends of the particle-damage permeability profiles, software called MATLAB (100) was used for the CFD-generated pressure drops from which permeability profiles were analysed as explained in chapter 5 and Appendix A-4. MATLAB is often used in the studies of graphical curve trends in order to extrapolate future predictions.

3.2.3 CFD Data Trends Prediction Using MATLAB Software

MATLAB (100) which is short for "**mat**rix **lab**oratory", is a numerical computing environment and programming language coded by The MathWorks company. It allows easy matrix manipulation, plotting of functions and data, implementation of algorithms, creation of user interfaces, and interfacing with programs in other languages. It has 2-D and 3-D graphics functions for visualizing data, for algorithm development, data visualization, data analysis, and numeric computation. In this research MATLAB was used in the studies of complex CFD-generated graphical curve trends in order to extrapolate future predictions. It was selected also due to its comprehensive data analysis capability and tools which can be used for building custom graphical user interfaces as well as functions for integrating MATLAB based algorithms with external applications and languages such as Microsoft Excel which was used in this research. In order to closely study the trends of the particle-damaged permeability profiles, MATLAB was used as explained in Appendix A-4. It has development environment for managing code, files, data, interactive tools for iterative exploration, design, and problem solving. It has mathematical functions for linear algebra, statistics, Fourier analysis, filtering, optimization, and numerical integration.

3.3 Simulations Process and Data Acquisition

Figure 3.3 portrays CFD micro model‘s results of crude velocity magnitudes in m/s. The velocity scale is given on the left side in colour codes. The more red the vector, the faster the speed. It is evident from the figure that the entrance of the porous medium zone causes significant velocity drop based on modelled reservoir properties. The crude started entering the free-flow zone at a maximum velocity of 1.211m/s (3.97ft/s) due to pressure energy which was not constant since in the real life the reservoir pressure is reducing (depleting during production). Hence both velocity and pressure were reducing as happens in the majority of oil and gas fields in which no reservoir pressure maintenance (such as water flooding) is carried out.

For example the CFD result of 1.211 m/s velocity in a well having a wellbore radius of 6”, is equivalent to 1,890 m3/d which for a high permeability (high pressure) reservoir is common while there are quite a few wells which exceed that production rate in real life especially in Saudi Arabia and Kuwait .

The velocity diminished as the crude flowed through the porous medium until it exited into the second un-restricted flow zone where the velocity increased again as it left the block. The minimum crude velocity at the end of the porous medium in this case was 3.266×10^{-4} m/s (10.716×10^{-4} ft/s). This clearly indicates that the most important trend is the porous medium trend; hence an average velocity in the medium is a more representative magnitude. It should be noted that the CFD simulation was designed to reflect a normal reservoir pressure depletion condition where initial reservoir pressure starts at high rate and then gradually decreases as in real life. So because of that, the flux is not constant, gradually the velocity and pressure reduce to minimum levels.

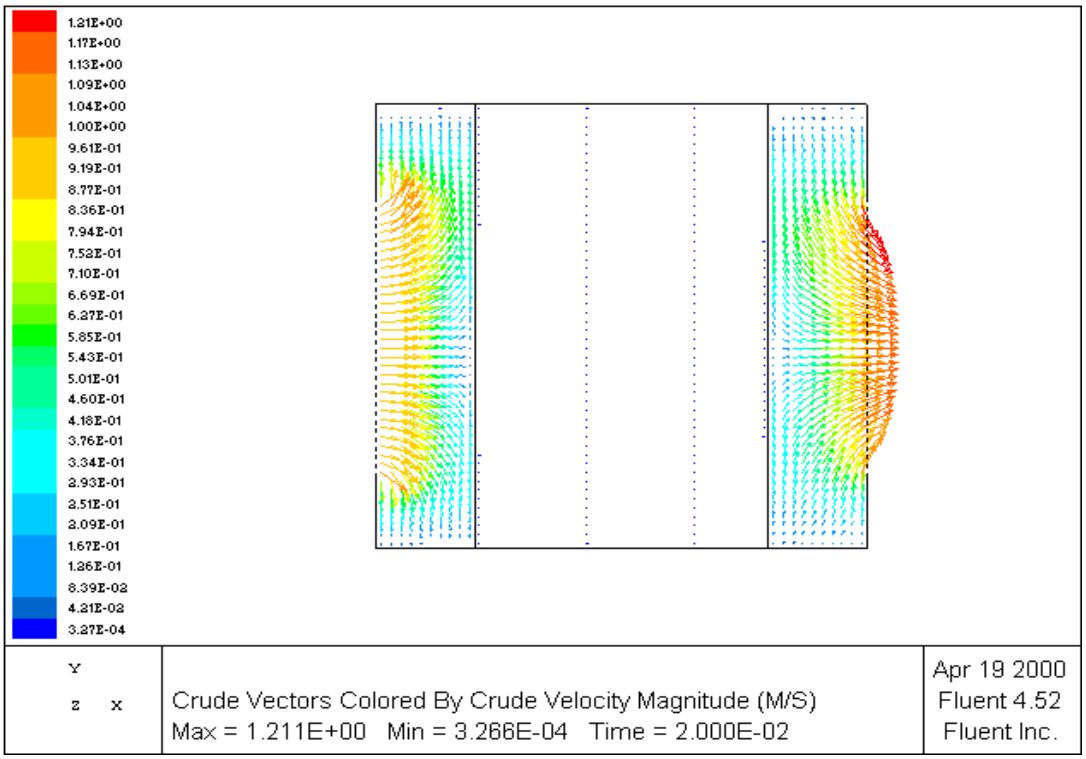

Figure 3.3:Crude (oil, gas and 20%water) simulated speeds across porous medium.

Statistical results of simulated water percentage sensitivities are given in table 3.3 which shows examples of average crude velocities, fines velocities, standard deviation magnitudes and number of cells penetrated within the porous medium grid per water cut %. Results corresponding to higher water cuts (31%- 100%) are given in Appendix A-5.

Average velocity in a porous medium is the average velocity travelled by a mixture flow of fluids and solid particles from the beginning of the reservoir to the wellbore and was dependant on water cut, crude density, porosity, permeability, particle sizes, flow viscosity etc. All velocities are eventually converted into flow rates which are averages fluid flow rates. In real life, when a well is reported to have produced at a certain rate, that rate is the average rate across a reservoir or during a certain period such as barrels per day or cubic meters per day and so forth.

Table 3.3: Statistical simulation results of crude and fines flow at each water cut

Parameter	Average Velocity (m/s)	Average Velocity (ft/s)	Standard Deviation (ft/s)	No of cells in the grid penetrated	Water cut (%)
Crude	0.210753	0.691481	1.024535	1204	20
Fines particles	0.066384	0.217806	0.713457	1797	
Crude	0.210827	0.691723	1.024683	1204	30
Fines particles	0.071069	0.233177	0.726364	1784	

In the 20% water cut case, the average crude velocity in the porous medium was 0.210753 m/s (0.691 ft/s) and the crude velocity standard deviation was 0.312263 m/s (1.025ft/s). The statistical distribution was a ~~"n~~ormal" distribution

Statistical analyses of the simulated results of crude and fines average velocities were calculated by the solver. In that case, a total of 1204 cells were penetrated by crude vectors and 1797 cells were penetrated by fines particle vectors. Appendix A-5 shows results of several other water cuts up to 100%.

A graph of crude (hydrocarbon liquid) velocity vs. % water cut is given in figure 3.4. A clear observation from the graph is the increase in velocities between 40% and 60% water cuts. This range of water cut % of the mixture of oil, water and solid particles is associated with gradual emulsion build-up behaviour. During this transition stage, the heavy emulsion which usually occurs between 20 – 40% water cut is reduced by the water increase above 40% when the mixture starts to receive more water. Hence the rise in velocity between 40 and 60% water cut in figure 3.4. However, due to increase in fluid density, when the liquid becomes mainly water, hence more dense, the velocity starts to decrease as shown in the figure when the water cut increased from 63% to 100%.

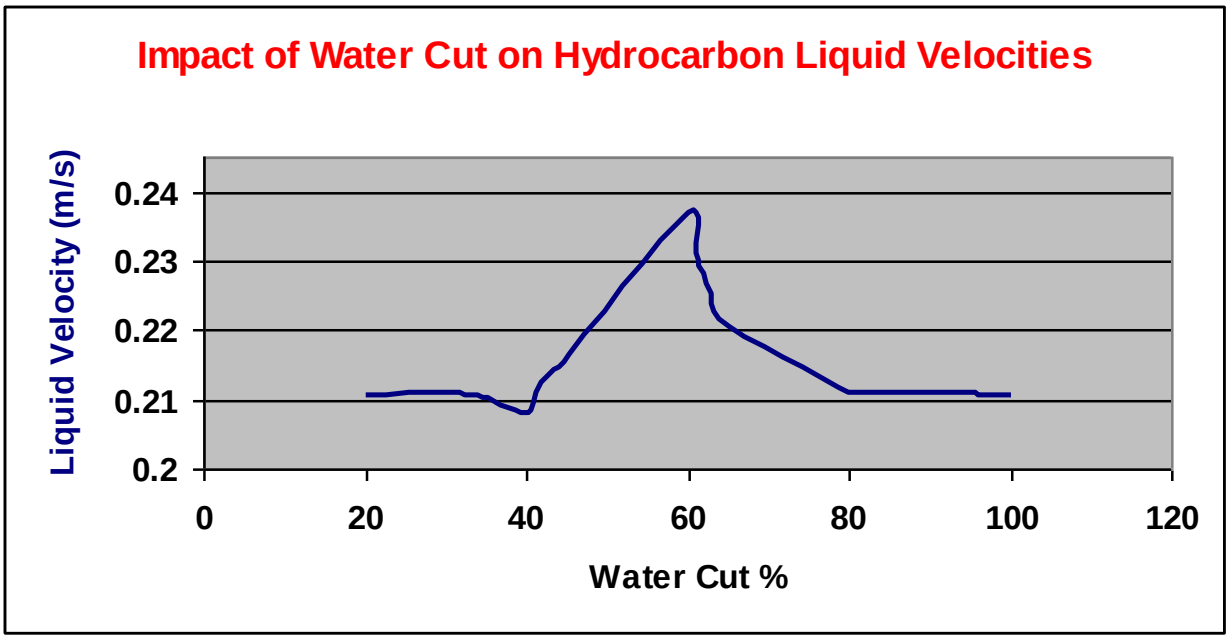

Figure 3.4: Hydrocarbon Liquid Velocities at Various % Water Cut

As such, at 20% water cut, the liquid was mainly oil continuous phase till approached 40% water cut at which range the oil-water emulsion became thicker and more difficult to move. As the water cut increased above 40%, the emulsion decreased as the mixture started to become water continuous or water dominant. Hence between 40% and 60% water cut, velocity increased due to emulsion decrease as the mixture began to move from oil continuous to water continuous. Above 60% water cut, the water which is heavier than oil dominated, hence the mixture density increase, resulted in velocity decrease.

As far as crude velocity behaviour versus grain size is concerned, figure 3.5 shows velocity vs. grain size for all data in table 3.4. Table 3.4 shows particle sensitivity of grain size on the average crude velocity (between the maximum and the minimum) for the simulated grain sizes 10, 50, 100, 150 and 200 microns. An important observation from this analysis is that the larger the grain size, the slower the average velocity.

Table 3.4: Impact of Particle Size on Average Crude Velocity

Grain size	Average velocity	Average velocity
(microns)	(m/s)	(ft/s)
10	0.211	0.692
50	0.169	0.554
100	0.105	0.345
150	0.070	0.230
200	0.053	0.174

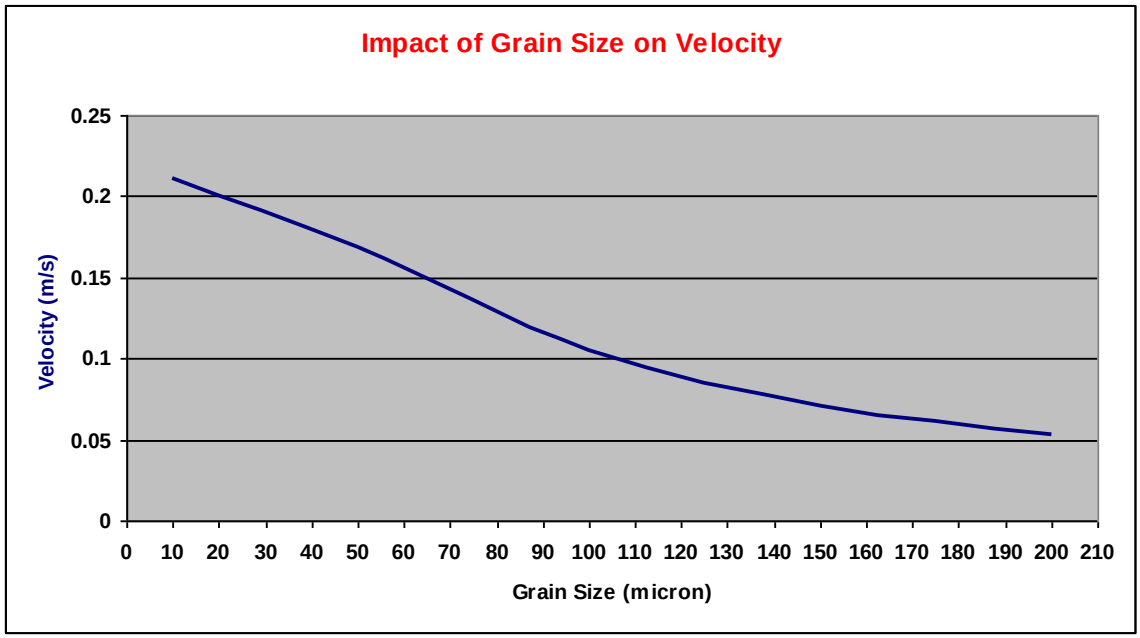

Figure 3.5: Average crude velocity per fines particle grain size

As far as solid particles velocities are concerned, CFD simulated fines velocity vectors are shown in figure 3.6. Since fines are mobilised by the crude, the figure shows crude vectors by sand velocity magnitudes in m/s. This is one of the key results as far as fines studies are concerned; as it exclusively revealed the fines particles impacts on the liquid-particle flow mixture in the porous medium while all flow together.

As per figure 3.6, the maximum observed fines velocity in that scenario was 1.07 m/s (3.51ft/s) as it entered the first un-restricted flow zone. The moment the fines entered the

porous medium, the velocity started to reduce until it reached the lowest magnitude, since the pressure was depleting throughout the period. An observation which was repeated in all simulations is that the fines velocities were always slower than crude velocities though both started at the same speed. This was an example of 10 microns fines grain size flowing at a concentration of 30% by volume of crude and 20% water cut hence total effective concentration was 6%. The most important fines velocity is the porous medium average velocity. Average velocity across the porous medium reflects start to end average flow resistance through the entire modelled reservoir properties, whereas maximum velocity is recorded as the fluid velocity is just at the entrance of the medium. Also as evident in this chapter, most of the particles / crude maximum velocities are similar because they start at the same rate but differ in average velocities.

Hence the average porous medium velocity is the important value because in actual field analysis, reservoir flow performance is measured as an average value such as average production rate per day per well. The reservoir pressure in the field depletes (decreases) with production hence velocity ultimately stops. The exception is in the pressure maintained reservoirs to which water flooding is maintained to keep the reservoir pressure from reducing or in other words to reduce pressure depletion rate. Even in such pressure maintenance scheme, if the scheme was introduced well after a pressure depletion period, it will take long time to replace "voidage" created by the initial depletion before pressure maintenance is achieved. Most fields are produced at pressure depletion mechanism as explained in chapter 2 section 2.9 in which the concept is elaborated in figure 2.13.

The Magnitude of the fines average velocity as well as statistical results of a number of cells penetrated at that average velocity were also revealed. Number of cells penetrated and

standard deviation numbers are automatically generated by the fluent package as part of statistical data. No relationship between velocity and number of cells penetrated. Referring to table 3.3 and figure 3.6, the average porous medium fines velocity simulated was 0.066384 m/s (0.21781 ft/s) which corresponds to 1797 cells penetrated. Standard deviation of 0.217451 m/s (0.71346 ft/s) for fines velocity was revealed as elaborated in table 3.3 which also lists similar information related to higher (30%) water cut. Results corresponding to even higher (30% - 100%) water cut percentages are given in Appendix A-5.

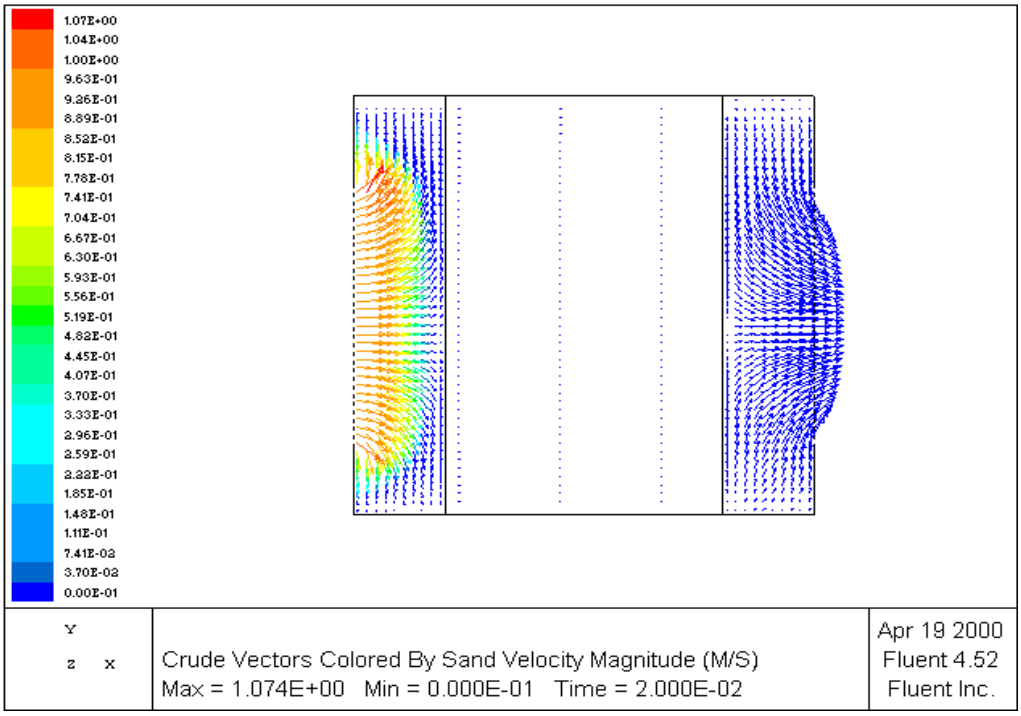

Figure 3.6: Fines (sand) simulated speed across modelled porous medium

3.4 Fines Interaction with the Porous Media

Fines interaction with the porous media is based on the measure of the resultant pressure drop across the medium caused by fluid-mobilised particle size impacts on pores. As explained in chapter 2, section 2.5 that permeability, porosity set of data in a porous medium

can be used to determine a corresponding pore size. According to the jamming ratio theories and corresponding pore damage mechanisms explained in sections 2.5.2 to and 2.5.4 fines particles may not or may penetrate pores in 2000 mD and 1000 mD porous media; however, like in reservoirs having similar or less permeabilities, where fluid flow pressure drop or drawdown is always observed, at each grain size simulation, pressure drop was observed across each of the porous medium. This in real life is also the case in all unconsolidated high permeability sandstone reservoirs where fines of various sizes co-exist with load-bearing sand particles from which hydrocarbon production at various drawdown pressures take place. A field having particle size range of up to 150 μm based on dry sieve analysis as well as Laser Particle Size Analysis (LPSA) had high rate producing wells; with one well reached 2000 b/d production (101). As such, from the title of this research, the fines migrations are analysed based on their impact on production related to pressure not on degree of pore opening size.

For transient porous media calculations, the effect of porosity on the time-derivative terms is accounted for in all transport equations and in the energy equations (102). . Input of pressure drop that is associated with the porous region requires permeability and inertial resistance factor inputs as well as porosity, thermal conductivity, turbulence effects etc… These values will then be used to compute an additional pressure drop in the momentum equations for the porous cells. The inertial resistance factor formulation (102) is given as follows:

$$\frac{\partial p}{\partial x_i} = C_{2i}\left(\frac{1}{2}\rho v_i |v_i|\right) \text{----------(3.2)}$$

Where:

$\frac{\partial p}{\partial x_i}$ = pressure drop through the medium at each ith distance (Pa/m)

C_{2i} = inertial resistance factor (m^{-1})

ρ = fluid density (kg/m^3)

v_i = velocity at the ith position in the medium (m/s)

Input of porosity of each porous region in the model is defined using the porosity Φ which is the volume fraction of fluid within the porous region.

By default, the effect of porosity is enabled for transient calculations in the Physical-Models panel in the CFD. The porous media model which can be used for a wide variety of problems, including flows through packed beds, filter papers, perforated plates, flow distributors, tube banks and any micro flow paths, in this research it was used for pore distributions. Typical high permeability sandstone reservoirs have ranges of porosities based on many rock and fluid properties. In this research 25% - 45% porosity range was used whereas rock permeabilities of 1 Darcy and 2 Darcy were used for various sensitivities and scenarios. The resultant pressure drops were calculated in the CFD solver for each sensitivity which include particle sizes (10 – 200 microns), oil, water cut, multiphase (where gas was added), porosity, permeability, viscosity, reservoir depth, thickness and so forth. Details of particles interaction with the porous medium are given below in this section.

The solid particles velocity at a wall is a nonzero (partial-slip) velocity based on a formula derived by Jackson and Johnson (103). In the Jackson-Johnson condition , the solids velocity at a wall is constructed by setting the lateral momentum flux transmitted to the boundary by particle collisions equal to the tangential stress exerted by the particle adjacent to the wall using the following formula:

$$\tau_{s,w} = \frac{\pi \rho_s \vec{u}_{s,w} \psi \sqrt{\Theta_s}}{2\sqrt{3}\left(\frac{\alpha_{s,\max}}{\alpha_s} - \frac{\alpha_{s,\max}^{2/3}}{\alpha_s^{2/3}}\right)} \quad \text{----------(3.3)}$$

where $\tau_{s,w}$ is the solids shear stress at the wall, $\vec{u}_{s,w}$ is the solids velocity at the wall, ψ is the specularity coefficient (equivalent to 1 minus the tangential coefficient of restitution) and Θ_s is the granular temperature.

The tangential stress exerted on the boundary by the solid (the right-hand side of Equation 3.3) is the product of the change of momentum per particle collision, the collision frequency, and the number of particles per unit area next to the wall (103).

For laminar flow or turbulent flow with the dispersed turbulence model (i.e., dilute-phase turbulent flow), a nonzero solids velocity boundary condition was used at the boundary walls and the Jackson-Johnson wall boundary condition for granular flow which is based on a balance of granular temperature over a thin region adjacent to the wall, indicates that the flux of granular temperature to the wall (q_w,Θ_s) added to the generation of granular temperature at the wall is balanced by the energy dissipation at the wall due to inelastic particle-wall collisions as per the following equation (103):

$$q_{w,\Theta_s} + \frac{\pi \rho_s \vec{u}_s^2 \psi \sqrt{\Theta_s}}{2\sqrt{3}\left(\frac{\alpha_{s,\max}}{\alpha_s} - \frac{\alpha_{s,\max}^{2/3}}{\alpha_s^{2/3}}\right)} - \frac{\sqrt{3}\pi \rho_s \left(1 - e_w^2\right) \Theta_s^{3/2}}{4\left(\frac{\alpha_{s,\max}}{\alpha_s} - \frac{\alpha_{s,\max}^{2/3}}{\alpha_s^{2/3}}\right)} = 0 \quad \text{----------(3.4)}$$

where e_w is the coefficient of restitution for particle-wall collisions and ψ is the specularity coefficient, and are both dimensionless. The Jackson-Johnson granular boundary wall

conditions are enabled in the CFD via the GUI (Graphical User Interface) under Eulerian Multiphase Modeling Options in the Multiphase Parameters panel.

The inputs required for this condition is the particle-wall restitution coefficient and the specularity coefficient (e_w and ψ in Equation 3.4). These parameters are specified in the physical-constants menu in the CFD.

The CFD also models granular multiphase flows using the Eulerian multiphase model which allows for simulation of a wide range of dispersed phase problems including particle separation and classification, spray drying, bubble stirring of liquids, liquid fuel combustion, and coal combustion (the last 2 were not enabled). The Lagrangian dispersed phase model given in equation 3.5 which handles flows in which particle streams are injected into a continuous phase flow with a well-defined entrance and exit conditions (104) was used. This force balance equates the particle inertia with the forces acting on the particle. The following is the Lagrangian dispersed phase model (104):

$$\frac{du_p}{dt} = F_D(u - u_p) + \frac{g_x(\rho_p - \rho)}{\rho_p} + F_x \quad \text{----------(3.5)}$$

Where:

$F_D(u - u_p)$ is the drag force per unit particle mass, in which,

$$F_D = \frac{18\mu}{\rho_P D_P{}^2}\left(\frac{C_D \,\mathrm{Re}}{24}\right) \quad \text{----------(3.6)}$$

Here, u is the fluid phase velocity, u_p is the particle velocity, μ is the molecular viscosity of the fluid, ρ is the fluid density, ρ_p is the density of the particle, and D_p is the particle diameter. F_D is a drag force, g_x is gravitational acceleration in horizontal (x) direction and R_e stands for the relative Reynolds number which is defined as follows:

$$R_e = \frac{\rho D_P \left| u_p - u \right|}{\mu}$$ ----------(3.7)

The drag coefficient, C_D, is a function of the relative Reynolds number of the following general form:

$C_D = a_1 + a_2/R_e + a_3/R_e^2$ ……(3.8)

Where a_1, a_2 and a_3 are constants that apply over several ranges of R_e (104).

The dispersion of particles due to turbulence in the fluid phase was predicted using ~~"r~~andom walk" models available in the CFD. These models include the effect of instantaneous turbulent velocity fluctuations on the particle trajectories through the use of stochastic methods. In order to carry out trajectory calculations Eulerian Multiphase Model was used. The trajectory equations, and any auxiliary equations describing heat or mass transfer to/from the particle, are solved by step-wise integration over discrete time steps. Integration in time of Equation 3.5 yields the velocity of the particle at each point along the trajectory, with the trajectory itself predicted via:

$$\frac{d_x}{d_t} = u_p$$ ---------- (3.9)

Where:

$\frac{d_x}{d_t}$ is the rate of change of distance travelled by particle with time (m/sec)

u_p is the velocity of the particle trajectory (m/sec).

Equation 3.9 is solved in each coordinate direction to predict the trajectories of the dispersed phase (105). The CFD provides options to colour the particles by either their injection numbers (the default) or by fluid velocity. In this research fluid velocity colour coding was

used as can be seen in the velocity vector figures. In this case the particles change colour as they move through the flow field to reflect the local fluid velocity magnitude.

The locations of particles as they travel for a specified amount of time can be displayed from the graphic menu using the particle-track command for any given particle-fluid flow. The particle position will be updated in the display at specified time-step intervals. Hence patterns can be traced in the flow field. This is done for any flow regime, steady state or unsteady state flow. Once the particle positions are defined, they can be checked using the List-Injections command. The initial positions will be stored in the case file when is saved the next time. The particle-track command also tracks the motion of the particles and writes streakline trajectories. In this case, particle tracks are displayed as one injection at a time, producing a static representation of the flow field (106).

Particle injection memory is allocated in the Memory panel (or using the Main/Allocate-Memory text command). If the allocated number was not large enough, the CFD used to be restarted to re-allocate enough memory for the desired number of particles. Thereafter the program and data were loaded before simulations resumed.

3.4.1 Particles Frictional Viscosity and Fluid Molecular Viscosity

In dense (liquid-solid particles) flow at low shear, where the secondary volume fraction for a solid phase nears the packing limit, frictional (or shear) viscosity model was used. The generation of stress is mainly due to friction between particles. An effective molecular viscosity, due to the presence of particles, is calculated for the fluid (107) as follows:

$$\mu_{f,eff} = \mu_f (1 + 2.5\alpha_S + 7.6\alpha_S^2)\left(1 - \frac{\alpha_S}{\alpha_{S,\max}}\right) \text{----------(3.10)}$$

Where

$\mu_{f,eff}$ is the effective intrinsic molecular viscosity, (cP)

α_S is the solids volume fraction (fraction)

$\alpha_{S,\max}$ is the solids volume fraction at the packing limit (fraction).

μ_f = is the intrinsic fluid molecular viscosity, (cP)

For turbulent flow modeled using the dispersed turbulence model (which models turbulence only for the primary phase), the effective turbulent viscosity for the fluid is calculated by adding $\mu_{f,eff}$ to the turbulent fluid viscosity.

As described below, the porous media model incorporates an empirically determined flow resistance in a region of the model. The porosity of the medium does impact the calculation of heat sources due to reaction and the calculation of body forces in the momentum equations. As the degree of coupling between phases depends strongly on the square of the perpendicular diameter, particle diameters were kept uniform for each grain size in all solid particle-fluid flows. The particle shapes were uniformly round and that the particle diameter is much smaller than the inter-particle spacing.

Figure 3.7 depicts pressure drop response inside and outside the porous medium. The vast change in pressure drop within a small block (micro model) highlights the fact that particles‘ impact on pressure is significant as it causes major velocity and drawdown pressure reductions which are quantified in section 3.5 and thereafter to the end of the chapter. Section 3.5 covers the macro (reservoir scale) models.

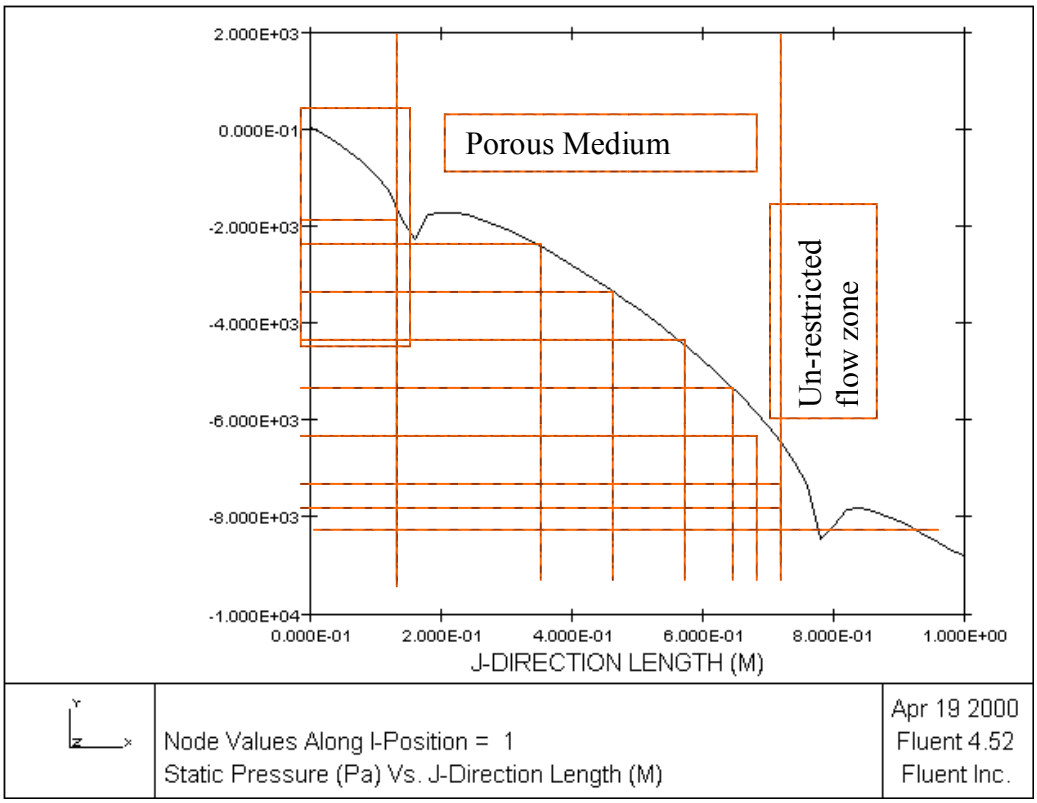

Figure 3.7: Pressure drop profile distribution across the computational grid.

Figure 3.7 is the most important figure in this analysis. It shows continuous pressure drop (ΔP) from the beginning of the block to the end. In the figure, vertical axis shows pressure in Pascal units. Red lines (left to right) are raw lines indicating pressure levels corresponding to computational grid length. Continuous pressure drop is referred to the pressure drop across the porous medium only and not the entire computational block. At each point in the block, a corresponding simulated ΔP is given. All pressure drop values were downloaded into a spreadsheet from which graphical analysis was accomplished. The analyses were carried out to identify all minute changes happening inside a porous medium.

3.5 Reservoir scale analyses

Reservoir scale analyses were then carried out to study changes in pressure. The reservoir model used was identical to the small scale (micro model) discussed in the preceding sections except for the length and width which were 2015 ft and 65 ft respectively. Of the several multiple sensitivities carried out, 4 fundamental scenarios each of which having its own corresponding sensitivities, are summarised as follows:

1. Study of liquid crude (oil and water) flow with solid fines particle sizes (10, 50, 100, 150 and 200 microns) through a 1000 mD porous medium rock model. Water cut was 30%.

2. Study of multiphase (oil, gas and water) flow with solid fines particle sizes (10, 50, 100, 150 and 200 microns) through a 1000 mD porous medium rock model. Gas content was 25% by volume of crude whereas water cut was 30%.

3. Study of liquid crude (oil and water) flow with solid fines particle sizes (10, 50, 100, 150 and 200 microns) through a 2000 mD porous medium rock model. Water cut was 30%.

4. Study of multiphase (oil, gas and water) flow with solid fines particles sizes (10, 50, 100, 150 and 200 microns) through a 2000 mD porous medium rock model. Gas content was 25% by volume of crude whereas water cut was 30%.

After each particle size analysis, comparisons between particle impact on liquid flow and particle impact on multiphase flow were analysed. Similarities and differences are further elaborated in section 3.5.5.

The 4 fundamental scenarios with corresponding sensitivities which are discussed from section 3.5.1 to section 3.6.5, are just examples, many other scenarios were carried out whose results are discussed in the result discussions section 3.7.

3.5.1 Study Of Liquid Carrying 10-200µm Fines Through A 1000 mD Rock.

3.5.2 Effect of 10 microns Fines Migration In Liquid Flow

Starting with a 10 µm fines particle analysis flowing along with crude liquid (oil and water) without gas, the CFD reservoir scale simulation results of liquid and particle velocities as well as pressures are given in Figures 3.8 to 3.10.

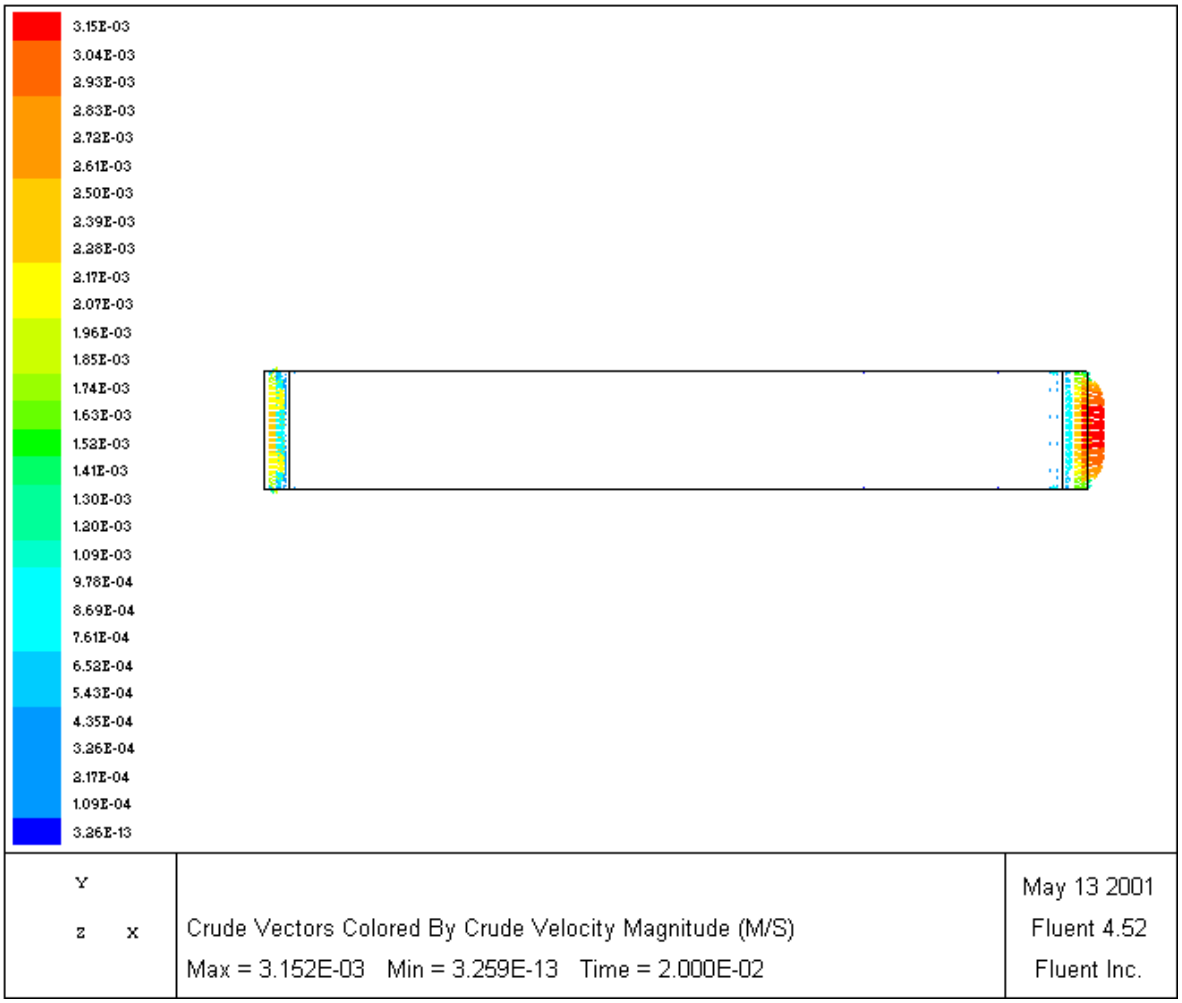

Figure 3.8: Liquid velocity changes during 10 µm fines particle mobilisation

Y-scale is a colour coded velocity in m/s, whereas the x-axis is the lateral reservoir length. As far as particle analysis is concerned, figure 3.9 demonstrates a unique feature in this study. Despite the simultaneous liquid and solid particle mixture flow complexity,

instantaneous particle velocities are exclusively being measured. This makes the dynamic flow analysis more comprehensive compared to today's conventional laboratory approaches since in a core laboratory analysis, the best that could be achieved are the fines injection velocities before mixing with liquid whereas when a fines-liquid mixture moves, there is no facility to measure separately solid velocity from liquid velocity during the motion while in this study that was possible.

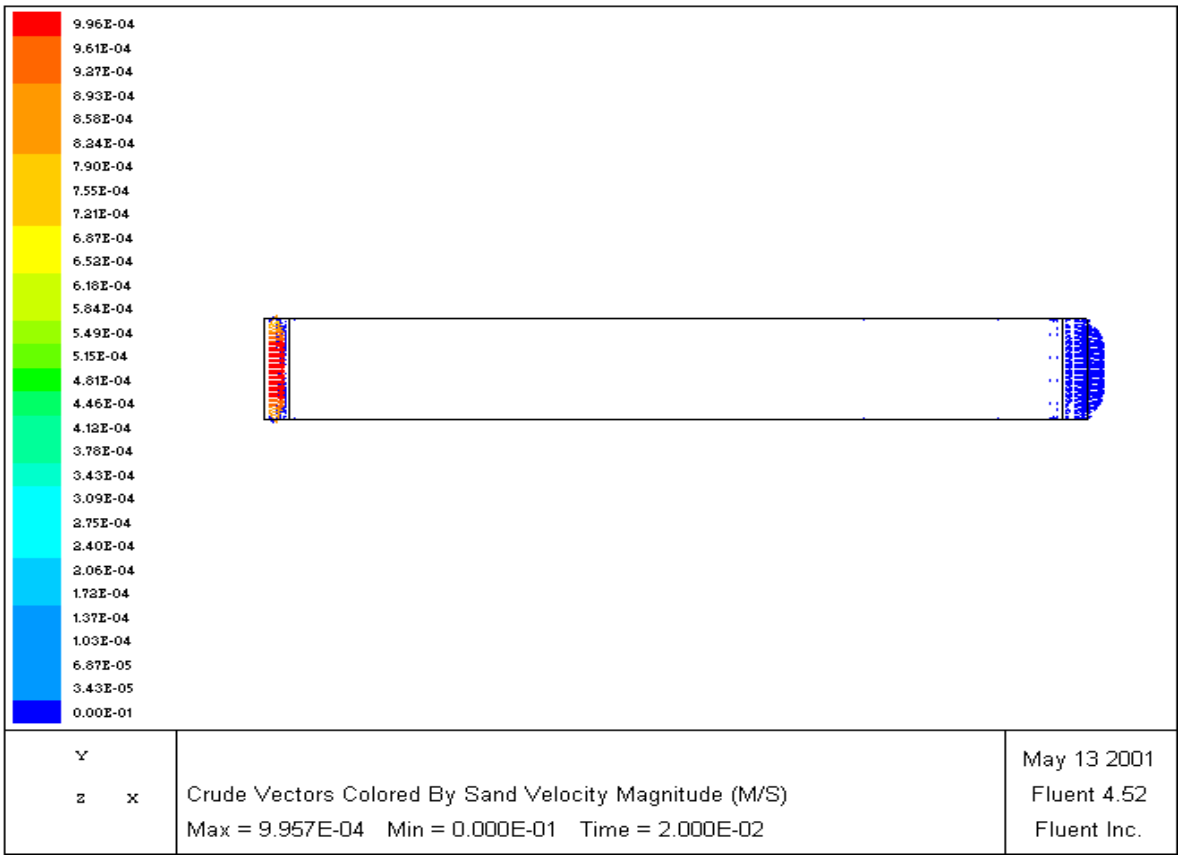

Figure 3.9: Velocity changes when 10 µm fines (sand) was flowing in a liquid medium

When pressure changes were analysed across the model, CFD results revealed distinct patterns. Figure 3.10 depicts pressure changes inside the computational reservoir block and provides very significant data which can be used to determine characteristics of fines migration. This is because reservoir pressure data is a fundamental information as far as

production performance and prediction analyses are concerned. Changes in pressure simulated by the CFD are given both quantitatively and qualitatively in figure 3.10.

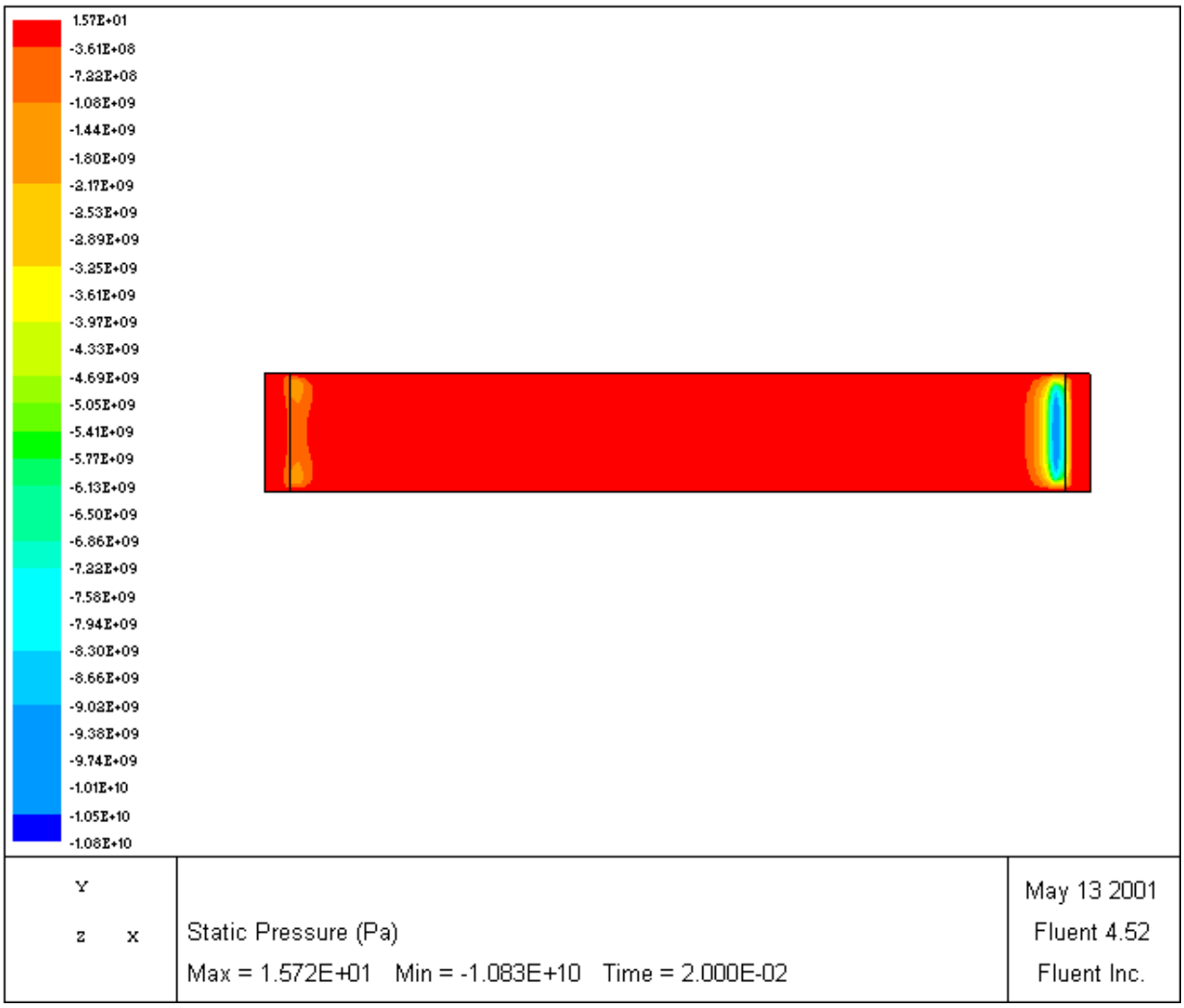

Figure 3.10: Pressure changes when 10 µm fines in hydrocarbon liquid flow was simulated.

Hence figure 3.10 offers qualitative as well as quantitative pressure change display as solid fines particle in liquid hydrocarbon (oil and water) flow through a modelled sandstone reservoir. The resultant pressures in Pascal units at each reservoir interval were converted into psi and so were the other parameters units. Reservoir interval in meters was converted into feet. Hence data were kept in field units.

3.5.3 Impacts of 200 µm Fines on Liquid Flow Through 1000mD Rock

When 200 µm fines was simulated in a liquid (oil and water) flow, various CFD simulation results were revealed as shown in figures 3.11 to 3.13. Figure 3.11 denotes liquid crude (oil and water) velocity vectors as the liquid flowed across the modelled porous medium having reservoir properties. The figure shows maximum and minimum velocities reached. Like in the finer grain size (10µm) result, the results of coarser (200µm) grain indicated that in a 1000 mD permeability drainage, the crude liquid velocity profiles (Figure 3.11) are higher compared to the corresponding velocity (m/s) profiles of fines (sand) in Figure 3.12. This is despite the fact that they all began at the same velocity.

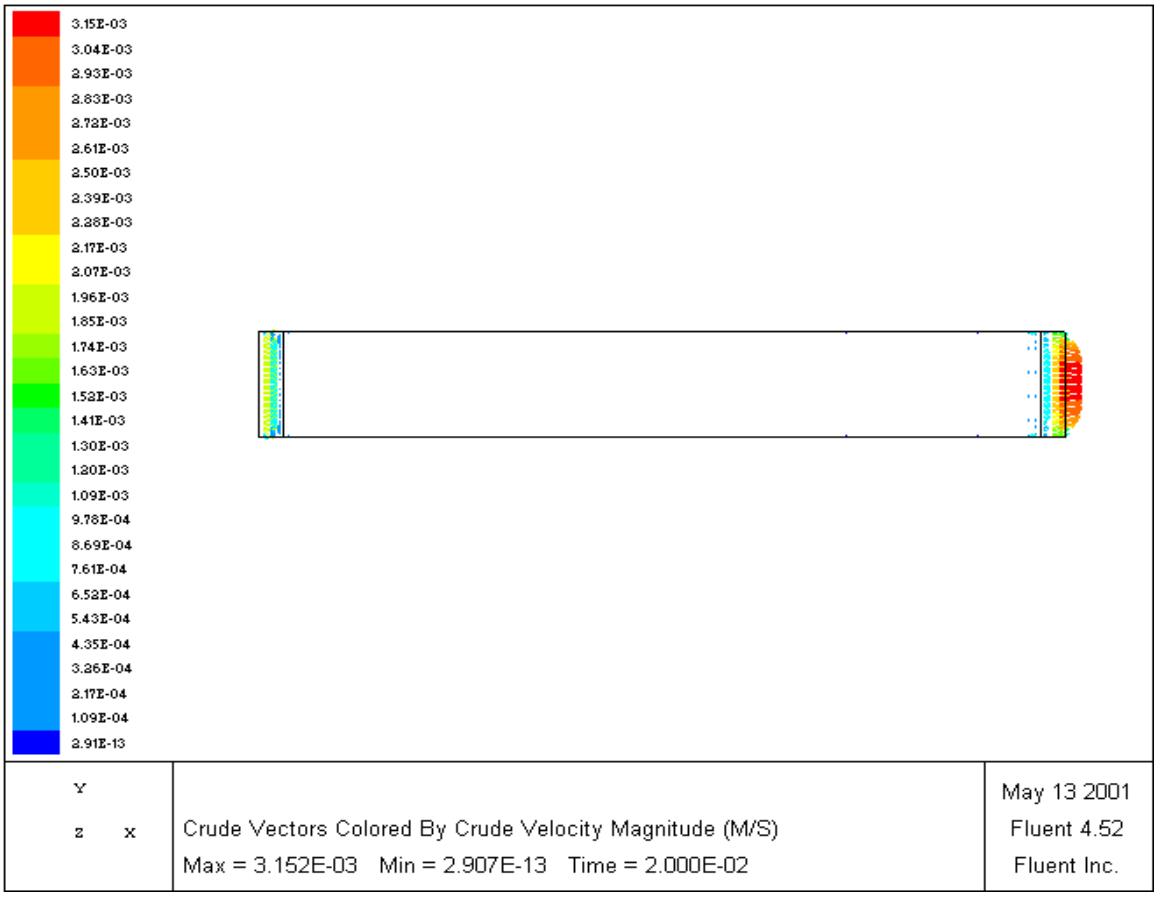

Figure 3.11: Liquid velocity profile when 200 µm fines mobilisation was simulated.

The minimum liquid velocity observed was lower in coarser (200µm) grain particles compared to the velocity observed in finer (10 µm) particles. This is in line with field observations when wells producing at lower rates mobilising 150-200 µm sand particles take less time to stop producing compared to the time observed in wells producing 10 - 50 µm particles at similar lower flow rates (108) and same reservoir conditions. Figure 3.12 revealed only fines velocity vectors exclusive from liquid velocity during the liquid/particle movement.

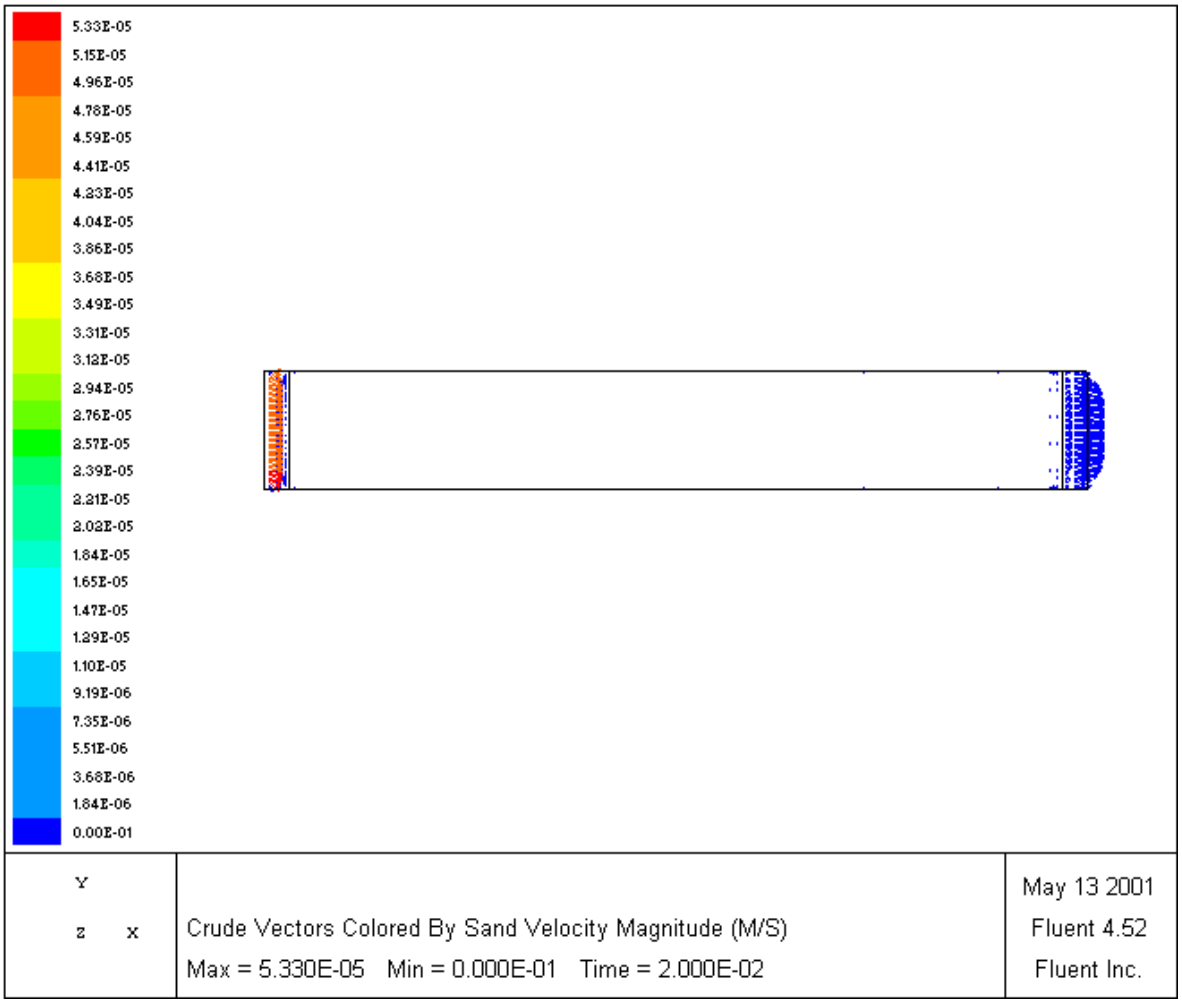

Figure 3.12: Particle velocity profiles when 200 µm fines was flowing in a liquid medium.

Figure 3.13 offers qualitative as well as quantitative display of pressure changes due to fines presence in liquid hydrocarbon as they all flow through modelled sandstone reservoir. The resultant pressures were thereafter converted into psi units from Pascal units at each reservoir interval. The length of the reservoir was also converted from meters to feet. Hence data units were converted to field units in order to carryout reservoir engineering analysis including pore plugging studies and related permeability declines analysis, covered in chapter 4.

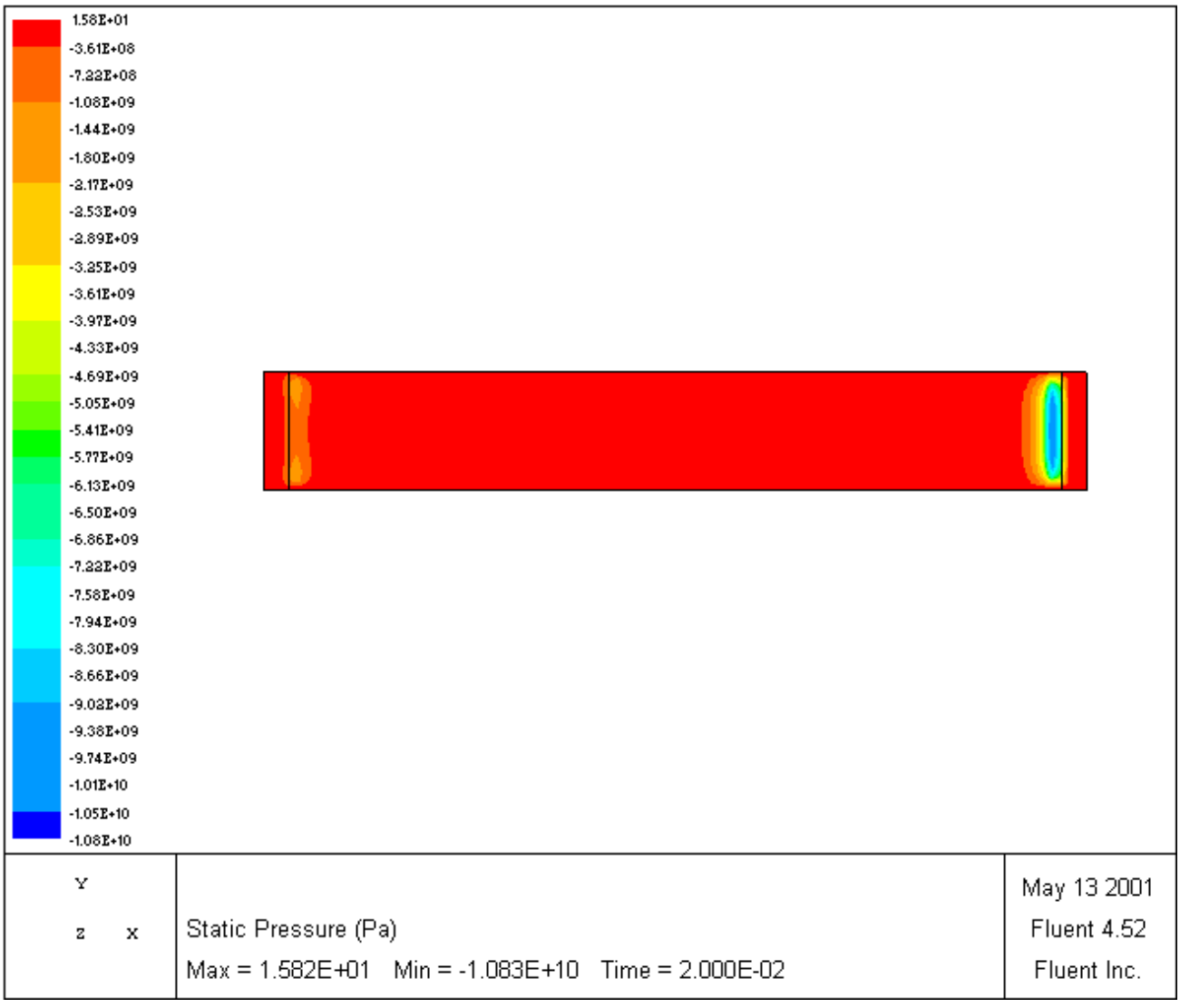

Figure 3.13: Pressure contours when 200µm fines was simulated in liquid flow.

Summaries of all pressure drop results at each reservoir length obtained in 10 sets of simulations of fines and liquid as well as fines and multiphase flows for each grain size sensitivity: 10 μm, 50 μm, 100 μm, 150 μm and 200 μm, are presented in the next sections.

3.5.4 Multiphase Flow Mobilising 10-200μm Fines Through 1000 mD rock.

3.5.5 Comparison of 10 μm Fines Impacts on Multiphase and in Liquid flow

Gas introduction into the liquid which resulted in multiphase flow, played a tangible role in fines migrations mechanisms in terms of pressure analyses as compared to gas-free liquid flow analyses. The study started with a 10 μm fines analysis flowing in multiphase (oil, water and gas) through a 1000 mD porous medium having 35% porosity. CFD simulation results are given in figures 3.14 to 3.16.

Figure 3.14 shows that when very fine grain particles are mobilised, multiphase crude velocity changes (shown in colour coded scale) are higher compared to the corresponding velocity (m/s) changes of fines (sand) (figure 3.15). This is despite the fact that they all began at the same velocity. A difference between multiphase flow (figure 3.14) and liquid flow (figure 3.11) was attributed to gas presence in the multiphase flow.

Gas having much lower density compared to water and oil densities, when the three are mixed, the overall density becomes lighter compared to the two liquid mixture density. As a result, the lighter multiphase mixture velocity is expected to be faster than the liquid velocity in the absence of gas fluid.

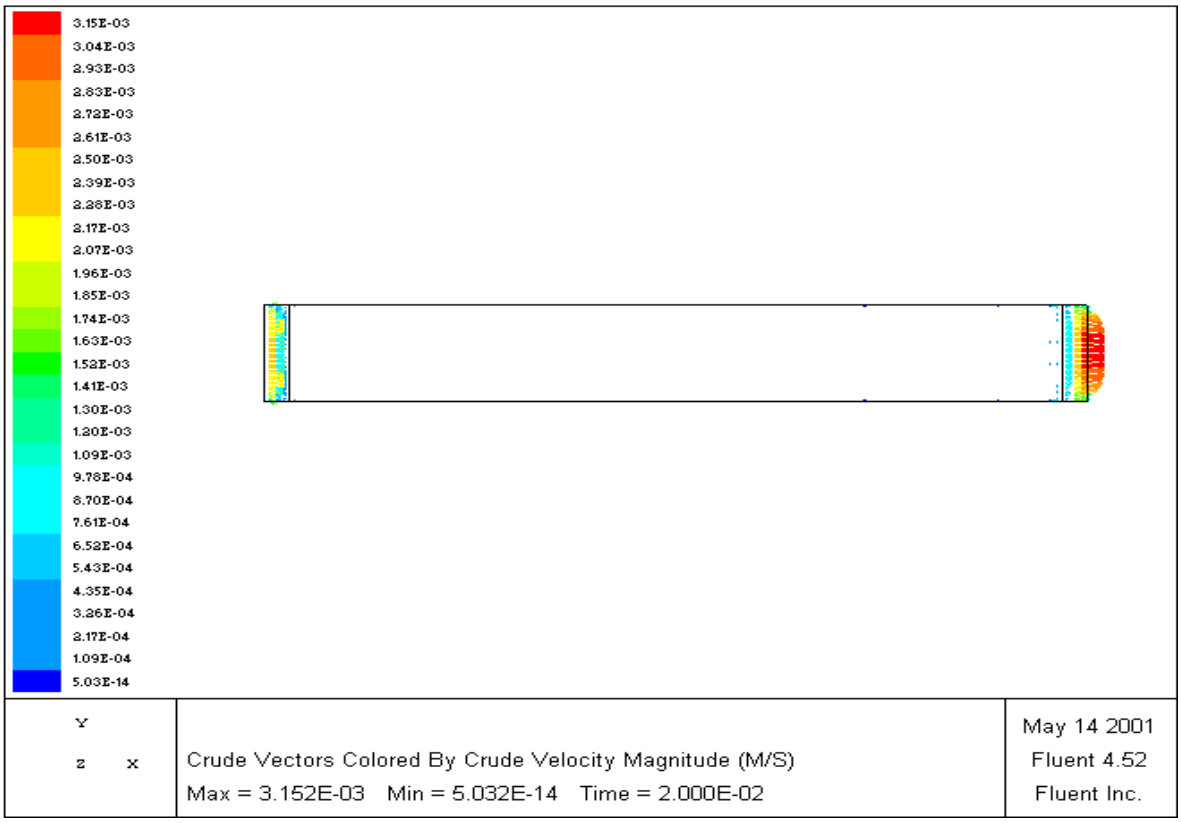

Figure 3.14: Multiphase (crude) velocity changes when 10 µm fines mobilisation was simulated

Pressure drop comparisons between the multiphase scenario and liquid scenario involving 10 µm grain size sensitivity is given in the next sections 3.6.

Since CFD measures solid particle velocity as a separate quantity from the multiphase crude mixture during the flow, fines velocity was not expected to be influenced by gas as in both cases the grain size (hence same mass) remained unchanged. As expected, sand velocities were similar although pressure values remained different due to gas presence in the multiphase flow which caused additional turbulence effects compared to pressure values in the absence of gas (liquid only).

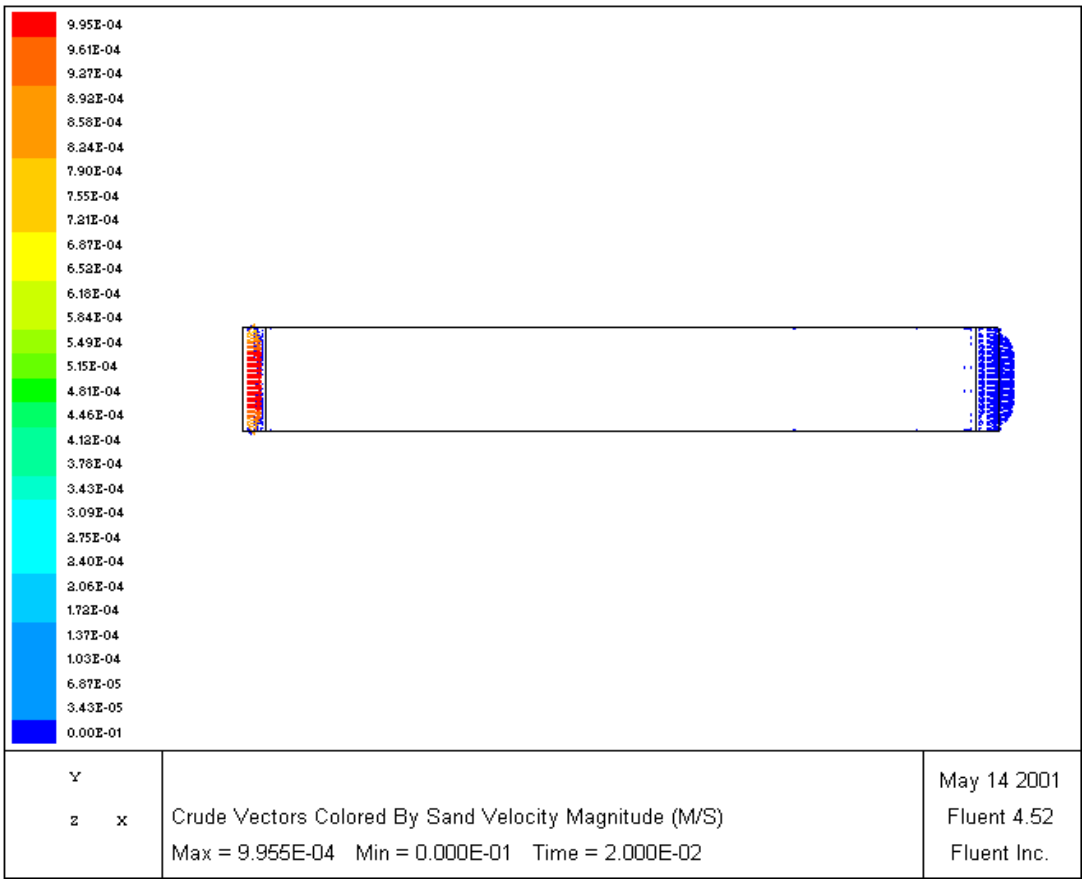

Figure 3.15: Sand velocity profiles when 10 µm fines was flowing in a multiphase flow.

As explained above, pressure analyses are fundamental in determining reservoir productivity or injectivity performance and prediction.

Figure 3.16 shows pressure distribution throughout the entire computational grid area through which multiphase flow carrying 10µm fines particles were mobilised.

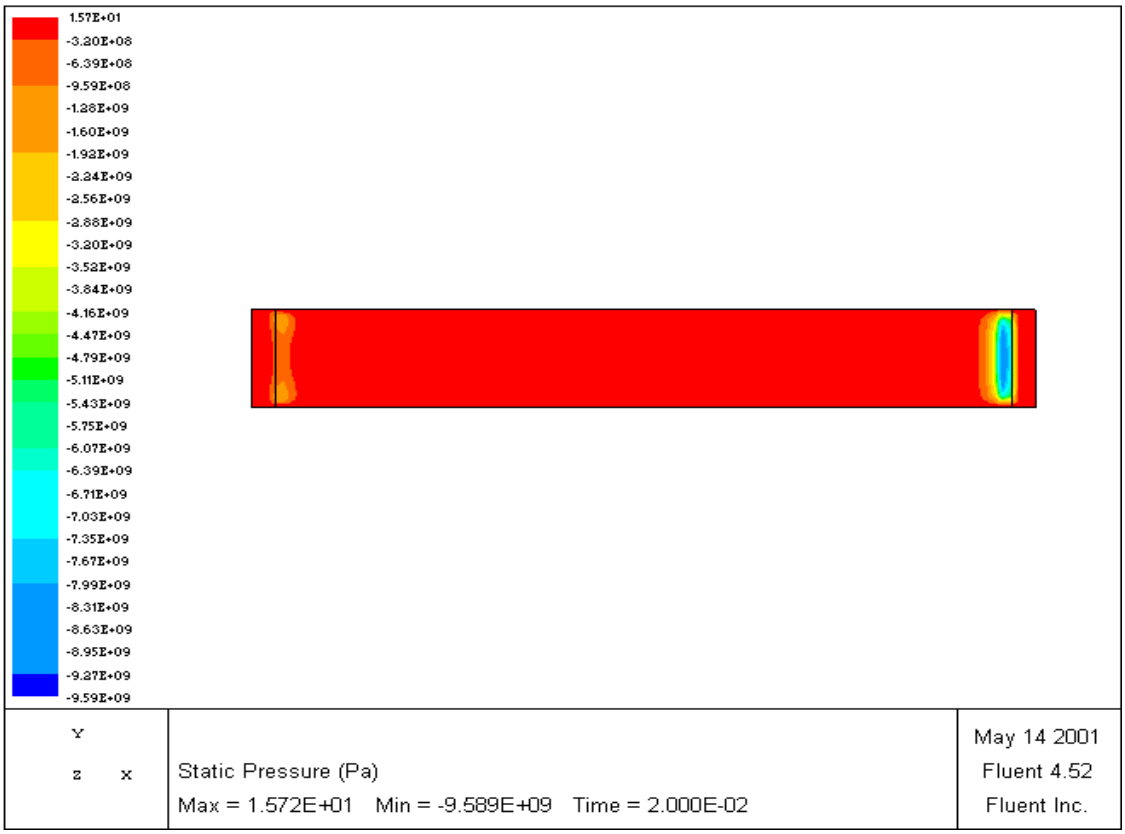

Figure 3.16: Pressure profiles when 10 µm fines flow in a multiphase fluid was simulated.

There is a magnitude of pressure decline difference between figure 3.10 (reflecting liquid and no gas effect) and figure 3.16. The pressure drop differences between multiphase and liquid scenarios for 10µm 50µm, 100µm, 150µm and 200µm fines particles sizes are given in the following sections 3.6 to 3.6.5.

3.6 Results of the Simulations

All results of the liquid and multiphase modelling were retrieved from the CFD and were used to analyse differences revealed in all sensitivities carried out. While this section provides results analyses, results discussions are given in section 3.7.

Referring to 10µm fines simulated in a 1000 mD drainage area, resultant pressure drop profiles observed in a liquid medium were different from the profiles revealed in a

multiphase medium. For comparison purpose, figure 3.17 demonstrates pressure drop difference observed in a scenario involving 10µm fines grain size between a liquid medium and multiphase medium through the same porous rock.

As shown on figure 3.17 (which compares multiphase and liquid results), when 10 micron fines in liquid hydrocarbon was analysed by the CFD, the corresponding pressure drop observed was from -1212.5 psi to -3381.1 psi.

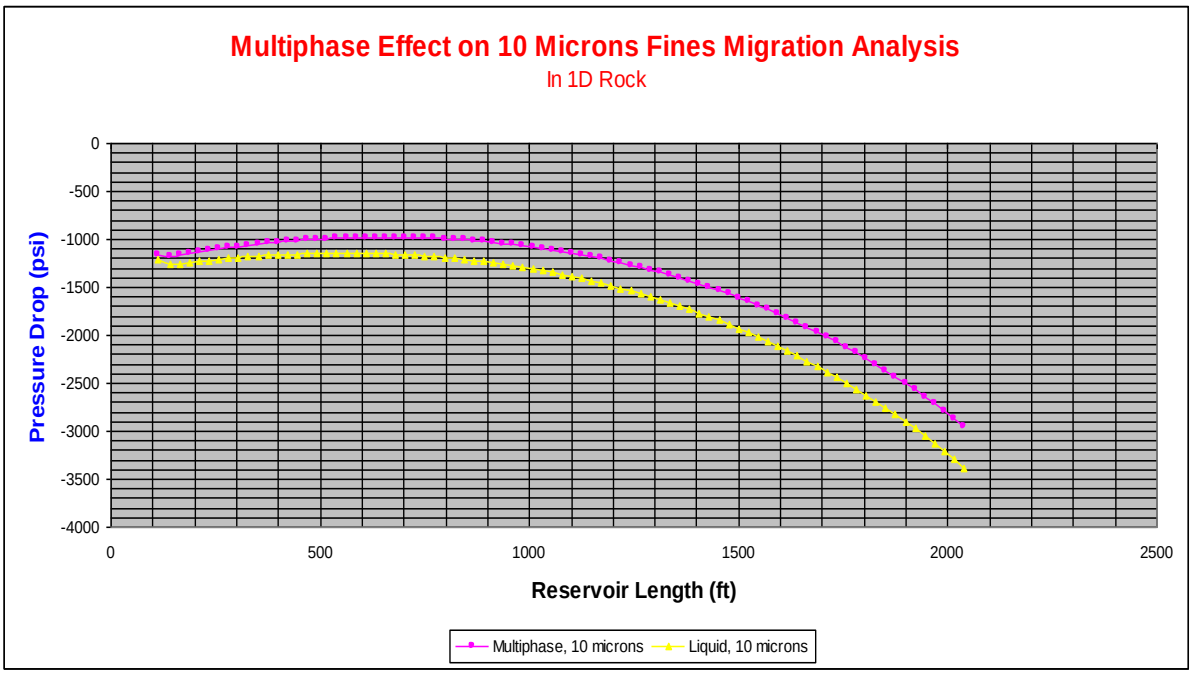

Figure 3.17: Pressure drop comparison in multiphase and liquid flowing 10µm fines

Hence a 2168.6 psi pressure drop was the liquid pressure drop observed. Whereas a comparatively less pressure drop value as observed when 10 microns fines was simulated in a multiphase flow where gas caused less pressure reduction as can be seen in figure 3.17. The net pressure drop difference between liquid and multiphase media which can be attributed to gas presence in this analysis is about 372.3 psi which unfortunately is not accounted for in laboratory studies where hydrocarbon gas analysis is usually not carried out alongside with

oil and water in this magnitude. Multiphase and liquid simulation investigations of coarser grain sizes are explained in section 3.6.1. The following section refers to 200 microns particles impact on pressure drop in multiphase medium.

3.6.1 Impacts of 200 µm Fines on Δp in Multiphase and Liquid Flow

This section presents a study of impact of gaseous (multiphase) fluid and coarse grained particle migration on pressure drop. The main difference between this and liquid analysis is gas fluid introduction to the flow system, whereas everything else was kept the same including the 200 µm particle sizes. CFD simulation results are given in figures 3.18 to 3.20. Velocity vectors of multiphase crude can be seen in figure 3.18.

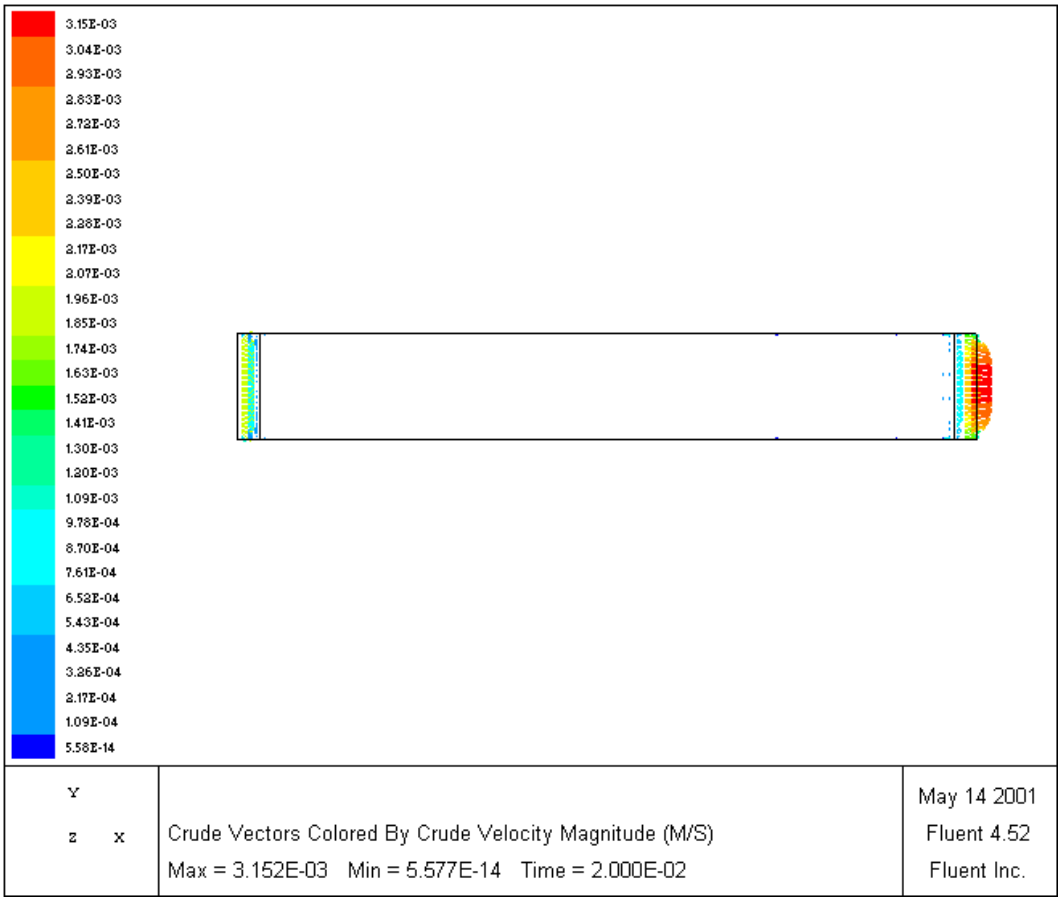

Figure 3.18: Multiphase velocity changes during 200 µm fines grains mobilisation

The difference between figure 3.18 and figure 3.11 (liquid velocity changes during 200 µm particle flow), is in the minimum velocity.

The CFD simulation results revealed sand (fines) flow vector velocities which were separate from multiphase fluid velocities as shown in figure 3.19. This approach makes fines migration analysis more focussed since in this case, particles velocity was measured separately from liquid velocity. Such results prompted more focussed granular fluid velocity studies to be carried out. Figure 3.19 portrays minimum and maximum solid particle velocities achieved when 200 microns fines grains were simulated in a multiphase medium.

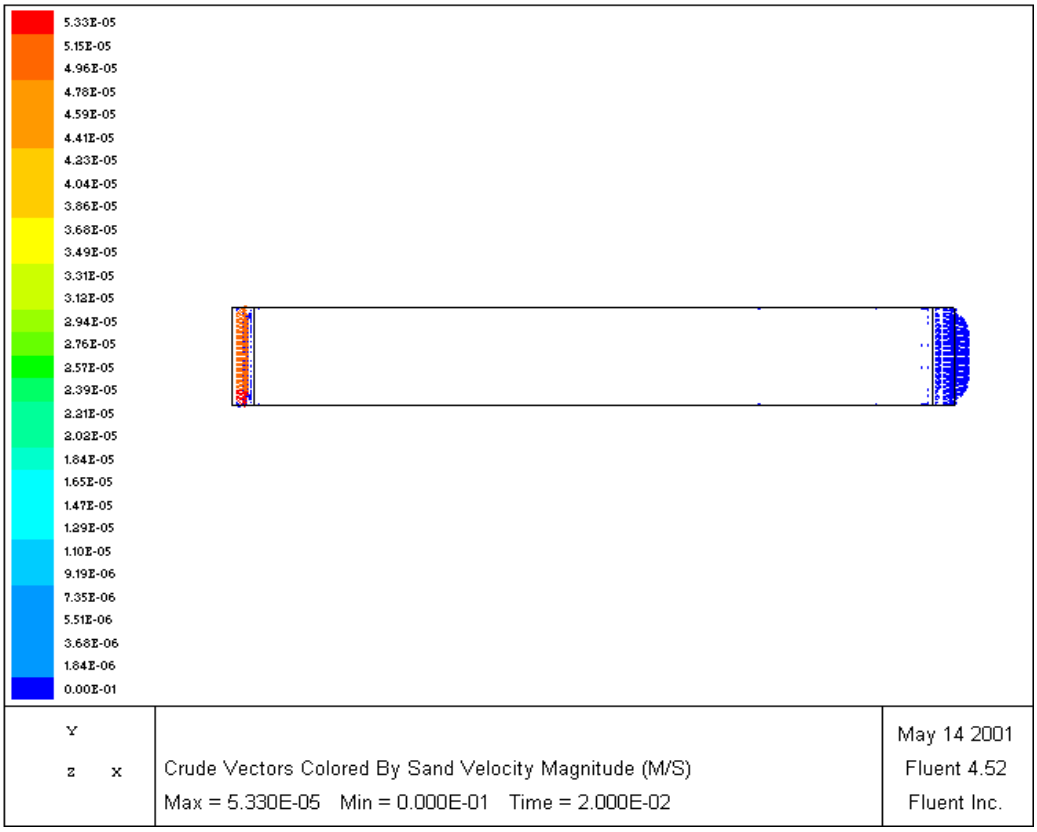

Figure 3.19: Velocity vectors of 200 µm fines grains flow in a multiphase medium

Figure 3.20 reveals a pressure profile which is a pressure pattern as a result of the particle flow in the multiphase medium. It is a combined pressure pattern of fines and multiphase flow. Pressure scale is given on the left in a colour code format.

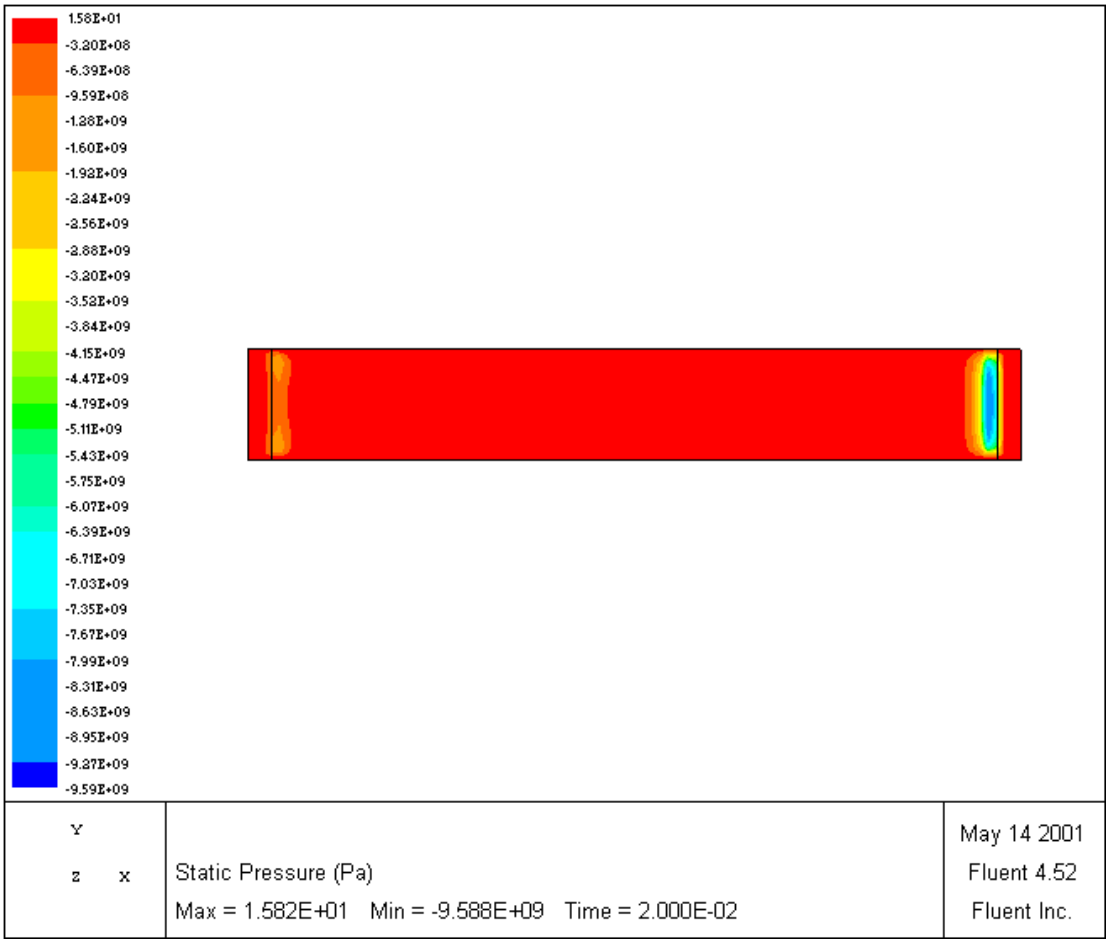

Figure 3.20: Pressure profiles during 200µm fines mobilisation in a multiphase flow.

In addition to the pressure pattern, the CFD package stores in its databases the actual pressure data after each simulation of the entire modelled reservoir. Figure 3.21 provides a comparison of particle impacts on pressure in both multiphase and liquid media.

Clear differences in pressure drop were revealed between coarser particle grains (200µm) flowing in a multiphase fluid and the same particle size flowing in liquid (gas free) fluid as shown in figure 3.21. While a total pressure drop in the case of multiphase flow was about

1922 psi across the entire porous medium, the corresponding total pressure drop in the liquid case was about 2301.5 psi. The 379.5psi difference is attributed to gas presence in the multiphase.

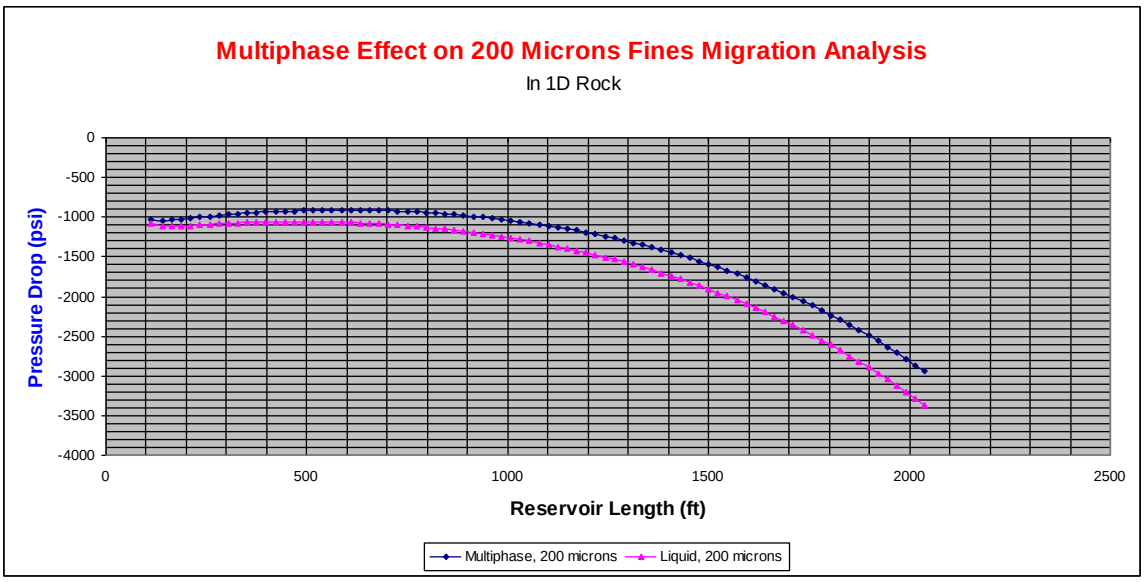

Figure 3.21: Multiphase and liquid pressure drops during 200 µm fines flow.

3.6.2 Impacts of 50- 150 µm fines on pressure in multiphase and liquid media

Having analysed impacts of 10 µm and 200 µm on pressure drop, analyses of other grain sizes: 50 µm, 100 µm and 150 µm were carried out in a similar manner as in the above sections 3.5 to 3.6.1. CFD simulated pressure drop results pertaining to those grain sizes in both multiphase and liquid media, were compiled, plotted and compared as in figures 3.22 to 3.24. Figure 3.22 shows a clear difference in pressure drop between multiphase fines migration and liquid fines migration as far as 50µm grain particles analysis is concerned. While total pressure reduction in the case of multiphase flow was about 1910 psi across the entire porous medium, total pressure reduction in the liquid analysis was about 2289 psi.

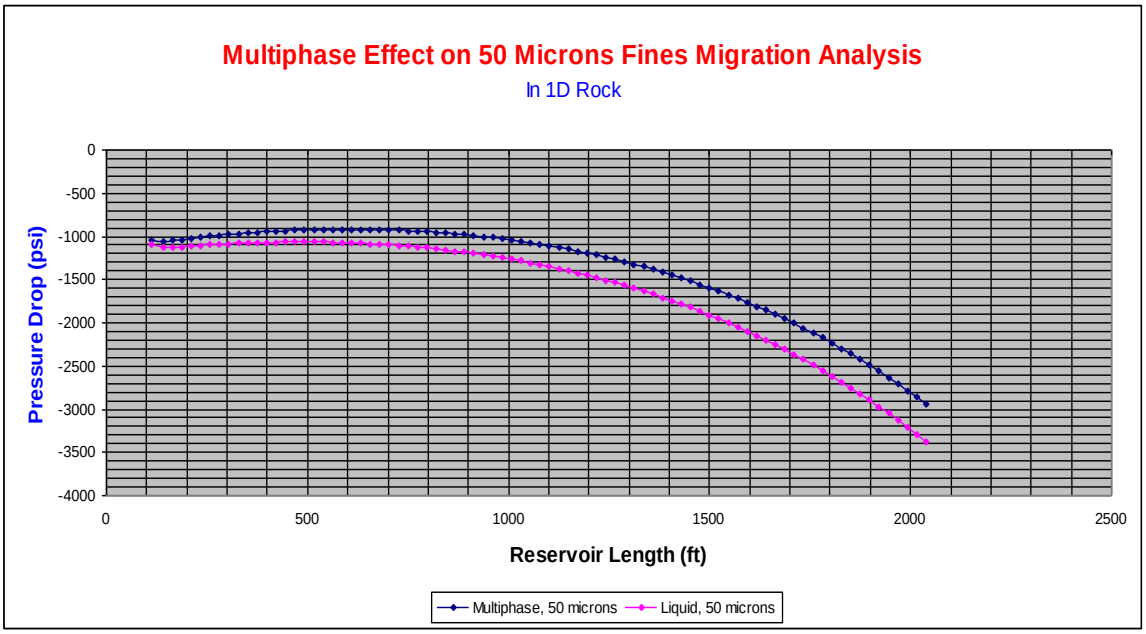

Figure 3.22: Multiphase and liquid pressure drops during 50 µm particles flow.

When comparison of the CFD pressure drop results due to 100µm grain particles flow in both multiphase and liquid media was made, clear difference in pressure drop between multiphase fines migration and liquid fines migration was observed. The difference is highlighted in figure 3.23.

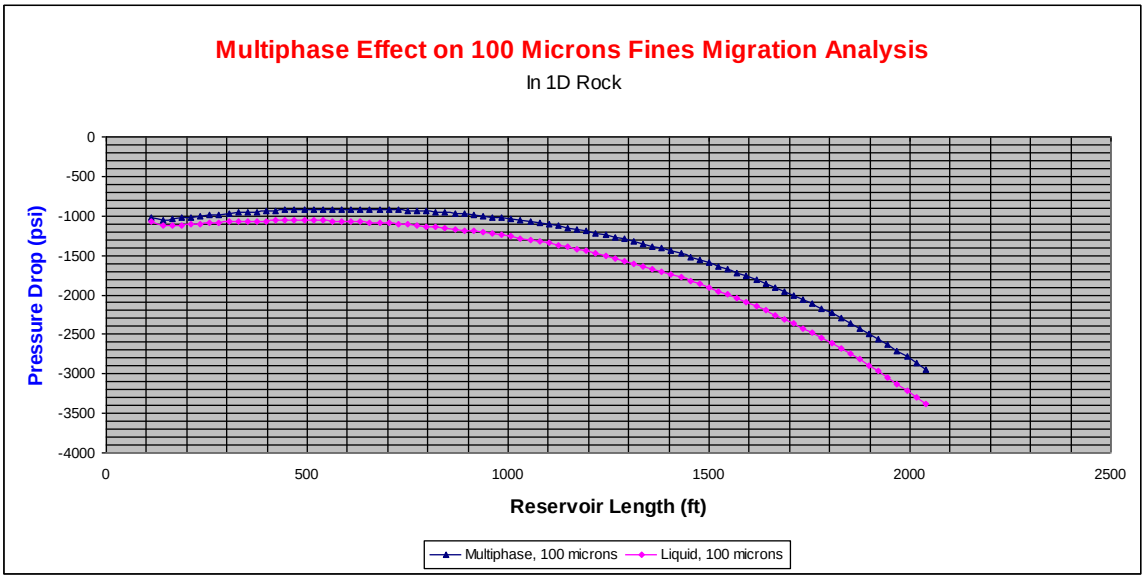

Figure 3.23: Multiphase and liquid pressure drops during 100 µm fines flow.

While total pressure reduction in the case of multiphase flow was about 1919.6 psi, total pressure reduction in the liquid case was about 2298.7 psi.

Simulation comparison was made between liquid and multiphase flows in which 150 µm fines particles were mobilised. The clear difference in pressure drop between multiphase fines migration and liquid fines migration is highlighted in figure 3.24. While total pressure drop across the porous medium in the case of multiphase flow was about 1921 psi, total pressure drop reduction in the liquid analysis was about 2300.7 psi. The 379.5 psi difference is attributed to gas presence in the multiphase.

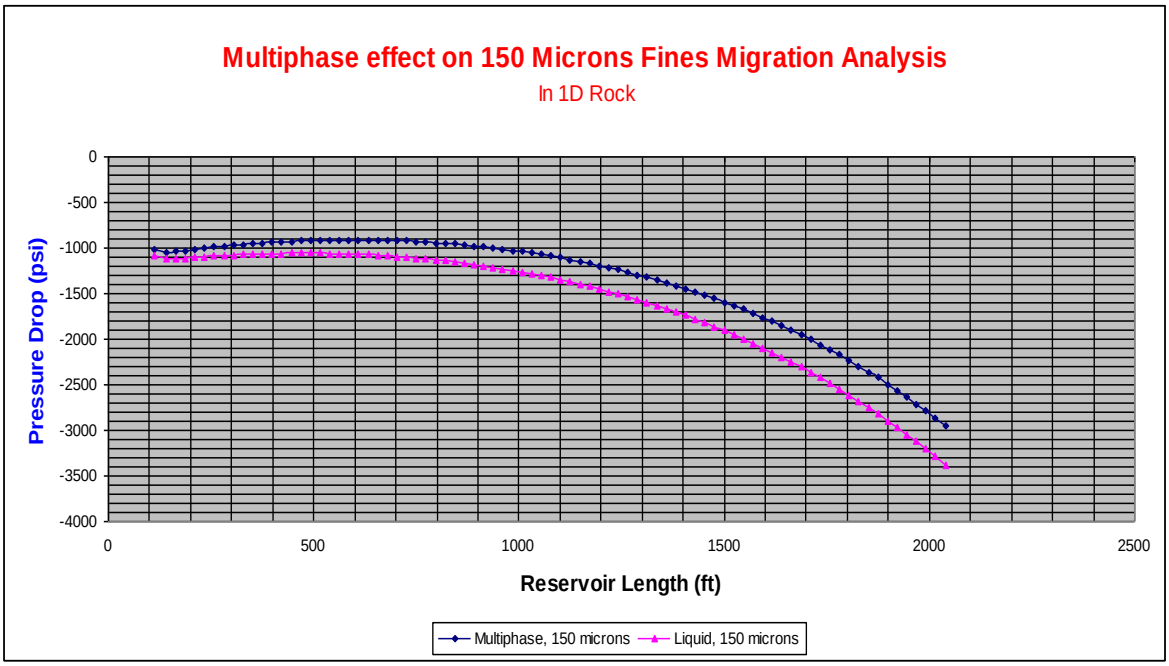

Figure 3.24: Multiphase and liquid pressure drops during 150 µm particles flow.

Finally results of pressure drop per reservoir depth related to 10 µm particle simulations were grouped and tabulated as in table 3.5. table 3.6 summarises differences in Δp for all particle sizes. As is evident from table 3.5, the overall multiphase pressure drop (drawdown) was comparatively lower across the computational model than the pressure drop observed in the liquid analysis. While the former was reduced by 1796.3 psi (from -1153.5 to -2949.8 psi),

the latter dropped by 2168.6 psi (from -1212.5 to -3381.1 psi). Those differences in pressure drawdowns show that gas fluid tends to help in pressure maintenance. That is why in certain oil fields such as Baker‘s field in California, USA, hydrocarbon gas injection is used to supplement reservoir pressure which enhances production. As such it is evident that gas fluid does boost pressure. Unfortunately in both conventional as well as special core lab analysis (Scal), hydrocarbon gas analysis (due to safety reasons) is not carried out despite the fact that core lab results are still the basis for many field development studies.

Table 3.5:Pressure drawdown in multiphase and liquid flowing with 10μm fines: 1000 mD rock

Reservoir	Drawdown Pressure	Drawdown Pressure	Drawdown Pressure
	(psi)	(psi)	difference
Length (ft)	Multiphase	Liquid	(psi)
113	-1153.5	-1212.5	-59
140.6	-1172.2	-1251.4	-79.2
164	-1162.6	-1252.5	-89.9
:	:	:	:
468.7	-1005.9	-1150	-144.1
492.1	-999.6	-1147.4	-147.8
515.6	-994.2	-1145.7	-151.5
:	:	:	:
679.6	-979.9	-1156.6	-176.7
703	-981.2	-1161.6	-180.4
726.5	-983.5	-1167.4	-183.9
:	:	:	:
1499.8	-1609.9	-1928.1	-318.2
1523.3	-1649.1	-1971.9	-322.8
1546.7	-1689.7	-2017.2	-327.5
1570.1	-1731.7	-2064.1	-332.4
1593.6	-1775.4	-2112.5	-337.1
1617	-1820.6	-2162.5	-341.9
:	:	:	:
1991.9	-2790.6	-3212	-421.4
2015.4	-2869	-3295.4	-426.4
2038.8	-2949.8	-3381.1	-431.3

Pressure results due to each grain size (10-200 μm), in both liquid and multiphase analyses in a 1000 mD initial rock permeability are given in Appendix A-6. The Appendix summarises all pressure results at each reservoir length due to the impacts of all particle sizes (10 μm – 200 μm) in both multiphase and liquid media.

Table 3.6 shows pressure drops across the entire porous medium due to the impacts of various fines particle sizes (10 – 200μm) flowing in both multiphase and liquid media through a 1000 mD drainage.

Table 3.6:Pressure drops across porous medium in multiphase and liquid: 1000 mD rock.

Grain size (μm)	Multiphase pressure drop ΔP (psi)	Liquid pressure drop ΔP (psi)	Multiphase impact on pressure drop ΔP (psi) gained
10	1796.3	2168.6	372.3
50	1909.5	2288.5	378.9
100	1919.6	2298.7	379.1
150	1921.2	2300.7	379.5
200	1922.0	2301.5	379.5

The above sections (3.5 to 3.6.2) present results of ten fundamental sensitivity analyses of 1000 mD porous medium scenarios through which flow of fines particle sizes (10 μm, 50 μm , 100 μm, 150 μm and 200 μm) in multiphase and gas-free liquid media were studied.

In sections 3.6.3 to 3.6.5, the analyses for each scenario were repeated but involved a more permeable (2000 mD) modelled reservoir.

3.6.3 Studies of 10 – 200 μm fines flow in Multiphase and liquid in 2000 mD rock

3.6.4 Effect of 10 microns Fines Migration in Liquid Flow in a 2000 mD model

CFD simulations were carried out starting with a 10 μm fines particles flowing along with liquid crude (oil and water) in the absence of gas. The results obtained are given in figures 3.25 to 3.27. Figure 3.25 shows the impact of 10 μm particles on liquid (gas free) velocities through a more permeable (2000 mD) porous medium. It is evident from figure 3.25 that in a

2000 mD permeability drainage, the very fine grain size (10 μm) effects on crude velocity range (shown with colour coded scale) are higher compared to the corresponding fines (sand) velocity range shown in Figure 3.26. This difference is greater compared to similar cases in a 1000 mD rock (Figures 3.8 and 3.9). The main difference is in the crude liquid velocity range and not in fines velocity range for reasons given above in sections 3.5 and 3.5.5.

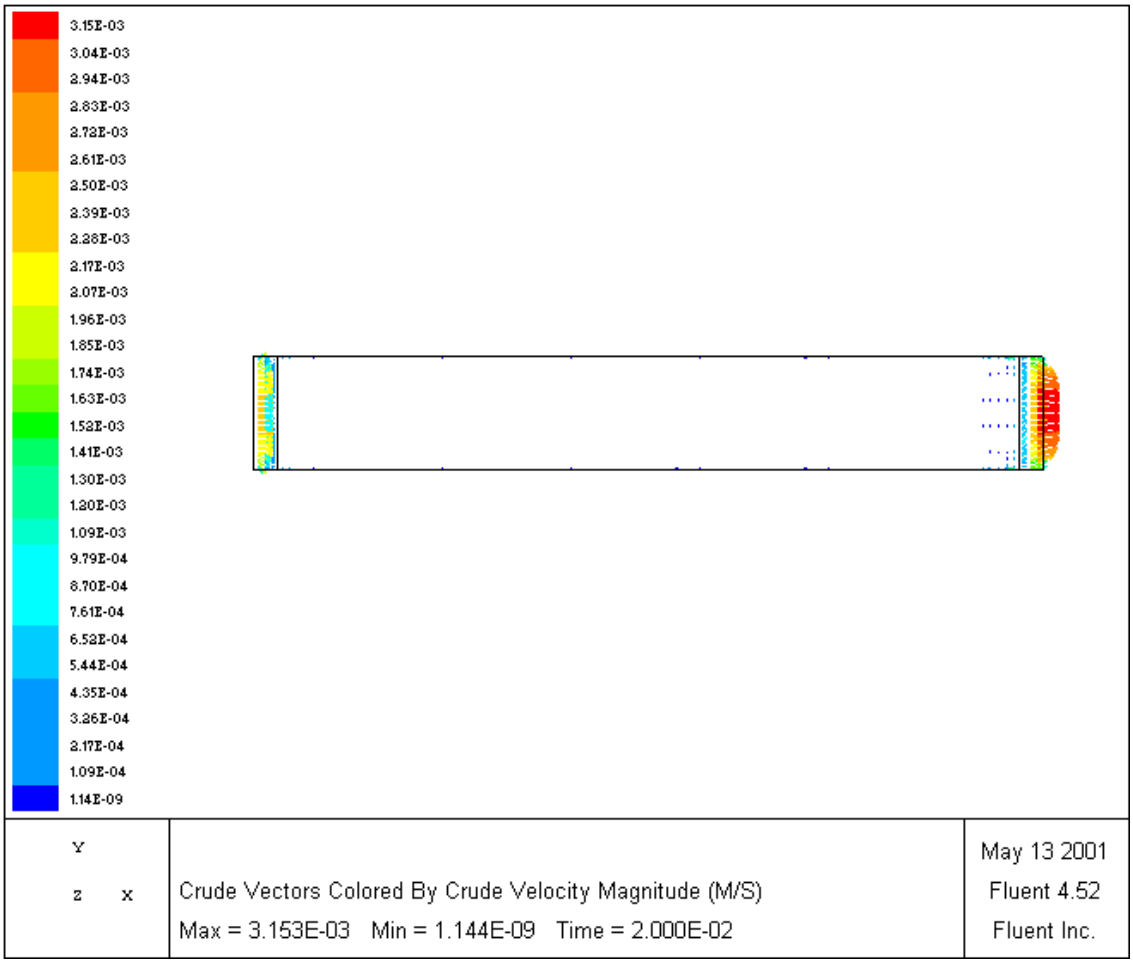

Figure 3.25: Liquid velocities during 10 μm particles flow simulation through 2000 mD rock

When the very fine particles were subjected into a comparatively much more permeable (2000 mD) flow path, the effects were less compared to the same conditions in a 1000 mD drainage.

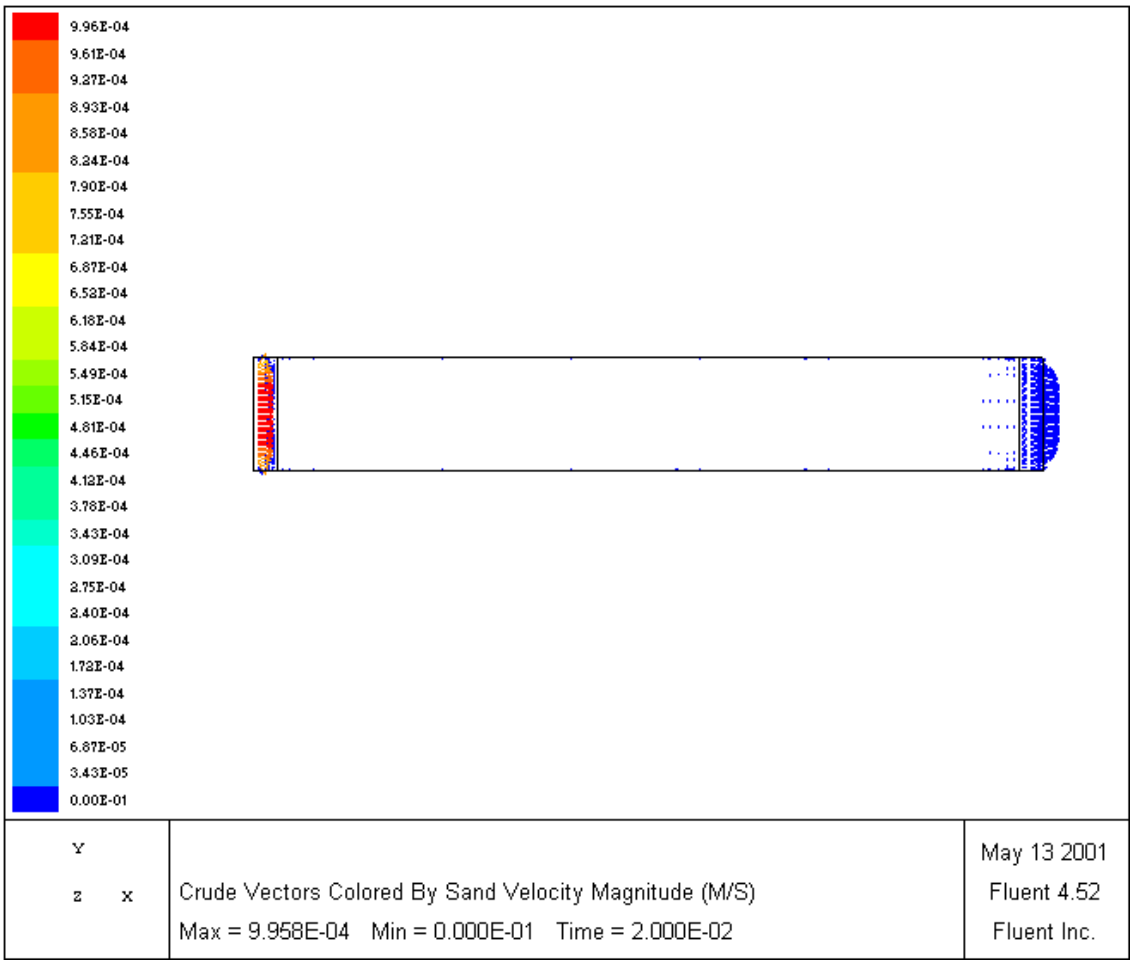

Figure 3.26: Velocities when 10 μm fines (sand) was simulated in liquid through 2000 mD rock

Figure 3.26 portrays lower fines particles velocity compared to figure 3.24 which depicts higher liquid crude velocity change, from entrance to exit,. This observation is similar but differs in magnitude to that observed in the 1000 mD scenario whose details are given above in sections 3.5 to 3.5.4.

As far as pressure analysis is concerned, figure 3.27 displays qualitative as well as quantitative pressure variation of fines particles in liquid hydrocarbon as they all flow through modelled 2000 mD sandstone reservoir. At each modelled reservoir interval, the resultant pressures in Pascal units were thereafter converted into psi. The length of the reservoir was also converted from meters to feet.

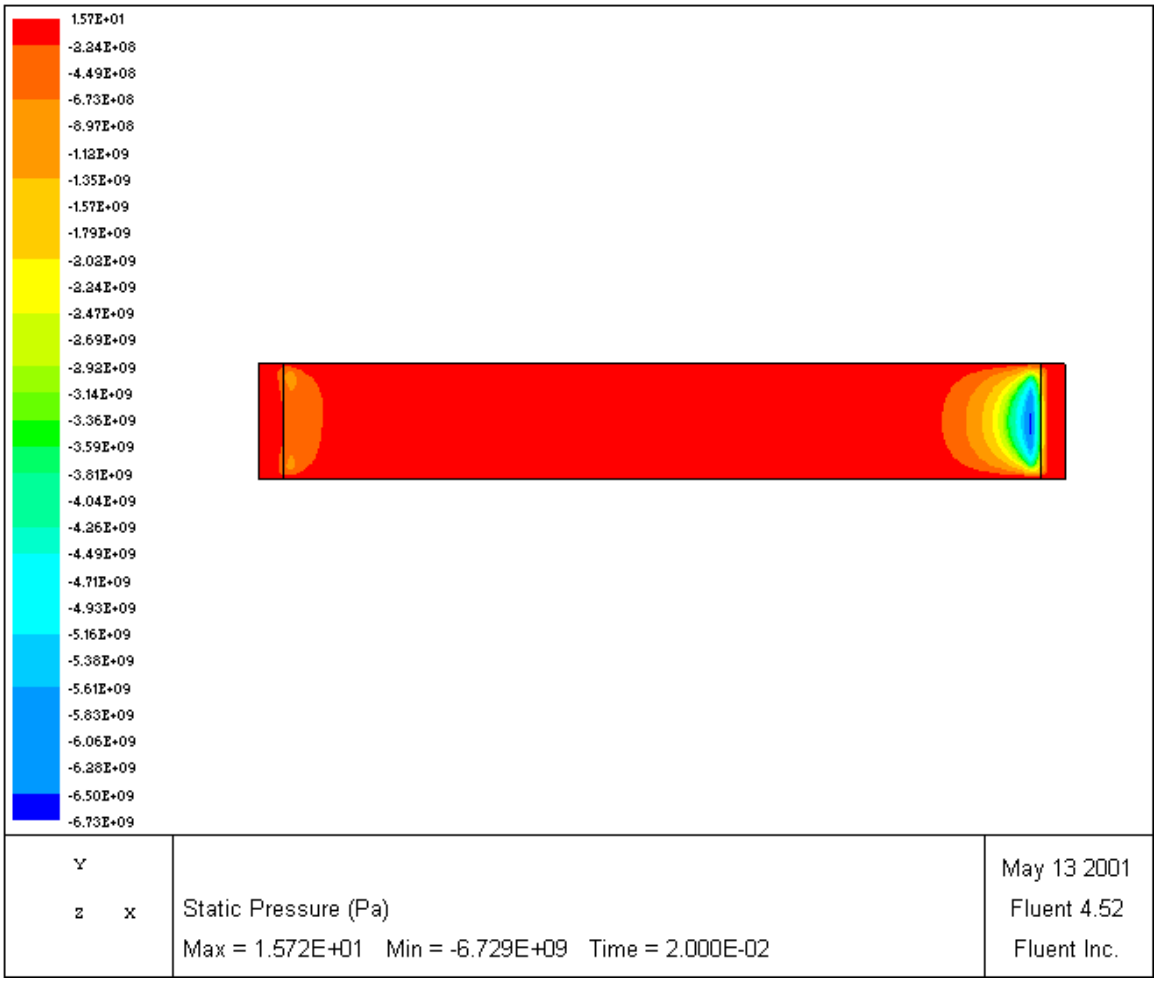

Figure 3.27: Pressure profiles results of 10 μm fines in liquid flow through 2000 mD drainage

To summarise the above results, when 10 microns fines in liquid hydrocarbon was simulated, corresponding pressure drop change observed across the drainage model was higher than the result observed in the less permeable model (1000 mD) for the same particle size. The difference observed between them was 1773 psi.

3.6.5 Multiphase analysis of 10 microns Fines Migration in a 2000mD rock

This section explains CFD multiphase simulations where gas played a tangible role in fines migrations mechanisms in terms of pressure reductions as compared to liquid (no gas) flow. The study started with a 10 μm fines particle grain analysis flowing along a multiphase (oil,

water and gas) medium in a 2000 mD computational grid having 35% porosity. CFD simulation results are shown in figures 3.28 to 3.30.

Figure 3.28 shows that the impacts of very fine grain size (10 μm) on crude multiphase velocities (shown with colour coded scale) are higher compared to the corresponding velocities of fines (sand) shown in figure 3.29. This is despite the fact that they all began with the same velocity. Difference between minimum multiphase flow velocity and minimum liquid flow velocity can be seen in figures 3.28 and 3.25 respectively. This indicates that gas presence influences liquid mobility and should be accounted for in order to minimize uncertainties carried out by laboratory analysis whose results are used in deciding expenditure levels as far as oil and gas field development is concerned.

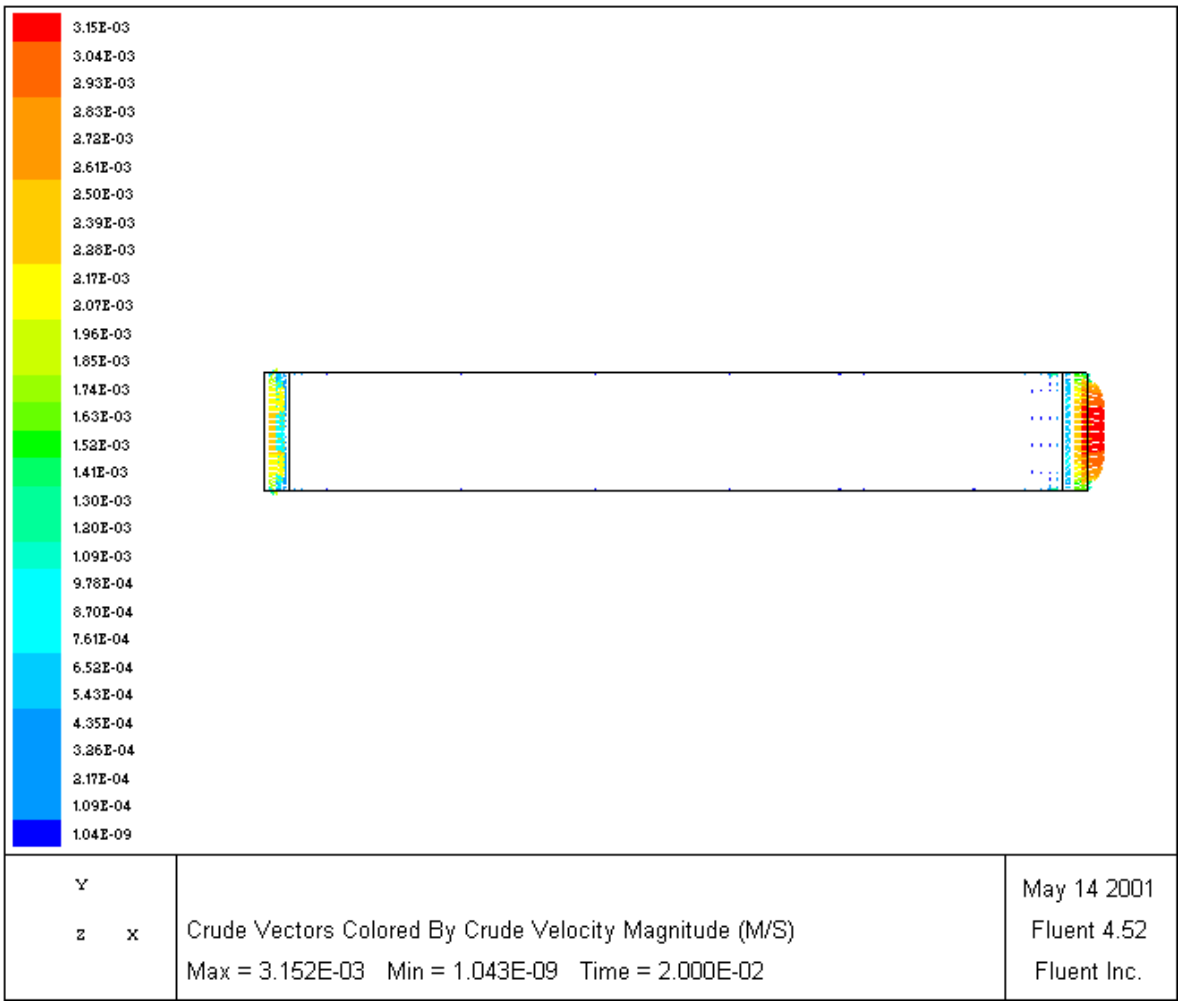

Figure 3.28: Multiphase crude velocities during 10 μm particles flow through 2000 mD rock

Figure 3.29 is a CFD simulation result of 10 microns particles velocity profiles flowing in a multiphase fluid through a 2000 mD rock. Compared to the velocities of multiphase crude, velocity vectors of particles are slower as multiphase fluid can penetrate much more easily through a 2000 mD porous medium compared to the movement of solid particles through the same rock.

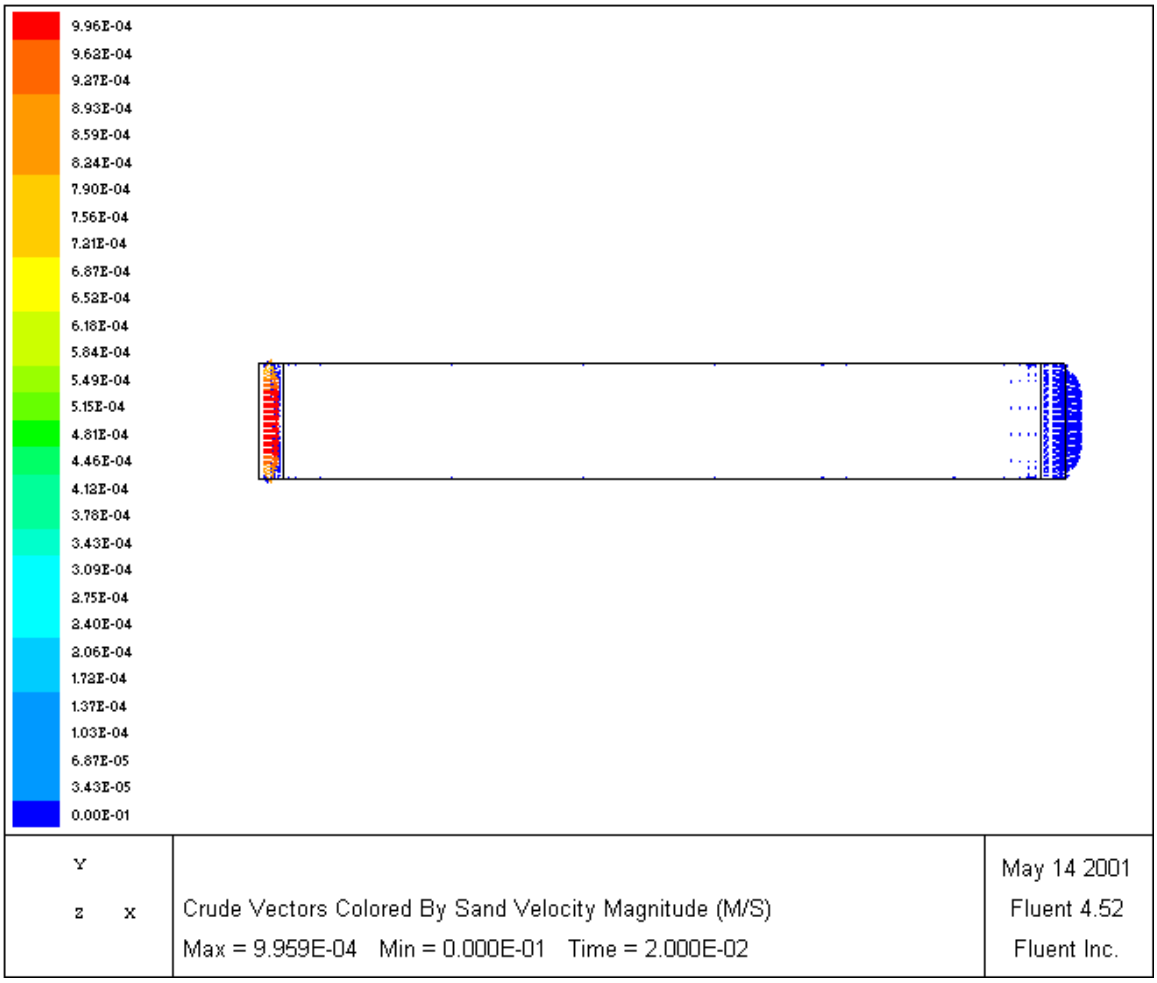

Figure 3.29: 10 μm fines velocities through a 2000 mD drainage in a multiphase medium

Figure 3.30 is a CFD simulation result of pressure profiles revealed in a pressure contour map. It is a result of the mixture of multiphase and 10 μm particles mobilised through the same computational model explained in this section. Pressure analysis is of fundamental importance in the studies of reservoir productivity and injectivity. Pressure data from the CFD, was thereafter converted from Pascal to Psi (field units) in order to carryout reservoir engineering analysis required for fines migration mechanisms studies.

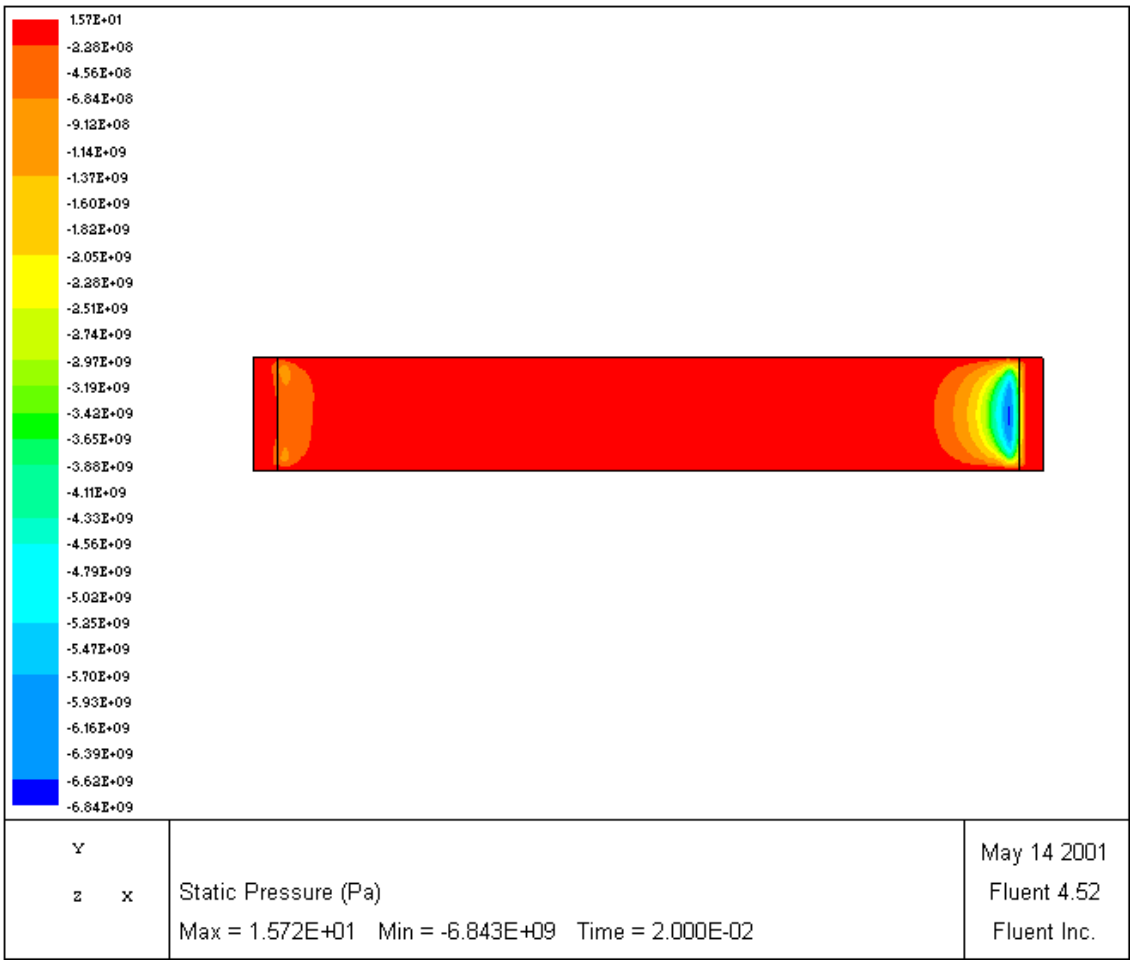

Figure 3.30: Pressure profiles of 10 µm particles in multiphase flow through 2D drainage

3.7 Results Discussions

This section discusses simulation results starting from the first analysis to the last.

Starting from figure 3.8, it is evident that in a 1000 mD permeability sand, the very fine grain size effects on crude liquid velocities, as shown with the colour coded scale, are higher compared to the corresponding velocity of fines (sand) shown in Figure 3.9. This is despite the fact that they all began at the same velocity.

This makes the dynamic flow analysis more comprehensive compared to today's conventional laboratory approaches since in a core laboratory analysis, the best that could be achieved are the fines injection velocities before mixing with liquid. When a fines-liquid

mixture moves, there is no facility to measure separately solid velocity from liquid velocity during the motion whereas in this study that was possible.

Differences observed in pressure drops revealed by the CFD simulation results between multiphase flow and liquid flow scenarios for each fines particle size sensitivity (10 - 200μm) across a 1000 mD block are listed in Appendix A-6. Based on the results in the table, gas presence (in multiphase) in all cases resulted in different pressure drops compared to the result revealed in liquid media. Pressure drops observed when particles flow in liquid and in multiphase mixtures through 2000 mD reservoir model are also listed in Appendix A-6. Comparison between 2000 mD results and 1000 mD (Appendix A-6), revealed that the higher the drainage permeability, the more the pressure drop in both cases (liquid and multiphase); however, multiphase (due to gas presence) always revealed relatively less pressure drops. In other words the difference in pressure drops between liquid and multiphase fluids increases with increase in reservoir permeability however multiphase revealed less pressure drop quantities compared to liquid results. This observation is similar to field observations where a reservoir having high gas-liquid ratio (GLR) tends to maintain the initial reservoir pressure for a longer time than a one having less GLR if both share similar conditions.

It is important to note that the current laboratory analyses which do not involve true multiphase experiments (which do not use hydrocarbon gas), result in pressure drop predictions that are different from the pressure drop results in presence of gas in the liquid. Hence over prediction may result, which means higher production expectations which in turn may end up with unnecessary over investment in field development projects. As a result,

higher than required pumps capacity may be installed which may exceed critical draw down rates and cause excessive influxes of both water and fines particles.

As such errors associated with pressure drop predictions such as those resulted in gas-free analysis directly affect investment and may jeopardize proper reservoir management.

Impacts of grain sizes (10 – 200 μm) on pressure drop in liquid and multiphase flow through 2000 mD drainage are compared in figures 3.31 to 3.40. Out of those figures, figures 3.32, 3.34, 3.36, 3.38 and 3.40 show comparison between particles impacts on pressure drop in 1000 mD drainage and 2000 mD drainage scenarios. The figures show clear differences in pressure drop profiles in multiphase and liquid media, due to various particle sizes flow. This further clarifies that hydrocarbon gas presence causes comparatively less impact on pressure drops in a multiphase flow compared to (gas-free) flow impact.

Details of pressure drops caused by particle sizes 10 μm, 50 μm, 100 μm, 150 μm and 200 μm, flowing in both multiphase and liquid media through both 1000 mD and 2000 mD porous media are shown in Appendix A-6.

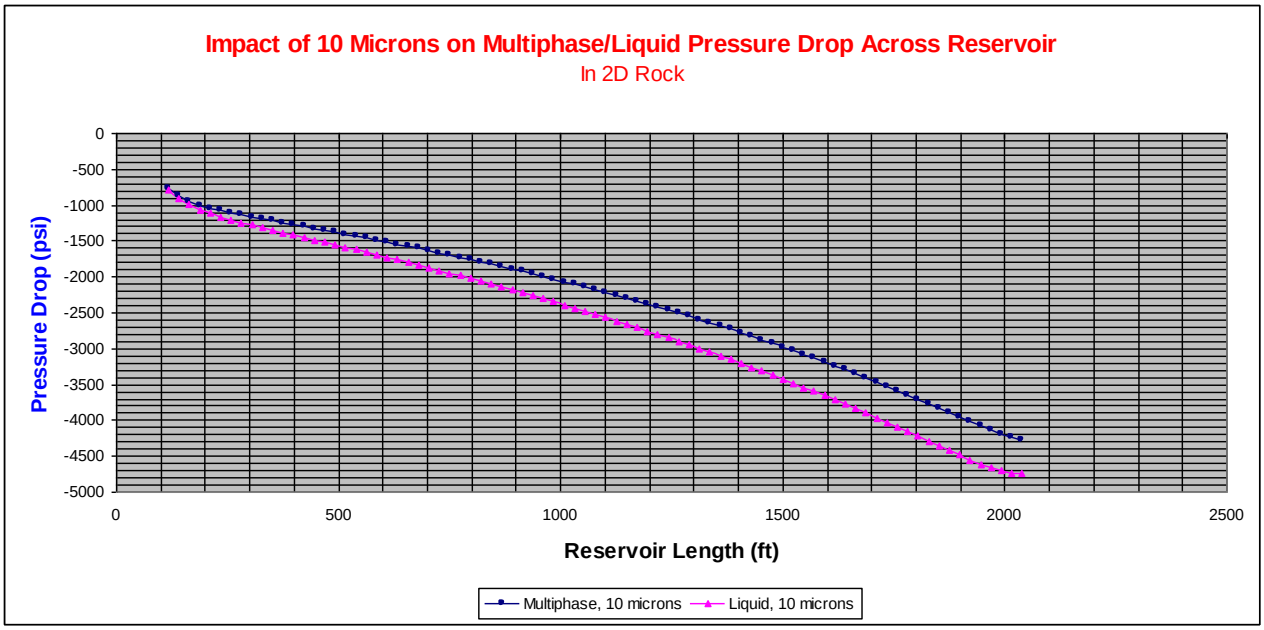

Figure 3.31: Multiphase-liquid pressure drops during 10 µm fines flow in a 2000mD rock.

For example pressure drop profiles pattern in the 2000 mD scenario due to 10 microns (figure 3.31) which differs from the pattern revealed in the 1000 mD scenario (figure 3.17) are all displayed in figure 3.32 to highlight their differences.

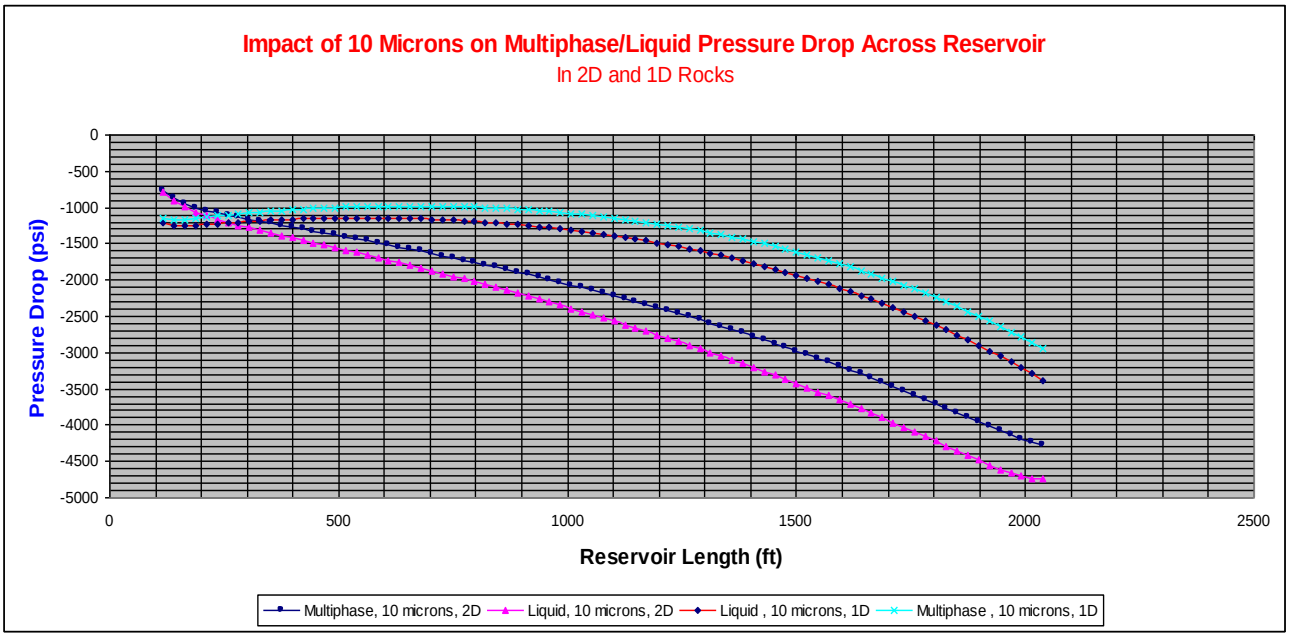

Figure 3.32: Pressure drops comparison in multiphase and liquid flows in 2000 mD and 1000 mD scenarios

Like in the 10 µm cases discussed above, various pressure drop profiles were revealed when 50 µm, 100 µm, 150 µm and 200 µm particle grains were simulated. The pressure drop patterns resulted from simulations of those particles also showed that in the case of less permeable drainage, the pressure drop ends in lower values while in more permeable environment, the draw down ends up with higher magnitudes.

Figures 3.33 to 3.40 show similar trends and profiles to those explained above but of different magnitudes as a result of impacts of particle grain sizes 50 µm, 100 µm, 150 µm and 200 µm on pressure drop.

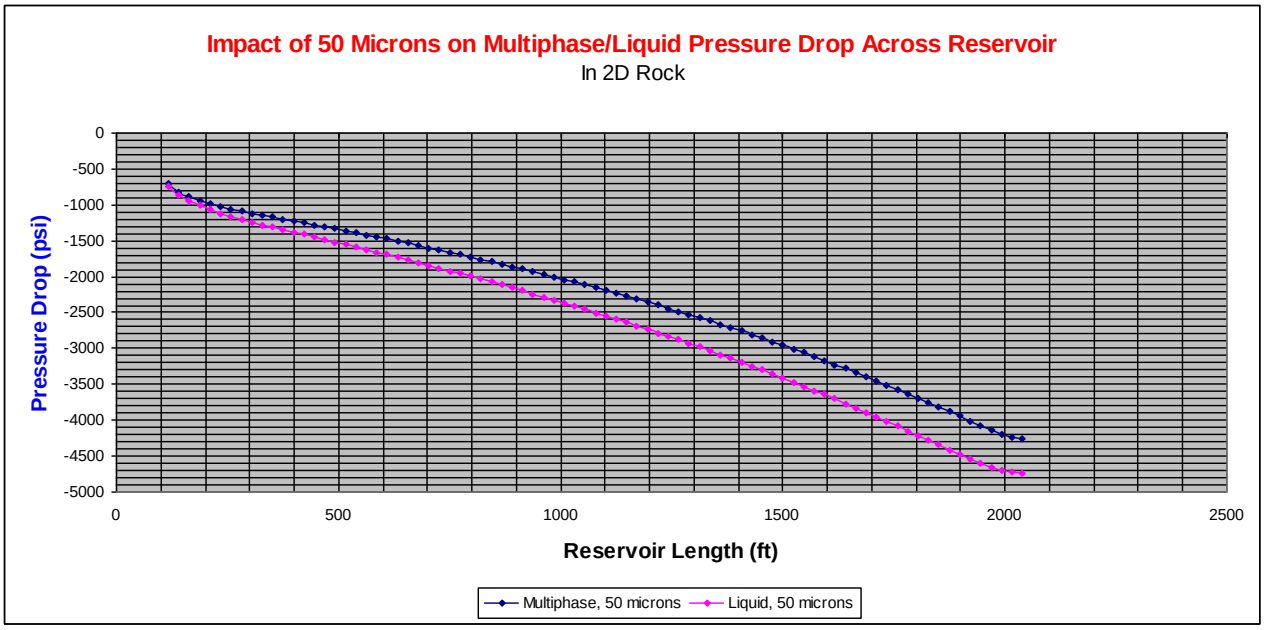

Figure 3. 33: Multiphase and liquid pressure drops when 50 µm fines flow was simulated in 2 D rock

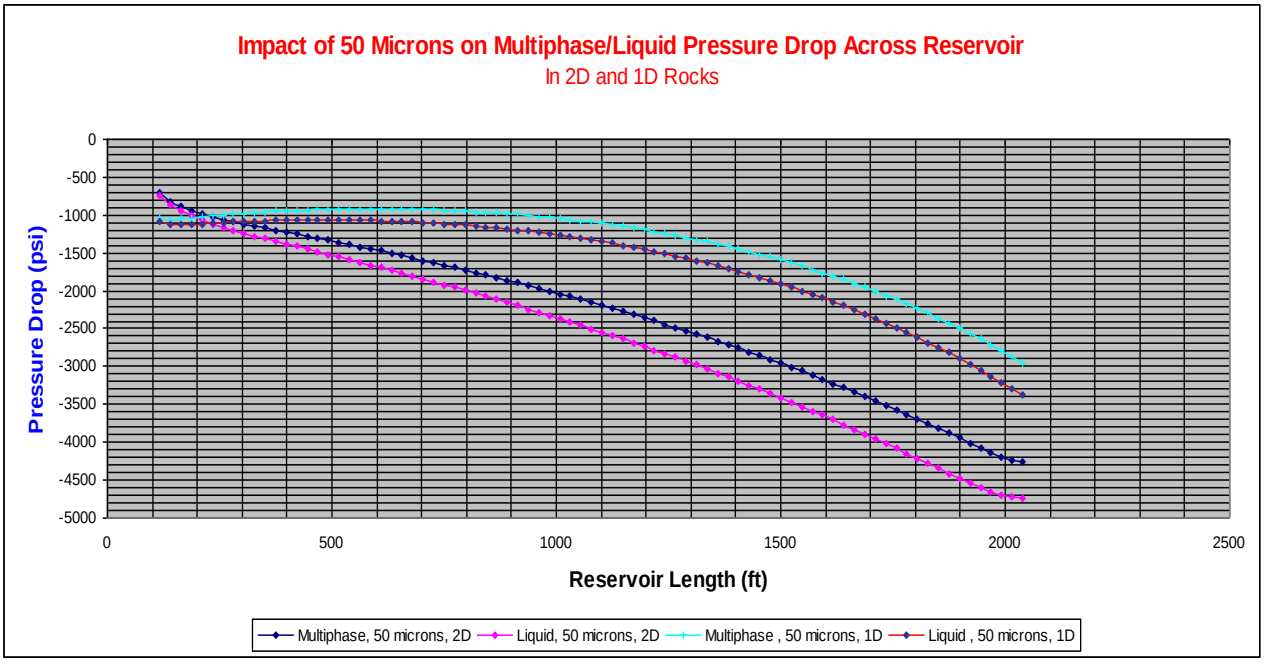

Figure 3. 34: Impacts of 50 µm grain on Δp in multiphase and liquid flow: 2000 mD and 1000 mD scenarios

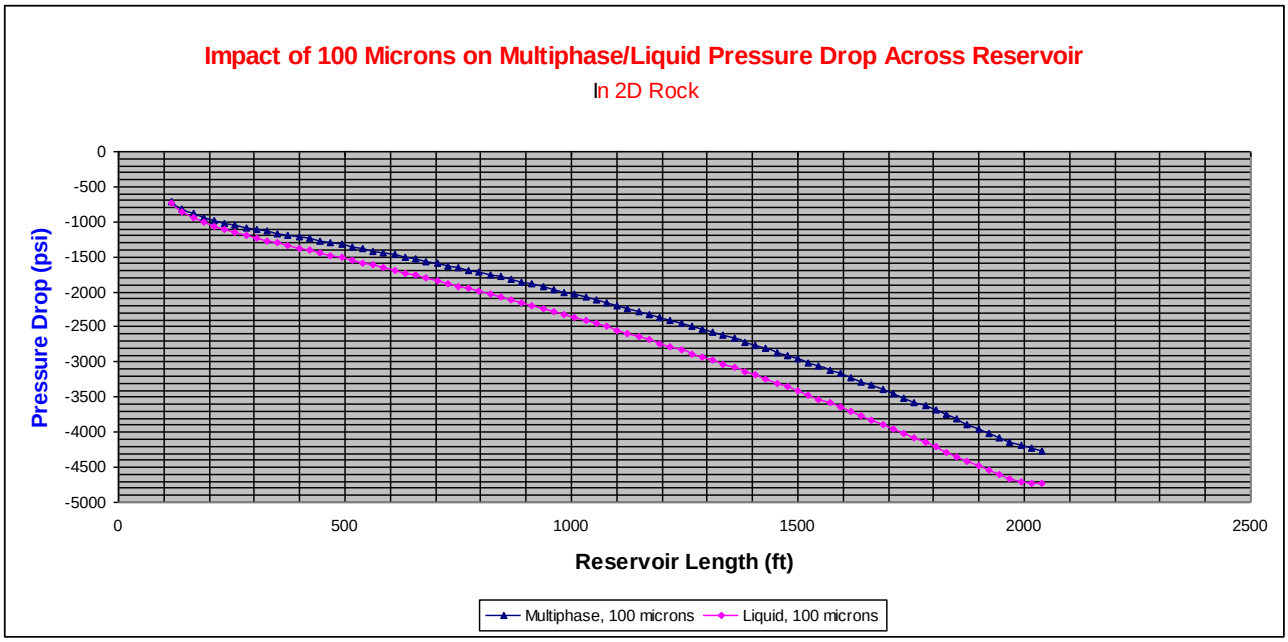

Figure 3. 35: Multiphase and liquid pressure drops due to 100 µm particles flow in 2000mD rock.

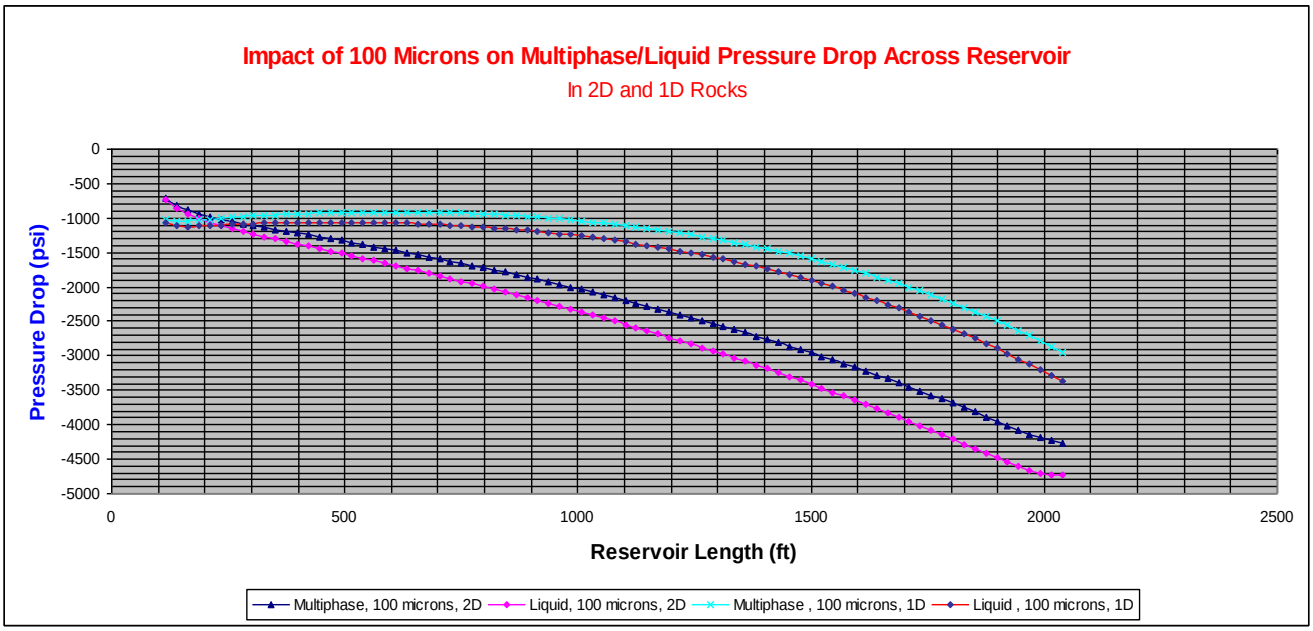

Figure 3.36: Comparison of multiphase and liquid pressure drops due to 100 µm fines flow in 2D and 1D rocks

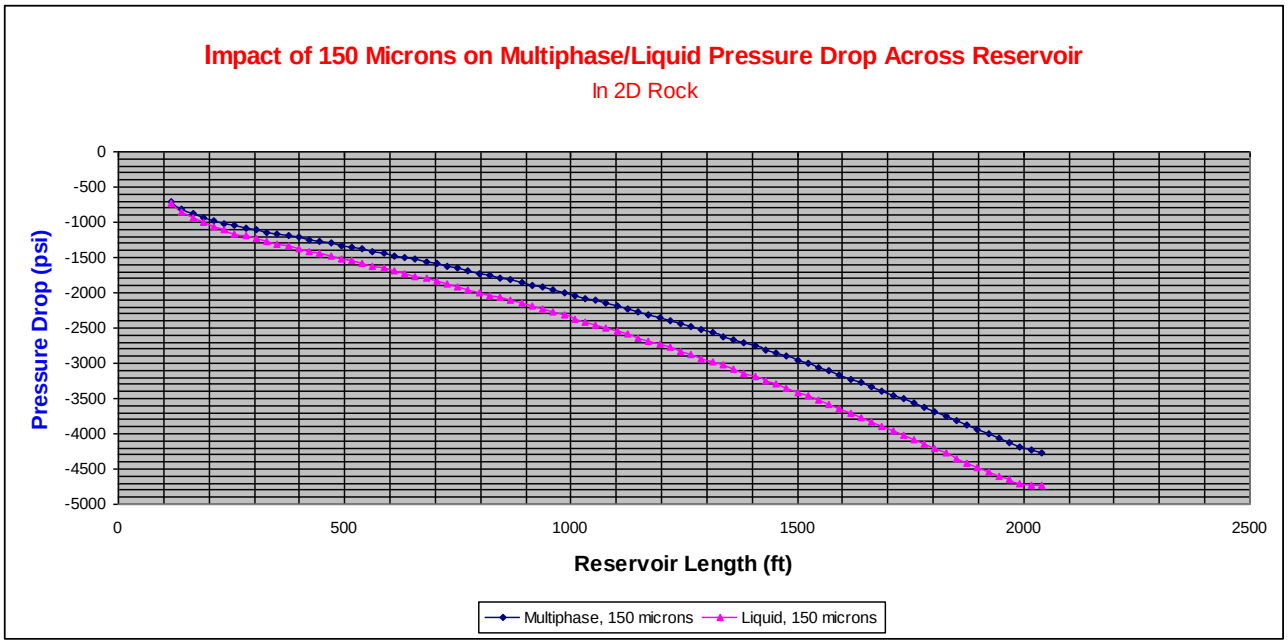

Figure 3. 37: Multiphase and liquid pressure drops during 150 µm fines flow in a 2000 mD drainage.

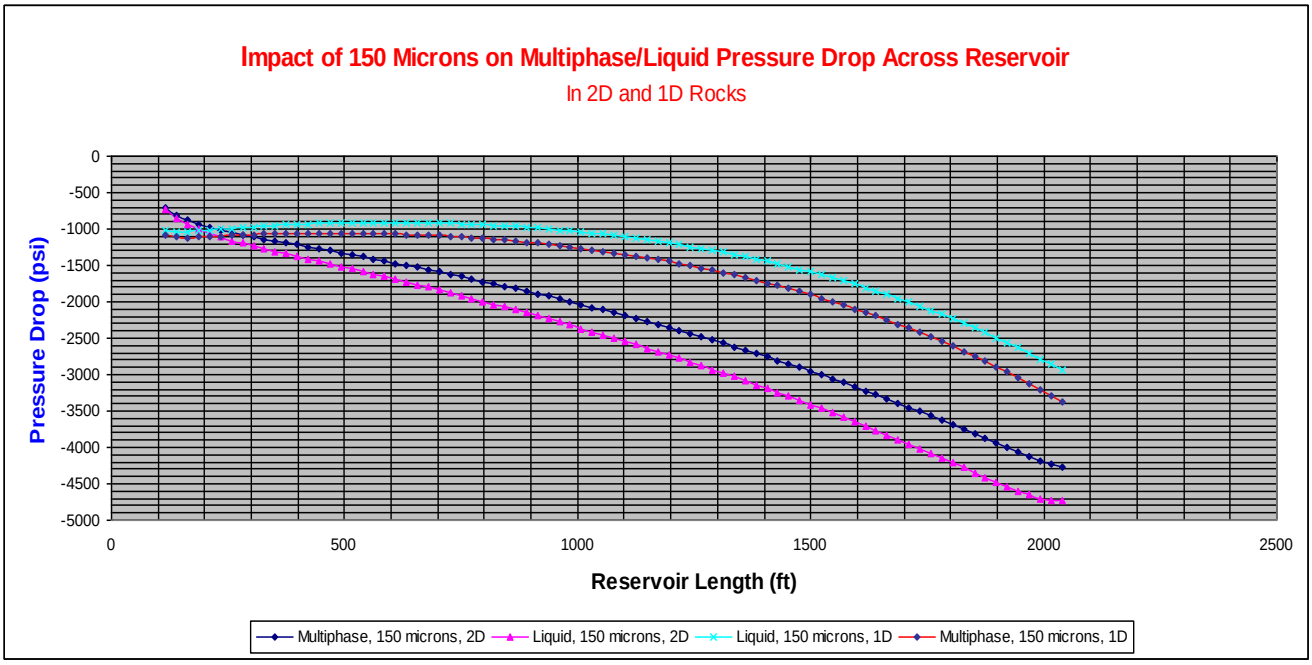

Figure 3.38: Comparison in multiphase and liquid pressure drops when 150 µm fines flow in 2D and 1D rocks

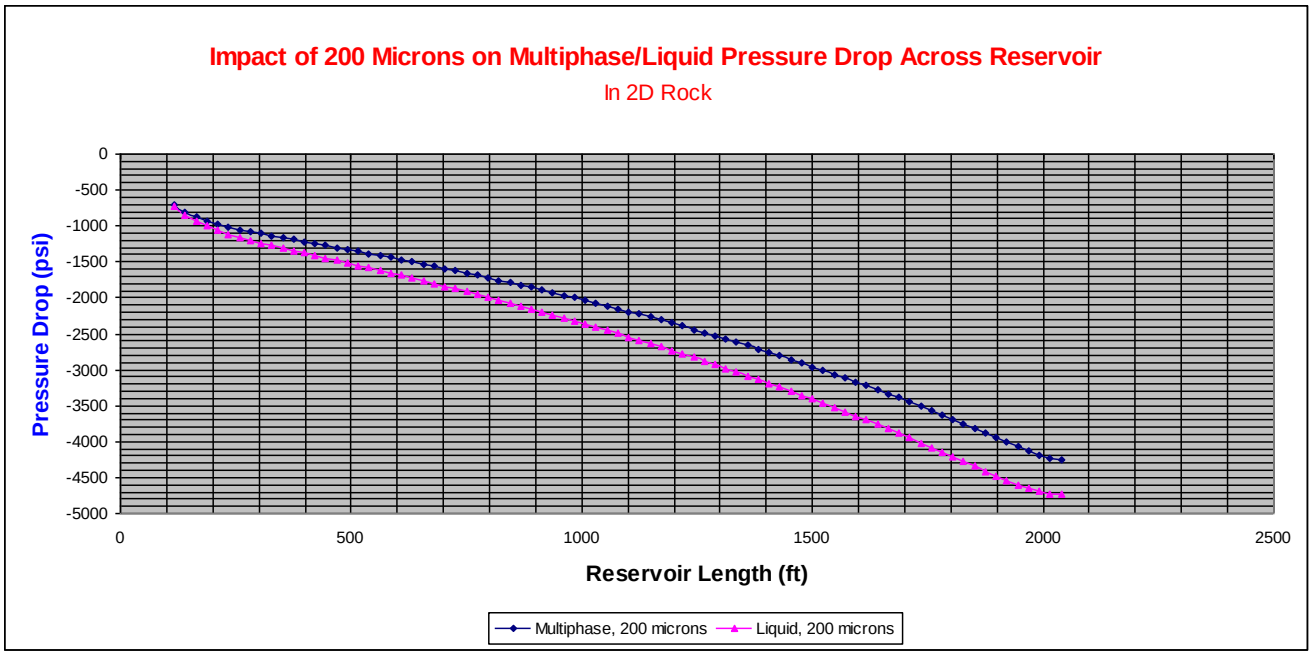

Figure 3. 39: Multiphase and liquid pressure drops due to 200µm fines flow in a 2000mD model.

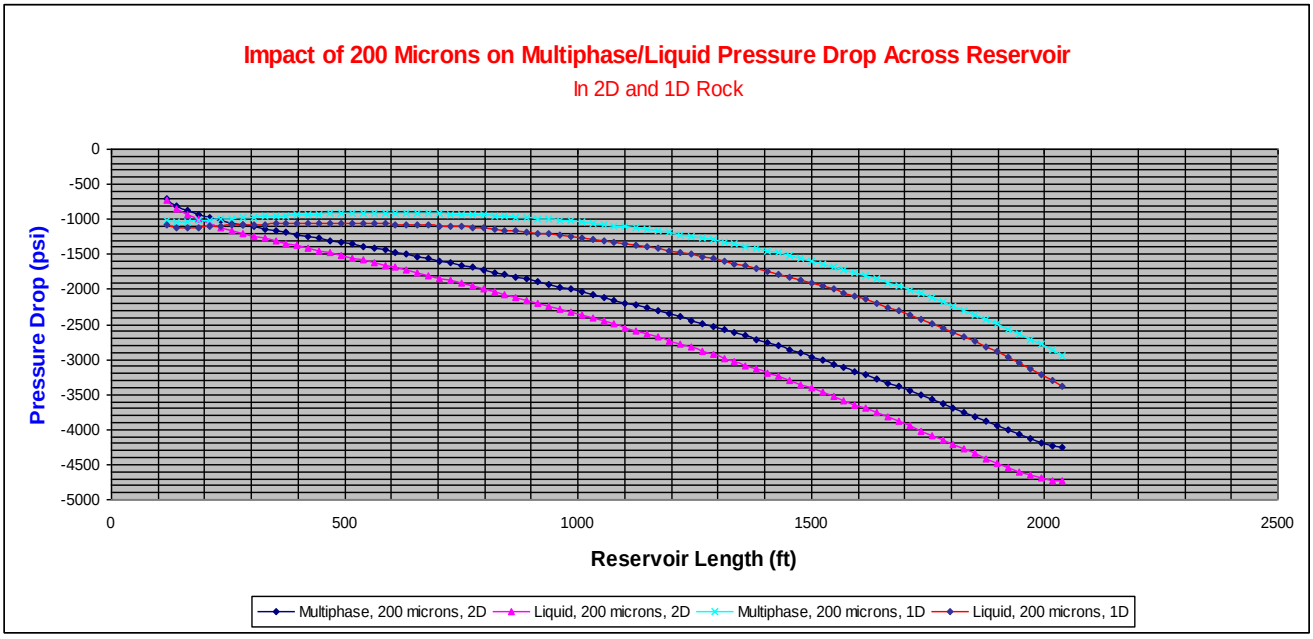

Figure 3. 40: Comparison of multiphase and liquid pressure drops due to 200 µm fines flow in 2D and 1D rocks

The particle size impacts on pressure drop in multiphase and liquid flows through 2000 mD drainage are highlighted in table 3.7 and are discussed below.

As shown in table 3.7, in the case of the 10 μm grain size, the multiphase related pressure drop was comparatively lower across the computational model than the pressure reduction observed in the liquid analysis. While the former dropped by 3496.9 psi, the later dropped by 3944.2psi. In this case the 447.3psi difference was attributed to gas presence in the multiphase fluid. The table also lists the differences observed in the case of other grain sizes.

Table 3.7: Pressure drops in multiphase and liquid at various grain sizes in a 2000mD rock.

Grain Size (μm)	Multiphase ΔP (psi)	Liquid ΔP (psi)	Effect of multiphase ΔP (psi) gained
10	3496.9	3944.2	447.3
50	3553.9	3995.8	441.9
100	3560.2	4002.0	441.8
150	3560.9	4003.2	442.3
200	3561.4	4003.3	441.9

Overall CFD results related to 2000 mD scenario can be seen in Appendix A-6 which summarises all pressure drop data at each reservoir length obtained in 10 sets of simulations of fines particles flowing with multiphase and liquid through 2000 mD drainage.

Finally, among the major outcomes of this research work is the ability to analyse solid fines velocities separately from liquid velocities while both flow simultaneously.

Based on the above analysis, fines migration has detrimental effects to the pore size resulting in pore plug damage. Pressure drop data from the CFD was further analysed in order to

carryout reservoir engineering analysis including pore plugging and related permeability decline analysis, which are presented in chapter 4.

There are several pore plug damage mechanisms which are subject to reservoir conditions which need careful analysis to effectively minimise the impact on productivity or injectivity. Chapter 4 covers all important issues related to pore plugging damage mechanisms which are essential in optimising hydrocarbon production.

Chapter 4

PORE BLOCKING MECHANISMS FROM FINES MIGRATIONS AND SOLID INTRUSIONS

4.1 Introduction

In chapter 3, several fines and solid particle CFD simulation analyses and their impacts on multiphase and liquid pressure drops and velocities were presented. Also presented were impacts of particle sizes ranging from 10 μm to 200 μm on pressure drops in multiphase and liquid media through 2000 mD and 1000 mD reservoir conditions. Chapter 4 explains how the pressure profiles of all scenarios explained in chapter 3 were used to determine corresponding damaged permeabilities and hence formation pore blocking mechanisms using published correlations. As pore plugging studies involve fines diameter, pore diameter, porosity and permeability, CFD simulation results of all sensitivities carried out were used in the pore plugging analyses.

4.2 Pore Plugging Analysis in Multiphase and Liquid Flows.

Pressure drop results of the five fines grain particle sizes (10μm, 50μm, 100μm, 150μm and 200μm) each mobilised by hydrocarbon multiphase and then by liquid flow through modelled porous media having absolute permeabilities of 1000 mD to 2000 mD at various properties (explained below) were analysed for pore plugging studies. The particle size range is based on several statistical analyses on fines particle size distributions (109) which showed that the majority of sandstone fields are covered with mainly medium to fine grain particles

ranging between 50 μm and 200μm mean diameter. Shell's grain size distribution statistical analyses in Europe, Africa, the Middle East and Asia revealed that in areas where Shell operates, the majority of load bearing sand particles (with high cumulative weight percentage >50%), have grain sizes ranging between 10 and 200 μm while the <50% particle grain sizes are coarser according to Amory (109, 110) and Mason et al report (74) in which the cut-off was 150 μm based on Laser Particle Size Analyser (LPSA) and sieve grain size analysis. Hence most of the sand control screen meshes used are 200 μm to filter the majority of grain sizes and based on observations, after installation, with time, finer particles tend to accumulate and thus reduce the mesh flow area. Hence, the partially plugged 200 μm mesh sizes happen to screen even 150 μm and smaller grain particles. Based on that information, this study was limited to particle sizes between 10 and 200 μm.

In each scenario simulated, sensitivity of porosity whose range is given in table 4.1 was carried out. From table 4.1, the higher the porosity %, the higher the pressure drop revealed for each particle size (10 – 200 microns). Such sensitivity results were used to determine pore diameters based on several published correlations (whose details are given in chapter 2 section 2.5) and others discussed below.

Hence for each CFD simulated particle size range (10 – 200μm) and each corresponding porosity and permeability, the pore diameter values were calculated.

Table 4.1: CFD simulated Pressure Drops from which Average Permeabilities were Calculated

Avg K (Darcy)	Porosity	D_F (μm)	Pdrop (Psi)
3.7	0.25	10	1225.5
3.3	0.3	10	1333.3
2.9	0.4	10	1531.9
2.7	0.45	10	1623.7
3.6	0.25	50	1247.1
3.3	0.3	50	1355.1
2.9	0.4	50	1553.8
2.7	0.45	50	1645.7
3.6	0.25	100	1249.2
3.3	0.3	100	1357.0
2.9	0.4	100	1555.7
2.7	0.45	100	1647.4
3.6	0.25	150	1249.4
3.3	0.3	150	1357.6
2.9	0.4	150	1556.4
2.7	0.45	150	1648.3
3.6	0.25	200	1249.6
3.3	0.3	200	1357.4
2.9	0.4	200	1556.5
2.7	0.45	200	1648.1
2.2	0.25	10	1975.0
2.0	0.3	10	2098.1
1.8	0.4	10	2293.2
1.7	0.45	10	2371.2
2.1	0.25	50	1985.1
2.0	0.3	50	2108.0
1.8	0.4	50	2302.6
1.7	0.45	50	2380.7
2.1	0.25	100	1986.3
2.0	0.3	100	2109.2
1.8	0.4	100	2303.6
1.7	0.45	100	2381.9
2.1	0.25	150	1986.3
2.0	0.3	150	2109.5
1.8	0.4	150	2303.9
1.7	0.45	150	2382.1
2.1	0.25	200	1986.4
2.0	0.3	200	2109.4
1.8	0.4	200	2304.1
1.7	0.45	200	2382.2

Table 4.1 is an example of hundreds of simulations and results involving sensitivities which were repeated for each particle grain size (10 μm – 200 μm) and each porosity fraction (0.25 – 0.45). While porosity range of 0.25 – 0.45 is a typical range in high permeability sandstone reservoirs as explained in section 2.9, the permeability range was back calculated from the CFD pressure drop results using the Darcy equation 2.29.

Each sensitivity analysis revealed unique pressure drop (psi) as can be seen in the table.

Table 4.2 lists corresponding pore blocking mechanisms calculated using the correlations elaborated in chapter 2 section 2.5 with input from table 4.1.

Table 4.2: Pore Plugging Mechanisms based on CFD simulated pressure drops

Blake-Kozeny	Coberly	Dullien	Pore blocking mechanism	Pore blocking mechanism
D_F/λ_p	D_F/λ_p	D_F/λ_p	Blake-Kozeny	Dullien
9.0	6.5	0.5	Int.bridging/single pore blocking	External cake/ no invasion
7.0	6.5	0.5	Int.bridging/single pore blocking	External cake/ no invasion
4.5	6.5	0.7	External cake/ no invasion	External cake/ no invasion
3.7	6.5	0.7	External cake/ no invasion	External cake/ no invasion
9.0	6.5	2.3	Int.bridging/single pore blocking	External cake/ no invasion
7.0	6.5	2.7	Int.bridging/single pore blocking	External cake/ no invasion
4.5	6.5	3.3	External cake/ no invasion	External cake/ no invasion
3.7	6.5	3.6	External cake/ no invasion	External cake/ no invasion
9.0	6.5	4.6	Int.bridging/single pore blocking	External cake/ no invasion
7.0	6.5	5.3	Int.bridging/single pore blocking	Shallow interna bridging
4.5	6.5	6.6	External cake/ no invasion	Int.bridging/single pore blocking
3.7	6.5	7.2	External cake/ no invasion	Int.bridging/single pore blocking
9.0	6.5	7.0	Int.bridging/single pore blocking	Int.bridging/single pore blocking
7.0	6.5	8.0	Int.bridging/single pore blocking	Int.bridging/single pore blocking
4.5	6.5	9.9	External cake/ no invasion	Int.bridging/single pore blocking
3.7	6.5	10.9	External cake/ no invasion	Pore filling
9.0	6.5	9.3	Int.bridging/single pore blocking	Int.bridging/single pore blocking
7.0	6.5	10.7	Int.bridging/single pore blocking	Pore filling
4.5	6.5	13.2	External cake/ no invasion	Pore filling
3.7	6.5	14.5	External cake/ no invasion	Pore filling
9.0	6.5	0.6	Int.bridging/single pore blocking	External cake/ no invasion
3.7	6.5	4.6	External cake/ no invasion	External cake/ no invasion
:	:	:	:	:
9.0	6.5	6.1	Int.bridging/single pore blocking	Shallow internal bridging
7.0	6.5	6.9	Int.bridging/single pore blocking	Int.bridging/single pore blocking
4.5	6.5	8.4	External cake/ no invasion	Int.bridging/single pore blocking
3.7	6.5	9.1	External cake/ no invasion	Int.bridging/single pore blocking
9.0	6.5	9.1	Int.bridging/single pore blocking	Int.bridging/single pore blocking
7.0	6.5	10.3	Int.bridging/single pore blocking	Pore filling
4.5	6.5	12.6	External cake/ no invasion	Pore filling
3.7	6.5	13.7	External cake/ no invasion	Pore filling
9.0	6.5	12.1	Int.bridging/single pore blocking	Pore filling
7.0	6.5	13.8	Int.bridging/single pore blocking	Pore filling
4.5	6.5	16.8	External cake/ no invasion	No interaction
3.7	6.5	18.3	External cake/ no invasion	No interaction
9.0	6.5	0.6	Int.bridging/single pore blocking	External cake/ no invasion
:	:	:	:	:
9.0	6.5	6.5	Int.bridging/single pore blocking	Int.bridging/single pore blocking
7.0	6.5	7.1	Int.bridging/single pore blocking	Int.bridging/single pore blocking
4.5	6.5	8.2	External cake/ no invasion	Int.bridging/single pore blocking
3.7	6.5	8.7	External cake/ no invasion	Int.bridging/single pore blocking
9.0	6.5	9.8	Int.bridging/single pore blocking	Int.bridging/single pore blocking
7.0	6.5	10.7	Int.bridging/single pore blocking	Pore filling
4.5	6.5	12.3	External cake/ no invasion	Pore filling
3.7	6.5	13.1	External cake/ no invasion	Pore filling
9.0	6.5	13.1	Int.bridging/single pore blocking	Pore filling
7.0	6.5	14.2	Int.bridging/single pore blocking	Pore filling

Pore plugging damage mechanism results based on Coberly and Carman-Kozeny correlations can be summarised as follows:

i) Whenever the Coberly's correlation (equation 2.7) was used in determining a damage mechanism, a unique pore plugging damage mechanism "instant bridging/external filter cake" was always revealed. ii) Each time Carman-Kozeny's equation was used, only one type of pore plugging damage mechanism namely "invasion and deposition" resulted. As stated in chapter 2 section 2.5 the equation was considered obsolete and hence was ignored.

4.3 Use of CFD Pressure Drops to Calculate Corresponding Permeabilities

From the CFD simulations explained in chapter 3, for each sensitivity, the resultant pressure drop value ($\bar{p} - p_{wf}$) was used to determine corresponding permeability using the Darcy equation 2.29. Volumetric flow rate ($q = A * v$), where v is fluid velocity, was calculated from the CFD simulations results of average velocities explained in chapter 3 and wellbore area A = πr^2_w was used in which typical wellbore radii r_w were used.

As an example, if a well has a 7" diameter liner, whose inner radius (r_w) is about 0.3 ft, the inner wellbore surface area can be calculated. Using the same reservoir and fluid properties (h, μ, r_e, v, $\bar{p} - p_{wf}$ and r_w) used in the CFD simulations, applying the Darcy equation, permeability can be determined for each sensitivity simulated by the CFD package. Figure 4.1 is an example of a CFD generated pressure drop curve from which the above method and equation 2.29 were used to determine the corresponding permeability at each depth to get a permeability profile as shown in figure 4.2. Figure 4.1 shows pressure drop profiles which resulted from flow mixtures of multiphase and liquid media carrying 10 μm particles through a 1000 mD porous medium.

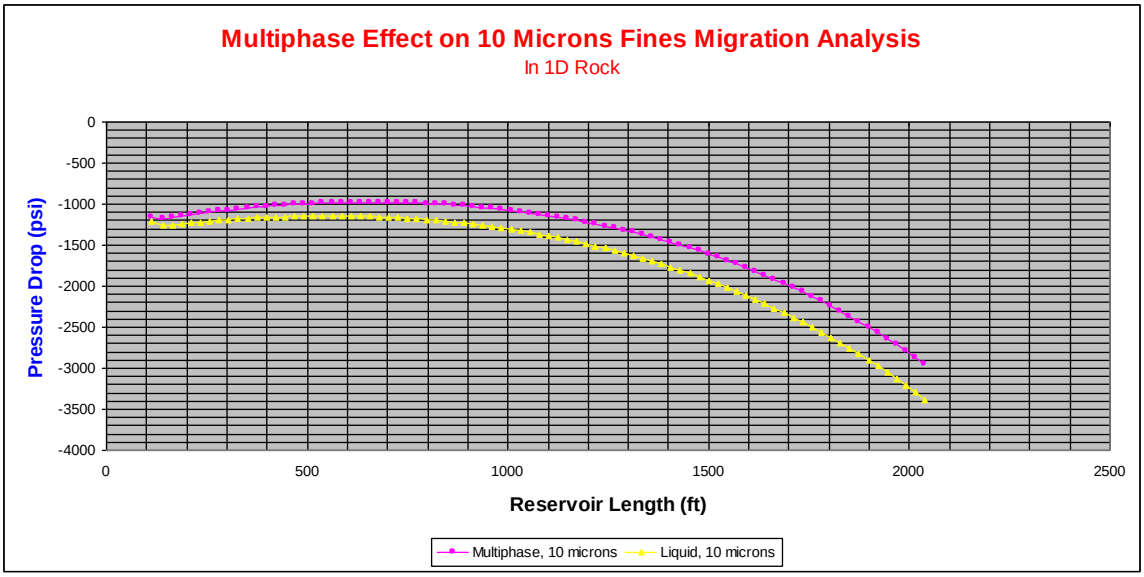

Figure 4.1: CFD generated pressure declines in multiphase and liquid flowing 10µm fines

Figure 4.2 displays corresponding permeability profiles which resulted from flow mixtures of multiphase and liquid media carrying 10 µm through 1000 mD porous medium.

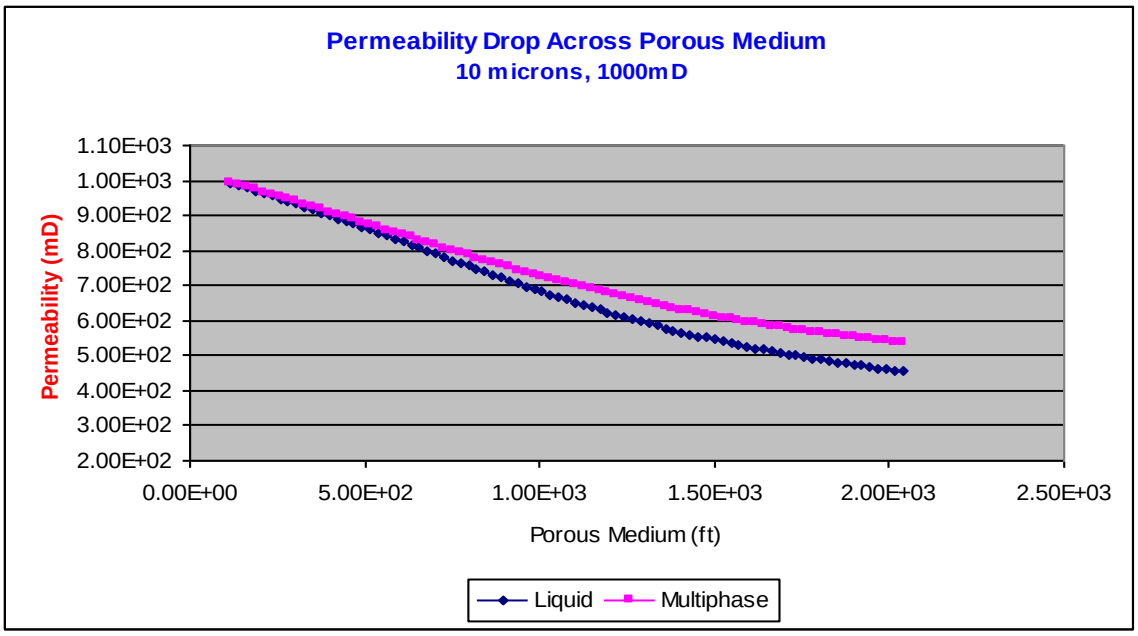

Figure 4.2: Permeability profiles in multiphase and liquid flowing 10µm fines

From pressure drop profiles of various grain size sensitivities, (10µm, 50µm, 100µm, 150µm and 200µm), the corresponding permeability declines were calculated. Table 4.3 shows

corresponding permeability for each pressure drop covering all sensitivities of grain sizes in a liquid medium flowing through a 1000 mD drainage. Since the presence of fines solid particles (10 - 200μm) affected the pressure drawdown as explained in chapter 3, the resultant permeabilities are referred to as fines-damaged permeabilities.

Table 4.3: Pressure drops and corresponding fines-damaged permeabilities in 1000 mD liquid drainage

Reservoir	10 µm		50 µm		100 µm		150 µm		200 µm	
Length	ΔP	k_d	ΔP	k_d	ΔP	k_d	ΔP	k_d	ΔP	k_d
(ft)	(psi)	(mD)	(psi)	(mD)	(psi)	(mD)	(psi)	(mD)	(psi)	(mD)
117	-343	706	-428	565	-548	441	-571	424	-733	330
141	-408	602	-511	482	-667	369	-681	362	-854	288
164	-461	541	-577	433	-765	327	-769	325	-943	265
187	-507	499	-633	399	-848	298	-844	299	-1013	250
211	-548	467	-684	374	-923	277	-912	280	-1071	239
234	-585	441	-731	353	-991	261	-975	265	-1120	230
258	-620	420	-775	336	-1053	247	-1033	252	-1164	224
281	-654	401	-817	321	-1112	236	-1089	241	-1204	218
305	-686	385	-857	308	-1168	226	-1142	231	-1241	213
328	-717	371	-896	297	-1221	218	-1194	223	-1277	208
352	-747	358	-933	287	-1272	210	-1244	215	-1312	204
375	-776	347	-970	278	-1323	204	-1293	208	-1346	200
398	-805	336	-1006	269	-1371	197	-1342	202	-1380	196
422	-834	326	-1042	261	-1419	192	-1389	196	-1414	192
445	-862	317	-1077	254	-1467	186	-1436	190	-1448	189
469	-890	308	-1112	247	-1514	181	-1483	185	-1482	185
492	-918	300	-1147	240	-1560	177	-1529	180	-1517	182
516	-946	293	-1182	234	-1606	172	-1575	176	-1552	178
539	-973	285	-1216	228	-1652	168	-1621	171	-1587	175
562	-1001	279	-1251	223	-1697	164	-1667	167	-1622	172
586	-1028	272	-1285	218	-1742	161	-1712	163	-1658	169
609	-1055	266	-1319	213	-1788	157	-1758	160	-1694	166
633	-1083	260	-1353	208	-1833	154	-1803	156	-1730	163
656	-1110	254	-1387	204	-1878	150	-1849	153	-1767	160
680	-1137	249	-1421	199	-1923	147	-1894	150	-1804	157
703	-1165	244	-1455	195	-1968	144	-1939	146	-1842	154
726	-1192	239	-1489	191	-2012	142	-1985	144	-1879	152
750	-1219	234	-1523	188	-2057	139	-2030	141	-1918	149
773	-1246	230	-1557	184	-2102	136	-2075	138	-1956	146
797	-1273	225	-1591	180	-2147	134	-2121	135	-1996	144
820	-1301	221	-1625	177	-2192	131	-2166	133	-2035	141
844	-1328	217	-1659	174	-2237	129	-2211	130	-2075	139
867	-1355	213	-1693	171	-2282	127	-2257	128	-2116	137
891	-1382	210	-1727	168	-2327	125	-2302	126	-2156	134
914	-1409	206	-1761	165	-2371	122	-2347	124	-2198	132
937	-1437	202	-1795	162	-2416	120	-2393	122	-2240	130

Pressure drops or drawdown pressures and corresponding permeabilities for several multiphase flow scenarios are shown in table 4.4.

Table 4.4: Pressure drops and corresponding damaged permeabilities in 1000 mD multiphase drainage

Reservoir	10 µm		50 µm		100 µm		150 µm		200 µm	
Length	ΔP	k_d	ΔP	k_d	ΔP	k_d	ΔP	k_d	ΔP	k_d
(ft)	(psi)	(mD)	(psi)	(mD)	(psi)	(mD)	(psi)	(mD)	(psi)	(mD)
117	-274	882	-329	735	-411	588	-548	441	-727	333
141	-334	737	-401	614	-501	492	-667	369	-848	290
164	-383	653	-459	544	-574	435	-765	327	-938	266
187	-424	596	-509	497	-636	397	-848	298	-1008	251
211	-462	554	-554	462	-692	369	-923	277	-1065	240
234	-496	521	-595	434	-743	347	-991	261	-1115	232
258	-527	494	-632	412	-790	330	-1053	247	-1159	225
281	-556	472	-667	393	-834	315	-1112	236	-1199	219
305	-584	453	-701	377	-876	302	-1168	226	-1236	214
328	-611	436	-733	363	-916	291	-1221	218	-1272	209
352	-637	421	-764	351	-955	280	-1272	210	-1307	205
375	-662	407	-794	339	-992	271	-1323	204	-1342	201
398	-686	394	-823	329	-1029	263	-1371	197	-1376	197
422	-710	383	-852	319	-1065	255	-1419	192	-1410	193
445	-734	372	-880	310	-1100	248	-1467	186	-1444	189
469	-757	362	-909	302	-1135	242	-1514	181	-1478	186
492	-781	353	-936	294	-1170	236	-1560	177	-1513	182
516	-804	344	-964	287	-1205	230	-1606	172	-1548	179
539	-826	336	-991	280	-1239	224	-1652	168	-1583	176
562	-849	328	-1019	274	-1273	219	-1697	164	-1618	172
586	-872	321	-1046	267	-1307	214	-1742	161	-1654	169
609	-895	314	-1073	262	-1341	209	-1788	157	-1690	166
633	-917	307	-1100	256	-1375	205	-1833	154	-1726	163
656	-940	301	-1127	251	-1409	201	-1878	150	-1763	160
680	-962	294	-1154	245	-1442	196	-1923	147	-1801	157
703	-985	288	-1181	241	-1476	192	-1968	144	-1838	155
726	-1007	283	-1208	236	-1510	189	-2012	142	-1876	152
750	-1030	277	-1235	231	-1543	185	-2057	139	-1914	149
773	-1052	272	-1262	227	-1577	182	-2102	136	-1953	147
797	-1075	267	-1289	223	-1611	178	-2147	134	-1992	144
820	-1097	262	-1316	219	-1644	175	-2192	131	-2032	142
844	-1120	258	-1343	215	-1678	172	-2237	129	-2072	139
867	-1142	253	-1370	211	-1712	169	-2282	127	-2113	137
891	-1165	249	-1397	207	-1745	166	-2327	125	-2154	135
914	-1187	245	-1424	204	-1779	163	-2371	122	-2195	132
937	-1209	240	-1451	201	-1813	160	-2416	120	-2237	130

Pressure profile differences between liquid and multiphase flows in a 1000mD computational grid scenario as shown in tables 4.3 and 4.4 confirm that gas presence in multiphase flow contribute to more productivity compared to liquid flow.

The same comparisons were repeated for more permeable (2000 mD) computational grids which are elaborated in chapter 5. Indeed the more permeable the model was, the wider the difference between multiphase and liquid flow characteristics as far as permeability decline profiles are concerned. Clear trends were manifest when the impact of fines grain size alone was analysed. The coarser the grain size the more the pressure reduction. This trend was expected in pore blocking correlations where the ratio of pore to particle grain size determines flow passage or blockage. The finer the grain size, the more easily it can pass through a certain pore diameter size as long as the pore size is much greater than the grain diameter as discussed in chapter 2.

Extensive sensitivities were carried out of which only some are reported since it requires voluminous space to cover them all. Table 4.5 combines several permeabilities with porosities, pore sizes, fines particle sizes along with several published correlations to determine corresponding formation damage mechanisms. Hence the pore blocking (damage) mechanism can be determined using this integrated procedure.

Table 4.5: Damage Mechanisms from CFD Determined Pressures

Avg K (D)	Particle (μm)	Porosity (Fraction)	Pdrop (Psi)	Pore blocking mechanism Blake-Kozeny	Pore blocking mechanism Dullien
3.7	10	0.25	1225.5	Int.bridging/single pore blocking	External cake/ no invasion
3.3	10	0.3	1333.3	Int.bridging/single pore blocking	External cake/ no invasion
2.9	10	0.4	1531.9	External cake/ no invasion	External cake/ no invasion
2.7	10	0.45	1623.7	External cake/ no invasion	External cake/ no invasion
3.6	50	0.25	1247.1	Int.bridging/single pore blocking	External cake/ no invasion
3.3	50	0.3	1355.1	Int.bridging/single pore blocking	External cake/ no invasion
2.9	50	0.4	1553.8	External cake/ no invasion	External cake/ no invasion
2.7	50	0.45	1645.7	External cake/ no invasion	External cake/ no invasion
3.6	100	0.25	1249.2	Int.bridging/single pore blocking	External cake/ no invasion
3.3	100	0.3	1357.0	Int.bridging/single pore blocking	Shallow interna bridging
2.9	100	0.4	1555.7	External cake/ no invasion	Int.bridging/single pore blocking
2.7	100	0.45	1647.4	External cake/ no invasion	Int.bridging/single pore blocking
3.6	150	0.25	1249.4	Int.bridging/single pore blocking	Int.bridging/single pore blocking
3.3	150	0.3	1357.6	Int.bridging/single pore blocking	Int.bridging/single pore blocking
2.9	150	0.4	1556.4	External cake/ no invasion	Int.bridging/single pore blocking
2.7	150	0.45	1648.3	External cake/ no invasion	Pore filling
3.6	200	0.25	1249.6	Int.bridging/single pore blocking	Int.bridging/single pore blocking
3.3	200	0.3	1357.4	Int.bridging/single pore blocking	Pore filling
2.9	200	0.4	1556.5	External cake/ no invasion	Pore filling
2.7	200	0.45	1648.1	External cake/ no invasion	Pore filling
2.2	10	0.25	1975.0	Int.bridging/single pore blocking	External cake/ no invasion
2.1	50	0.25	1985.1	Int.bridging/single pore blocking	External cake/ no invasion
2.1	100	0.25	1986.3	Int.bridging/single pore blocking	Shallow interna bridging
2.1	150	0.25	1986.3	Int.bridging/single pore blocking	Int.bridging/single pore blocking
2.1	200	0.25	1986.4	Int.bridging/single pore blocking	Pore filling

As a result of all the foregoing analyses, CFD simulations revealed continuous fines impact in both liquid and multiphase flows which were clearly indicated by pressure drop profiles which varied according to fines grain size, porosity, porous medium permeability and other properties mentioned above. In general, the permeabilities determined across the modelled computational grid in the liquid (gas-free) medium were lower than the permeabilities determined in a multiphase medium. Hence particle-damaged permeability differences between multiphase and liquid media analysis are clear.

The permeability profiles determined from the CFD results were further analysed to develop particle-damaged permeability models for both multiphase and liquid scenarios as described

in Chapter 5. Integration of the developed damaged-permeability models into a comprehensive, field-proven 3-dimensional reservoir modular simulator also forms part of chapter 5.

Chapter 5

PARTICLE-DAMAGED PERMEABILITY MODELS DEVELOPMENT

5.1 Introduction

In chapter 4, results of the Computational Fluid Dynamics (CFD) simulations in terms of pore plugging damage mechanisms as well as damaged absolute permeability profiles were presented. Factors which caused pore damage, hence permeability damage such as fines grain sizes, pore size, drawdown pressure, water cut and porosity as well as other reservoir rock and fluid properties, were also discussed in the chapter. In order to determine corresponding reservoir production performance predictions, particle-damaged permeability models were developed as explained in this chapter. The particle-damaged permeabilities were back-calculated from the CFD-generated drawdown pressure profiles. The developed models can be assigned into a 3D reservoir simulator such as MoReS, Eclipse, Stars, CMG, etc. to quantify reservoir performance in which fines grains impact on production will be carried out. As such, a more realistic approach was taken which resulted in a new contribution to reservoir analysis knowledge since the approach is unique and does not exist in today‘s established 3-D reservoir simulation methodologies in which particles analysis is missing. All high permeability sandstone reservoirs suffer from fines migration‘s production reduction impact, hence the importance of particle analysis.

The approach takes into consideration the effects of fines particles of various sizes (10-200 μm) across the entire reservoir at numerous variable sensitivities of multiphase, liquid, rock and fluid conditions. Gas was analysed as part of the multiphase fluid mixture comprised of oil, water and gas. When dealing with more than one fluid phase, concepts of relative

permeability (k_r) and effective permeability (k_e) for example effective oil permeability (k_o) and /or effective water permeability (k_w) were utilised and are explained in section 5.3.1.

This chapter explains a very important contribution to reservoir knowledge. The contribution is a development of particle damaged permeability models which can be incorporated into reservoir simulators. The study focused on damage caused by fines particles inside the reservoir and by fine solid particles injected at the wellbore. The reservoir damage study ended up with several developed computational correlations which incorporate particle impact on rock permeability across the drainage area. The models developments are explained from section 5.3.1 to 5.4, whereas section 5.5 covers steps to be taken to incorporate them into a numerical reservoir simulator such as the Shell's 3-D Modular Reservoir Simulator (MoReS) explained in the same section 5.5 with additional features given in Appendix A-2. As it is, like any other commercial reservoir simulator, currently MoReS does not have particle analysis facility. The steps taken in the damaged permeability model determination and development, are summarised as follows:

CFD simulation results, particularly particle-affected drawdown pressures discussed in chapters 3 and 4, were further analysed and were used to back-calculate corresponding permeability declines across the entire drainage area. The process involved permeability equation 2.29 for every particle-affected pressure drawdown per particle size as simulated by the CFD. The CFD‘s drawdown pressures were transferred into the equation replacing the pressure drop term $\left(\overline{p} - p_{wf}\right)$ from which permeability was calculated.

In the CFD simulations, for every solid particle size (10-200 μm) and for each rock absolute permeability range (1000 – 2000mD) in each fluid medium (liquid and / or multiphase), drawdown pressure $\left(\overline{p} - p_{wf}\right)$ values were quantified. Hence the pressure drop function was

directly related to fines diameter, permeability and flowing phase (liquid and multiphase). Thus:

$$\frac{\Delta p}{\Delta \delta}(L_P) = f(D_F, k, L_P) \text{----------(5.1)}$$

$$\frac{\Delta p}{\Delta \delta}(M_P) = f(D_F, k, M_P) \text{----------(5.2)}$$

Where:

$\frac{\Delta p}{\Delta \delta}$ = Change in pressure with drainage distance (psi/ft)

D_F = Fines or solid particle diameter (μm)

k = permeability (mD)

L_P = liquid phase

M_P = multiphase.

5.1.1 The Need for Damaged Permeability Models in the Reservoir Studies

Traditionally, simulation engineers tend to assign constant values of permeabilities during the initialisation stage of simulation studies when dealing with reservoirs. It is assumed that the same values will prevail over the production life cycle and across the entire drainage area. These assumptions tend to result in erroneous reservoir performance predictions, upon which major investments are nevertheless committed. In addition, ongoing laboratory core sample analyses lack in-depth simultaneous particle and hydrocarbon gas analyses due to safety limitations as discussed in chapters 1, 2 and 3. In addition the core lab methodology also does not incorporate continuous multiple sensitivity analysis of fines grain size and various fines

concentrations in oil, gas, water and particle flow mixtures. Furthermore, the results obtained from core plug analysis may not be representative of the entire reservoir drainage area despite the fact that the data is scaled-up to reservoir size and used in field development activities. Incorporation of the developed models is intended to narrow down uncertainties related to those effects on reservoir production performance and prediction.

5.2 Particle-Damaged Permeability Model Development Strategy

Developments steps of the particle-damaged permeability models from CFD determined pressure drop profiles in scenarios involving 10-200 μm particles, flowing through 1000 mD and 2000 mD modeled sandstone rock permeability in both liquid and multiphase sensitivities, are given in sections 5.2.1, 5.3 and 5.4. The methods used in the particle-damaged permeability model development involved 4 rock and fluid scenarios which were published previously in (111, 112). The scenarios are summarized in section 5.2.1.

5.2.1 Summary of the 4 permeability model development scenarios

The first scenario involved a drainage area having absolute permeability of 1000 mD through which a flow mixture of liquid (oil and water) and fines particles having grain sizes range of 10 – 200 microns were simulated using the CFD.

The second scenario involved a drainage area having absolute permeability of 1000 mD through which a flow mixture of multiphase (oil, water and gas) and fines particles having grain sizes range of 10 – 200 microns were simulated using the CFD.

The third and fourth scenarios were same as the first and the second except that a higher absolute permeability of 2000 mD was used instead of 1000 mD drainage.

For all scenarios, resultant particle affected drawdown pressures from which damaged permeabilities were calculated as explained in chapter 4, were put together and can be seen in appendix A-7 which shows tables of particle damaged permeabilities. As such appendix A-7 summarizes CFD particle-affected permeabilities caused by particle injections of various grain sizes (10 µm, 50 µm, 100 µm, 150 µm, 200 µm) as far as the four scenarios are concerned. Example input well data are summarised in table 5.1.

Table 5.1: Input well data

h	35	ft
q	3000	stb/d
μ	1.5	cp
r_e *	937	ft
r_w	0.29	ft
S	5	
B_O	1.3	rb/stb

* r_e = reservoir radius and can be of any length

The reservoir radius as explained in chapter 4, is the reservoir extent or lateral length from the wellbore.

Figure 5.1 displays CFD simulated drawdown pressures for each particle size mobilised in the liquid fluid medium.

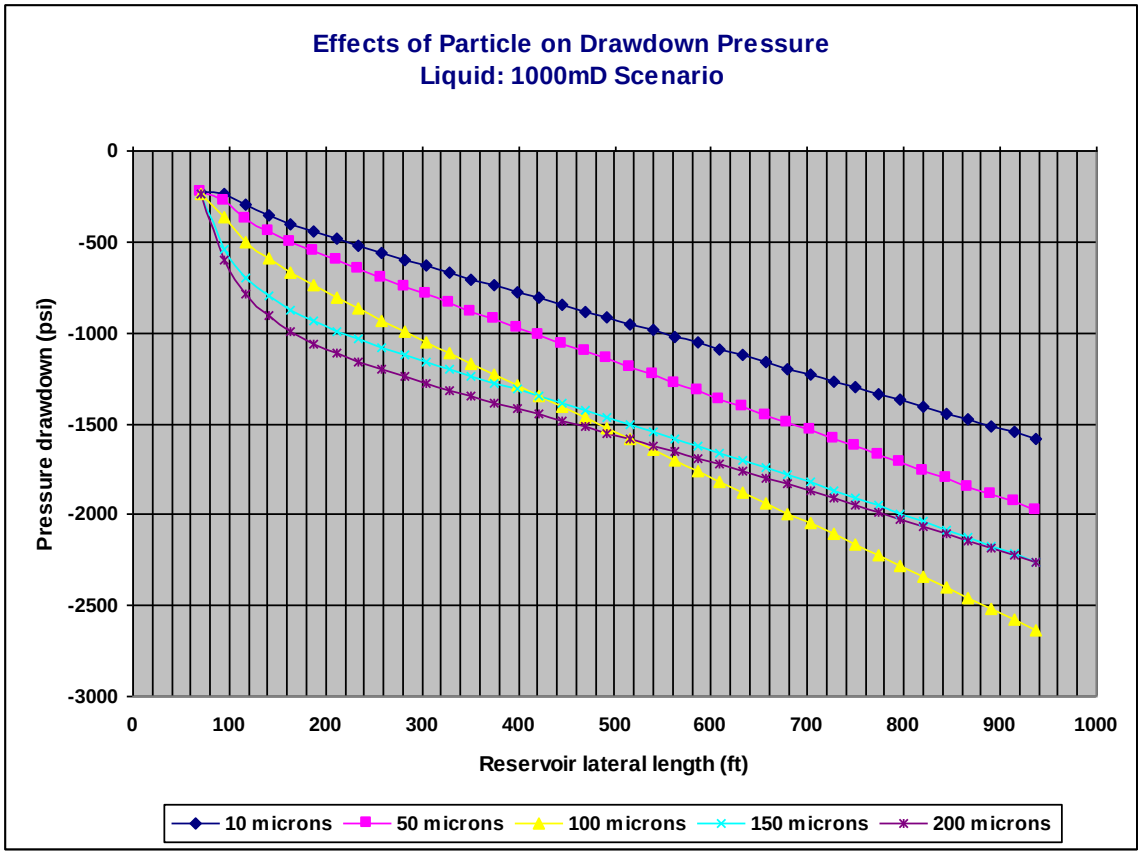

Figure 5.1: Particle size impacts on drawdown pressure in a 1000 mD drainage

It is evident that as the particles carried by fluid enter the porous medium, the absolute permeability starts to reduce from its initial value (1000 mD) and permeability damage continues to occur until drawdown pressure stops.

From the figure, it is evident that the finer the grain size the less the impact on the drawdown pressure, and that drawdown pressure profiles related to coarser grained particles (>100µm) are different from the profiles related to finer particles 10, 50 and 100 µm.

Corresponding absolute damaged permeability profiles are given in figure 5.2.

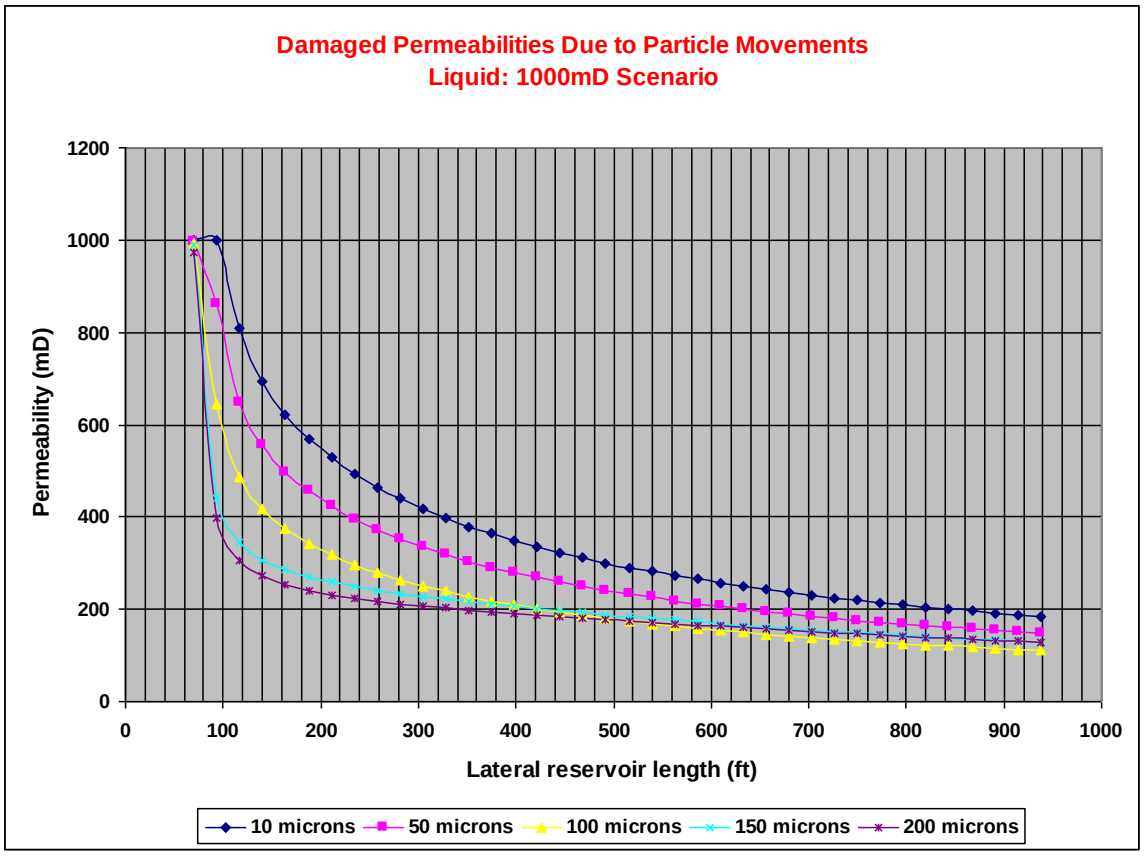

Figure 5.2: Particle size impact on permeability in a liquid scenario

Figure 5.2 shows corresponding damaged permeabilities caused by particle-affected drawdown pressure profiles for each particle size mobilised in the liquid flow.

A log-log scale of Figure 5.2 was plotted to obtain more clarity of the particles impacts on permeability as shown in figure 5.3.

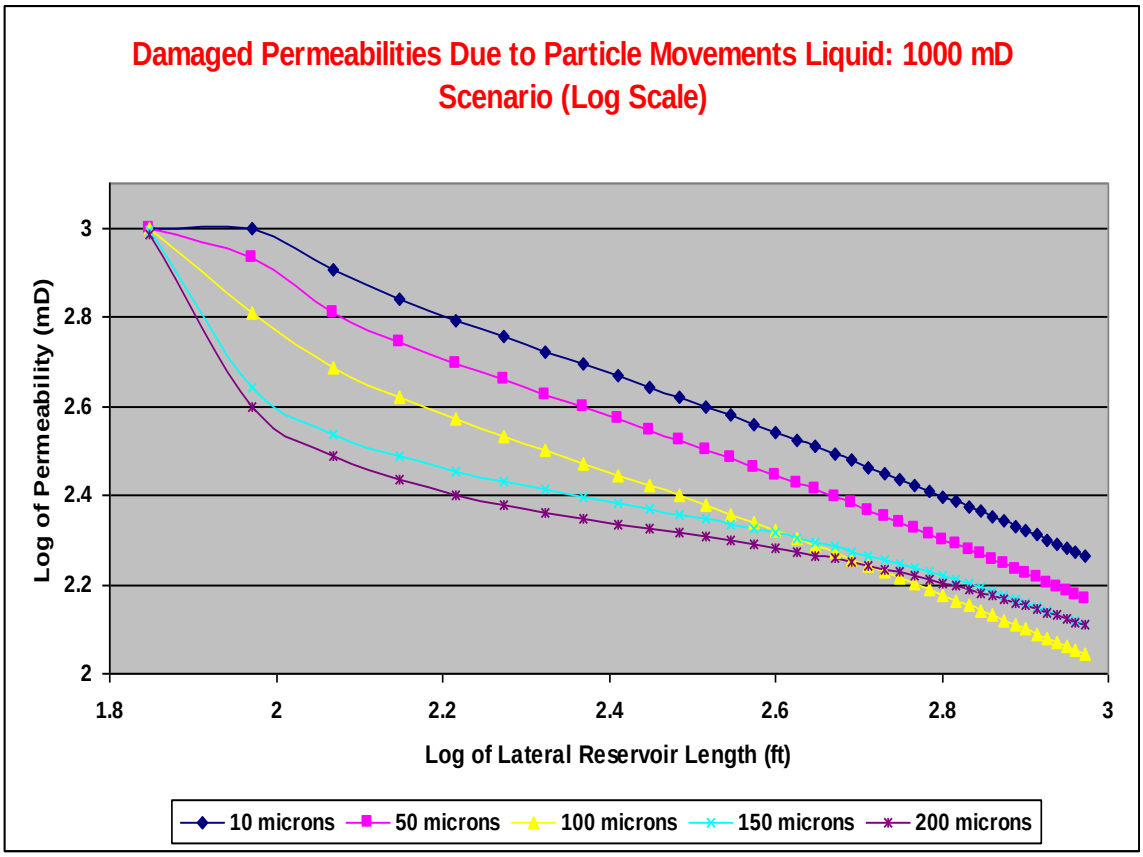

Figure 5.3: Log-log scale of particle size impact on permeability in a liquid scenario

While 10, 50 and 100 microns grain sizes revealed gentle slopes of permeability decline, coarser grained particles (150 and 200 microns) revealed relatively steeper slopes initially in the first quarter of the reservoir length after which almost followed the 100 micron pattern. Hence in a 1D rock the finer the grain size the less the permeability damage it may cause.

The second scenario which involved multiphase fluid (oil, water and gas) and particles sizes (10 – 200 microns) flowing through a 1000 mD drainage, was simulated using a similar process.

A graph of drawdown pressure vs. lateral reservoir length as shown in figure 5.4 revealed different profiles compared to profiles resulted in the liquid scenario.

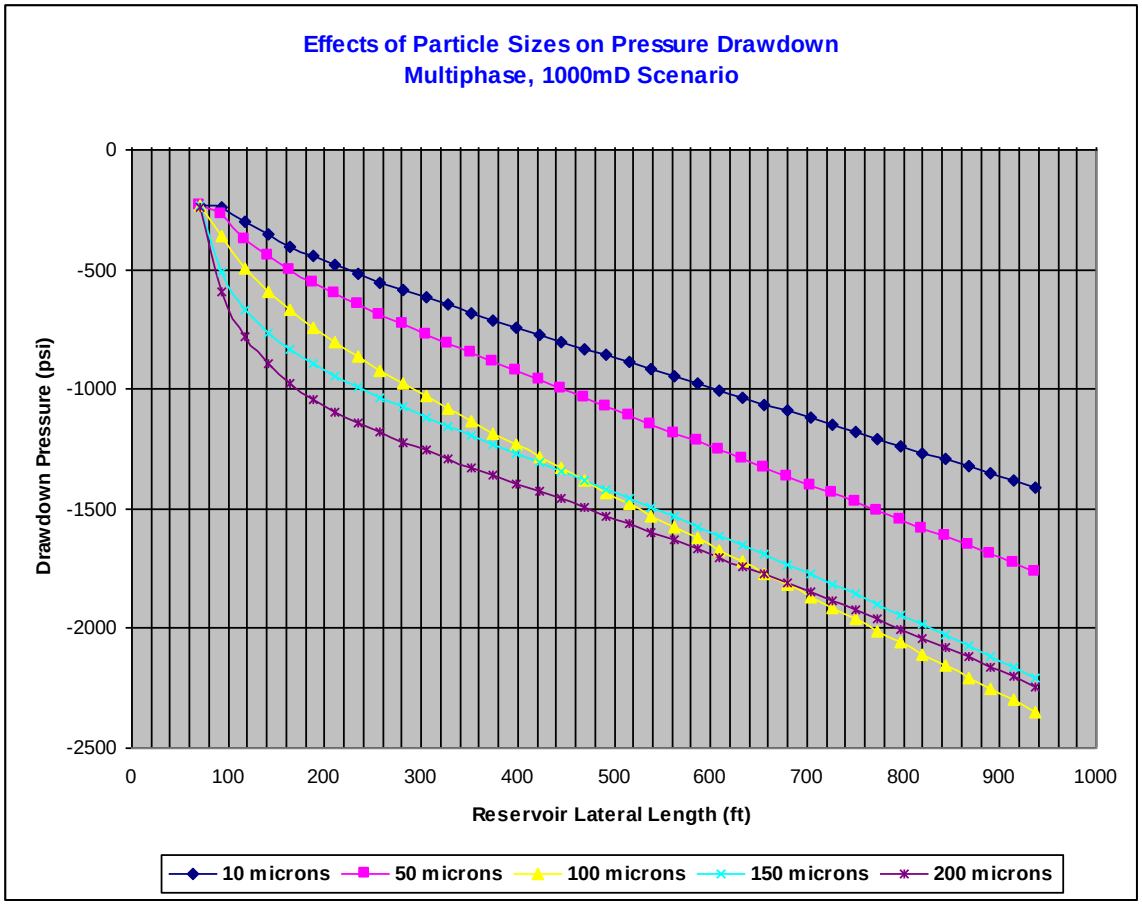

Figure 5.4: Particles impacts on drawdown pressures in a 1000mD multiphase drainage

From the figure, impacts of all particles sizes (10µm, 50µm, 100µm, 150µm, and 200µm) on drawdown pressure depicted initial gentle ΔP slopes from the beginning. The slopes were directly proportional to the particle diameter. The finer the grain size (10 µm to 50 µm) the less drawdown pressure was required to produce the same flow rate through the damaged rock. Whereas the coarser grain sizes (100, 150 and 200 µm) demonstrated sharper initial drawdown pressure slopes which continued almost to half the drainage length and then almost merged together; then eventually the 100 µm particle profile ended up with a steepest slope of all. Corresponding particle-damaged permeabilities were calculated in a similar

manner as explained in the liquid scenario. The results are presented in graphical format as shown in figure 5.5.

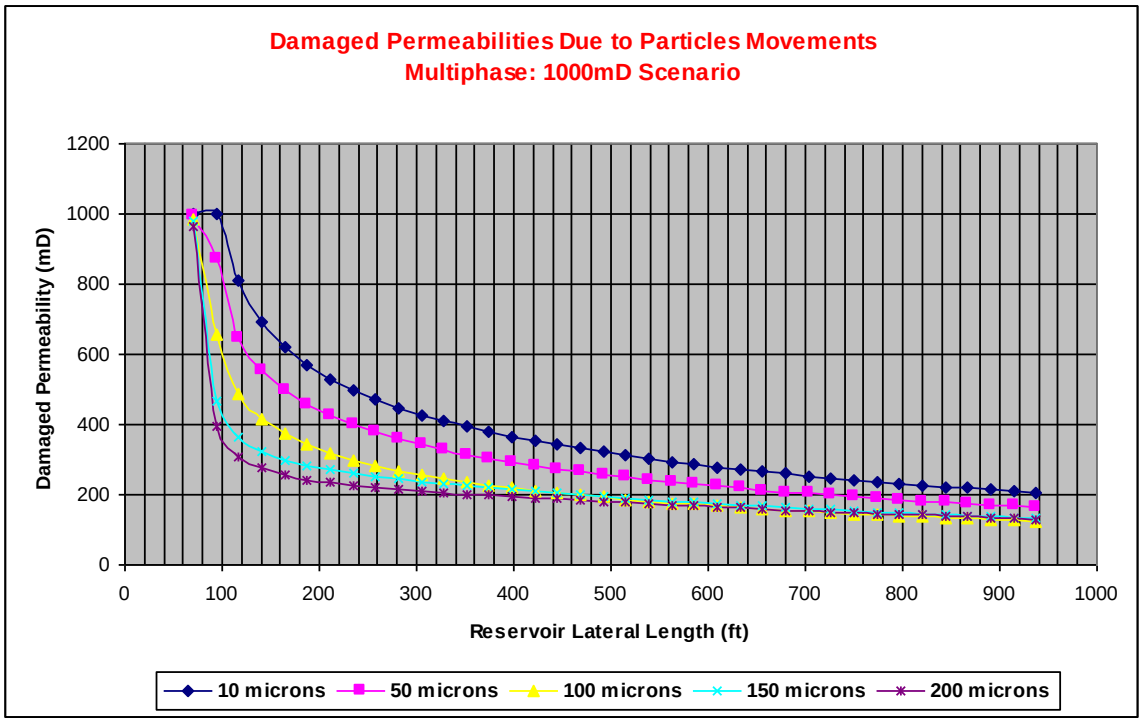

Figure 5.5: Particle size effects on permeability in multiphase scenario

Figure 5.5 shows particle damaged permeability profiles in a multiphase environment through a drainage area which had initial 1000 mD absolute permeability. From the figure, within less than 100ft into the reservoir, the overall absolute permeability is reduced to half the initial value especially in the case of coarser grains (100, 150 and 200 µm grain sizes). The finer grain sizes (10-50 µm) took about twice the distance to reduce the initial permeability to half the original value compared to the coarser grained particles results.

Like in the first scenario, a log-log scale of figure 5.5 was plotted to obtain more clarity of the particles impacts on permeability in the second scenario as shown in figure 5.6.

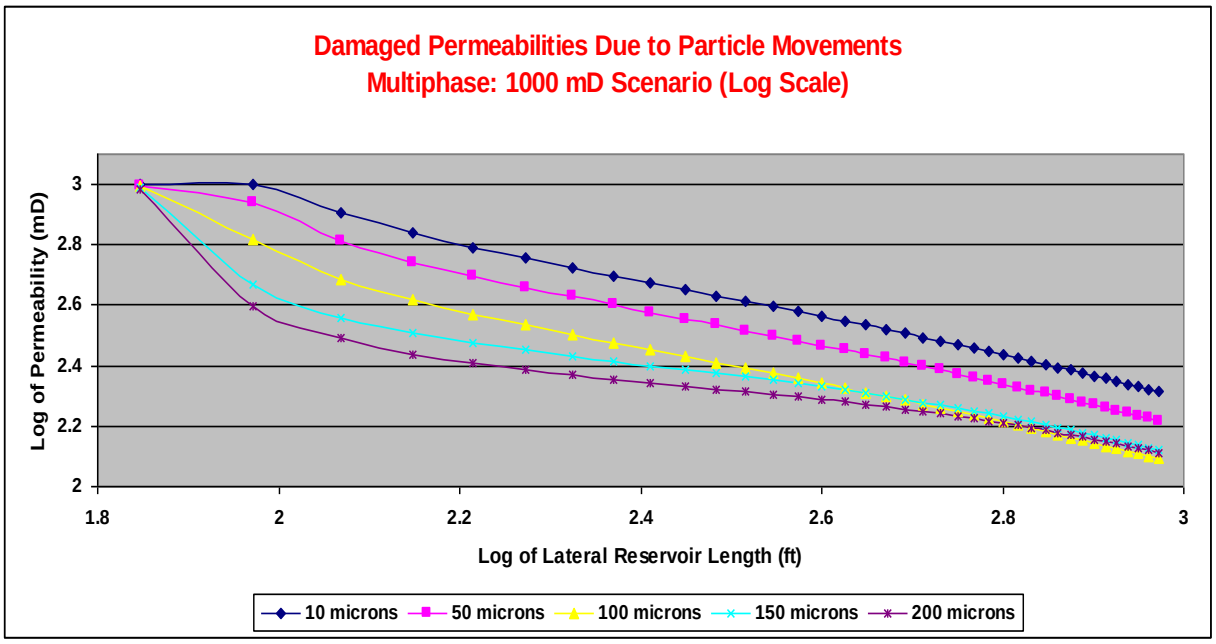

Figure 5.6: Log-log scale of particle size effects on permeability in multiphase scenario

Referring to figures 5.3 and figure 5.6, there is a difference between the first scenario and the second one. The slopes and gaps between the finer grained particles profiles (10, 50 and 100 microns) are less in the multiphase scenario (figure 5.6) than the ones revealed in the liquid scenario (figure 5.3). In addition, in the first half of the liquid scenario (figure 5.3), much wider separations were revealed between impacts of 150 μm, 100 μm, 50 μm and 10 μm on log of permeability profiles compared to separation revealed in the multiphase scenario (figure 5.6). The third and fourth scenarios involved a higher (2000 mD) permeability drainage through which liquid-particles flow and multiphase-particles flow were simulated. The objective was to get more insight on the particle size influence in the higher initial rock permeability in order to analyse particle-damaged permeabilities trends.

Figures 5.7 and 5.8 are graphical displays of impacts of particle sizes on pressure drawdowns in liquid and multiphase scenarios respectively.

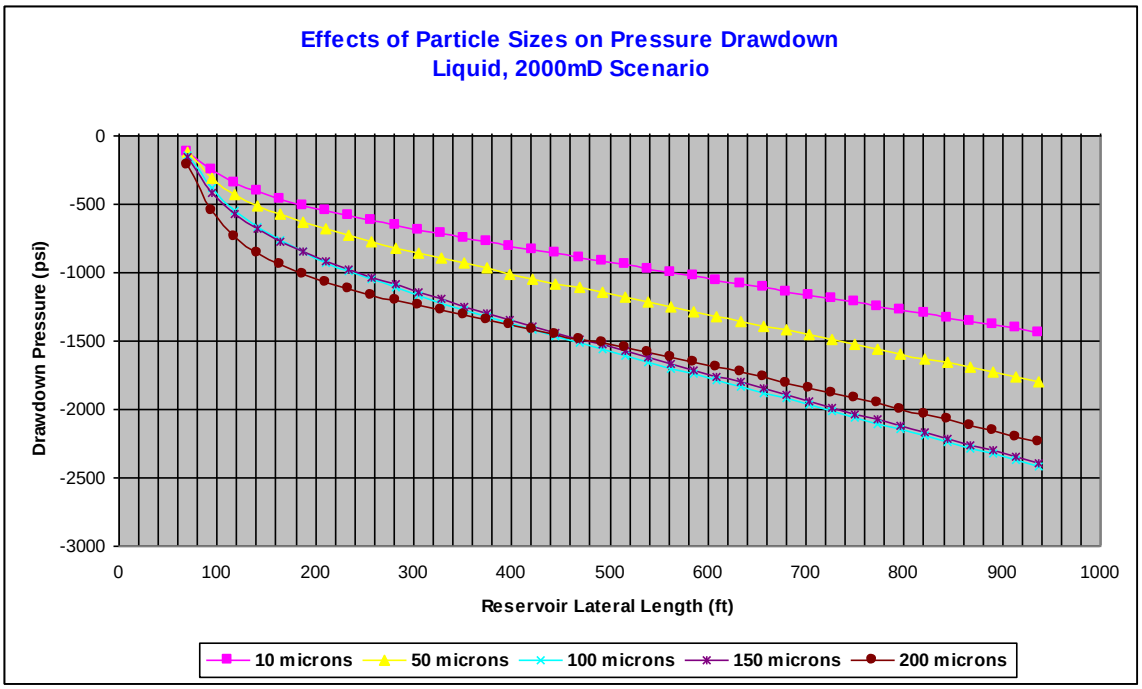

Figure 5.7: Particle size impacts on drawdown pressure in a 2000 mD liquid drainage

Each particle size (10 – 200 µm) caused a specific pressure drop profile across the drainage length as can be seen in the figures. Figure 5.8 clearly shows that the multiphase environment caused less particle size impact on pressure drawdown compared to the impact observed in the liquid flow (figure 5.7) while everything else was kept the same. The difference is clearer in the finer grained particles (10, 50 and 100µm) as can be seen in the figures. While in the liquid case (figure 5.7) impact of 100 µm on drawdown pressure is similar to the 150 and 200 µm impacts, in the multiphase case (figure 5.8), the impact profile of 100 µm is between the finer (10 and 50 µm) grains and coarser (150 – 200 µm) grains profiles. Hence trend or pattern of the 100 µm in the liquid case clearly differs from the 100 µm pattern observed in the multiphase case.

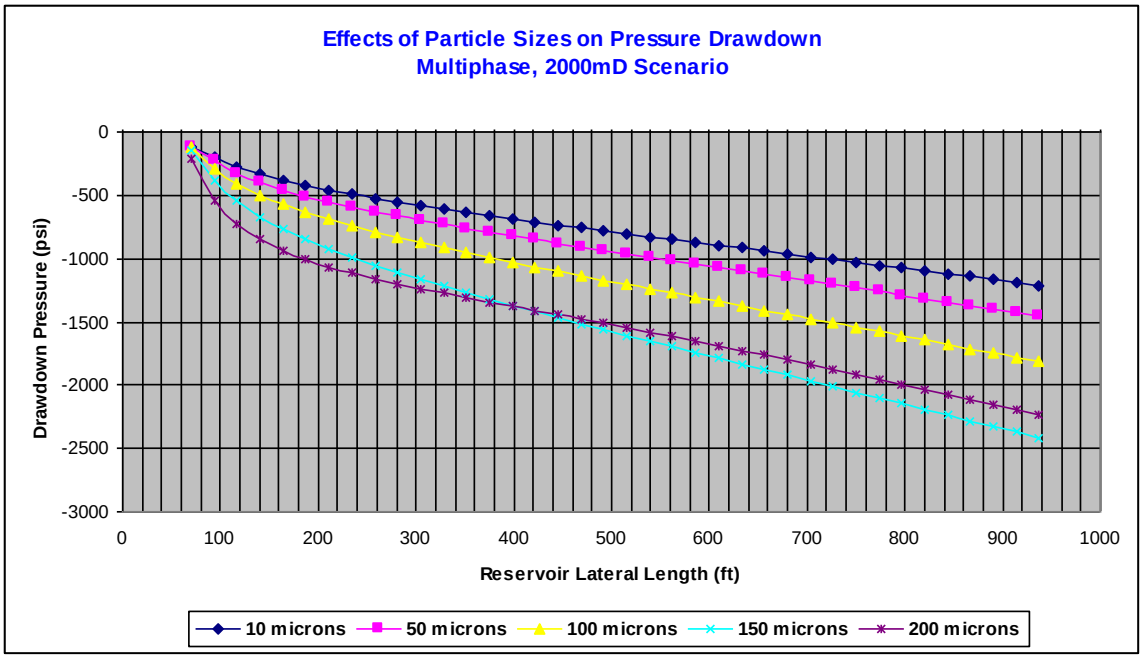

Figure 5.8: Particle size impacts on drawdown pressure in a 2000mD multiphase drainage

Compared to the liquid scenario, in the multiphase case, drawdown pressures profiles of the finer grain sizes especially 10, 50 and 100µm particles, were more distinct from the coarser grained profiles both qualitatively and quantitatively. Corresponding damaged permeabilities to the liquid scenario (as determined from the drawdown pressures) is displayed in figure 5.9.

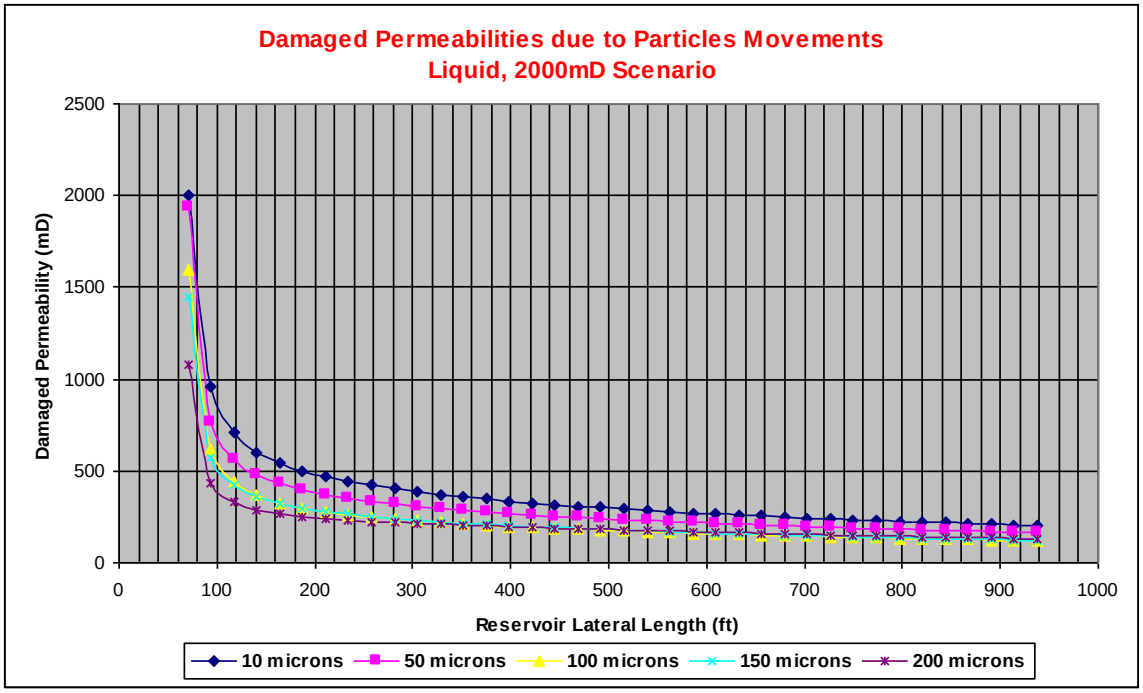

Figure 5.9: Particle size impacts on permeability in liquid scenario

To obtain more clarity of the particles impacts on permeability in the liquid scenario a log-log scale of figure 5.9 was plotted as shown in figure 5.10. From the figure, it is evident that particles grain sizes have different impacts on permeabilities especially the finer ones (10 and 50 microns). The 100 microns trend was almost similar to the 150 microns trend. However, both of them (100 μm and 150 μm) were different from the 200 microns trend in the first two third although ultimately all the three curves revealed similar impacts in the last third of the reservoir length as in figure 5.10.

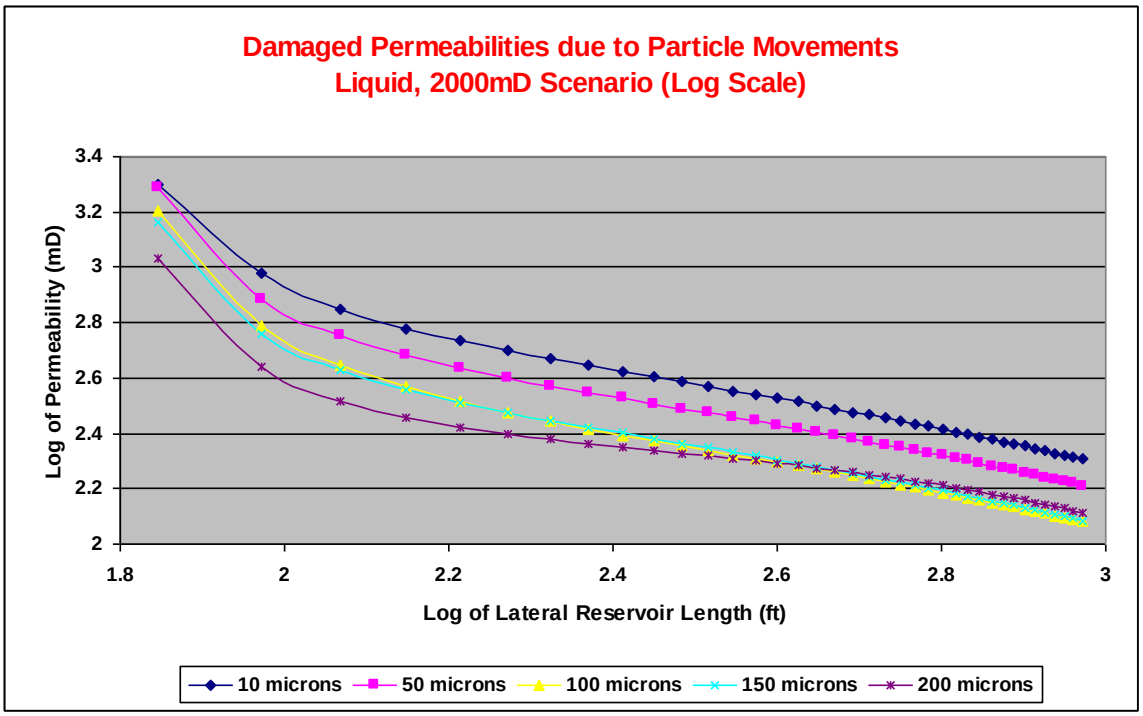

Figure 5.10: **Log-log scale of particle size impact on permeability in a liquid scenario**

Similar analyses were repeated for the multiphase scenario in the 2000 mD drainage. While the normal scaled graph in figure 5.11 showed almost curves convergence towards the last third of the drainage length, distinct curves separation were revealed in the 1st third of the graph.

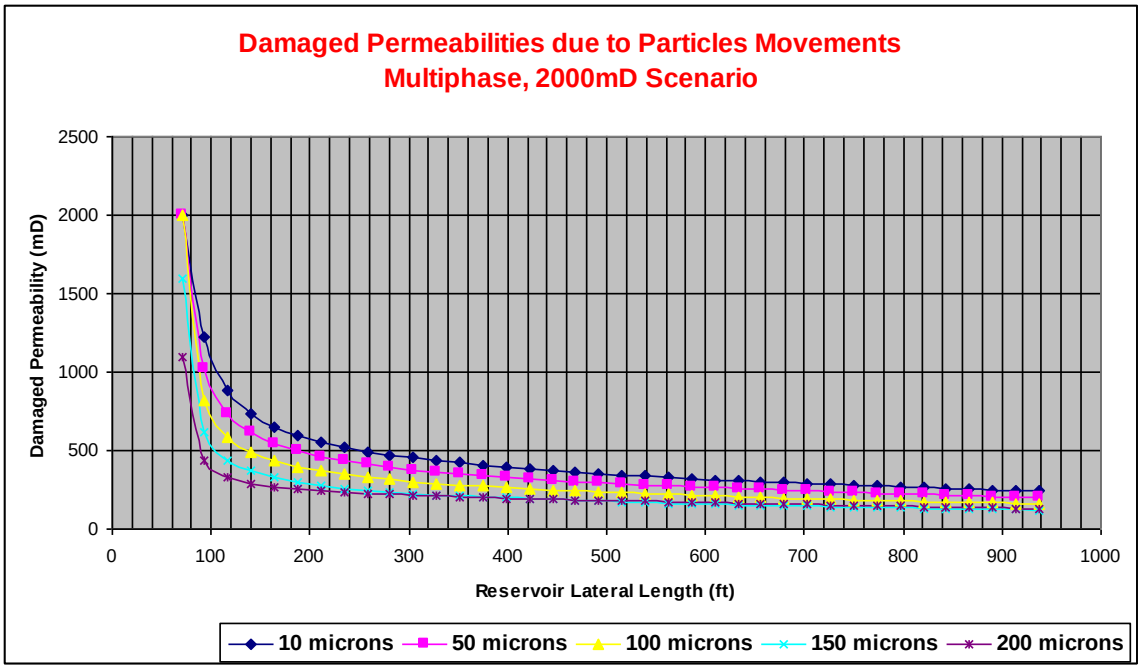

Figure 5.11: Particle size effects on permeability in multiphase scenario

Like in the above scenarios, a log-log scale of the multiphase conditions was plotted to obtain more clarity of the particles impacts on permeability in the 2000 mD scenario as shown in figure 5.12. The slopes and gaps of the finer grained particles profiles (10, 50 and 100 microns) are less in the multiphase scenario (figure 5.12) than in the liquid scenario (figure 5.10).

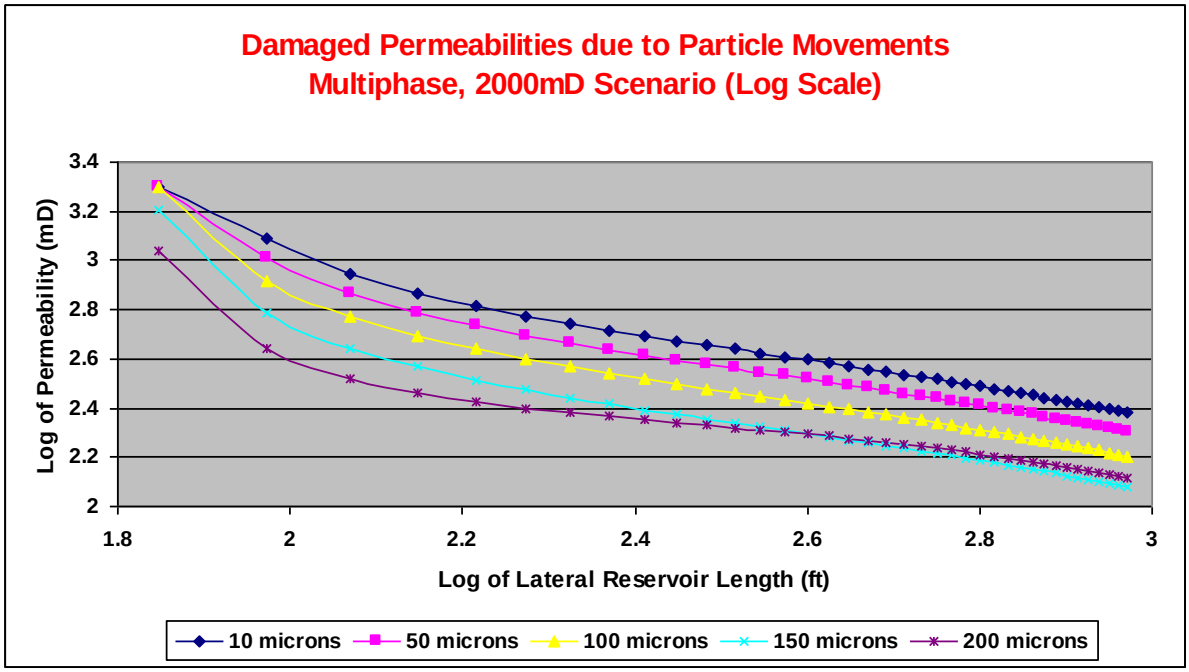

Figure 5.12: Log-log scale of particle size impacts on permeabilities in a multiphase scenario

From figure 5.12, it is evident that in a multiphase environment, impact of 100 µm fines particles on permeability is less than the same particle impact observed in the liquid environment shown in figure 5.10. Also while there were hardly any difference between 100 µm and 150 µm profiles in the liquid scenario (figure 5.10) clear difference between them was revealed in the multiphase scenario (figure 5.12).

It is clear that the finer grained particles reflected more gentle permeability decline gradients in the multiphase environment compared to the trends in the liquid case. For example, in the case of the liquid scenario (figure 5.9) referring to the impact caused by 10 µm grain particles on permeability reduction in the initial permeability, value was reduced to its quarter value (500 mD) after particle penetration of about 200 ft into the drainage area, whereas similar permeability reduction happened after the same particles had penetrated a distance of about

280 ft into the drainage area in the case of multiphase scenario (figure 5.11) as clearly indicated in the comparison graph of figure 5.13.

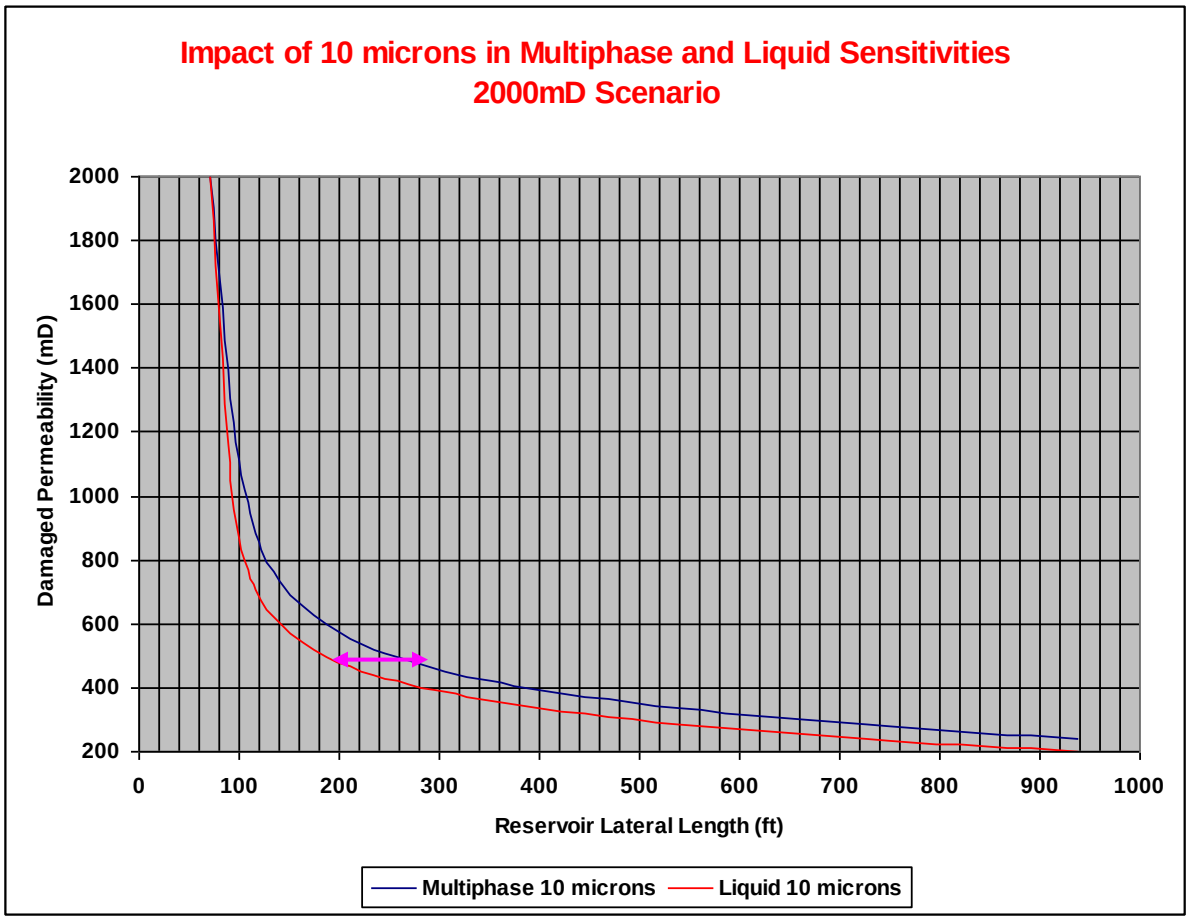

Figure 5.13: Comparison of particle size impact on permeability in liquid and multiphase

Similarly in the case of 50 micron particles, as can be seen in figure 5.14 (and also in figures 5.11 and 5.9), 200 ft penetration occurred in the multiphase flow compared to 140 ft penetration in the liquid before the permeability was reduced to a quarter of its initial value (from 2000 to 500 mD).

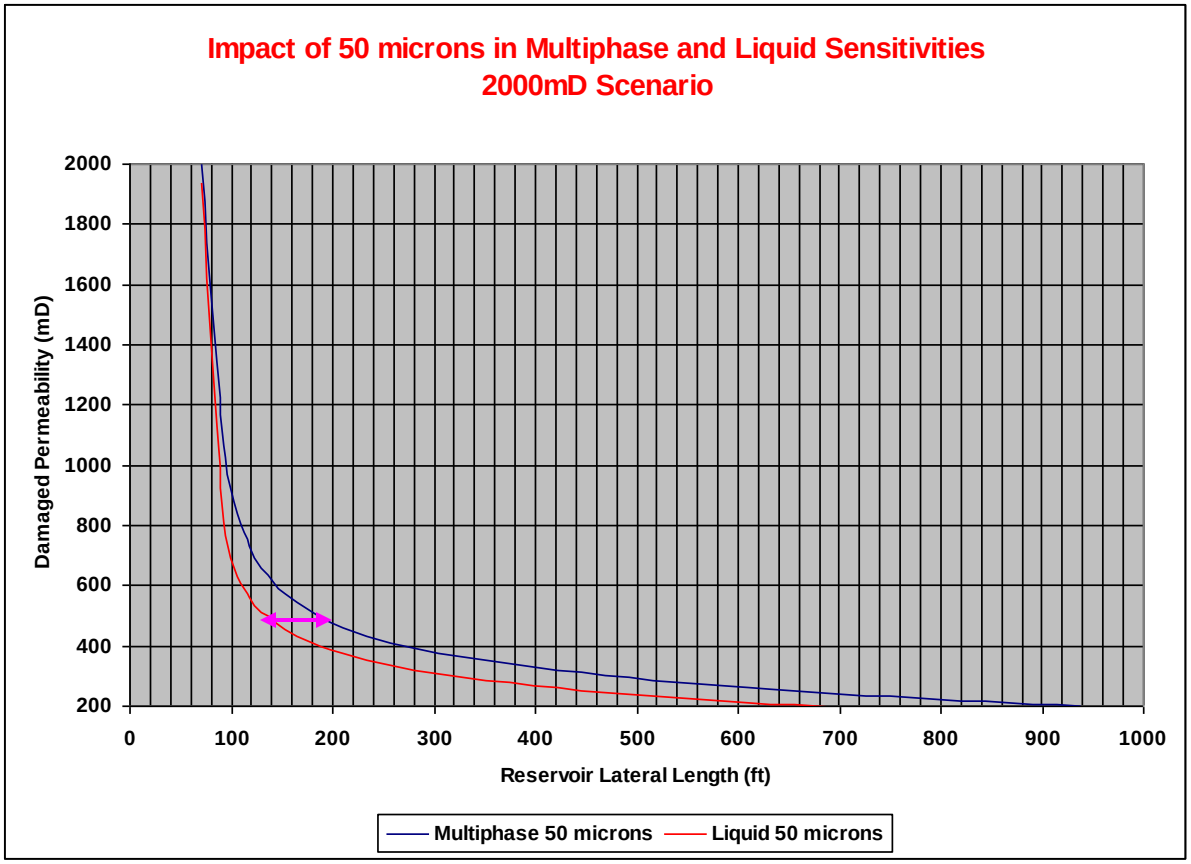

Figure 5.14: Comparison of particle size impact on permeability in liquid and multiphase

The fact that for each of the two permeabilities (1000 mD and 2000 mD) multiple sensitivities simulations of several parameters such as porosities, water cuts, particle sizes (10 - 200μm), velocities etc. were carried out and the fact that for each of the sensitivities four different scenarios involving oil, water, gas and multiphase reservoir conditions were carried out, results of those multiple sensitivities and scenarios were enough to develop particle-damaged permeability models as explained in the next sections.

5.3 Analysis of Particle-damaged Permeability in Liquid through 1000 mD Rock

This section discusses methods and procedures used in developing a particle-damaged permeability model in a porous medium having an initial absolute permeability of 1000 mD through which flowing liquid (oil and water) carrying particles of various sizes were simulated. The first step was to get the best curves to match the simulated drawdown pressure curves and then repeat the process of getting the best matching curves to match the damaged permeability curves. Starting with the impact of 10 µm particles, the trends of all other grain sizes were then matched one at a time. Figures 5.15 and 5.16 show curve matching of both damaged permeability and drawdown pressure curves respectively.

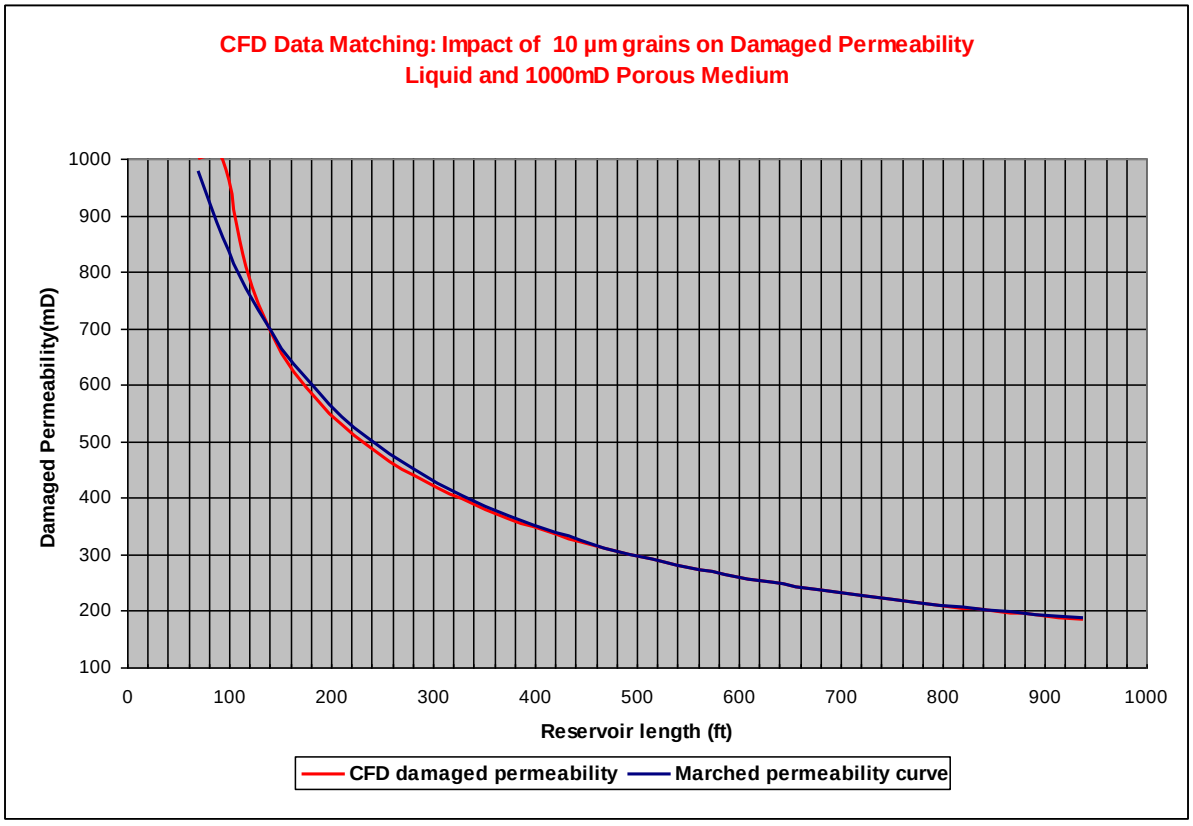

Figure 5.15: Damaged permeability matching. Effects of 10 µm grain on permeability

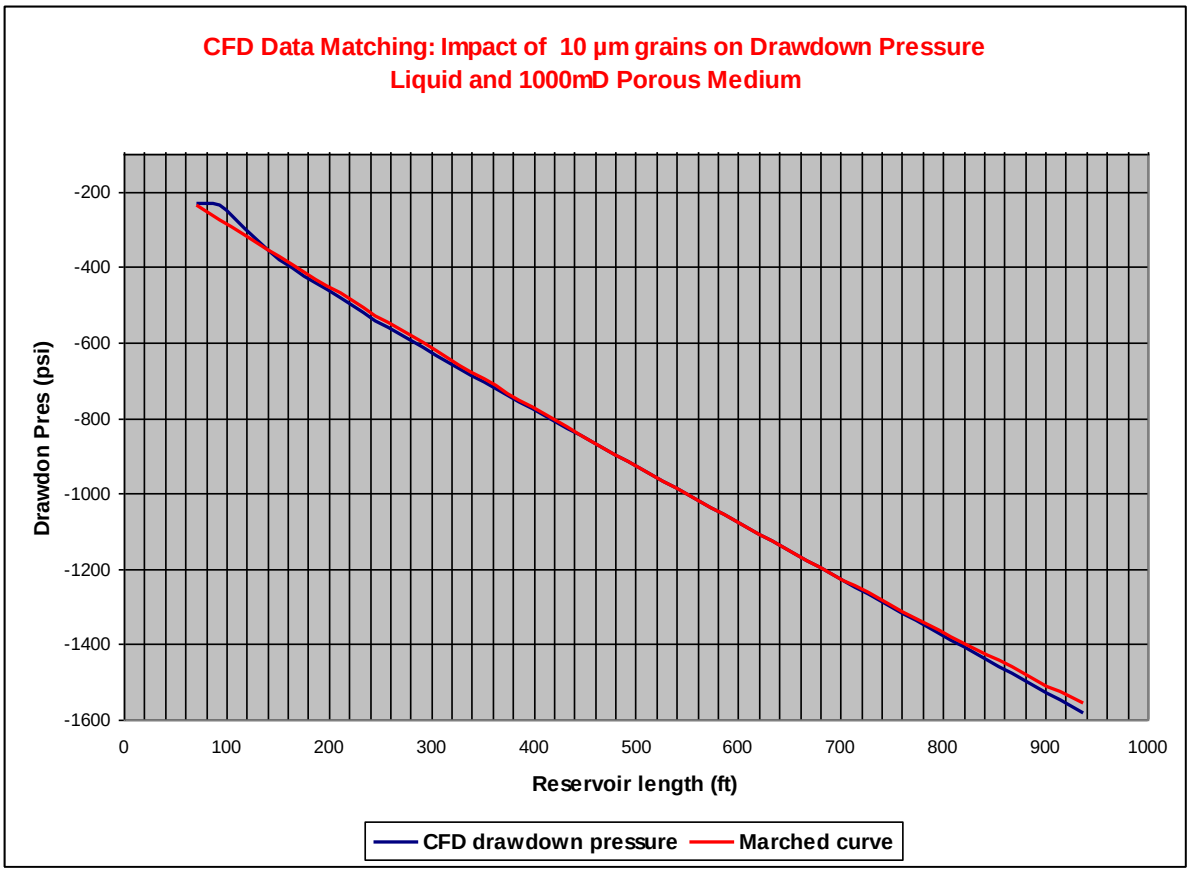

Figure 5.16: Matching of impacts of 10µm grain size on drawdown pressure

Like in the case of 10 µm grains, impact of 50 µm particles on permeability was matched in a similar manner. Figure 5.17 shows matching of the 50 µm particles impact on permeability.

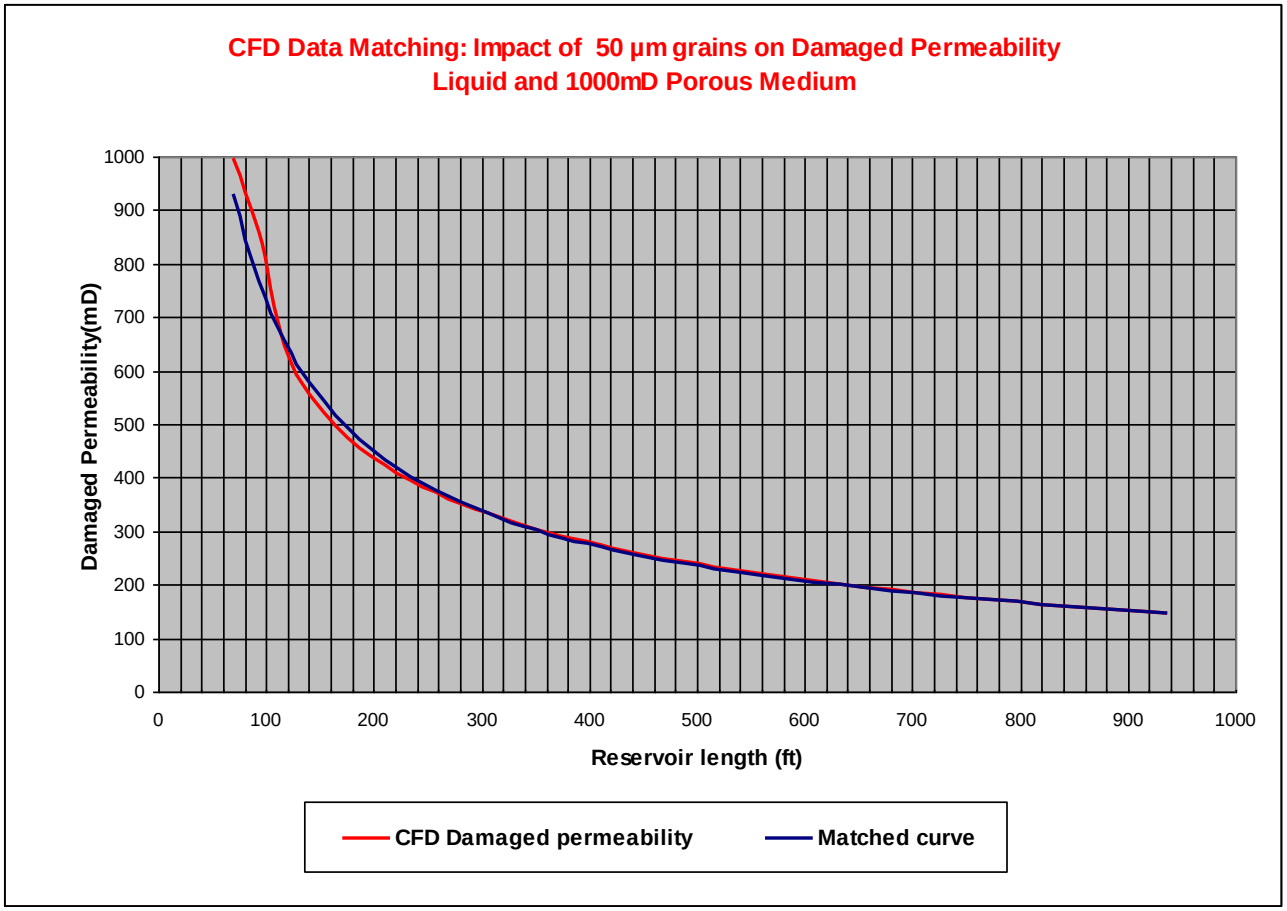

Figure 5.17: Matching impact of 50 microns grains on permeability

Figure 5.18 shows a match of the 50 µm particles impact on drawdown pressure.

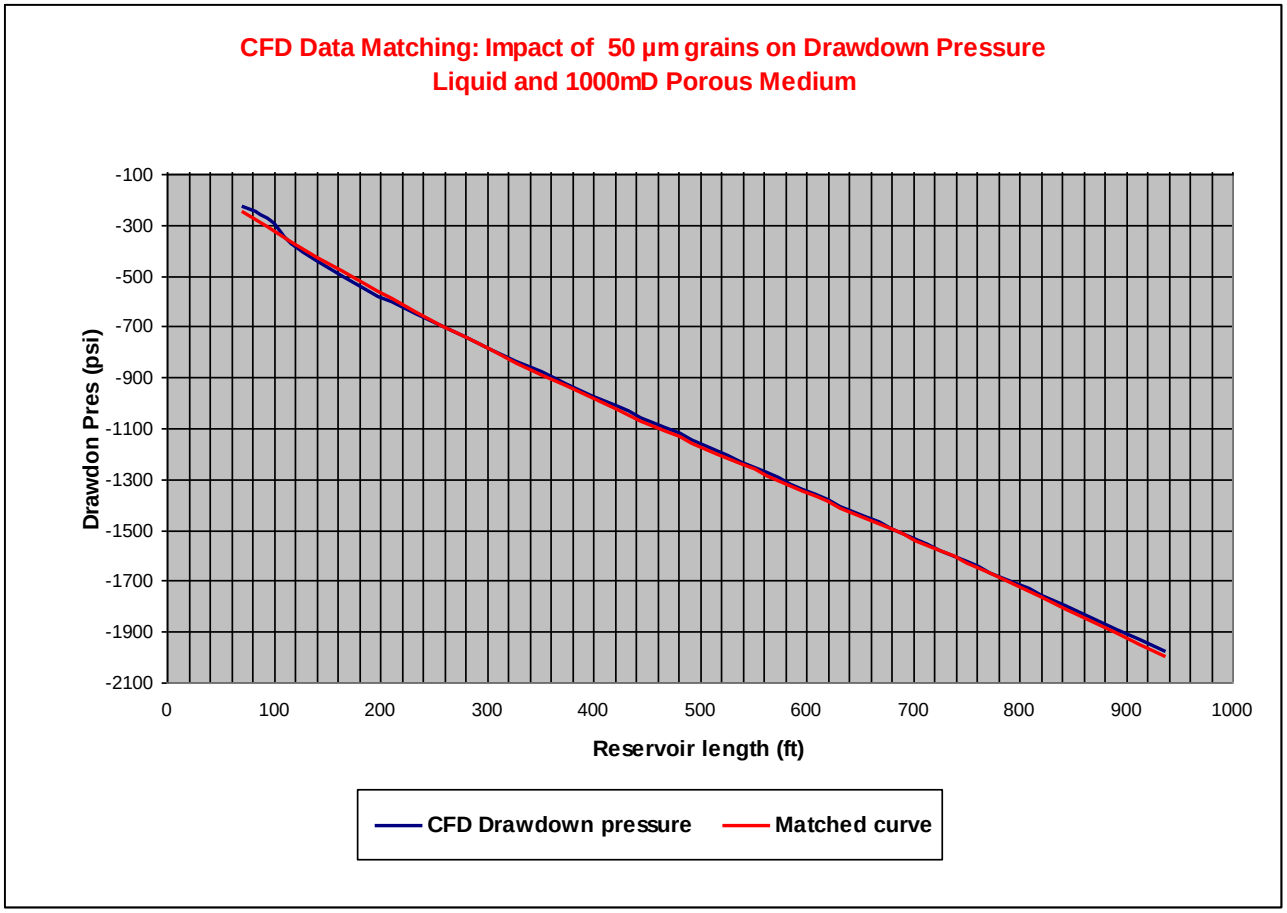

Figure 5.18: Drawdown pressure matching. Impact of 50 µm grain size

5.3.1 Particle-Damaged Permeability Model Development in Liquid Scenario

Particle-damaged permeability model development was accomplished in a scenario in which liquid flow carried various fines grain sizes (10µm – 200µm) covering both simulated and non-simulated particle sizes in a 1000 mD drainage area. A matching process of all the simulated data using MATLAB was the basis of the model development. A comprehensive model was then generated which can reproduce similar damaged permeabilities for the grain sizes within and outside the simulated range. Within the range, matching is demonstrated in figure 5.19. The figure portrays profiles matching of the impacts of other particle sizes (100, 150, and 200µm) on damaged permeabilities.

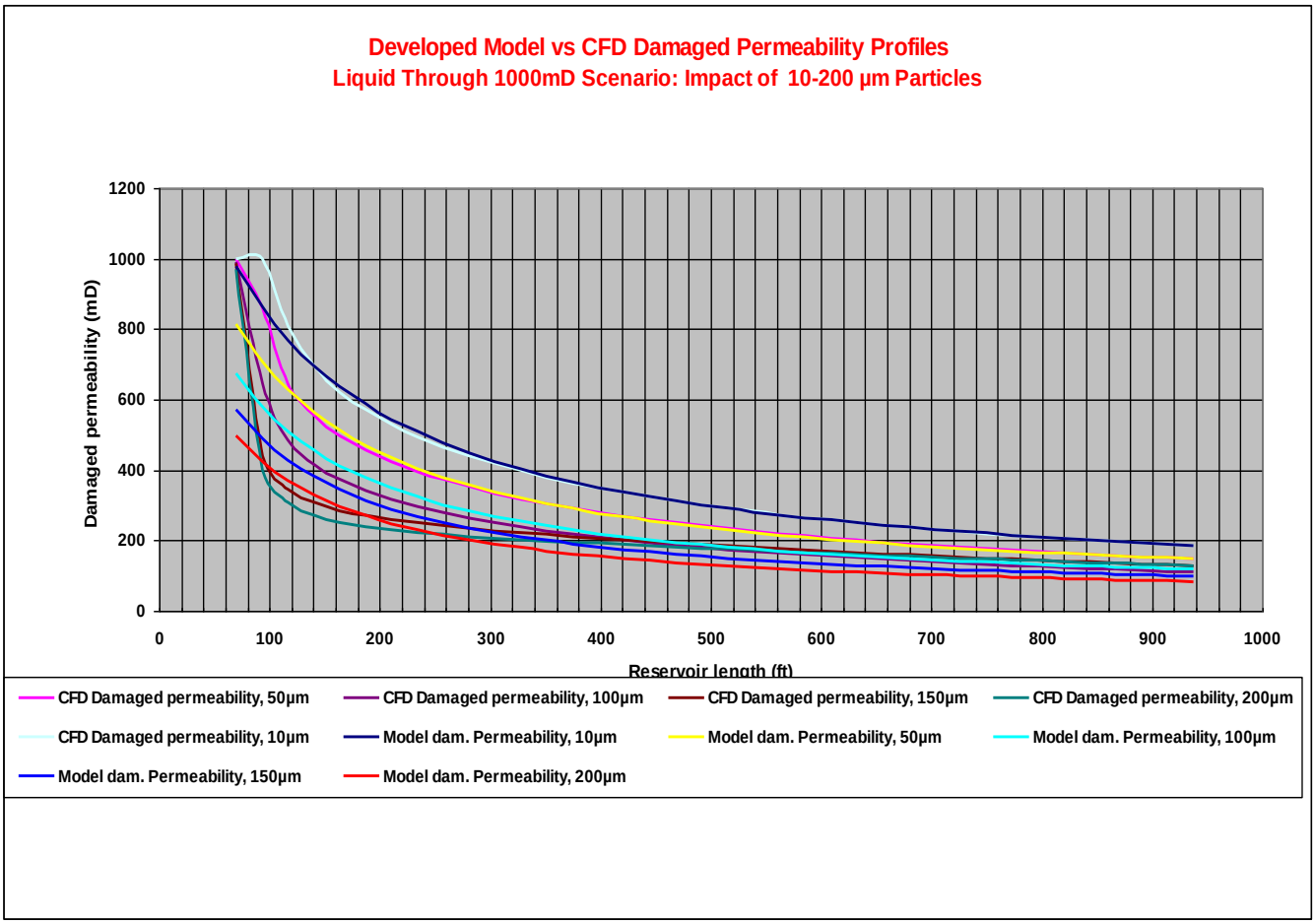

Figure 5.19: Permeability matching of CFD simulated trends in a 1000 mD liquid scenario

The developed particle-damaged model for the above scenario which can be used in calculating the damaged-permeability value for any grain size up to 300 µm is given in equation 5.3 and tested as well as validated using field data in chapter 6.

$$k_{di}(D_G, \chi_i) \approx \left\{ \frac{C\,(\mathrm{LN}(\chi_i))}{\Delta P(D_G, \chi_i)} \right\} \text{----------(5.3)}$$

Where:

$k_{di}(D_G, \chi_i)$ = Damaged permeability at ith length of the drainage length as a function of D_G and χ_i (mD)

χ_i = ith length of the drainage length (ft)

D_G = Mean grain size (microns)

ΔP = pressure drop (psi)

$$C = \frac{141.2q\mu B}{h}(-\ln(r_w) - \frac{3}{4} + S) \text{ ----------(5.4)}$$

Testing and validation of the developed models are detailed in chapter 6; in which testing was carried out for all simulated and non simulated fines particle sizes and resulted in acceptable trends. Thereafter the models were validated with real field data.

A general damaged permeability expression at depth *i*, due to grain size G_F, is as follows:

$$\sum_{i=1}^{i=n} k_{di}(G_F) = \sum_{i=1}^{i=n} \left\{ \frac{\{-1*141.2(\mu)(B)(q)*(\ln(r_{ei}) - \ln(r_w) + S - 3/4)\}}{\Delta_{pi}(G_F)} \left\{ \frac{1}{h} \right\} \right\} \text{ ----------(5.5)}$$

Where: $\Delta_{pi}(G_F)$ is a pressure drop which is a function of fine grain size at the i_{th} reservoir length. Any fines grains sizes including beyond the ones simulated by the CFD (up to 300 microns) can be analysed. For example for grain sizes between 1 and 300 microns, using reservoir data in table 5.1, in section 5.2.1 pressure drawdown can be calculated as follows:

$$\sum_{i=1}^{i=n} \Delta_{pi}(G_F) = \sum_{i=1}^{i=n} \left\{ 0.0005(r_{ei}^{\,2}) - 3.0693(r_{ei}) - 140.42 \right\} - \left\{ \{(0.0003(r_{ei}^{\,2}) - 1.3426(r_{ei}) - 25.87)\} \frac{\{(100-(G_F-10))\}}{100} \right\} \text{---(5.6)}$$

Therefore the summation of particle affected permeabilities per grain size in a liquid medium in a reservoir which had a clean initial absolute permeability of 1000 mD can be calculated by the following developed model:

$$\sum_{i=1}^{i=n} k_{di}(G_F) = \sum_{i=1}^{i=n} \left\{ \frac{\{-1*141.2(\mu)(B)(q)*(\ln(r_{ei}) - \ln(r_w) + S - 3/4)\}}{\left\{ 0.0005(r_{ei}^{\,2}) - 3.0693(r_{ei}) - 140.42 \right\} - \left\{ \{(0.0003(r_{ei}^{\,2}) - 1.3426(r_{ei}) - 25.87)\} \frac{\{(100-(G_F-10))\}}{100} \right\}} \left\{ \frac{1}{h} \right\} \right\} \text{---(5.7)}$$

NB: In case actual field data of drawdown pressure per hour or any time frame as function of D_G and χ_i is available,

$$\Delta P_t(D_G, \chi_i) = \bar{p} - p_{wf}\ (D_G, \chi_i)$$ ----------(5.8)

then the denominator should be replaced by that per reservoir length. In other words, the denominator which is

$$\sum_{i=1}^{i=n} \Delta_{pi}(G_F) = \sum_{i=1}^{i=n} \left\{0.0005(r_{ei}^{\ 2}) - 3.0693(r_{ei}) - 140.42\right\} - \left\{\{(0.0003\ (r_{ei}^{\ 2}) - 1.3426(r_{ei}) - 25.87)\}\ \frac{\{(100-(G_F-10))\}}{100}\right\}$$

should be replaced with measured ΔP_t field data if available.

Field's pressure drawdown per hour data in this case can be converted into distance covered by the pressure as explained in chapter 6.

Using equation 5.7 substituting values from table 5.1 for each i^{th} reservoir length, particle-affected permeability can be calculated as follows:

$$\sum_{i=1}^{i=n} k_{di}(G_F) = \sum_{i=1}^{i=n} \left\{ \frac{\{-1 * 23600.571 * (\ln(r_{ei}) + 5.482)\}}{\left\{0.0005(r_{ei}^{\ 2}) - 3.0693(r_{ei}) - 140.42\right\} - \left\{\{(0.0003\ (r_{ei}^{\ 2}) - 1.3426(r_{ei}) - 25.87)\}\ \frac{\{(100-(G_F-10))\}}{100}\right\}} \left\{\frac{1}{h}\right\} \right\}$$ -------(5.9)

Figure 5.20 shows the model's output of damaged permeability profiles across the modeled reservoir covering impacts of fines grain sizes even beyond those simulated by the CFD.

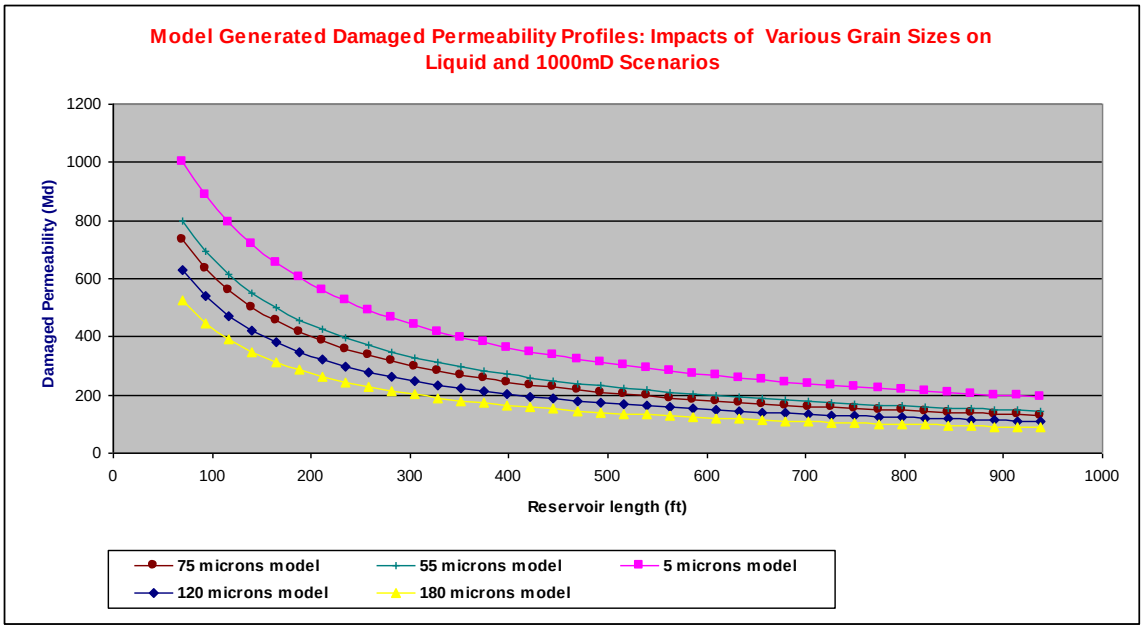

Figure 5.20: Model generated damaged permeability profiles of non-simulated grain sizes

In order to determine individual liquid phase effective permeability (k_e), the concept of relative permeability analysis was employed (113, 114). The CFD drawdown pressure profiles were used in the Darcy equation for the absolute permeability (k_{abs}) as a function of grain size as outlined in section 5.1 above. Effective permeabilities of oil and water are both functions of the k_{abs} as follows:

$k_o = (k)(k_{ro})$ ----------(5.10)

$k_w = (k)(k_{rw})$ ----------(5.11)

k_{rw} and k_{ro} calculations are given below in this section.

Where:

k_o = effective oil permeability (mD)

k_{ro} = relative oil permeability (dimensionless)

k_w = effective water permeability (mD)

k_{rw} = relative water permeability (dimensionless)

Figure 5.21 shows relationships between effective oil permeability k_o and effective water permeability k_w with water saturation S_w. it also shows corresponding relative oil permeability k_{ro} and relative water permeability k_{rw}.

In the figure,

S_{wc} = connate water saturation (fraction)

S_{or} = residual oil saturation (fraction)

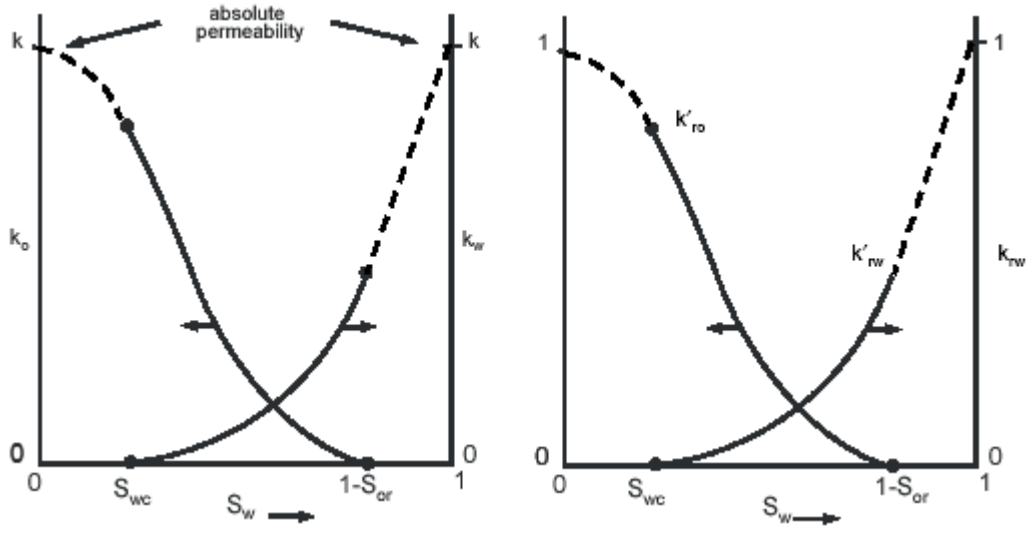

Figure 5.21: Effective oil and water permeabilities and corresponding relative permeabilities (113)

General expressions of oil and water relative permeabilities as functions of water saturations, are given as follows:

$$k_{ro}(S_w) = \frac{k_o S_w}{k_{abs}}; and, k_{rw}(S_w) = \frac{k_w S_w}{k_{abs}} \text{ ----------(5.12)}$$

Initial water relative permeability, k_{rw} (114) is calculated as follows:

$$k_{rw} = 3.5388 * 10^{-2}\left[\frac{S_w - S_{wi}}{1 - S_{wi} - S_{orw}}\right] - 1.0874 * 10^{-2}\left[\frac{S_w - S_{orw}}{1 - S_{wi} - S_{orw}}\right] + 0.56556 * S_w{}^{3.6} * [S_w - S_{wi}] \text{--(5.13)}$$

Where:

S_{wi} = initial water saturation (fraction)

S_{orw} = residual oil saturation to water (fraction)

S_o and S_w are determined as follows:

$$S_o = S_{orw} + \left(\frac{[1-WC]* B_o}{[1-WC]B_o + WC * B_w} \right) * [1 - S_{wi} - S_{orw}] \quad \text{----------(5.14)}$$

$$S_w = S_{wi} + \left(\frac{WCB_w}{[1-WC]B_o + WC * B_w} * [1 - S_{wi} - S_{orw}] \right) \quad \text{----------(5.15)}$$

Where:

WC = water cut (fraction)

B_o = oil formation volume factor, (res bbl/STB)

B_w = water formation volume factor (res bbl/STB)

Relative oil permeability k_{ro} is calculated as follows (114):

$$k_{ro} = 0.76067 * \left[\frac{\frac{S_o}{1-S_{wi}} - S_{orw}}{1-S_{orw}} \right]^{1.8} * \left[\frac{S_o - S_{orw}}{1-S_{wi}-S_{orw}} \right]^2 * 2.6318\phi[1-S_{orw}][S_o - S_{orw}] \text{------(5.16)}$$

Where: ϕ = porosity (fraction)

All parameters calculated by formulae (5.10 to 5.16) are shown in table 5.2.

Table 5.2: Oil and Water Relative and Effective Permeabilities

Water Cut %	W/C (fraction)	S_w	k_{rw}	S_o	k_{ro}	k_o	k_w
10	0.10	0.27	-0.01	0.74	0.95	947	-12
15	0.15	0.30	-0.01	0.71	0.84	839	-11
20	0.20	0.33	-0.01	0.69	0.74	740	-9
25	0.25	0.36	-0.01	0.66	0.65	650	-7
30	0.30	0.40	0.00	0.63	0.57	569	-5
33	0.33	0.42	0.00	0.62	0.52	524	-3
34	0.34	0.42	0.00	0.61	0.51	510	-2
40	0.40	0.46	0.00	0.58	0.43	431	2
41	0.41	0.47	0.00	0.57	0.42	419	3
42	0.42	0.48	0.00	0.57	0.41	407	4
43	0.43	0.48	0.01	0.56	0.40	395	5
44	0.44	0.49	0.01	0.56	0.38	384	6
50	0.50	0.53	0.01	0.52	0.32	321	14
51	0.51	0.54	0.02	0.52	0.31	311	15
52	0.52	0.55	0.02	0.51	0.30	302	17
53	0.53	0.55	0.02	0.50	0.29	293	18
54	0.54	0.56	0.02	0.50	0.28	284	20
60	0.60	0.60	0.03	0.46	0.23	234	32
61	0.61	0.61	0.03	0.46	0.23	226	34
62	0.62	0.62	0.04	0.45	0.22	218	37
63	0.63	0.63	0.04	0.44	0.21	211	39
64	0.64	0.63	0.04	0.44	0.20	204	42
80	0.80	0.75	0.11	0.34	0.10	104	107
81	0.81	0.76	0.11	0.33	0.10	99	113
82	0.82	0.77	0.12	0.32	0.09	94	119
83	0.83	0.78	0.13	0.32	0.09	88	126
84	0.84	0.79	0.13	0.31	0.08	83	132
90	0.90	0.83	0.18	0.27	0.05	52	179
91	0.91	0.84	0.19	0.26	0.05	46	187
92	0.92	0.85	0.20	0.26	0.04	41	197
93	0.93	0.86	0.21	0.25	0.04	36	206
94	0.94	0.87	0.22	0.24	0.03	31	216
95	0.95	0.88	0.23	0.24	0.03	26	227
96	0.96	0.88	0.24	0.23	0.02	21	238
97	0.97	0.89	0.25	0.22	0.02	16	249
98	0.98	0.90	0.26	0.21	0.01	10	261
99	0.99	0.91	0.27	0.21	0.01	5	273
100	1.00	0.92	0.29	0.20	0.00	0	286

Figures 5.22 and 5.23 show oil and water relative and effective permeabilities respectively.

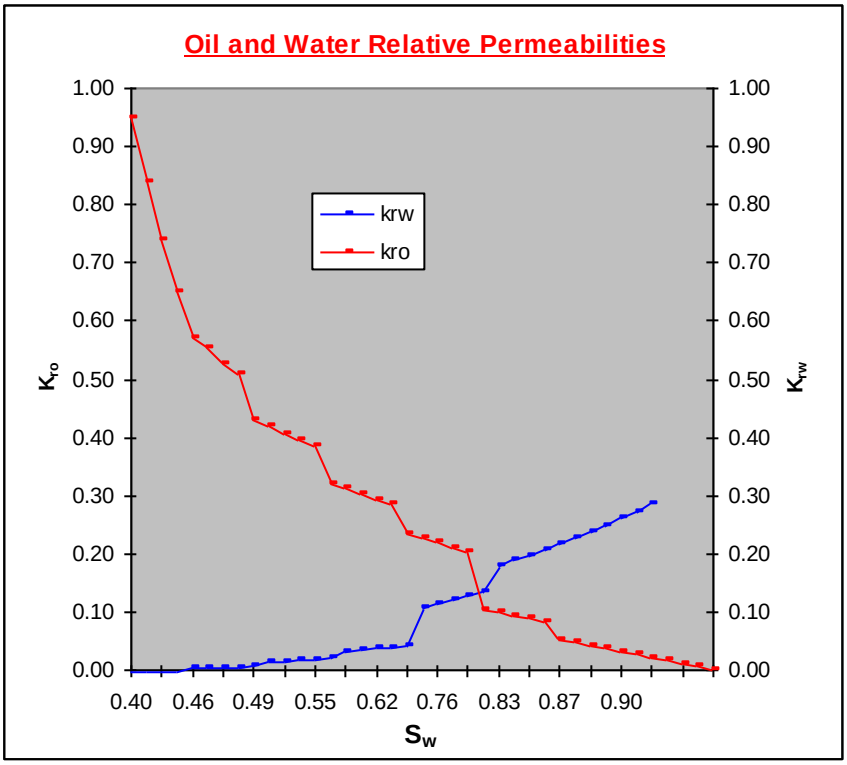

Figure 5.22: Relative permeabilities of oil and water

In order to calculated effective permeability of oil or water, relative permeability of each of the fluids was calculated first using equations 5.12 to 5.13 from which corresponding effective permeability (k_o and k_w) values were calculated using equations 5.10 and 5.11 respectively. Figure 5.22 shows relative permeability curves of oil and water while Figure 5.23 depicts effective permeabilities of oil and water.

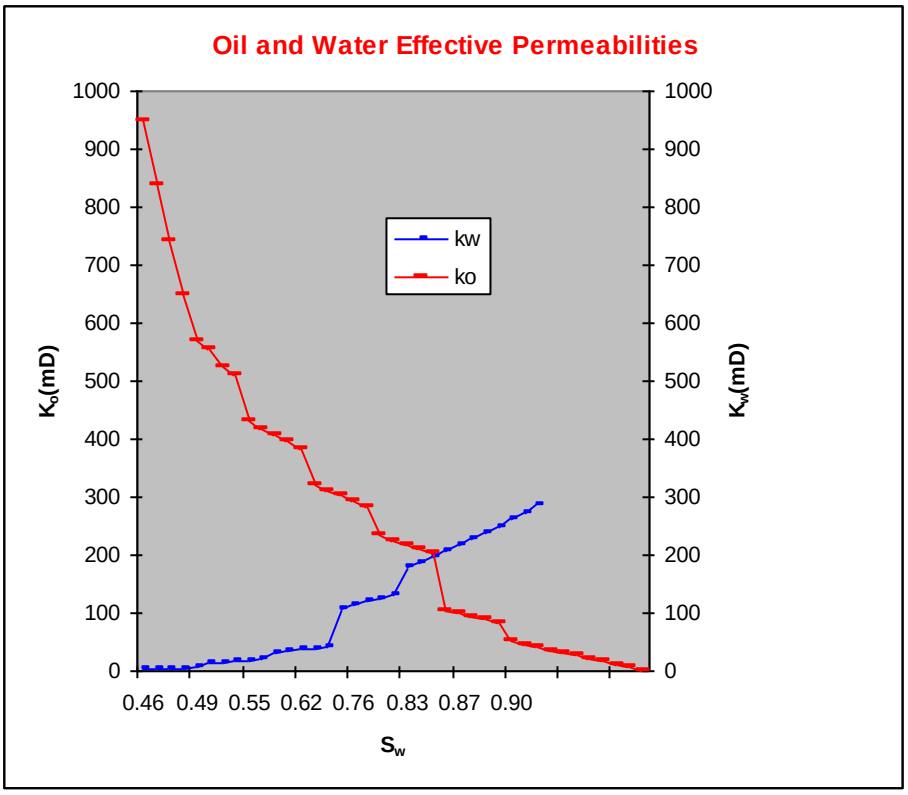

Figure 5.23: Effective permeabilities of oil and water

Hence for each fluid (oil or water) individual flow rates can be calculated using the Darcy equation 2.29 in which the absolute permeability k should be replaced with k_o or k_w for effective oil permeability or effective water permeability respectively.

5.4 Damaged Permeability Model Development: Multiphase Scenario

The second scenario involved multiphase sensitivities where gas fluid was added keeping the rest of the parameters as in the first liquid scenario the same (115). Figure 5.24 shows sets of particle-damaged permeabilities due to 10 – 200 μm particle impacts on the original permeability in a multiphase scenario. As in the liquid scenario, similar procedures and steps were taken to establish correlations which could match the simulated pressure drop, hence damaged permeability profiles as shown in figure 5.24.

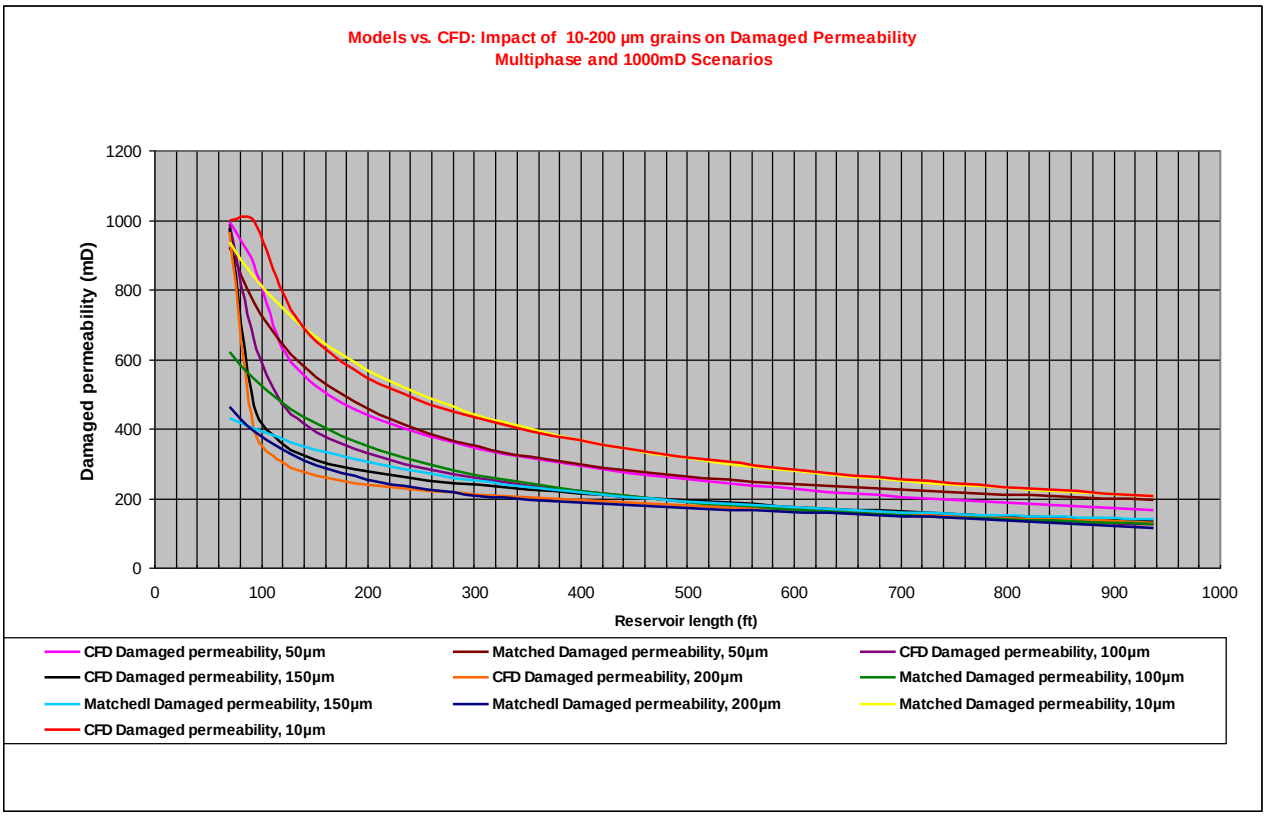

Figure 5.24: CFD based permeability profiles matching in a 1000mD multiphase scenario

For multiphase simulated conditions, the study revealed a drawdown pressure model governing various grain size impacts as follows:

$$\sum_{i=1}^{i=n}\Delta_{pi}(G_f)=\sum_{i=1}^{i=n}\left\{0.0007(r_{ei}^{\ 2})-2.9365(r_{ei})-166.92\right\}-\left\{\{(0.0004\ (r_{ei}^{\ 2})-1.2916(r_{ei})-35.88)\}\frac{\{(100-(G_f-10))\}}{100}\right\} \quad \text{-----(5.17)}$$

The corresponding damaged permeability per lateral reservoir length as a function of fines grain size impact in a multiphase condition was as follows:

$$\sum_{i=1}^{i=n}k_{di}(G_f)=\sum_{i=1}^{i=n}\left\{\frac{\{-1*141.2(\mu)(B)(q)*(\ln(r_{ei})-\ln(r_w)+S-3/4)\}}{\left\{0.0007(r_{ei}^{\ 2})-2.9365(r_{ei})-166.92\right\}-\left\{\{(0.0004\ (r_{ei}^{\ 2})-1.2916(r_{ei})-35.88)\}\frac{\{(100-(G_f-10))\}}{100}\right\}}\left\{\frac{1}{h}\right\}\right\} \quad \text{-----(5.18)}$$

Since equation 5.18 is for multiphase containing oil, water, gas and particle sizes, it should be used only for multiphase fluid mixture. However for dry gas analysis especially related to

pressure surveys such as build-up or drawdown surveys, equation 5.19 should be the numerator of equation 5-18 without the $\{pe - pws\}$ term.

Hence dry gas permeability is calculated as follows:

$$k_g = -162.6\left\{\frac{[q_g \mu_g B_g]}{[h]\{pe - pws\}}\right\}\log\left(\frac{t+\Delta t}{\Delta t}\right) \text{ ----------(5.19)}$$

In the equation 5.19, B_g is expressed as follows:

$$B_g = Z\frac{T}{T_{sc}}\frac{P_{sc}}{\left\{\frac{pe+pws}{2}\right\}} \text{ ----------(5.20)}$$

Where:

pe is extrapolated pressure in the pressure test curve where $\log\left\{\frac{t+\Delta t}{\Delta t}\right\} = 1$ (psi)

Z is gas compressibility (deviation) factor (dimensionless)

pws is shut-in well pressure (psia)

T is absolute temperature (°R)

B_g is gas formation volume factor (rb/stb)

q_g is gas flow rate, (stb/d) (converted from MMscf/d)

μ_g is gas viscosity (cP)

k_g is gas permeability (mD)

t is total production time before the well was shut-in (hr)

Δt is time interval during which pressure measurement was taken (hr)

h is gas reservoir thickness (ft)

Tsc is standard temperature = 520 °R

Psc is standard pressure = 14.65 psia

NB: In case drawdown pressure per hour or at any time frame was carried out, then the denominator of equation 5.18 or of equation 5.19 should be replaced by that measured drawdown per reservoir length.

Figure 5.25 shows the model's output of damaged permeability profiles across the simulated reservoir showing impacts of non-simulated fines grain sizes on permeabilities in a multiphase medium using equation 5.18 in which table 5.1 values were substituted for each ith reservoir length as follows:

$$\sum_{i=1}^{i=n} k_{di}(G_f) = \sum_{i=1}^{i=n} \left\{ \frac{\{-1*23600.571*(LN(r_{ei})+5.482)\}}{\left\{0.0007(r_{ei}^{\,2})-2.9365(r_{ei})-166.92\right\} - \left\{\{(0.0004\,(r_{ei}^{\,2})-1.2916(r_{ei})-35.88)\}\,\frac{\{(100-(G_f-10))\}}{100}\right\}} \left\{\frac{1}{h}\right\} \right\} \text{------(5.20)}$$

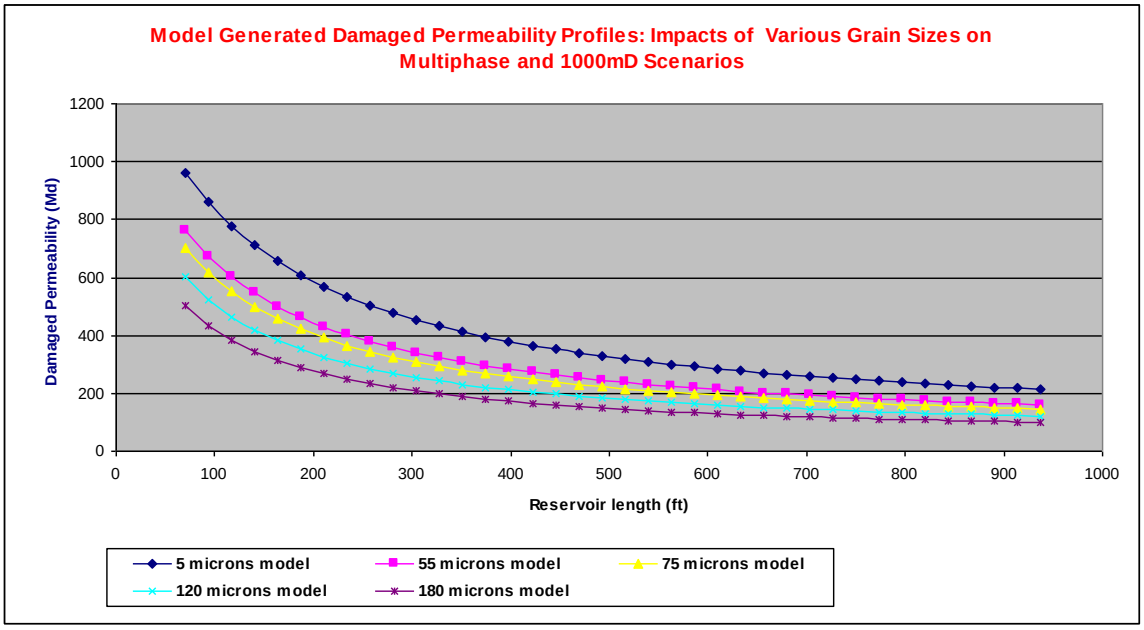

Figure 5.25: Model generated damaged permeability profiles of non-simulated grain sizes

In order to analyse reservoir performance effectively, the developed models should be incorporated into reservoir simulators. Section 5.5 elaborates on this aspect.

5.5 Reservoir Simulator Which Analyzed the Damaged Permeability Models

The reservoir simulator applied in this study is one of the most advanced packages in the oil and gas industry. It is the Modular Reservoir Simulator (MoReS) software and is a Shell International's preferred commercial package. A technical description of MoReS is given in section 5.5.1, while accounts on MoReS's capabilities and features are given in Appendix A-2. MoReS was provided by the collaborating establishment (Shell UK) to perform comprehensive reservoir performance studies (Appendix A-3).

The CFD-generated damaged pressure drop profiles from which damaged permeability profiles were determined, were initially expressed in a form of correlation in a depth-permeability plot from which deterministic and predictive methods were used to thoroughly study all the profiles and trends as part of the permeability model development stage. The damaged permeability models were then incorporated into the 3D reservoir simulator, MoReS. Hence, for each of the sensitivity groups described above, corresponding damaged permeability model was incorporated into the 3D simulator for comprehensive reservoir performance prediction.

5.5.1 Reservoir Simulator (MoReS)

MoReS is a 3-dimensional modular reservoir simulator capable of handling fractured and non-fractured reservoirs.

The software is a modular simulator which means is unitised into modules which contain several models which calculate several reservoir properties. For each module, a number of variables are present in files which are referred to as "Include Files". Each of these include

files‘ contains input which is complete for a certain module and they can be directly used in the input decks. Example of modules and what they simulate are:

Geometry which can generate rectangular, top-map and radial geometries.

Porosity which simulates uniform porosity over the entire reservoir

PVT (Pressure, Volume, Temperature) which simulates PVT data for standard black oil, volatile oil, gas/water reservoir, single phase gas reservoir etc..

Relative permeabilities which simulate oil, water and gas relative permeabilities for five different reservoir fluid combinations.

And so many others which require more space to cover them. Additional MoReS capabilities and features are given in Appendix A-2.

Major MoReS results are hydrocarbon production rate predictions, gross (oil and water) rate prediction, reservoir pressure distribution, cumulative gross volume prediction and water cut forecast.

Although MoReS is designed for a wide range of simulation applications which vary from simple black oil simulations to specialised applications, like all other industrial or commercial reservoir simulators, it does not facilitate solid particles analysis (116).

It is a multi-purpose reservoir simulator offering a wide range of fluid descriptions, ranging from standard black oil to user-specified multi-component mixtures. The simulator can be operated in either non-fractured or fractured mode. In addition, the simulator can handle tracers, polymers and chemical reactions for various specialist applications (e.g. reservoir souring, environmental modelling, etc.) (117).

The simulator is embedded in the Reservoir Engineering powerful command language software platform –Front-End" for interactive pre- and post-processing.

The command language software –Front-End" strengths (117) are summarised as follows:

A comprehensive and programmable input language which is used to send data to the reservoir simulator and to control its actions.

Provides the reservoir simulator user with context-sensitive help in preparing input and viewing output.

Capabilities to save all reservoir data of several fields and wells on a –run file" and can restart simulations from that file in different modes desired by the user.

It can run in both interactive and batch operating modes interchangeable without changes in input data.

It has various facilities to make colour fill plots of arrays, surface network plots, line plots of tables etc.. through PostScript printers.

Graphical user interface based on latest industry-standard user interface.

Multiple MoReS runs can be made, coupled in an integrated field model, or for multi-scenario modelling, using –Math" (116). It is coupled to the geological modelling 3D package –GEOCAP" via the –Reduce" package. MoReS PVT (Pressure, Volume, Temperature) data may be prepared using the –Libra" package (117). Figure 5.26 shows how a static geological model (MONARCH) is embedded and transformed into a dynamic full field model in MoReS (118).

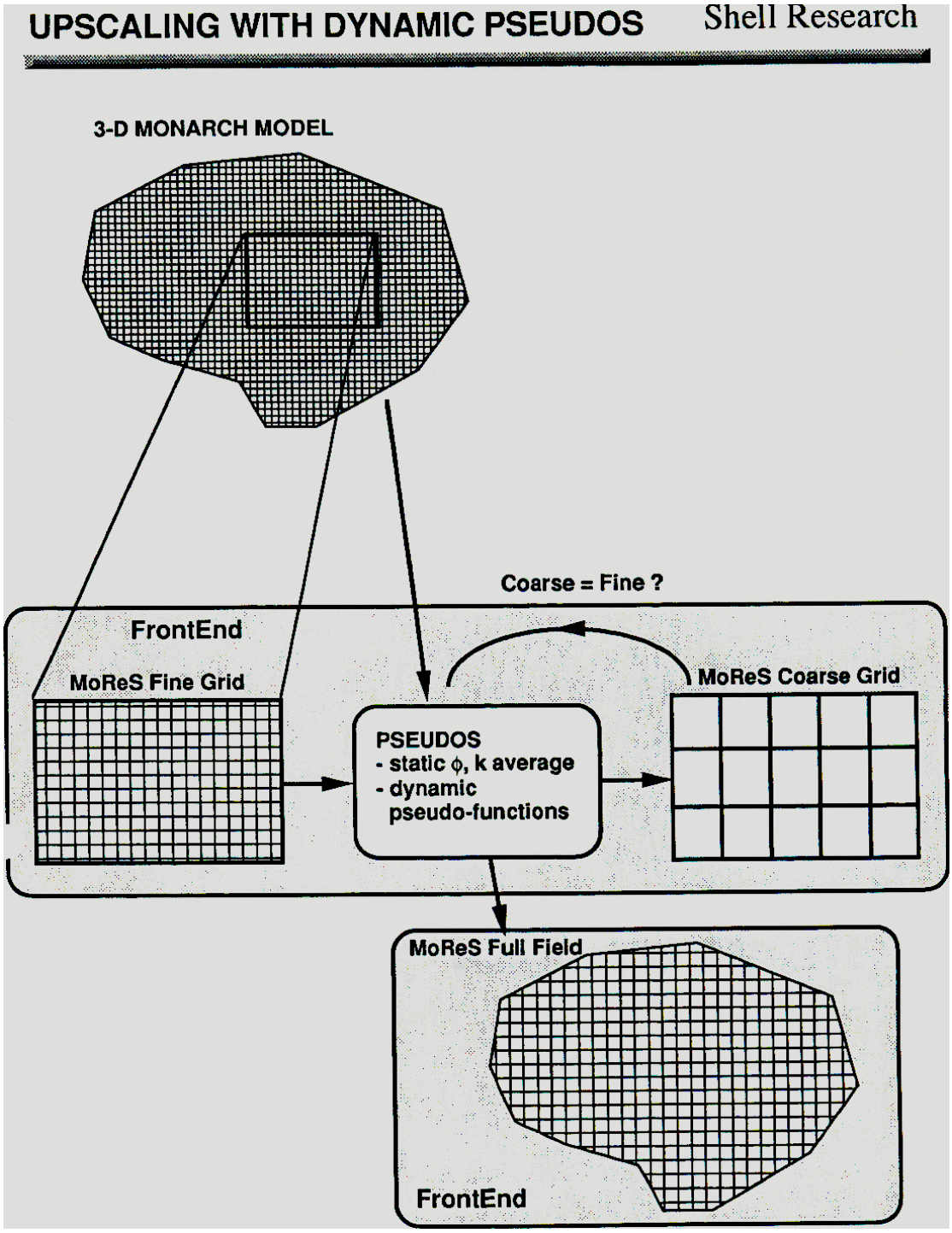

Figure 5.26: How a static geological (permeability) model can be imported into MoReS (117)

The geological subroutine is highlighted since all major reservoir simulators (Stars, CMG, Eclipse, MoReS, etc.) perform simulation using similar strategies where geological data (or a

group of data) containing permeability descriptions is treated as an –include" file to the main simulation code. Additional description of MoReS are given in (118, 119, 120).

In checking the robustness of the developed simulation methodology, effects of reservoir inclination or dipping, skin factors at various grain sizes and fines particles concentrations were all tested and revealed results similar to those observed in the field practice. The model's robustness check was necessary to ensure that outcomes are consistent with observed field results. Parameters considered are listed below and the outputs are given in table 5.3.

Ranges analysed for each reservoir property are as follows:

Porosity range from 25% to 45% which covers all the possibilities.

Reservoir dipping/inclination angles from -89° to +30° which goes beyond the normal cases as the range exceeds the typical anticline structures.

Reservoir pressure range between 4000 psi and 7000 psi, which covers most of the sandstone field pressures.

Skin damage range covering typical variation in many fields.

All the ranges listed were used. Table 5.3 shows reservoir simulator's (MoReS) results which are 1. Cumulative oil production prediction 2. Cumulative water production prediction, 3. Average water cut % prediction and 4. Cumulative gross (oil and water) production prediction. All those were carried out at various sensitivities of porosity, reservoir inclination (dipping), reservoir pressure and skin damage indices.

Table 5.3: Results of the Scenarios Simulated

		Porosity Sensitivities							
Porosity (%)	**5**	**10**	**20**	**25**	**30**	**35**	**40**	**45**	
Cum oil (million bbls)	**0.72**	**1.41**	**2.72**	**3.33**	**3.93**	**4.53**	**5.1**	**5.64**	
Cum water (million bbls)	**13.9**	**14.5**	**12.5**	**11.4**	**10.4**	**9.44**	**8.58**	**7.78**	
Avg % water cut	**95**	**90**	**78**	**71**	**62**	**52**	**41**	**27**	
Cum gross (million bbls)	**14.62**	**15.91**	**15.22**	**14.73**	**14.33**	**13.97**	**13.68**	**13.42**	
		Reservoir Dipping Sensitivities							
Dip angle (degs.)	**-75**	**-60**	**-45**	**-30**	**-15**	**-10**	**0**	**5**	**30**
Cum oil (million bbls)	**5.95**	**7.02**	**8.72**	**10.9**	**2.72**	**2.67**	**0**	**0**	**0**
Cum water (million bbls)	**0**	**0**	**0**	**0**	**12.5**	**14.5**	**72**	**77.2**	**102**
Avg % water cut	**0**	**0**	**0**	**0**	**78**	**82**	**100**	**100**	**100**
Cum gross (million bbls)	**5.95**	**7.02**	**8.72**	**10.9**	**15.22**	**17.17**	**72**	**77.2**	**102**
		Reservoir Pressure Sensitivities							
Res pressure(psi)	**4000**	**4500**	**5000**	**5200**	**5500**	**6000**	**6500**	**7000**	
Cum oil (million bbls)	**1.75**	**2.54**	**2.68**	**2.72**	**2.76**	**2.81**	**2.86**	**2.89**	
Cum water (million bbls)	**0**	**3.9**	**9.91**	**12.5**	**16.5**	**23.4**	**30.4**	**37.6**	
Avg % water cut	**0**	**35**	**73**	**78**	**83**	**88**	**91**	**92**	
Cum gross (million bbls)	**1.75**	**6.44**	**12.59**	**15.22**	**19.26**	**26.21**	**33.26**	**40.49**	
		Skin damage Sensitivities							
Skin	**0**	**0.5**	**1**	**2**	**3**	**4**	**5**	**6**	
Cum oil (million bbls)	**2.72**	**2.71**	**2.71**	**2.71**	**2.7**	**2.69**	**2.68**	**2.67**	
Cum water (million bbls)	**12.5**	**12.2**	**11.8**	**11.2**	**10.7**	**10.2**	**9.7**	**9.25**	
Avg % water cut	**78**	**78**	**77**	**76**	**75**	**74**	**72**	**71**	
Cum gross (million bbls)	**15.22**	**14.91**	**14.51**	**13.91**	**13.4**	**12.89**	**12.38**	**11.92**	

The testing and validation of these developed models are given in chapter 6 where the error margins are outlined.

Chapter 6

TESTING AND VALIDATION OF THE DEVELOPED PERMEABILITY MODELS

6.1 Introduction

The developed particle-damaged permeability models explained in chapter 5 were tested using non simulated data. Testing and validation procedures using field data are explained in this chapter from section 6.1.2 to 6.2.11. Ten conventional field practices using actual field well data were used to validate the developed models. As such there are ten validations of the developed models which involve standard oil field practices namely ―pressure build-up survey", ―pressure drawdown survey" and ―pressure fall-off survey". These pressure drop surveys whose theories are explained in chapter 2, are commonly used to determine reservoir permeabilities as shown in this chapter. The fact that the pressure surveys share something in common with the CFD simulation's pressure drops, the surveys are the most relevant field practices as far as the developed models validation is concerned. In each validation, the corresponding accuracy or error margins are presented with explanations. The majority of the validations revealed marginal errors.

6.1.1 Testing the Developed Liquid Permeability Model at Various Scenarios

The developed liquid permeability model presented in chapter 5 was initially analysed for error margins. Error analysis involved comparison of results of grain size sensitivities on pressure drop and the corresponding permeabilities obtained from the developed model with the results obtained from CFD simulations for the same particle size sensitivities. Table 6.1 shows outputs of both the developed damaged permeability data per grain size per reservoir lateral length and the CFD simulated damaged permeability at the same conditions. Although

table 6.1 lists permeabilities affected by particle sizes 10 μm to 200 μm as simulated, the model as stated and demonstrated in chapter 5 can be used to calculate the impact of particle sizes other than those sizes listed. The model can be used to quantify damaged permeability of any grain size up to 300 μm i.e. beyond the 10 μm to 200 μm simulated range. The limit is due to the fact that in the oil and gas industry, most sand control measures happen to manage less than 300 μm particles since the majority are less than 200 μm as explained in chapters 2 and 3.

Table 6.1: Results Comparison of Developed Permeability Model and CFD Simulations in Liquid

Res. Length	Model's Damaged Permeabilities per grain size (mD)					CFD Simulated Damaged Permeabilities per grain size (mD)				
(ft)	10 µm	50 µm	100 µm	150 µm	200 µm	10 µm	50 µm	100 µm	150 µm	200 µm
70	1054	813	672	573	499	978	928	650	988	461
94	912	708	579	489	424	861	766	558	441	389
117	802	627	509	428	370	770	657	490	345	341
141	717	563	455	381	328	696	577	438	307	306
164	649	512	412	344	296	636	517	396	285	280
187	590	470	377	314	269	586	470	362	270	260
211	545	435	347	289	248	544	432	334	259	245
234	506	405	323	268	230	508	401	310	249	232
258	481	379	302	251	214	477	375	290	241	221
281	441	357	283	235	201	449	352	272	234	213
305	416	337	267	222	189	425	333	257	228	205
328	393	319	253	210	179	403	316	243	222	199
352	374	304	241	200	170	384	301	231	217	194
375	360	290	230	190	162	367	288	221	211	189
398	346	277	220	182	155	351	276	211	206	185
422	334	266	211	174	149	337	265	202	202	182
445	323	256	202	167	143	324	255	194	197	179
469	312	246	195	161	137	312	246	187	193	176
492	302	237	188	155	132	301	238	180	188	174
516	292	229	181	150	128	291	231	174	184	171
539	282	222	175	145	124	281	224	168	180	169
562	275	215	170	141	120	273	217	163	176	167
586	270	209	165	136	116	265	211	158	173	165
609	263	203	160	133	113	257	205	154	169	163
633	254	197	156	129	110	250	199	150	166	161
656	243	192	152	126	107	243	194	146	162	159
680	237	187	148	122	104	237	189	142	159	156
703	229	182	144	119	102	231	184	139	156	154
726	224	178	141	117	99	225	180	135	153	152
750	219	174	138	114	97	220	175	132	150	149
773	215	170	135	111	95	215	171	129	147	146
797	211	166	132	109	93	211	167	127	144	144
820	207	163	129	107	91	206	163	124	141	141
844	203	160	127	105	89	202	159	121	139	137
867	198	156	124	103	88	198	156	119	136	134
891	194	154	122	101	86	194	152	117	133	131
914	188	151	120	99	85	190	149	115	131	127
937	184	148	117	97	83	187	145	113	129	124

From table 6.1, distributions of damaged permeability curves per reservoir lateral length per particle size, were plotted as shown in figure 6.1.

From the figure, it is evident that the finer the particle grain size, the more accurate the model is.

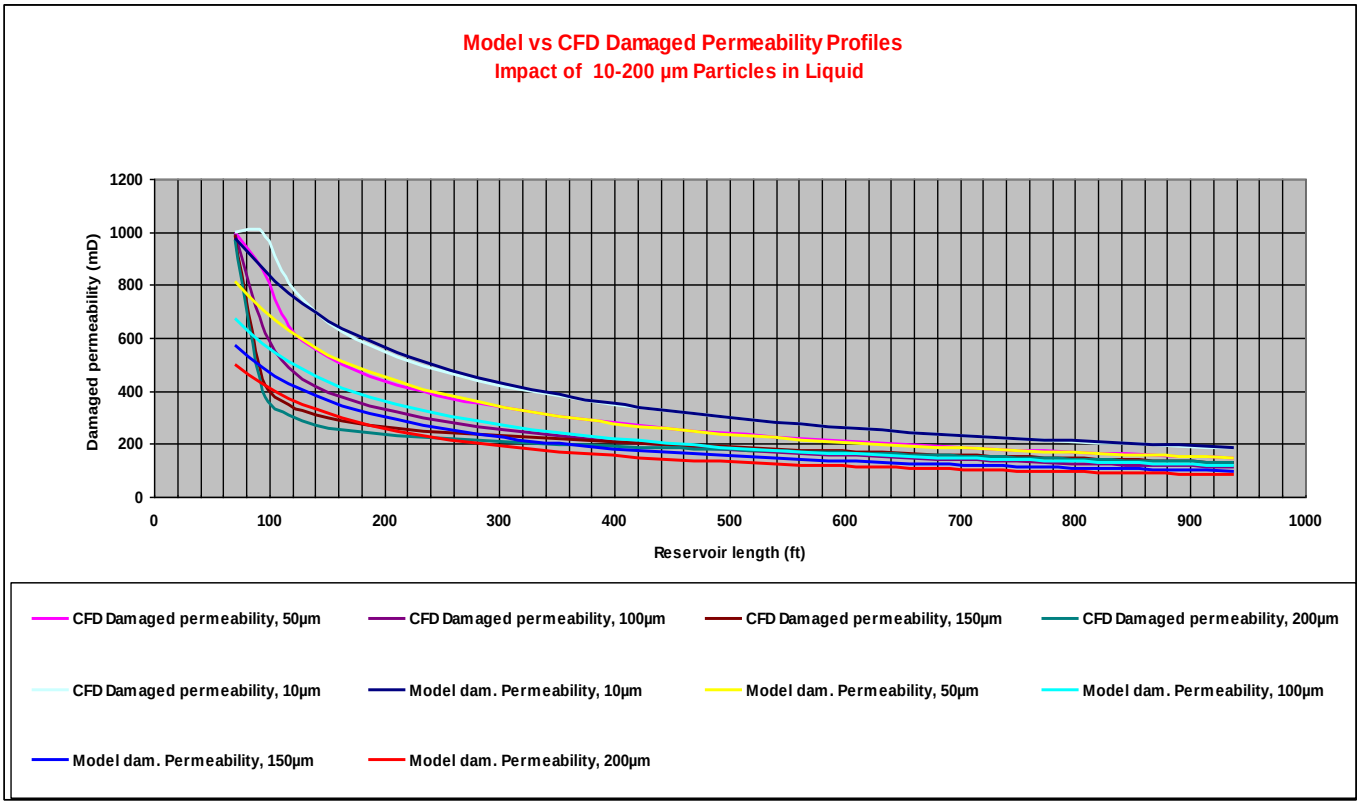

Figure 6.1: Comparison between developed model's and CFD results in the liquid medium

Table 6.2 summarises percentage errors revealed by the developed model compared to CFD simulations. The average error for the 10µm grains was only -0.4 as indicated in table 6.2. In the case of 50 µm grains, the average percentage error was just -0.7%.

The average error associated with 100 µm grains was 4.1% while for 150 µm and 200 µm particle sizes the average error percentages revealed were -11.1% and -19.1% respectively.

Table 6.2: Error % when the Developed Liquid Model was Compared with CFD Simulation results

Reservoir Length	10 µm	50 µm	100 µm	150 µm	200 µm
(ft)	% Error	% Error	% Error	% Error	% Error
70	-7.8	-12.4	3.5	40.4	8.2
94	-5.9	-7.7	3.6	28.5	8.9
117	-4.2	-4.5	3.8	20.1	8.4
141	-3	-2.4	3.9	13.8	7.1
164	-2.1	-1.0	3.9	8.9	5.4
187	-0.7	-0.1	4.0	5.0	3.4
211	-0.1	0.5	4.0	1.8	1.3
234	0.3	0.9	4.1	-1.0	-0.9
258	-0.9	1.1	4.1	-3.3	-3.2
281	1.7	1.2	4.1	-5.3	-5.5
305	2.1	1.2	4.1	-7.0	-7.8
328	2.4	1.1	4.1	-8.6	-10.0
352	2.6	0.9	4.1	-10.0	-12.2
375	1.9	0.7	4.2	-11.3	-14.3
398	1.5	0.5	4.2	-12.4	-16.4
422	0.9	0.3	4.2	-13.5	-18.3
445	0.2	0.1	4.2	-14.4	-20.2
469	0.1	-0.2	4.2	-15.3	-22.0
492	-0.2	-0.4	4.2	-16.2	-23.7
516	-0.2	-0.6	4.2	-16.9	-25.3
539	-0.4	-0.7	4.2	-17.7	-26.8
562	-0.9	-0.9	4.2	-18.4	-28.2
586	-1.7	-1.0	4.2	-19.0	-29.4
609	-2.2	-1.1	4.2	-19.7	-30.6
633	-1.5	-1.1	4.2	-20.3	-31.6
656	-0.2	-1.2	4.2	-20.9	-32.5
680	0.1	-1.2	4.2	-21.4	-33.3
703	0.9	-1.1	4.2	-21.9	-33.9
726	0.6	-1.0	4.2	-22.5	-34.4
750	0.3	-0.9	4.2	-23.0	-34.8
773	0.1	-0.7	4.2	-23.4	-35.1
797	-0.2	-0.5	4.2	-23.9	-35.2
820	-0.4	-0.2	4.2	-24.4	-35.1
844	-0.3	0.1	4.1	-24.8	-34.9
867	-0.1	0.4	4.1	-25.2	-34.6
891	0.1	0.9	4.1	-25.7	-34.1
914	0.9	1.3	4.1	-26.1	-33.5
937	1.4	1.8	4.1	-26.5	-32.7
Average error%	-0.4	-0.7	4.1	-11.1	-19.1

Similar comparison and error analyses were carried out for the multiphase scenario as explained in section 6.1.2.

6.1.2: Testing the Damaged Permeability Multiphase Model at Various Scenarios

The second developed particle-damaged model (equation 5.18) results were analysed and compared with CFD simulations results under multiphase conditions where impact of each grain size (10 - 200 μm) on absolute permeability of 1000 mD was simulated.

Table 6.3 summarizes both outputs, of the developed model and of the simulations.

From the table, the finer the grain size the more closely the results were to the CFD simulated results.

Data from table 6.3 were used to graphically show the comparison of the two approaches as a justification of the developed model since the difference is quite minimal especially in the finer grained particles. Unlike in the liquid scenario, in the multiphase scenario, the 10 μm fines impact on permeability calculated by the model was more compared to the CFD simulated impact as in table 6.3.

Table 6.3: Comparison of Multiphase Model and Simulated Damaged Permeability Results

Res. Length	Model's Damaged Permeabilities per grain size (mD)					Simulated Damaged Permeabilities per grain size (mD)				
(ft)	10 µm	50 µm	100 µm	150 µm	200 µm	10 µm	50 µm	100 µm	150 µm	200 µm
70	1067	779	643	547	477	937	923	621	429	462
94	932	688	562	476	412	837	762	542	399	392
117	802	616	500	421	364	756	655	482	373	344
141	712	559	452	379	326	691	578	435	350	310
164	645	512	412	345	296	636	520	397	330	284
187	596	473	379	317	272	590	475	365	312	264
211	553	440	352	293	252	550	439	339	296	248
234	517	412	329	274	234	516	410	316	282	235
258	483	388	309	257	220	487	385	297	270	224
281	458	366	291	242	207	461	365	280	259	215
305	434	347	276	229	196	437	347	265	248	207
328	421	331	263	218	186	417	332	252	239	201
352	402	316	251	208	177	398	318	241	231	195
375	388	302	240	199	170	382	306	230	223	190
398	378	290	230	191	163	366	296	221	216	186
422	366	279	221	183	156	353	287	212	209	182
445	355	269	213	177	151	340	279	205	203	178
469	348	260	206	170	145	328	271	198	198	175
492	340	251	199	165	141	318	264	191	192	172
516	330	243	193	160	136	308	258	185	188	169
539	321	236	187	155	132	299	252	180	183	167
562	313	229	182	151	129	290	247	175	179	164
586	307	223	177	147	125	282	242	170	175	162
609	300	217	172	143	122	275	238	165	171	159
633	294	212	168	139	119	268	234	161	168	156
656	287	207	164	136	116	261	230	158	165	154
680	281	202	160	133	114	255	226	154	162	151
703	276	198	157	130	111	249	223	151	159	148
726	271	193	154	127	109	244	219	148	156	145
750	267	189	151	125	107	239	216	145	154	142
773	262	186	148	123	105	234	213	142	151	139
797	258	182	145	120	103	229	210	139	149	136
820	254	179	142	118	101	225	208	137	147	133
844	250	176	140	116	99	221	205	134	145	129
867	247	173	138	114	98	217	202	132	143	126
891	243	170	135	113	96	213	200	130	141	122
914	241	167	133	111	95	210	197	128	140	119
937	237	165	131	109	94	206	194	126	138	115

Impacts of the grain sizes on permeability are graphically displayed in figure 6.2, as far as multiphase scenario is concerned. The comparison became clearer after error percentages were calculated as shown in table 6.4.

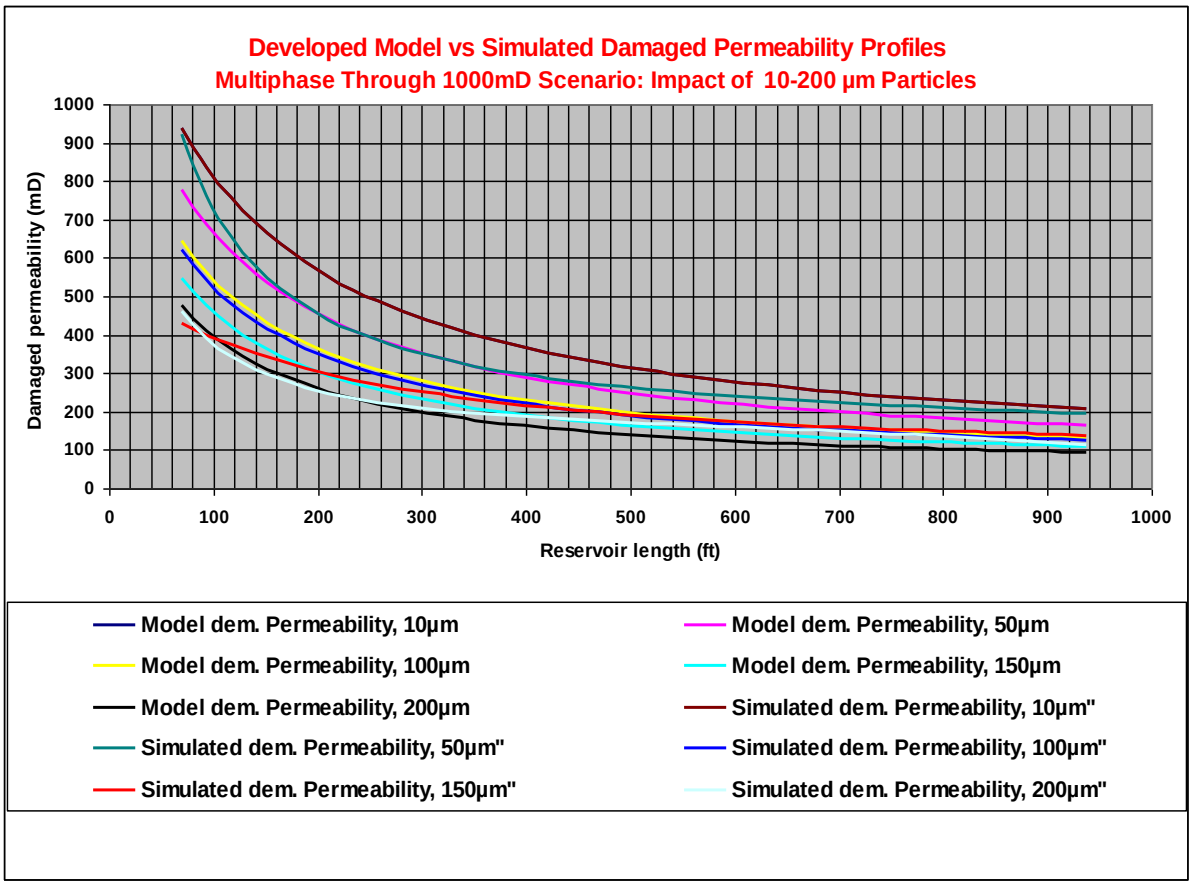

Figure 6.2: Comparison of developed model results and CFD results in multiphase medium

Table 6.4 provides error margins or percentage errors when the developed model results were compared to the CFD simulation results in the multiphase scenario.

Table 6.4: Error % When the Developed Multiphase Model was Compared with the CFD Simulation

Reservoir Length (ft)	10 µm % Error	50 µm % Error	100 µm % Error	150 µm % Error	200 µm % Error
70	-13.9	-15.6	3.5	27.7	3.2
94	-11.3	-9.8	3.6	19.1	5.2
117	-6.1	-5.9	3.8	12.8	5.7
141	-3.1	-3.3	3.8	8.1	5.3
164	-1.4	-1.6	3.9	4.4	4.4
187	-1.1	-0.4	4.0	1.4	3.1
211	-0.5	0.2	4.0	-1.0	1.6
234	-0.1	0.5	4.0	-3.1	-0.1
258	0.9	0.6	4.1	-4.9	-1.9
281	0.6	0.4	4.1	-6.4	-3.7
305	0.7	0.1	4.1	-7.7	-5.5
328	-0.9	-0.3	4.1	-8.9	-7.3
352	-1.1	-0.8	4.1	-9.9	-9.1
375	-1.7	-1.4	4.1	-10.8	-10.8
398	-3.2	-2.1	4.1	-11.7	-12.5
422	-3.6	-2.8	4.1	-12.4	-14.1
445	-4.5	-3.5	4.1	-13.1	-15.6
469	-6.2	-4.2	4.1	-13.8	-17.0
492	-6.9	-4.9	4.1	-14.4	-18.3
516	-7.1	-5.7	4.1	-14.9	-19.6
539	-7.3	-6.4	4.1	-15.4	-20.7
562	-8.1	-7.2	4.1	-15.9	-21.7
586	-8.9	-7.9	4.1	-16.3	-22.6
609	-9.2	-8.6	4.1	-16.7	-23.4
633	-9.6	-9.3	4.1	-17.1	-24.0
656	-10.1	-10.0	4.1	-17.5	-24.5
680	-10.3	-10.6	4.1	-17.8	-24.9
703	-10.7	-11.3	4.1	-18.2	-25.1
726	-10.2	-11.8	4.1	-18.5	-25.2
750	-10.9	-12.4	4.1	-18.8	-25.1
773	-11.1	-12.9	4.1	-19.1	-24.9
797	-11.5	-13.4	4.1	-19.4	-24.5
820	-11.9	-13.8	4.1	-19.6	-23.9
844	-12.3	-14.2	4.1	-19.9	-23.2
867	-11.7	-14.6	4.1	-20.1	-22.3
891	-12.1	-14.9	4.1	-20.4	-21.3
914	-12.6	-15.1	4.1	-20.6	-20.0
937	-12.9	-15.4	4.0	-20.8	-18.6
Average error%	-6.9	-7.1	4.1	-10.3	-13.7

Based on the acceptable accuracy of the developed models as shown in tables 6.2 and 6.4, model validations were carried out using field data as explained in sections 6.2. to 6.2.11. Theories of field practices used in the model‘s validation were introduced in chapter 2 sections 2.11 to 2.11.3

6.2 First Validation Using Field’s Liquid Build-Up Pressure Survey

The following is a well test data from Shell‘s oil producing well No.16 in the Netherlands whose build-up pressure survey is given in table 6.5 as analysed by Shell‘s reservoir engineers. The same drawdown pressures were used to back-calculate the permeability using the developed model since reservoir fluids and rock properties were similar to one of the sensitivities among the hundreds of sensitivities in the CFD simulations. The particle size in that well ranged between 100 and 120 μm on average.

Table 6.5 and the other similar ones shown in the next seven sections are explained as follows:

The first column from left contains ―well closed-in” time intervals during which shut-in well pressures (pws) were measured as reported in column 4. Column 6 contains specific average reservoir properties and production related data from the same well. The black bar separates the pressure-time survey data from average well data. Column 2 and 3 are calculated values whereas columns 5 and 7 respectively refer to data symbols and units of column 6 values. The same table layout is used in the field analyses.

Table 6.5: Build-up pressure-time survey data used in field practices

Closed-in time Δt (hrs)	$\frac{t+\Delta t}{\Delta t}$	$\text{Log}\left(\frac{t+\Delta t}{\Delta t}\right)$	pws (psi)	parameter	value	unit
0			4506			
0.5	196	2.29	4675	**q**	123	stb/d
0.7	149	2.17	4705	**t**	97.6	hrs
1.0	99	1.99	4733	**h**	20	ft
1.5	66	1.82	4750	**μ**	1	cp
2.0	50	1.70	4757	**Boi**	1.22	rb/stb
2.5	40	1.60	4761	**rw**	0.3	ft
3.0	34	1.53	4763	**m**	25	psi/log cycle
4.0	25	1.40	4766			
6.0	17	1.24	4770			
8.0	13	1.12	4773			
10.0	11	1.03	4775			
12.0	9	0.96	4777			

Data from table 6.5 were used to carry out conventional field pressure build up analysis such as the one shown in figure 6.5. In the table, ‗t' is total production time in hours. The figure shows a graph of shut-in well pressure (pws) vs $\log\left(\frac{t+\Delta t}{\Delta t}\right)$. Prior to the well shut-in, the well was producing at a constant rate of 123 b/d for a cumulative production (Np) of 500 stb. Hence total production time t was:

t = (Np/q) (24hr/day) ----------(6.1)

= (500 / 123)(24) = 97.6 hrs.

Traditionally analysis of pressure build-up surveys such as the one shown in figure 6.3 involved determination of slope of extrapolated curve from the graph in which the x-axis values increase from left to right. However, in either direction the same results are obtained. From the survey analysis, the absolute permeability *k* in mD was calculated using the conventional pressure build-up equation 6.2 (121). The curve's slope ‗m' was determined as

shown in figure 6.3 and was found to be 25 psi/log cycle. From that k was calculated as follows:

$$k = \left[\frac{162.6(q)(\mu)(Boi)}{m(h)}\right]. \text{----------(6.2)}$$

$$= \left[\frac{162.6(123)(1)(1.22)}{25(20)}\right] = 49mD.$$

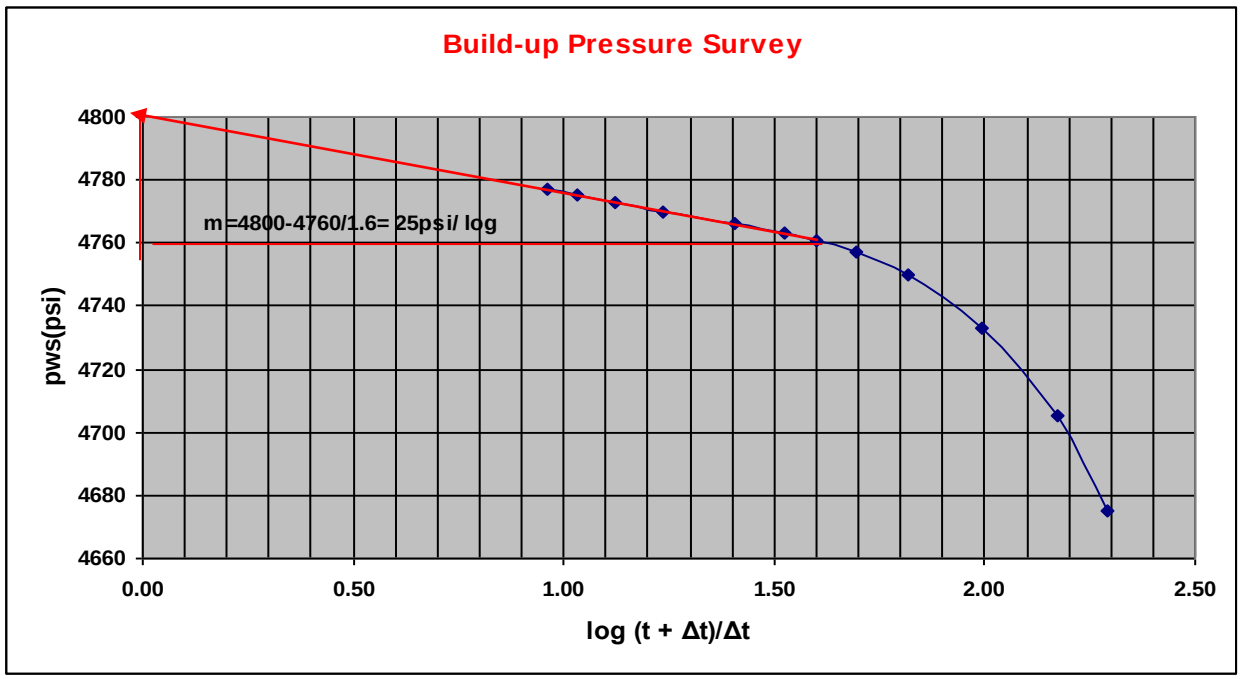

Figure 6.3: Pressure build-up test analysis

The developed model for a liquid scenario was then used to generate absolute permeability values in this single phase oil well using the developed model equation as follows:

$$\sum_{i=1}^{n} k_{di}(G_F, \chi_i) \approx \sum_{i=1}^{n} \left\{\frac{C(\ln(\chi_i))}{\Delta P(G_F, \chi_i)}\right\} \text{.....(6.3)}$$

When well data from table 6.5 were substituted into the model, a corresponding damaged permeability profile per drainage length ‗i' was calculated as follows:

$$k_{di} = \frac{\frac{141.2(q)(\mu)(B)}{h}\left[\left((S-0.75)-\ln(r_w)\right)+\left\{\ln(r_{ei})\right\}\right]}{\left\{Pws - Pwf_{\Delta t=0}\right\}} \quad \text{.....(6.4)}$$

As an example, at a shut-in pressure of 4675 psi,

$$k_{di} = \frac{(((141.2)*123*1.22)/20)*((5.25-\text{LN}(0.3))+(\text{LN}(((123/24)*(0.5+97.6)*0.159)\text{^}(1/3)*3.28084)))}{\{4675-4506\}}$$

= 57.06 mD.

The skin factor as determined from the survey was 6 (dimensionless). Skin factor is a measure of how much damaged the reservoir is. Impact of formation damage on well productivity depends on two key factors: magnitude of near-wellbore permeability reduction and depth of damage zone. These two combined factors form the near-wellbore skin factor. The reservoir damage extent is proportional to the skin factor value. From 0.5 to 3 the damage is considered not significant whereas more than 5, will require the well to be cleaned or ~~"tr~~eated" using hydrochloric and hydrofluoric acids depending on well's to reservoir properties. A skin factor of 0 or negative value means the reservoir is undamaged or has a natural fracture through which fluid flow occurs, hence does not require ~~"tr~~eatment" .

Table 6.6 shows results of the developed model in terms of particle-damaged permeabilities using same field pressure data.

Table 6.6: Developed Model's Damaged Permeabilities Using Pressure Data from Table 6.5

Permeability (mD)	Depth (ft)	Pws (psi)	Δp (psi)
57.06	141	4675	169
48.46	141	4705	199
42.49	142	4733	227
39.54	142	4750	244
38.44	142	4757	251
37.85	142	4761	255
37.56	143	4763	257
37.14	143	4766	260
36.60	144	4770	264
36.22	145	4773	267
35.97	146	4775	269
35.73	147	4777	271

Figure 6.4 is a graph of the developed particle-damaged permeability model results shown in table 6.6. The graph also shows the survey's single permeability (49 mD) on the model generated curve. It is important to note that the field's pressure survey approach involved a semi-log graphical method whereas the model does not require graphical analysis and yet provides similar results around the wellbore and additional results deeper into the reservoir. Furthermore, the model resulted in a continuous distribution of permeabilities across the entire drainage area. The survey result (49 mD) is very close to the average of the first four model permeability results (47 mD) in table 6.6. In this case, the difference is about 4% only. However, if the average of all of the model results is taken, the difference between the model and the survey is 17.5% taking into consideration that all the same data used in the field survey were applied in the model. As this research aims at detailed mapping of corresponding impairment profiles, all permeability values were graphically presented as functions of operating conditions in terms of build-up pressures. Similar results were

observed when other field‘s well tests data were compared to the model‘s results as explained in section 6.2.1.

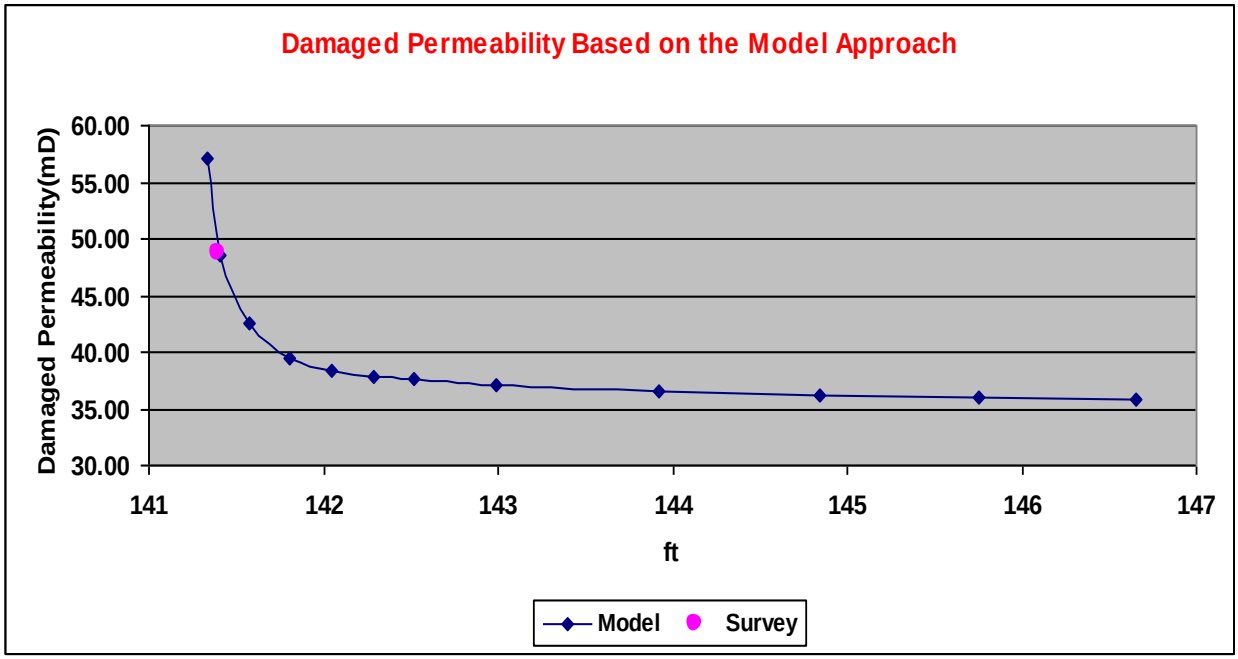

Figure 6.4: Model’s permeability profile based on all pressure build-up data vs. survey result

6.2.1 Second Validation Using Field Build-up Pressure Survey

A second model validation was carried out using data obtained from Shell‘s exploration (oil producing) well No. 1 located in Center field Texas, USA; whose build up survey data are presented in table 6.7.

Table 6.7: Build-up pressure-time survey data used in field practice

Closed-in time Δt (hrs)	t + Δt / Δt	$\mathrm{Log}\left(\frac{t+\Delta t}{\Delta t}\right)$	pws (psi)	parameter	value	unit
				q=	250	stb/d
0.00			3534.00	t =	13633	hrs
2.14	6363.05	3.80	3700.00	h=	69	ft
4.11	3320.33	3.52	3780.00	μ=	0.8	cp
5.00	2727.59	3.44	3900.00	Boi=	1.136	rb/stb
6.25	2182.27	3.34	3980.00	rw=	0.198	ft
6.79	2010.07	3.30	4140.00	m=	60	psi/log cycle
7.50	1818.73	3.26	4280.00			
8.21	1660.66	3.22	4350.00			
8.39	1625.35	3.21	4355.00			
8.75	1559.05	3.19	4360.00			
11.54	1182.52	3.07	4360.50			
19.23	709.91	2.85	4370.00			
33.08	413.16	2.62	4375.00			
39.23	348.51	2.54	4383.00			
43.85	311.93	2.49	4385.00			
51.54	265.52	2.42	4400.00			
54.62	250.62	2.40	4400.50			
65.38	209.50	2.32	4401.00			
71.54	191.57	2.28	4402.00			
79.23	173.07	2.24	4403.00			
86.92	157.84	2.20	4403.00			
93.08	147.47	2.17	4404.00			

Data from table 6.7 was used to construct a conventional field practice pressure build-up survey analysis graph shown in figure 6.5. From the survey analysis results, ‗m' was 60 psi/log cycle from which the calculated skin factor was 6.37.

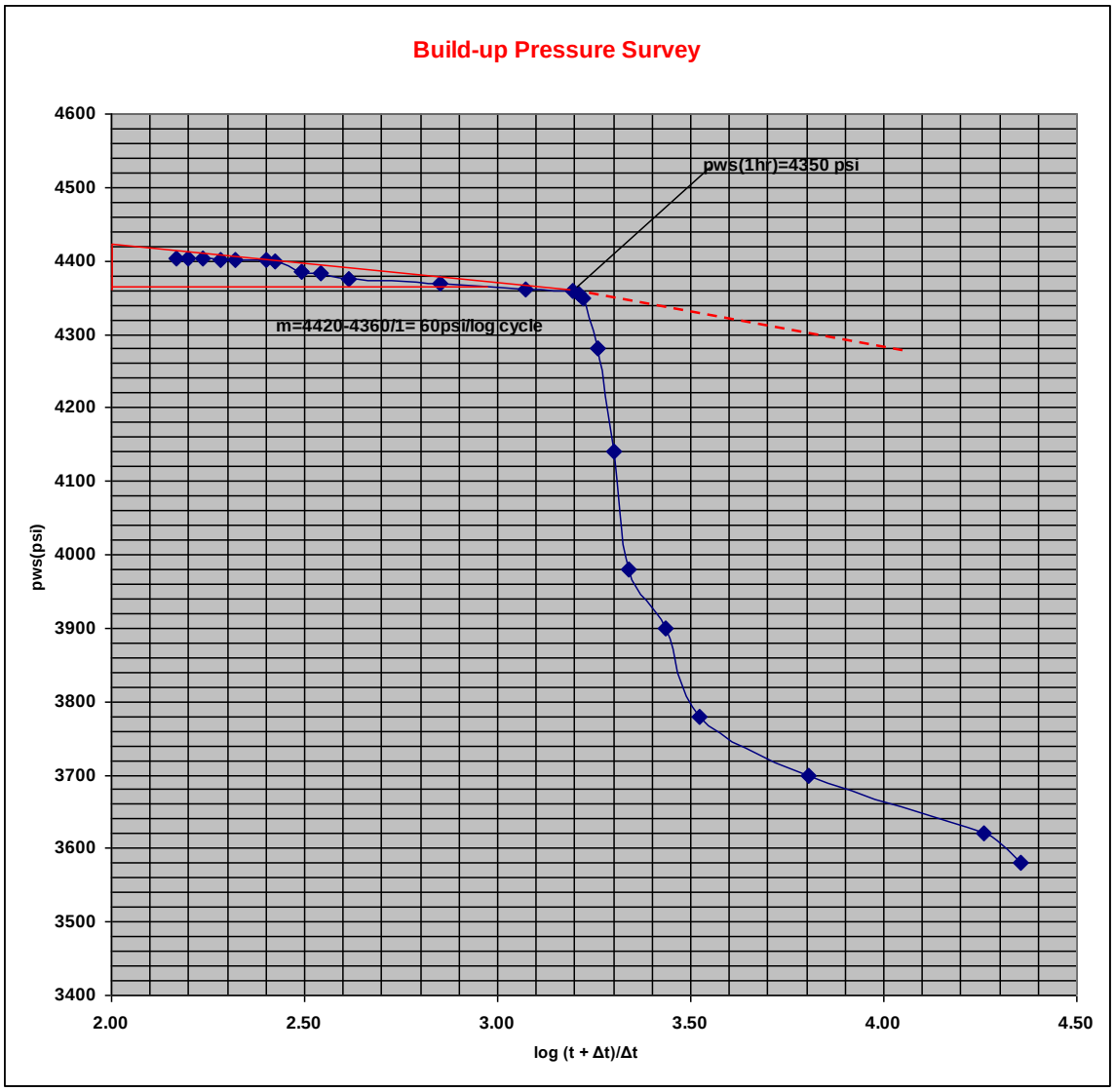

Figure 6.5: Pressure build-up survey analysis using field practices

Applying equation 6.2, for a single phase liquid, the effective permeability calculated was 8.92 mD. This permeability result from the build-up survey analysis was compared with the results obtained from the developed model as follows:

Using the developed model, the same procedures explained in section 6.2.3 were repeated to determine the damaged permeability profile by substituting pressure build-up survey data in table 6.7 into the model.

For example, for pws = 3900 psi pressure build-up corresponding to a shut-in time of **Δt =** 2.14hrs, using the developed model, the resultant damaged permeability was calculated as follows:

$$k_{di} = \frac{(((141.2)*250*0.8*1.136)/69)*((5.62-\ln(0.19791667))+(\ln(((250/24)*(2.14+13633)*0.159)\text{^}(1/3)*3.28084)))}{\{3900-3534\}}$$

$$= 14.95\ mD$$

Thereafter, for each shut-in well pressure (pws) in table 6.7, a corresponding damaged permeability was calculated whose results are shown in table 6.8. The average model permeability in the table, was 9.3 mD. Comparing that with the pressure build-up survey analysis (8.9 mD), only a 4.3% difference was observed.

Table 6.8: Model Damaged Permeabilities Based on Build-up Survey Data

Permeability (mD)	Depth (ft)	pws (psi)	Δp (psi)
14.95	10.00	3900.00	366.00
12.27	20.00	3980.00	446.00
9.03	30.00	4140.00	606.00
7.34	40.00	4280.00	746.00
6.71	50.00	4350.00	816.00
6.67	60.00	4355.00	821.00
6.62	70.00	4360.00	826.00
6.62	80.00	4360.50	826.50
6.55	90.00	4370.00	836.00
6.51	100.00	4375.00	841.00
6.45	110.00	4383.00	849.00
6.43	120.00	4385.00	851.00
6.32	130.00	4400.00	866.00
6.32	140.00	4400.50	866.50
6.31	150.00	4401.00	867.00
6.31	160.00	4402.00	868.00
6.30	170.00	4403.00	869.00
6.30	180.00	4403.00	869.00
6.29	190.00	4404.00	870.00

Table 6.8 and figure 6.6 show the model permeability distributions across a drainage length. The figure also displays the single damaged permeability obtained from the pressure build-up survey.

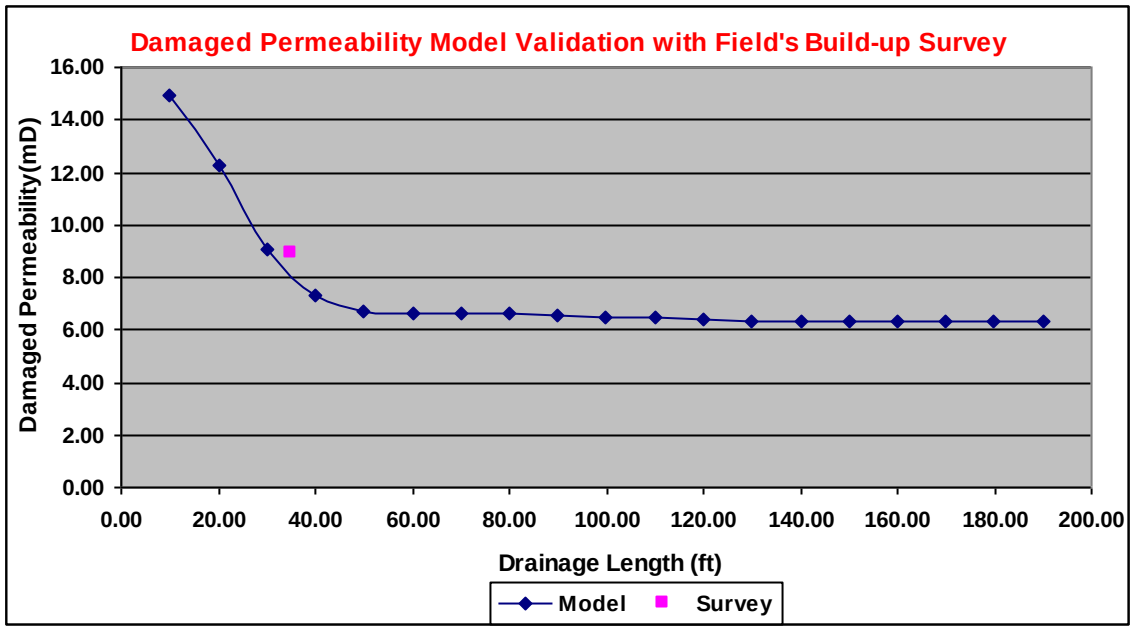

Figure 6.6: Model's permeability profile based on pressure build-up data

6.2.2 Third Validation Using Field Build-up Pressure Survey

Continuing to validate the model with field data, Petrogas well No. 9 from the Central Oman field whose pressure build-up survey is presented in table 6.9 was used.

Table 6.9: Build-up pressure-time survey data used in field practices

Closed-in time Δt (hrs)	$\frac{t+\Delta t}{\Delta t}$	$\text{Log}\left(\frac{t+\Delta t}{\Delta t}\right)$	pws (psi)	parameter	value	unit
				q=	400	stb/d
0	---	---	1889	t =	4464.0	hrs
0.5	8929.00	3.95	2683	h=	20	ft
1	4465.00	3.65	2713	μ=	1	cp
1.5	2977.00	3.47	2743	Boi=	1.23	rb/stb
2	2233.00	3.35	2752	m	80.00	psi/log cycle
2.5	1786.60	3.25	2760	rw=	0.3ft	
3	1489.00	3.17	2766			
3.5	1276.43	3.11	2771			
4	1117.00	3.05	2777			
4.5	993.00	3.00	2779			
5	893.80	2.95	2783			
6	745.00	2.87	2790			
7.5	596.20	2.78	2795			
10	447.40	2.65	2804			
12	373.00	2.57	2809			
14	319.86	2.50	2813			
16	280.00	2.45	2817			
20	224.20	2.35	2823			
25	179.56	2.25	2833			
30	149.80	2.18	2840			
36	125.00	2.10	2844			

Data in table 6.9 was used to graphically analyse the survey as shown in figure 6.7. The calculated slope (m) of the plot was 80 psi/log cycle.

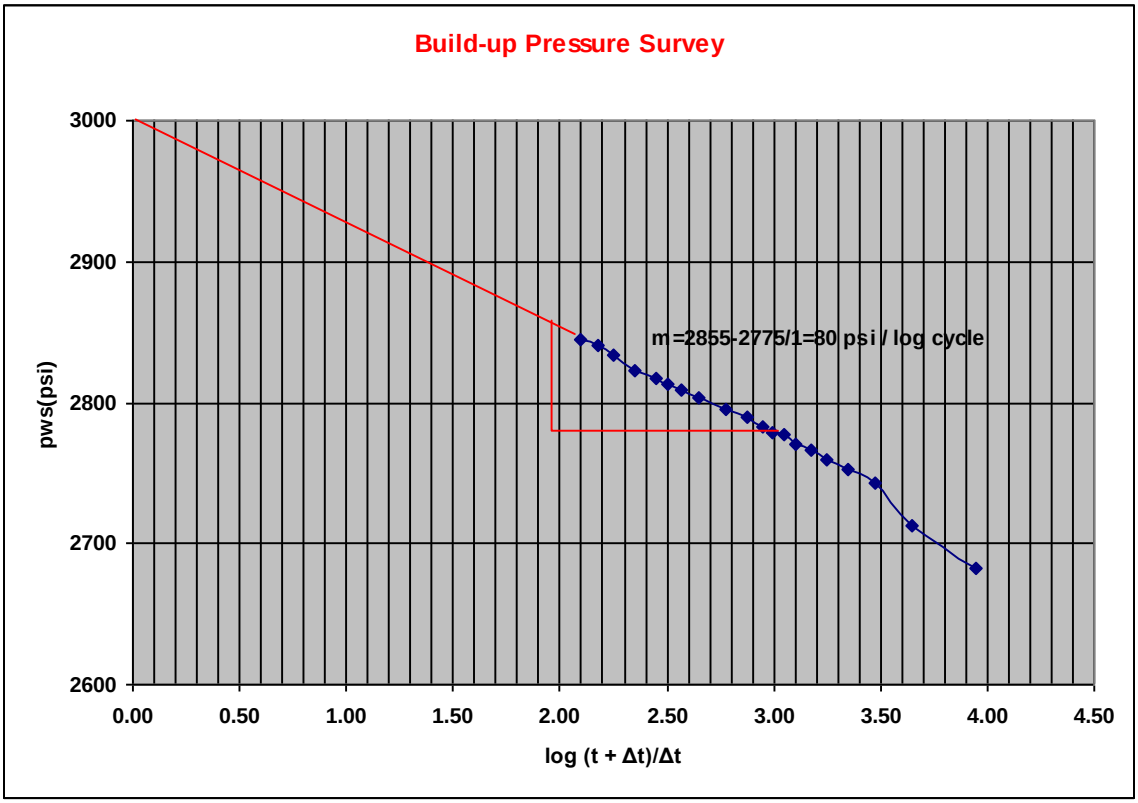

Figure 6.7: Conventional pressure build-up survey field practice analysis

Using equation 6.2, the corresponding permeability was calculated as follows:

$$k = \left[\frac{162.6(400)(1)(1.23)}{(80)(20)}\right] = 50\, mD$$

Using the developed model approach, for each measured pressure build-up, and shut-in time, the corresponding damaged permeability was calculated as follows:

For pws = 2683 psi, at Δt = 0.5hr, the corresponding damaged permeability k_{di} was:

$$k_{di} = \frac{(((141.2)*400*1*1.23)/20)*((5.65-\ln(0.3))+(\ln(((400/24)*(0.5+4464)*0.159)\text{^}(1/3)*3.28084)))}{\{2683-1889\}}$$

$= 48.9\ mD.$

Table 6.10 summarises the model's results of all damaged permeabilities calculated from each measured pressure and time during the pressure build-up period. Average permeability

value as in table 6.10, was 43.4mD vs. 50mD from the survey analysis. Hence an error percentage of only 13% resulted. However the model covered the entire drainage area while these types of survey always provide single values only.

Table 6.10: Model's Damaged Permeabilities Based on Build-up Survey Data

Permeability (mD)	depth (ft)	pws (psi)	Δp (psi)
---	---		
48.9	10	2683	794
47.1	20	2713	824
45.4	30	2743	854
45.0	40	2752	863
44.5	50	2760	871
44.2	60	2766	877
44.0	70	2771	882
43.7	80	2777	888
43.6	90	2779	890
43.4	100	2783	894
43.1	110	2790	901
42.8	120	2795	906
42.4	130	2804	915
42.2	140	2809	920
42.0	150	2813	924
41.8	160	2817	928
41.5	170	2823	934
41.1	180	2833	944
40.8	190	2840	951
40.6	200	2844	955

Figure 6.8 depicts the model permeability profile graphically. The figure also shows the single permeability value obtained from the pressure build-up survey.

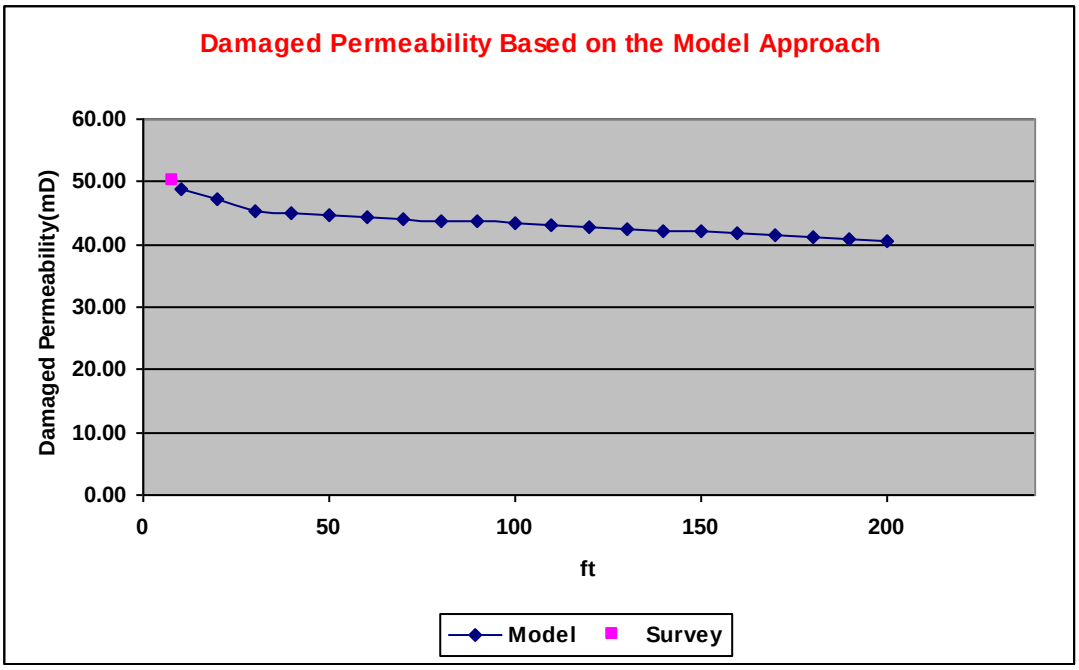

Figure 6.8: Model's permeability profile based on pressure build-up data

6.2.3 Fourth Validation Using Field Drawdown Pressure Survey

This time a different field practice was used to validate the model. The model validation was performed using pressure drawdown test data from a PDO well, Sadad-3 (located in the South Oman field). Well data are given in table 6.11.

Table 6.11: Drawdown pressure-time survey data used in field practices

Time (hrs) (Δt)	Pwf (psi)	log time (Δt)	parameter	value	unit
0	4000				
0.1	3641	-1.00	**q**	500	stb/d
0.25	3559	-0.60	**t**	27800.	hrs.
0.5	3498	-0.30	**h**	10	ft
1	3438	0.00	**μ**	1	cp
2	3377	0.30	**Boi**	1.25	rb/stb
5	3295	0.70	**m_1**	205	psi/log cycle
7	3265	0.85	**m_2**	2.25	psi/hr
10	3234	1.00			
15	3198	1.18			
20	3169	1.30			
25	3149	1.40			
30	3133	1.48			
35	3118	1.54			
40	3105	1.60			
45	3092	1.65			
50	3080	1.70			
60	3055	1.78			
70	3032	1.85			
80	3008	1.90			
90	2986	1.95			
100	2963	2.00			

This being a production pressure survey, the approaches are different from the pressure build-up approach, and are reflected in figures 6.9 and 6.10.

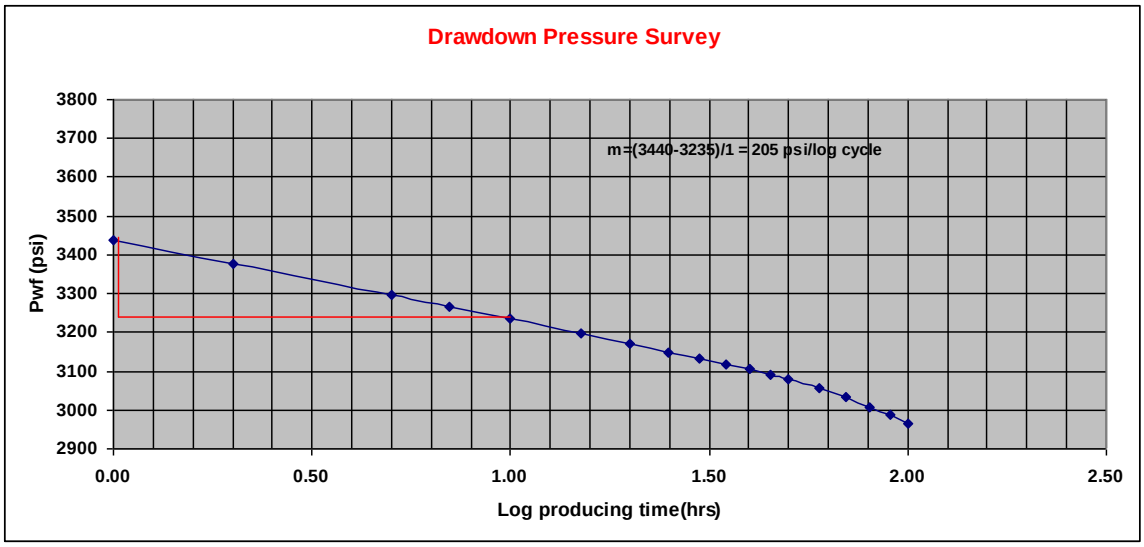

Figure 6.9: Conventional drawdown analysis using logarithm of production time

Figure 6.9 which is a graph of flowing well pressure versus logarithm of producing times was used to determine a line whose slope ~~"m~~" was 205 psi/log cycle as indicated in the figure. From equation 6.2, and data from table 6.11, the calculated corresponding *k* value was 49.6 mD.

As part of drawdown field analysis, another graph of flowing pressure vs. producing time was generated in order to calculate pore volume produced using the slope ~~"m~~" of the extrapolated curve in figure 6.10.

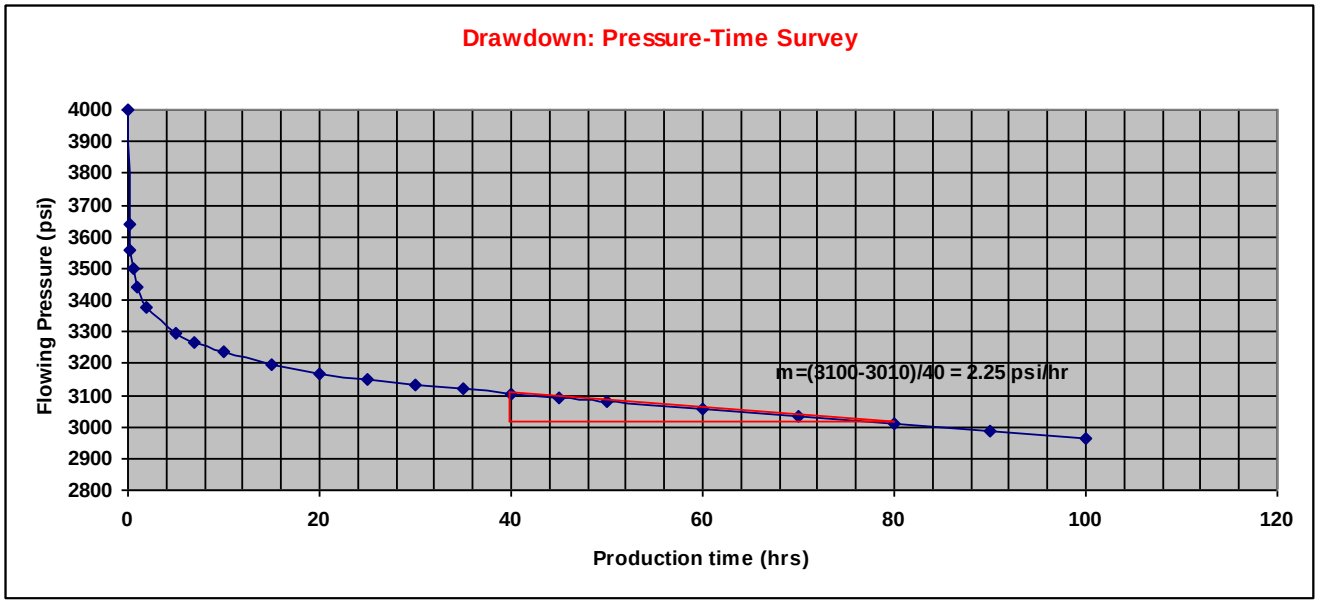

Figure 6.10: Drawdown analysis using production time

Pore volume was required to calculate total production time t which in this case was 27800 hrs as shown in table 6.11.

Using the developed damaged permeability model, calculations of damaged permeability profile were then carried out in the same manner as explained above for each drawdown pressure and corresponding producing time **(Δt).** Model generated permeability values are given in table 6.12.

Table 6.12: Model Damaged Permeabilities Based on Drawdown Survey Data

Permeability (md)	depth (ft)	Pwf (psi)	Δp (psi)
65	148	3641	359
53	158	3559	441
46	168	3498	502
41	178	3438	562
37	188	3377	623
33	198	3295	705
32	208	3265	735
30	218	3234	766
29	228	3198	802
28	238	3169	831
27	248	3149	851
27	258	3133	867
26	268	3118	882
26	278	3105	895
26	288	3092	908
25	298	3080	920
25	308	3055	945
24	318	3032	968
23	328	3008	992
23	338	2986	1014
22	348	2963	1037

Figure 6.11 shows a profile of the developed model‘s permeabilities as well as the single value obtained from the conventional drawdown pressure survey. If an average of the first five data in table 6.12 is taken, then that almost matches the survey results. The average of the first five results from the model is 48.5 mD compared to 49.6 mD hence in this case the percentage error is about 2% only. However if an average of the entire results (32 mD) across the drainage length is taken, then the percentage error is more than that. In section 6.2.11, table 6.29 shows results comparisons between the model and field practices and associated error percentages in all validations.

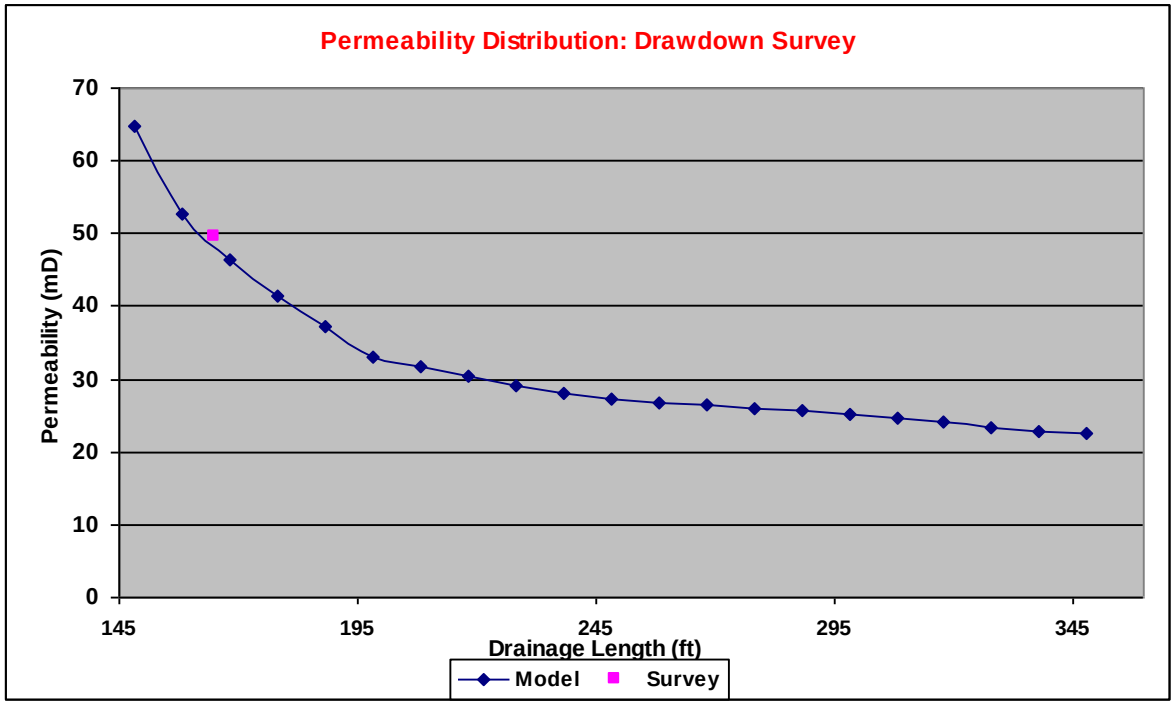

Figure 6.11: Model's permeability profile based on pressure drawdown data

6.2.4 Fifth Validation Using Field Pressure Fall-off Survey

The fifth validation was carried out using a different well test namely a fall-off pressure survey which is one of the most conventional tests carried out in water injecting wells for decades. The following are pressure fall-off data from Shell's well No. 4 from the Bent field in Illinois USA.

Table 6.13: Fall-off pressure-time survey data used in field practice

Closed-in time Δt (hrs)	pressure (psi)	it + Δt / Δt	$\text{Log}\left(\frac{it+\Delta t}{\Delta t}\right)$	parameter	value	unit
0	270	---	---	**Cum wi**	2,380,000	bbls
1	250	40057.10	4.60	**qi**	1426	b/d
2	230	20029.05	4.30	**it**	40056.1	hrs.
3	225	13353.03	4.13	**h**	49	ft
5	210	8012.22	3.90	**μ**	0.6	cp
6	200	6677.02	3.82	**Bwi**	1	rb/stb
7	190	5723.30	3.76	**m**	150	psi/log cycle
8	180	5008.01	3.70	**rw**	0.35	ft
9	170	4451.68	3.65			
10	155	4006.61	3.60			

In the table:

Cum wi is cumulative water injected (bbls)

qi is injection rate (b/d)

Bwi is injection water formation volume factor (rb/stb)

it is injection time (hrs).

Pressure and closed-in time data in table 6.13 were used to carry out the conventional fall-off survey analysis to determine the slope ‗m' from the extrapolated curve obtained from a graph of pressure vs. logarithm of time ratio as shown in figure 6.12. From the graph, ‗m' was 150 psi /log cycle.

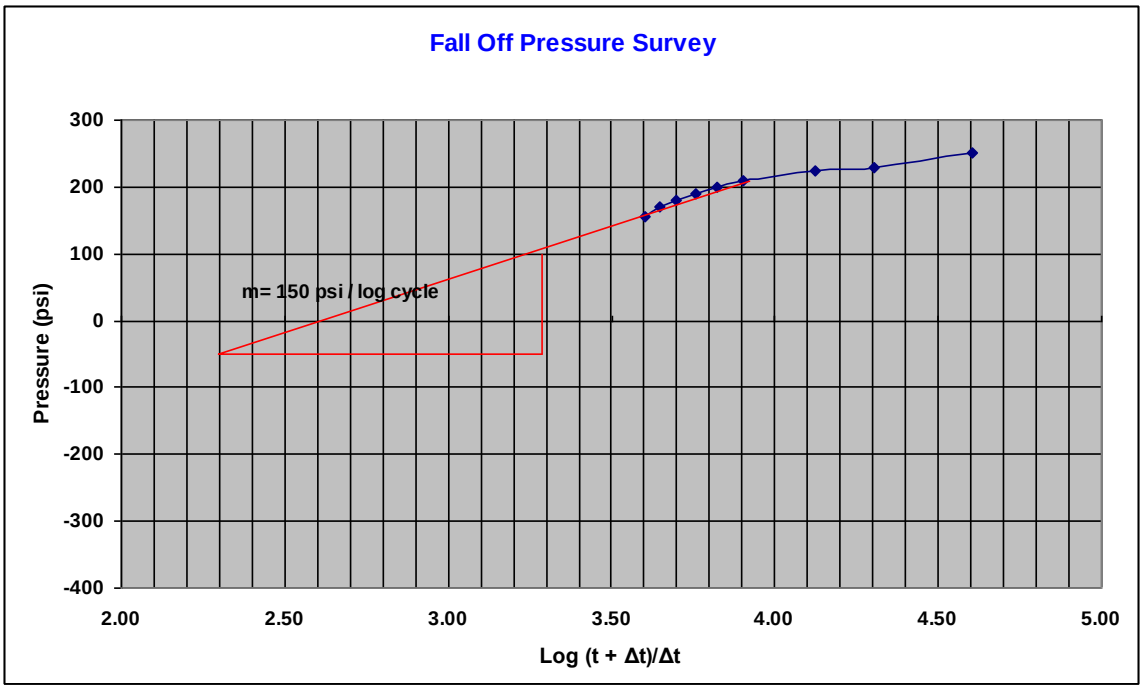

Figure 6.12: Water injection well pressure fall-off survey analysis

The value of ‗m' was then substituted in equation 6.2 to calculate the effective permeability of the rock through which this well was injecting. The calculated permeability was 21 mD and a corresponding skin factor was -3.75 which meant that the well was not affected by formation impairment or damage (being less than zero).

Using the same methodology explained above, the developed model was used to calculate the corresponding damaged permeability for all pressures and corresponding shut-in times given in table 6.13. Table 6.14 shows the damaged permeability results from the model.

Table 6.14: Model Damaged Permeabilities Based on Fall-off Survey Data

Permeability (md)	depth (ft)	Δp (psi)
11.8	105.6	250
15.3	133.1	230
17.1	152.3	225
20.4	180.6	210
22.1	191.9	200
24.0	202	190
25.9	211.2	180
28.0	219.7	170
31.3	227.5	155

Average model permeability across the entire length was 22 mD, hence error percentage was about 5% only.

The results were then plotted along with the survey‘s determined single permeability value as shown in figure 6.13.

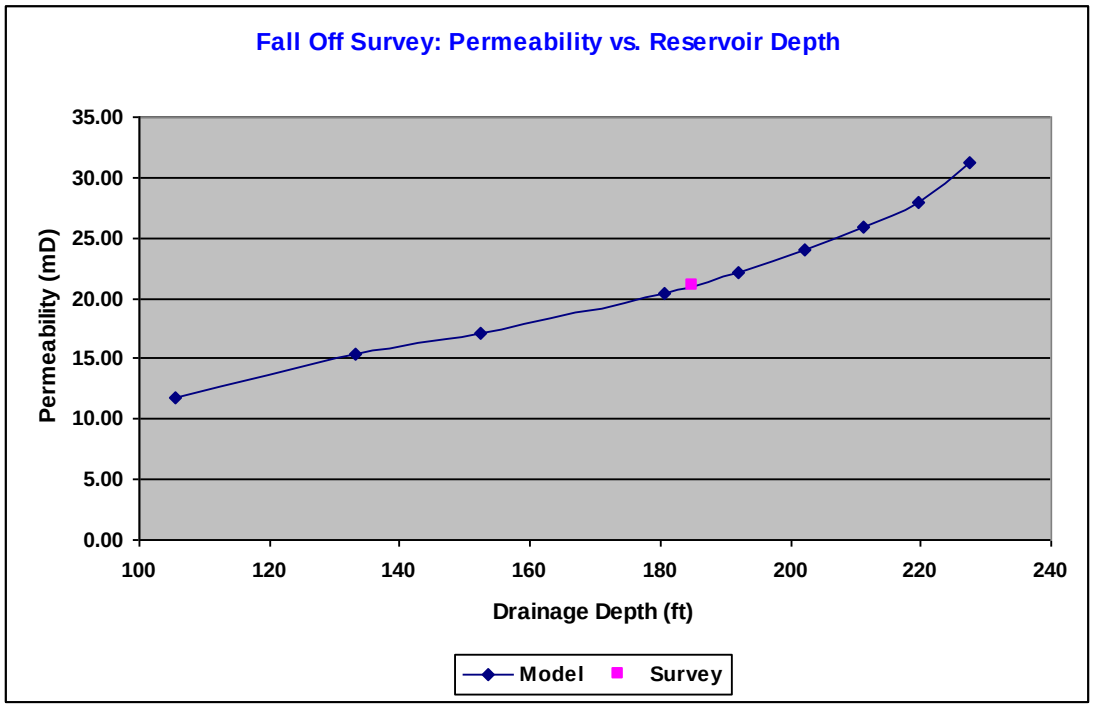

Figure 6.13: Model permeability profile of a water injection well

While the above five model validations involved transient pressure surveys carried out in liquid producing/ injecting wells, the following validations involved gas producing wells.

6.2.5 Sixth Validation Using Gas Wells Pressure Build-up Survey Analysis

Transient pressure build-up survey of a PDO's dry gas well Y-482 was used in this validation. Unlike liquid pressure build up processing, in a gas analysis, temperature, pressure and compressibility factor (Z) play a direct role in the gas formation volume factor B_g. Apart from that the analysis is somehow similar to the liquid analysis.

Table 6.15 shows the well data as well as the pressure build-up survey readings taken from a pressure gauge during the closed-in time intervals listed.

Table 6.15: Gas well pressure build-up survey and other data

Closed-in time Δt (hrs)	$\frac{t+\Delta t}{\Delta t}$	$\mathrm{Log}\left(\frac{t+\Delta t}{\Delta t}\right)$	pws (psi)	parameter	value	unit
0.0	-		4306	**Np**	117795.29	MMScf
0.1	507800.8	5.7	4587	**q**	55.67	MMScf/d
0.2	253900.9	5.4	4711	**t_p**	50779.98	hrs
0.3	169267.6	5.2	4853	**h**	21.00	ft
0.5	101561.0	5.0	4951	**μ_g**	0.0241	cp
0.7	72543.8	4.9	4967	**B_g**	0.00543	rb/stb
1.0	50781.0	4.7	4996	**m**	20.00	psi/log cycle
2.0	25391.0	4.4	5008	**rw**	0.38	ft
4.0	12696.0	4.1	5013			
6.0	8464.3	3.9	5022			
10.0	5079.0	3.7	5028			
30.0	1693.7	3.2	5049			

A graph of $\log\left\{\frac{t+\Delta t}{\Delta t}\right\}$ vs. shut-in well pressure (pws) was constructed using data from table 6.15 as shown on figure 6.14. from which gradient _m' and extrapolated pressure _*pe'* values were determined.

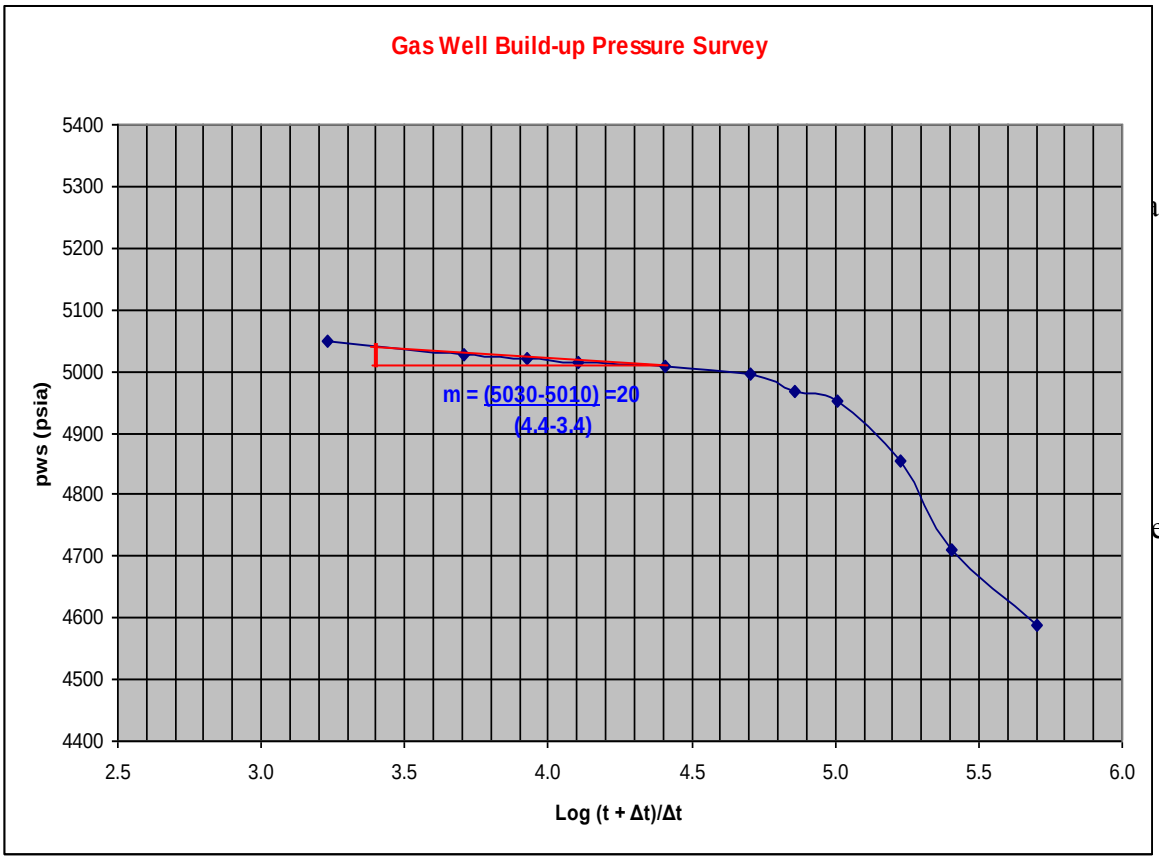

Figure 6.14: Gas reservoir pressure build-up survey analysis

Using the same procedures explained above, particle-damaged permeabilities at each shut-in well pressure were calculated. Results are in table 6.16.

Table 6.16: Model Damaged Permeabilities From Gas Pressure Build-up Survey

Permeability (mD)	Depth (ft)	pws (psi)	Δp (psi)
861	10	4587	281
597	100	4711	405
442	200	4853	548
375	300	4951	645
366	400	4967	661
351	500	4996	690
344	600	5008	702
342	700	5013	708
338	800	5022	716
335	900	5028	722
326	1000	5049	743

Then data from table 6.16 was used to draw the graph shown in figure 6.15. From the graph, it is evident that there is a significant difference between the survey determined single permeability value and the model‘s permeability values.

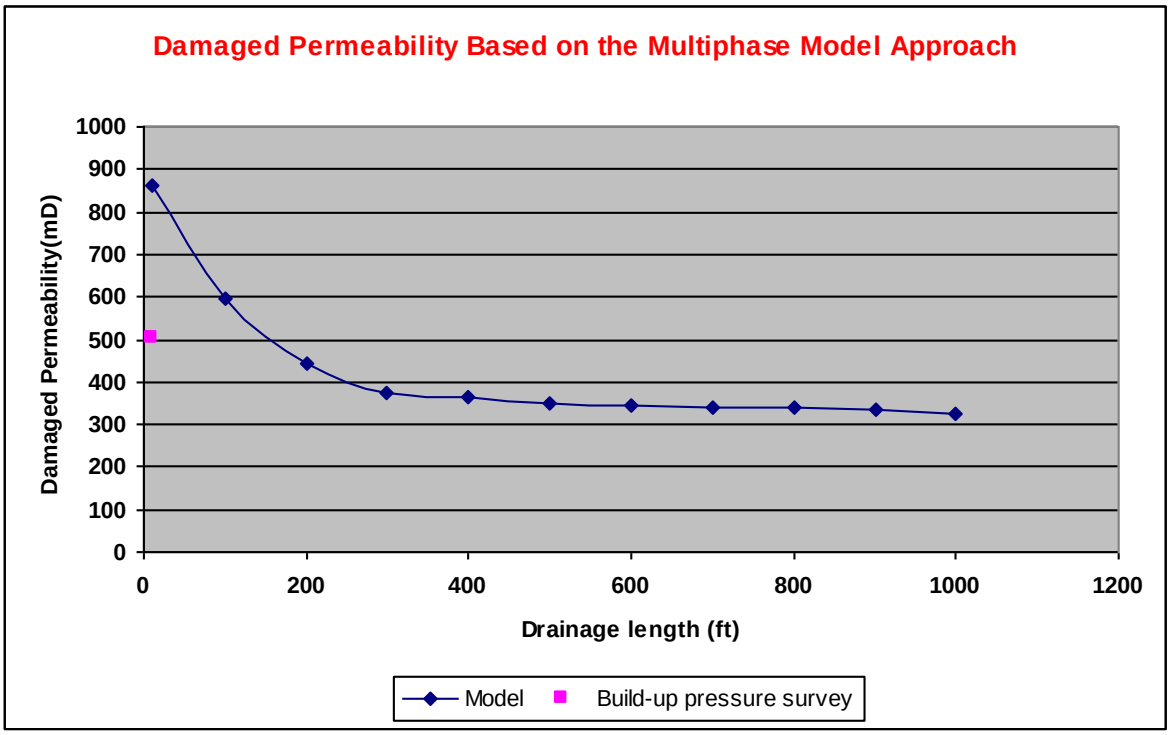

Figure 6.15: Multiphase Model’s permeabilities based on gas pressure build-up data

The difference between the survey value and the model curve is very clear when figure 6.15 is compared with figures 6.4, 6.6, 6.8, 6.11 and 6.13. The error percentage in this case was 16.1%. The difference is attributed to the fact that the CFD simulations involved a mixture of gas and liquid hydrocarbon and not dry gas on its own which is compared to in this case.

6.2.6 Seventh Validation Using Gas Well's Pressure Build-up Survey Analysis

Another PDO well, Y-467, was used to validate the developed multiphase model. Table 6.17 shows well data as well as gas pressure build-up survey readings. The data was used to construct the pressure build-up analysis graph shown in figure 6.16.

Table 6.17: Gas well pressure build-up survey and other data

Closed-in time Δt (hrs)	$\frac{t+\Delta t}{\Delta t}$	$\mathrm{Log}\left(\frac{t+\Delta t}{\Delta t}\right)$	pws (psi)	parameter	value	unit
0.0	-		5490	**Np**	110766.47	MMScf
0.1	294515.1	5.5	5848	**q**	90.26	MMScf/d
0.4	73629.5	4.9	6007	**t_p**	29451.41	hrs
0.6	49086.7	4.7	6188	**h**	23.00	ft
0.8	36815.3	4.6	6313	**μ_g**	0.021	cp
1.0	29452.4	4.5	6333	**B_g**	0.006	rb/stb
2.0	14726.7	4.2	6369	**m**	35.00	psi/log cycle
4.0	7363.9	3.9	6385	**rw**	0.46	ft
6.0	4909.6	3.7	6392			
10.0	2946.1	3.5	6403			
20.0	1473.6	3.2	6410			
35.0	842.5	2.9	6437			

Referring to figure 6.16, the extrapolated pressure *pe* was 6635 psig, and gradient ‗m' was 35 psi/log cycle. Permeability was then calculated as follows:

$$\mathrm{k} = \left[\frac{162.6(90.26/5.615)(10^6)(0.021)(0.006)}{(23)(35)}\right] = 408\, mD.$$

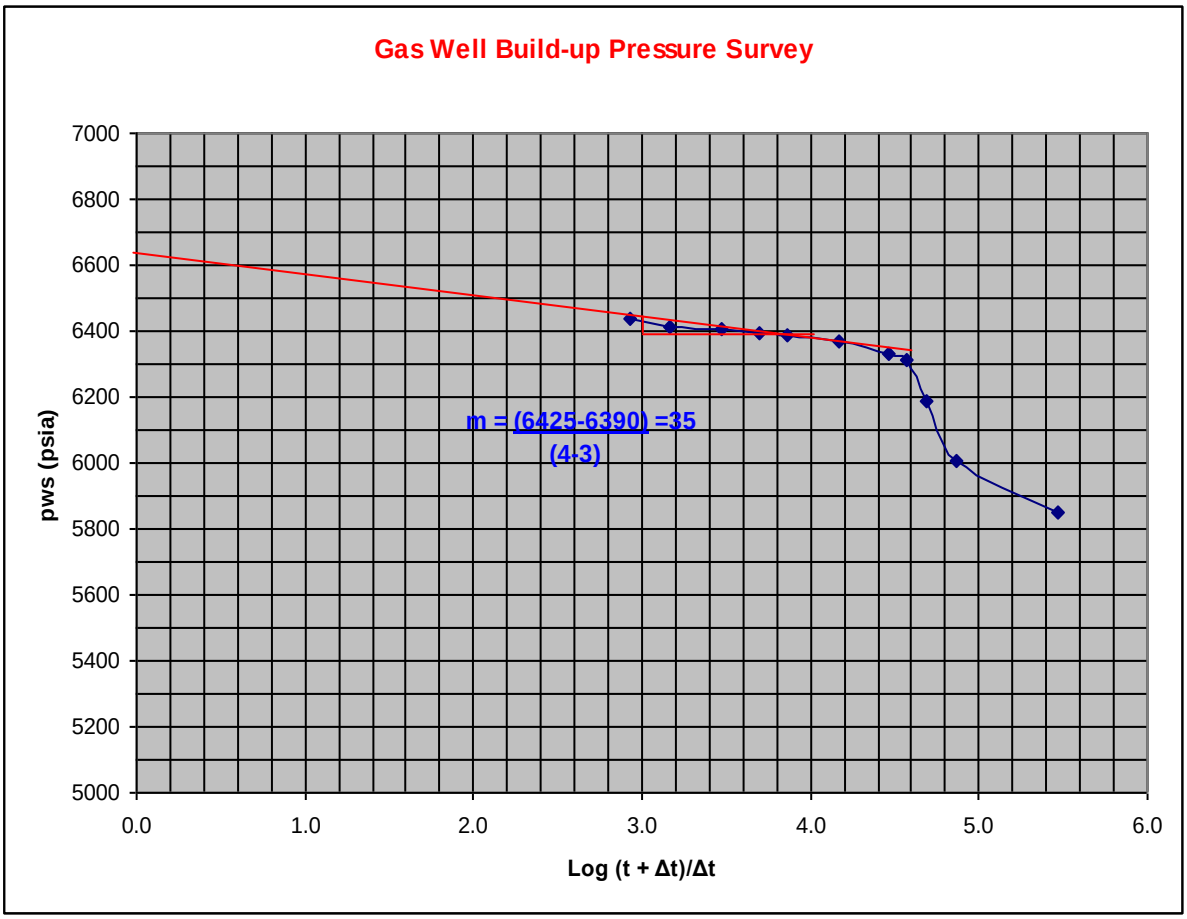

Figure 6.16: Pressure build-up analysis of a dry gas producing well

Using the developed model in the methods explained in sections 6.2.1 to 6.2.5, the corresponding permeability per measured pressure build-up was calculated. The results are in table 6.18.

Table 6.18: Model's Damaged Permeabilities

Permeability (mD)	Depth (ft)	pws (psi)	Δp (psi)
1185	10	5848	358
821	100	6007	517
608	200	6188	698
516	300	6313	823
503	400	6333	843
483	500	6369	879
474	600	6385	895
470	700	6392	902
465	800	6403	913
461	900	6410	920
448	1000	6437	947

Using table 6.18 data, figure 6.17 was constructed. The figure shows the model generated permeability profile as well as the single permeability value obtained from the field's pressure build-up survey analysis.

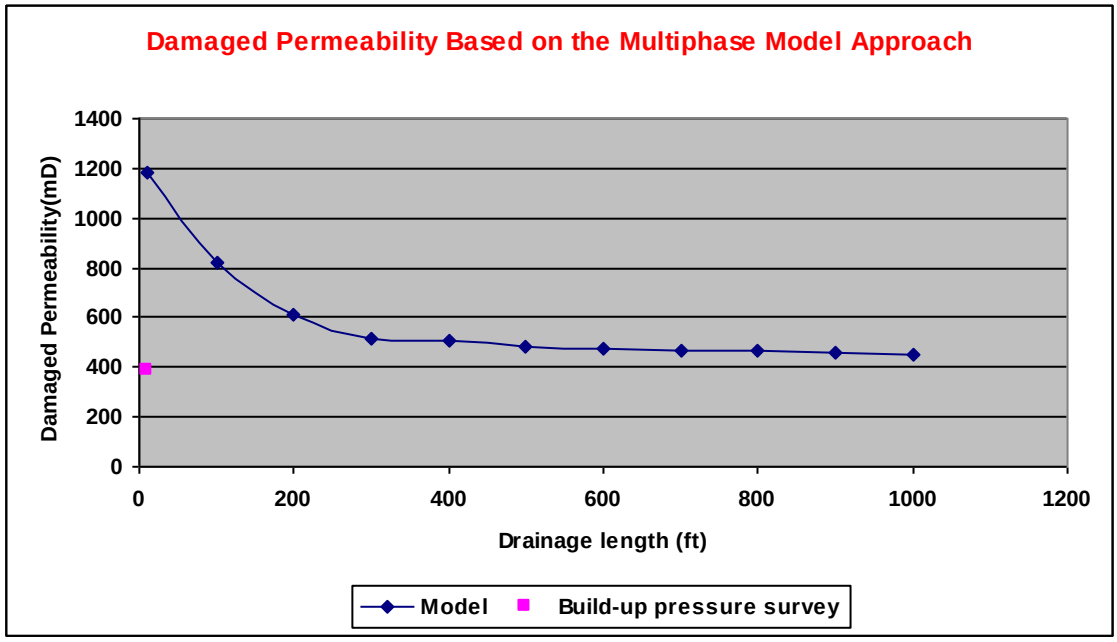

Figure 6.17: Model's permeability profile based on all gas pressure build-up data

As in figure 6.17, the error percentage in a gas well analysis is larger compared to a liquid well analysis. In this particular case the percentage error was 52.9% when the average permeability from the model generated curve was compared to the single pressure survey permeability value. As suggested in chapter 8, further work to reduce the error margin for dedicated dry gas CFD simulation analyses is strongly recommended.

Dry gas CFD analysis is very complex at reservoir level. Hydrocarbon gas which is compressible under pressure and expands when pressure is released yet its thermodynamic change is different from liquid‘s, is very complex to model especially in studying impacts of solid particles of various grains on pressure drawdown. Usually gas producing wells do produce condensate oil and water along with gas at the reservoir level. Hence dry gas CFD simulation should initially include multiphase flow then dry gas to be analysed as the fluid leaves the reservoir section while particles are flowing with the gas fluid.

6.2.7 Eighth Validation Using Gas Well’s Pressure Build-up Survey

In order to validate the developed multiphase model using a highly consolidated reservoir with low reservoir pressure and low production rate, Shell‘s gas well No. 3 located in Oman whose data is given in table 6.19 was used.

Table 6.19: Gas well pressure build-up survey and other data

Closed-in time Δt (hrs)	$\frac{t+\Delta t}{\Delta t}$	$\text{Log}\left(\frac{t+\Delta t}{\Delta t}\right)$	pws (psi)	parameter	value	unit
0.0	-		2422	**Np**	6389.87	MMScf
0.1	508699.1	5.7	2580.0	**q**	3.01	MMScf/d
0.3	203480.2	5.3	2650.0	**t**	50869.81	hrs
0.4	127175.5	5.1	2730.0	**h**	84.00	ft
0.5	101740.6	5.0	2785.0	**μ_g**	0.020	cp
0.7	72672.2	4.9	2794.0	**B_g**	0.006	rb/stb
1.0	50870.8	4.7	2810.0	**m**	18.00	psi/log cycle
3.0	16957.6	4.2	2817.0	**rw**	0.29	ft
4.0	12718.5	4.1	2820.0			
5.5	9250.1	4.0	2825.0			
9.0	5653.2	3.8	2828.0			
40.0	1272.7	3.1	2840.0			

From the table, figure 6.18 was constructed. The figure shows a pressure build-up analysis where stabilized pressure data was used to determine the slope ‗m' which in this case was 18.

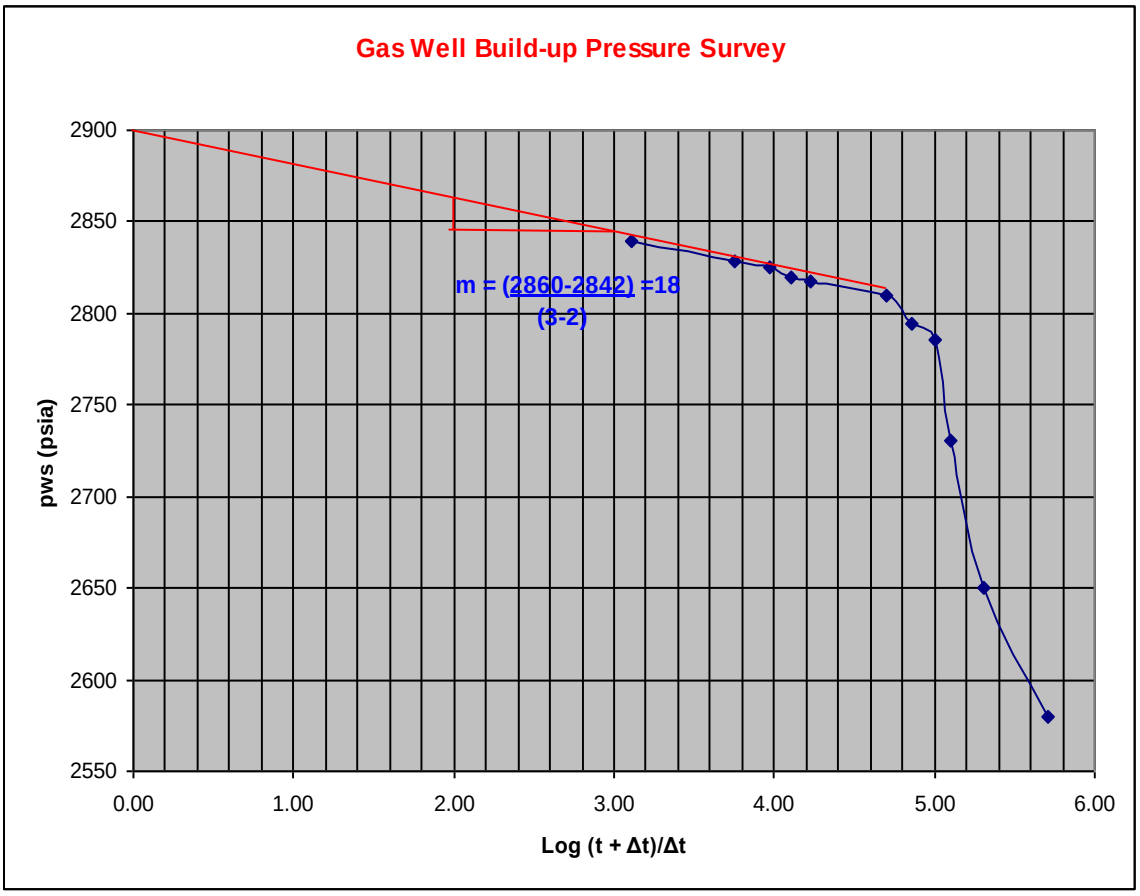

Figure 6.18: Pressure build-up analysis of a gas producing well

From figure 6.18, the extrapolated pressure *pe* was 2900 psig. Hence using relevant data from table 6.19, the permeability was calculated as follows:

$$k = \left[\frac{162.6(3.01/5.615)(10^6)(0.0201)(0.006)}{(84)(20)}\right] = 7.24\ mD.$$

Substituting the measured pressure drop data into the developed multiphase model, the corresponding damaged permeabilities were calculated whose values are listed in table 6.20.

Table 6.20: Model Damaged Permeabilities Based on Gas Build-up Survey Data

Permeability (mD)	Depth (ft)	pws (psi)	Δp (psi)
18.8	10	2580.0	158.0
13.0	100	2650.0	228.0
9.7	200	2730.0	308.0
8.2	300	2785.0	363.0
8.0	400	2794.0	372.0
7.7	500	2810.0	388.0
7.5	600	2817.0	395.0
7.5	700	2820.0	398.0
7.4	800	2825.0	403.0
7.3	900	2828.0	406.0
7.1	1000	2840.0	418.0

Figure 6.19 shows both the single permeability value determined from the gas pressure build-up field analysis and the curve generated using the developed multiphase model. In this case, as in the above two gas well surveys, the error percentage (42.2%) was very high for the same reasons given in sections 6.2.5 and 6.2.6. Aiming at error reduction in this respect, suggestions for further work are given in chapter 8.

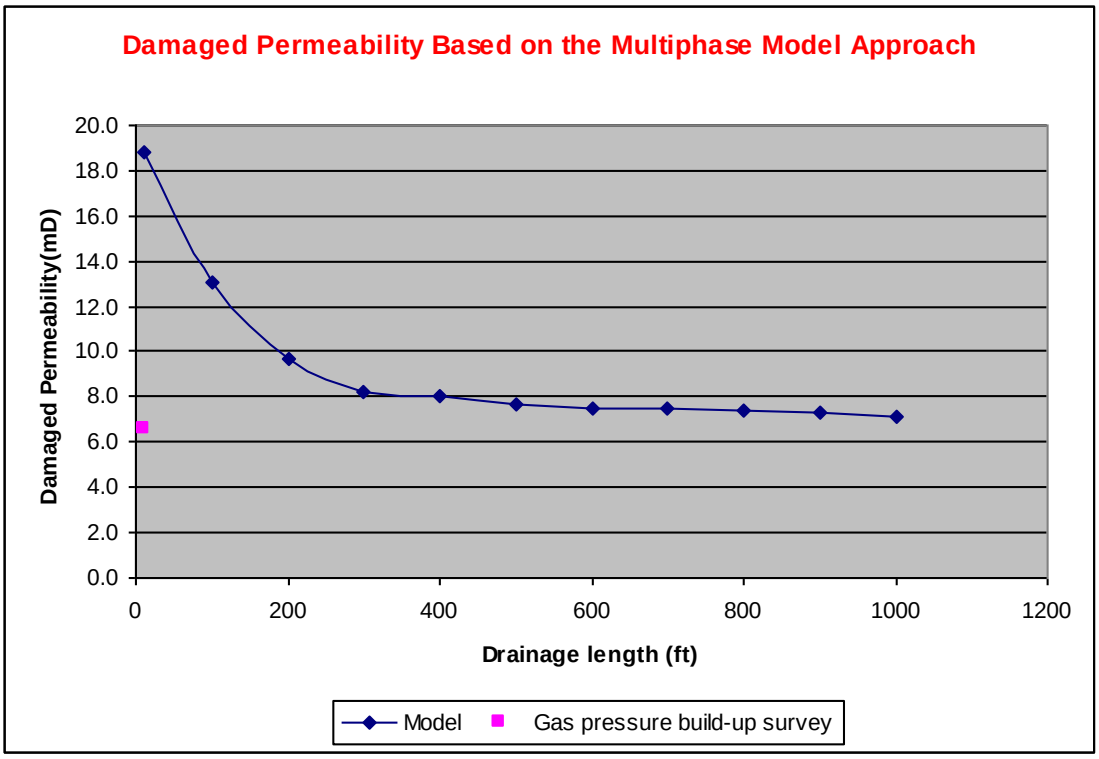

Figure 6.19: Model permeability profile based on gas pressure build-up data

6.2.8 Gas Well Production Analysis

This section briefly explains how to determine the maximum production rate from a gas well after having obtained pressure and flow rate surveys. Data in table 6.21 is from PDO gas well No. 9 in the Yibal field.

Table 6.21: Gas well pressure and flow rate test data

test	pwf (psia)	q_g (MMscf/d)	p^2-pwf^2 ($psia^2$)	$\frac{(p^2-pwf^2)}{q_g}$	$\log(p^2-pwf^2)$	$\log\left(\frac{(p^2-pwf^2)}{q_g}\right)$	$\log q_g$
	408.20	0.00					
1.00	403.10	4.29	4137.63	964.93	3.62	2.98	0.63
2.00	394.00	9.27	11391.24	1229.49	4.06	3.09	0.97
3.00	378.50	15.55	23364.99	1502.38	4.37	3.18	1.19
4.00	362.60	20.18	35148.48	1742.01	4.55	3.24	1.30
	14.70	AOFP	166411.15		5.22		

Where:

pwf = flowing wellhead pressure (psi)

q_g = gas flow rate (MMscf/d)

In table 6.21, the first three columns on the left contain the test data while the rest of the table contains calculated data using formulae clearly indicated above each column. Figure 6.20 was constructed from table 6.21 and was used to determine coordinates necessary to calculate the maximum or the absolute open-flow potential (AOFP) production rate of the gas well.

In figure 6.20, when the curve was extrapolated upwards and downwards, the following coordinates were obtained:

$y = 900; \quad x = 2.78$

$y = 1900; \quad x = 23.547$

The straight line connecting the four points is mathematically expressed as follows:

$900 = a + (2.78)\,b$, hence $a = 900 - (2.78)\,b$;

Thus $1900 = \{900-(2.78)\,b\}+23.54b$; and

$1900 = a + (23.54)\,b$

From the two simultaneous equations, a and b values are:

$b = 48.17$ = slope in figure 6.22

$a = 766.10$ = the y-intercept of the graph in the figure 6.22

Equation 6.5 calculates Absolute Open Flow Potential flow (AOFP) which is the flow rate that would be obtained if the bottom-hole pressure at the reservoir were reduced to zero psia. It is a mathematical expression of the graphical approach given in figure 6.22 in which a is the y-axis straight intercept and b is the slope in the figure.

The absolute open-flow potential (AOFP) was then calculated as follows:

$$q_g = \mathrm{AOFP} = \frac{a + \sqrt{a^2 + 4b\{\Delta p\}^2}}{2b} \quad \ldots\ldots\ldots\ldots\ldots\ldots\ldots\ldots\ldots\ldots\ldots\ldots\ldots\ldots\ldots\ldots\ldots\ldots (6.5)$$

$= 67.3$ MMScf/d

Where Δp^2 is a square of average pressure minus standard pressure = 166411.15psia^2 as shown in table 6.21.

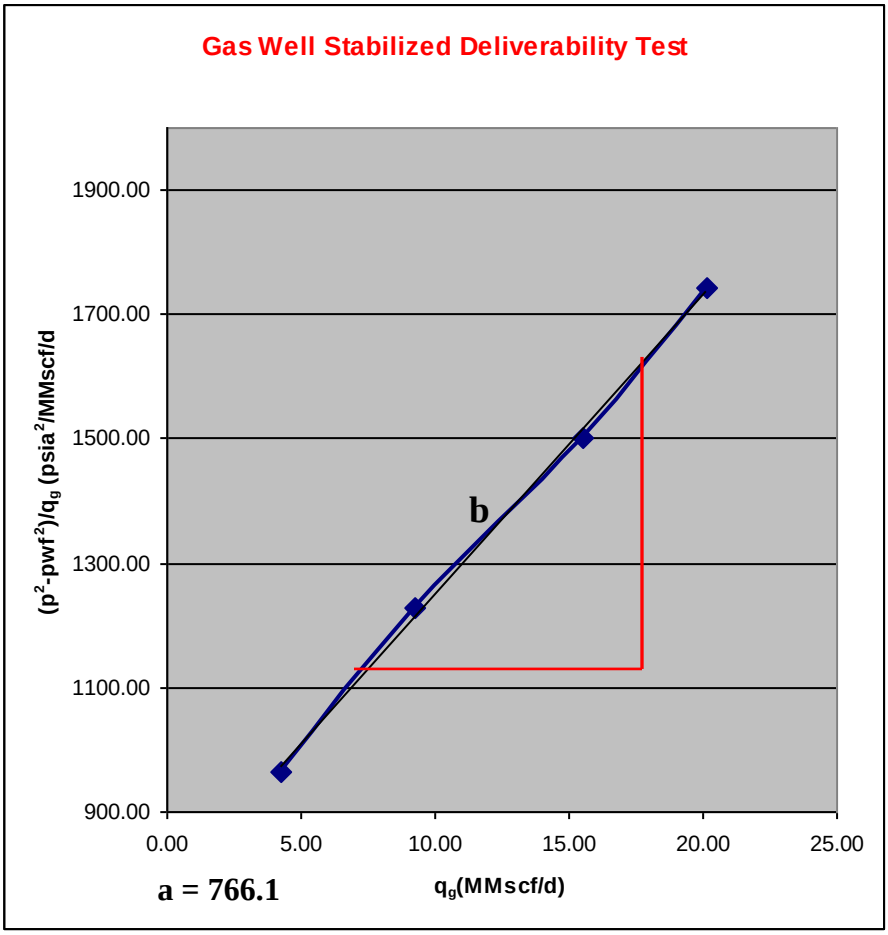

Figure 6.20: Stabilized test analysis to obtain coordinates for AOFP calculations

6.2.9 Second Gas Well Production Analysis

Table 6.22 shows well data of PDO gas well SR-202.

Table 6.22: Gas Well Multirate and Pressure Test Data

test	pwf (psia)	q_g (MMscf/d)	p^2-pwf^2 ($psia^2$)	$\frac{(p^2-pwf^2)}{q_g}$	log(p^2-pwf^2)	$\frac{\log((p^2-pwf^2)}{q_{g)}}$	log q_g
	612.30	0.00					
1	604.65	6.43	9309.67	1447.40	3.97	3.16	0.81
2	591.00	13.90	25630.29	1844.24	4.41	3.27	1.14
3	567.75	23.33	52571.23	2253.57	4.72	3.35	1.37
4	543.90	30.27	79084.08	2613.01	4.90	3.42	1.48
	14.70	AOFP	374695.20		5.57		

Similar methodology was used as explained in section 6.2.8 to determine the results shown in table 6.22. From the table, figure 6.21 was constructed.

When the curve in figure 6.21 was extrapolated upwards and downwards, the following coordinates were obtained:

y = 1400; x = 5.20

y = 2700; x = 32.19

Hence, the straight line connecting the four points is mathematically expressed as follows:

1400 = a + (5.2) b, thus a = 1400 - (5.2) b.

Where: a is the y-axis intercept and b is the slope in the figure 6.21.

Therefore 2700 = {1400 - (5.2) b } + 32.2 b; and

2700 = a + (32.2) b.

From the two simultaneous equations, a and b values were:

b = 48.15

a = 1149.63

$$q_g = \text{AOFP} = \frac{a + \sqrt{a^2 + 4b\{\Delta p\}^2}}{2b}$$

= 100.96 MMScf/d.

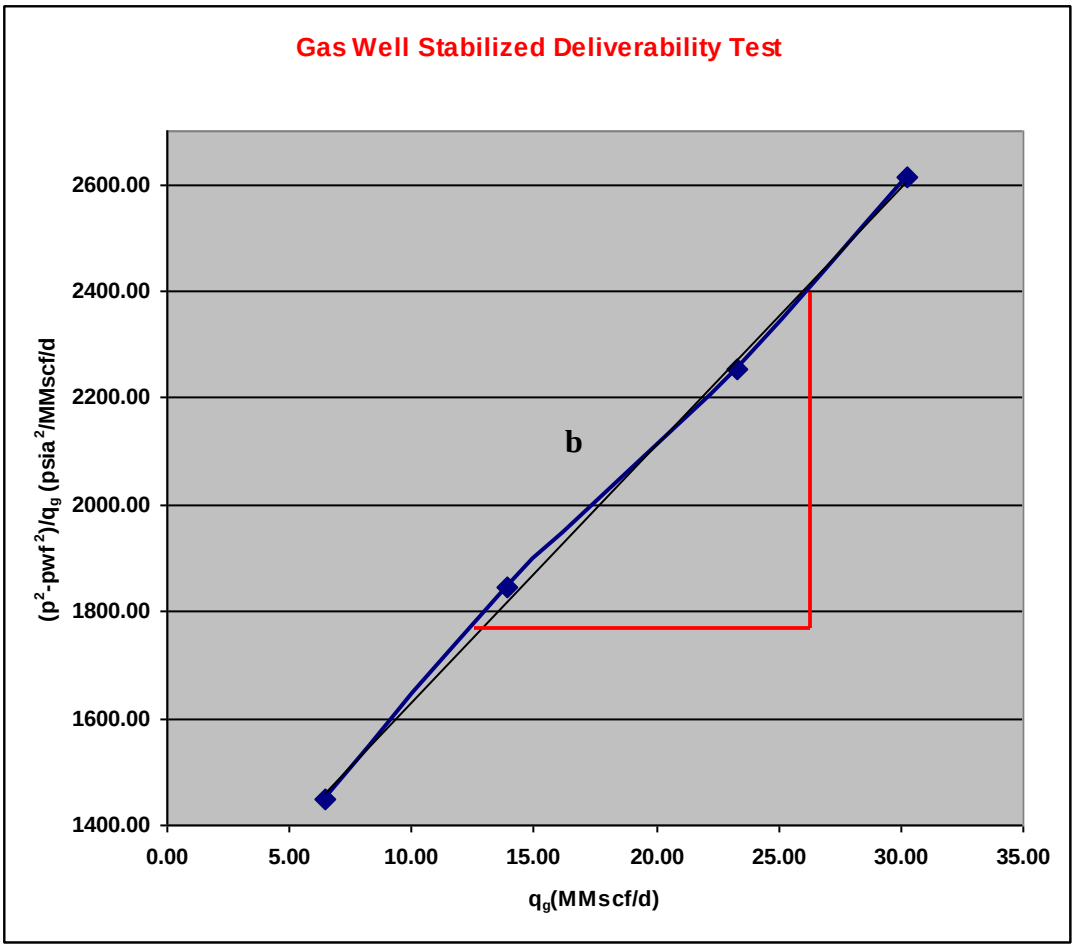

Figure 6.21: Coordinate determination for AOFP analysis

6.2.10 Ninth Validation Using Horizontal Well Productivity Analysis

This section briefly explains the most recent and reliable horizontal well performance analysis carried out in field practice. Theory of horizontal well‘s performance analysis is given in chapter 2 section 2.11.3.

Field applications using horizontal well performance equation 2.34 and comparison with the developed model‘s results as part of the validation process are explained in this section.

The following is a real case reservoir analysis carried out to justify drilling a horizontal well versus a vertical well in Oman‘s Sadad Southern Central oil field using SDD-36(a) well.

Table 6.23 depicts the well‘s rock and fluid properties.

Table 6.23: SDD-36(a) Well data

Parameter	Value	Units
k_h	900	mD
k_v	90	mD
h	16	ft
p_i	1218	psia
p_{wf}	116	psia
μ	42	Cp
B_o	1.04	bbl/STB
r_w	0.2552	ft
r_{eh}	1850	ft
L_x	234	ft
L_y	234	ft

Using a horizontal ellipsoid inflow pattern approach in the mixed steady-state horizontal plane and pseudo-steady state vertical plane conditions (explained in chapter 2), the permeability anisotropy, I_{ani}, was calculated as follows:

$$I_{ani} = \sqrt{\frac{k_h}{k_v}} = \sqrt{\frac{900}{90}} = 3.16. \text{ ----------(6.6)}$$

Then the major half-axis of the drainage ellipsoid ***a,*** was determined as follows:

$$a = \frac{234}{2}\left\{\sqrt{0.5 + \sqrt{0.25 + \left\{\frac{1850}{(234/2)}\right\}^4}}\right\} = 1852\, ft. \text{ ----------(6.7)}$$

The well is installed with 200µm wire-wrapped screen sand control, hence is supposed to have various particle sizes with the majority of them close to 200µm. As such from the

developed model, pressure drawdown corresponding to 200μm grain size as mentioned in chapter 5, is given as:

$$\Delta p_{200\mu m} = -0.000005(L_h)^3 + 0.0085(L_h)^2 - 5.9569(L_h) - 119.92$$

In this case, lateral length L_h, vertical permeability k_v and horizontal permeability k_h were the major uncertainties for which sensitivity analyses were carried out to analyse their impact. Starting with L_h = 234ft, using equation 2.34 in which table 6.23 (well data) values were substituted, the corresponding value of horizontal flow rate q_h was calculated as shown below.

$$q_h = \frac{900(16)(1113)}{141.2(1.04)(42)\left\{\left[\ln\left[\frac{1852+\sqrt{(1852)^2-\left(\frac{234}{2}\right)^2}}{\frac{234}{2}}\right]\right] + \left(\frac{3.16(16)}{234}\right)\ln\frac{(3.16(16))}{[0.2552(3.16)+1)]}\right\}} = 606 STB/d.$$

----------(6.8)

Table 6.24 shows how the horizontal flow rate (q_h) was calculated using equations 2.38, 2.39, 2.40, 2.41 and 2.42, as well as equations 6.6, 6.7 and 6.8.

Table 6.24:Calculated pressure drop per reservoir length and horizontal parameters

L_h	a (ft)	I_{ani}	α	β	χ	δ	ε	q_h (STB/d)
234	1852	3.16	16033556	6168	3.45	0.22	3.86	606

Similar analyses were repeated for each of the lateral length. The corresponding horizontal flow rate q_h results obtained from the field practice are shown in table 6.25.

Table 6.25: Calculated production rate q_h and pressure drop

L_h	a (ft)	I_{ani}	α	β	χ	δ	ε	q_h (stb/d)	Model Δp@200μm
70	1850	3.16	7177498	6168	4.66	0.72	3.86	156	498
94	1850	3.16	8751451	6168	4.37	0.54	3.86	220	608
117	1850	3.16	10213209	6168	4.15	0.43	3.86	285	709
141	1851	3.16	11568287	6168	3.96	0.36	3.86	350	803
164	1851	3.16	12822341	6168	3.81	0.31	3.86	416	890
187	1851	3.16	13980870	6168	3.68	0.27	3.86	480	971
211	1852	3.16	15049392	6168	3.56	0.24	3.86	544	1045
234	1852	3.16	16033556	6168	3.45	0.22	3.86	606	1113

From table 6.25, it is clear that the longer the lateral length L_h, the greater the q_h value. Thereafter, keeping the same flow rate (606 stb/d), additional sensitivities on lateral length were carried out as shown in table 6.26 to get corresponding pressure drops Δps.

Table 6.26:Calculated pressure drop per reservoir length and horizontal parameters

L_h	a (ft)	I_{ani}	α	β	χ	δ	ε	q_h (stb/d)	Model Δp@200μm
258	1852	3.16	16938839	6168	3.36	0.20	3.86	606	1176
281	1853	3.16	17770878	6168	3.27	0.18	3.86	606	1234
305	1853	3.16	18535161	6168	3.19	0.17	3.86	606	1287
328	1854	3.16	19237313	6168	3.12	0.15	3.86	606	1336
352	1854	3.16	19882860	6168	3.05	0.14	3.86	606	1381
375	1855	3.16	20477338	6168	2.98	0.13	3.86	606	1422
398	1855	3.16	21026358	6168	2.92	0.13	3.86	606	1460
422	1856	3.16	21535432	6168	2.86	0.12	3.86	606	1496
445	1857	3.16	22010164	6168	2.81	0.11	3.86	606	1528
469	1857	3.16	22456072	6168	2.76	0.11	3.86	606	1559
492	1858	3.16	22878755	6168	2.71	0.10	3.86	606	1589
516	1859	3.16	23283753	6168	2.66	0.10	3.86	606	1617
539	1860	3.16	23676609	6168	2.62	0.09	3.86	606	1644
562	1861	3.16	24062917	6168	2.58	0.09	3.86	606	1671
586	1862	3.16	24448203	6168	2.54	0.09	3.86	606	1698
609	1863	3.16	24838060	6168	2.50	0.08	3.86	606	1725
633	1864	3.16	25238014	6168	2.46	0.08	3.86	606	1753
656	1865	3.16	25653660	6168	2.42	0.08	3.86	606	1782
680	1866	3.16	26090541	6168	2.39	0.07	3.86	606	1812
703	1867	3.16	26554195	6168	2.35	0.07	3.86	606	1844
726	1868	3.16	27050224	6168	2.32	0.07	3.86	606	1878
750	1869	3.16	27584142	6168	2.29	0.07	3.86	606	1916
773	1870	3.16	28161558	6168	2.26	0.07	3.86	606	1956
797	1872	3.16	28787979	6168	2.23	0.06	3.86	606	1999
820	1873	3.16	29469021	6168	2.20	0.06	3.86	606	2046
844	1874	3.16	30210216	6168	2.17	0.06	3.86	606	2098
867	1876	3.16	31017090	6168	2.14	0.06	3.86	606	2154
891	1877	3.16	31895271	6168	2.12	0.06	3.86	606	2215
914	1878	3.16	32850244	6168	2.09	0.06	3.86	606	2281
937	1880	3.16	33887650	6168	2.07	0.05	3.86	606	2353

Figure 6.22 shows drawdown pressure per lateral length corresponding to 200 microns grain size.

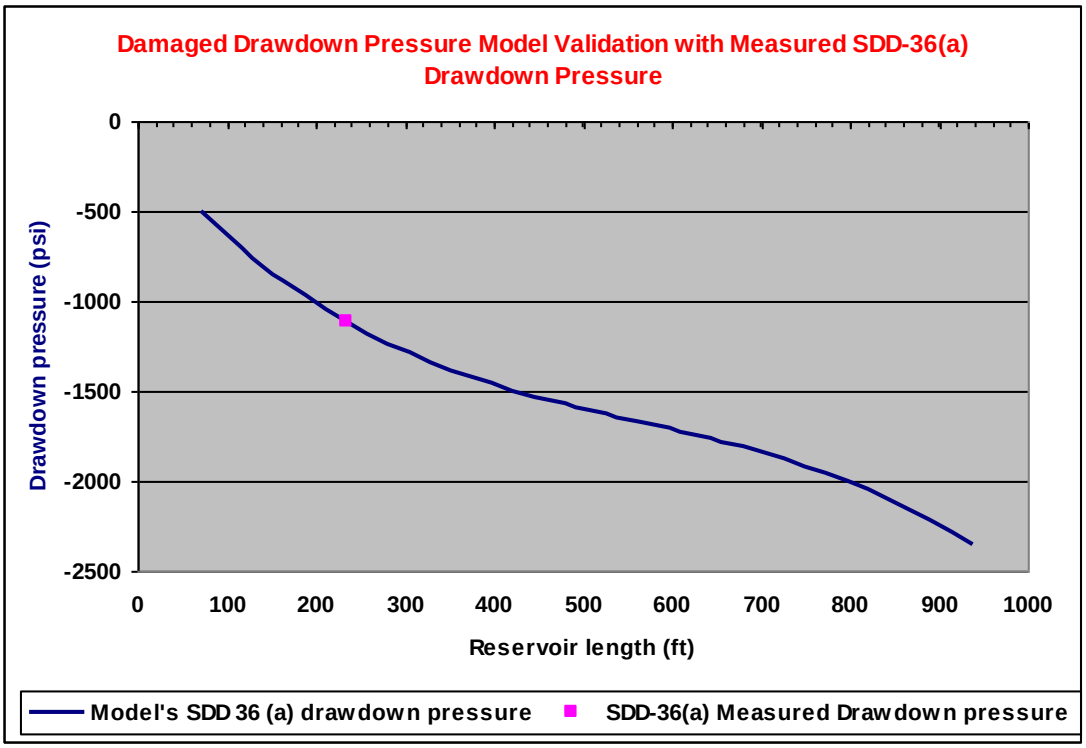

Figure 6.22: Measured drawdown pressure and model generated profile

Field measurements of drawdown pressure were carried out at 234 ft of the horizontal pay zone in the SDD-36(a) well. Drawdown pressures affected by 200µm particles ($\Delta_{p@200\mu m}$) at each lateral length from that depth onwards were calculated using the corresponding relevant particle-damage equation of the model given above. Results can be seen in figure 6.23.

The permeability corresponding to each of those model determined drawdown pressures for each horizontal length was calculated as follows:

$$k_h = \frac{(q_h(\beta)(\chi + \left\{\sqrt{\frac{900}{10}}\left(\frac{h}{L}\right)\right\}\ln\left\{\frac{\left(\sqrt{\frac{900}{10}}h\right)}{\left[r_w\left(\sqrt{\frac{900}{10}}+1\right)\right]}\right\}}{h(\Delta p_{@200\mu m})} \quad \text{.....(6.9)}$$

Figure 6.23 shows the corresponding particle-damaged permeability distribution. Comparing the model‘s average permeability result with the survey‘s single permeability, a difference of about 20% was revealed. One reason for this being the assumption that the vertical well data may be the same for the entire horizontal sidetrack; in other words, vertical well data was used to analyse a horizontal well.

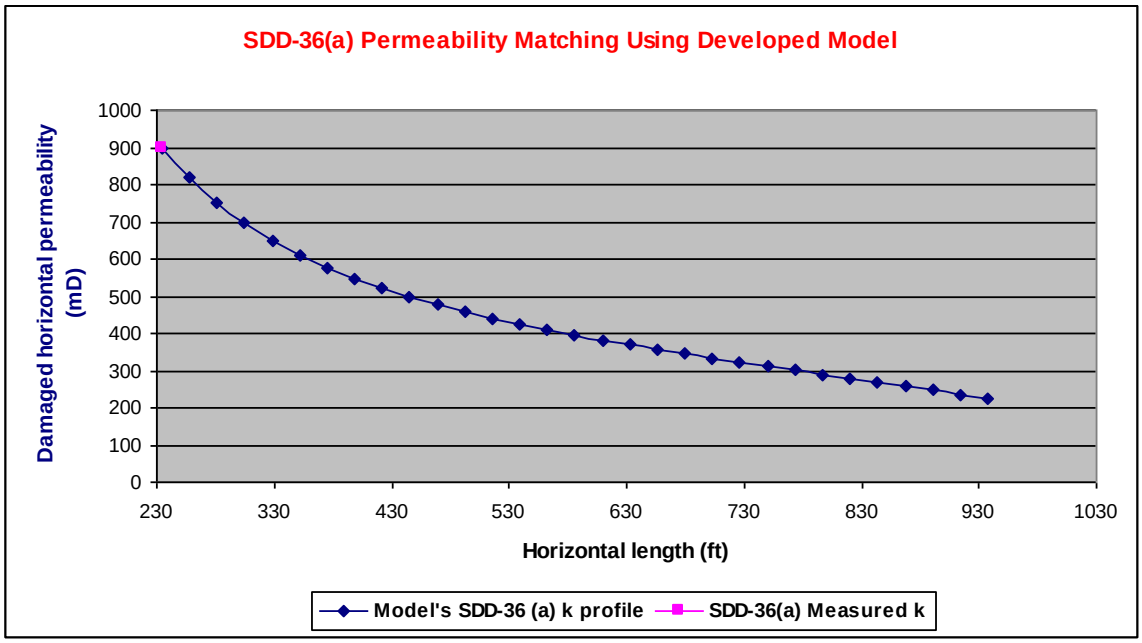

Figure 6.23: Field measured permeability vs. model’s distribution of permeabilities

6.2.11 Tenth Model Validation Using Field Vertical Well (SDD-36 (b))

To demonstrate vertical productivity, the conventional equations used was:

$$q_v = \frac{kh(p_i - p_{wf})}{141.2B_o\mu\left\{\frac{1}{2}\left[\ln\left[\frac{4L_xL_y}{\gamma C_a(r_w)^2}\right]\right]\right\}} \text{----------(6.10)}$$

This equation is used as part of field practice in determining reservoir vertical productivity. The terms are:

k = Permeability (md)

h = Reservoir height (ft)

p_i = Initial reservoir pressure (psi)

p_{wf} = Flowing bottom hole pressure (psi)

μ_o = Viscosity (cP)

B_o = Oil formation volume factor (res. bbl/STB)

r_w = Wellbore radius size (inches)

q_v = Vertical flow rate (bbl/d)

L_x=L_y = Reservoir lateral length (ft).

C_a = Dietz factor

γ = Constant =1.78

Because this well is located just near the horizontal SDD-36(a) well, some of the reservoir properties were similar as given in table 6.27

Table 6.27: SDD-36(b) data

Parameter	Value	Units
k	900	mD
h	16	ft
p_i	1218	psia
p_{wf}	116	psia
μ	42	Cp
B_o	1.04	bbl/STB
r_w	0.2552	ft
γ	1.78	Constant
C_a	30.9	Dietz factor
L_x	1320	ft
L_y	1320	ft

Dietz factor is a number used in calculating average reservoir pressure based on the pressure boundary shape of the drainage area in which the well is located. For example if the well is located in the middle of a square shaped drainage area, then the Dietz factor is 30.9 as in this case. In the average pressure equation, the relevant factor should be used.

When data from table 6.27 were substituted into equation 6.10, it resulted in q_v = 355 STB/d, from which a corresponding vertical productivity index (J_v) was calculated as follows:

$$J_v = \frac{q}{(p_i - p_{wf})} = 0.322 \text{ STB/d/psi} \text{----------(6.11)}$$

Productivity index is the measure of how productive the reservoir is. The index is a ratio of flow rate and pressure drawdown as shown in equation 6.11. It is used to compare well performance with another well or after a treatment has been done to check post-treatment performance of the same well. The bigger the ratio the more productive the well is.

Using the model for fines-affected permeability in multiphase flow mobilising 200μm particle size, particle-damaged drawdown pressure data was used to calculate the corresponding permeability by substituting the pressure data in the following equation:

$$k = \frac{(q_v)141.2B_o\mu\left\{\frac{1}{2}\left[\ln\left[\frac{4L_xL_y}{\gamma C_a(r_w)^2}\right]\right]\right\}}{h(\Delta p_{@200\mu m})} \quad \text{.....(6.12)}$$

Corresponding particle-damaged permeabilities were then mapped as per figure 6.24. It is to be noted that the well is vertical but calculations are for lateral (or horizontal) distributions of damaged permeabilities which may be encountered if the well was to be drilled horizontally to the reservoir. This uncertainty is likely to be the reason for the 21% difference between the single permeability value from the drawdown pressure survey analysis and the average permeability value from the model. The model generated permeability profile across Sadad 36 (b) reservoir as shown in figure 6.24. In order to compare productivity of a vertical well with a horizontal well, productivity improvement factor (PIF) which is the ratio of horizontal production rate over vertical production rate is used.

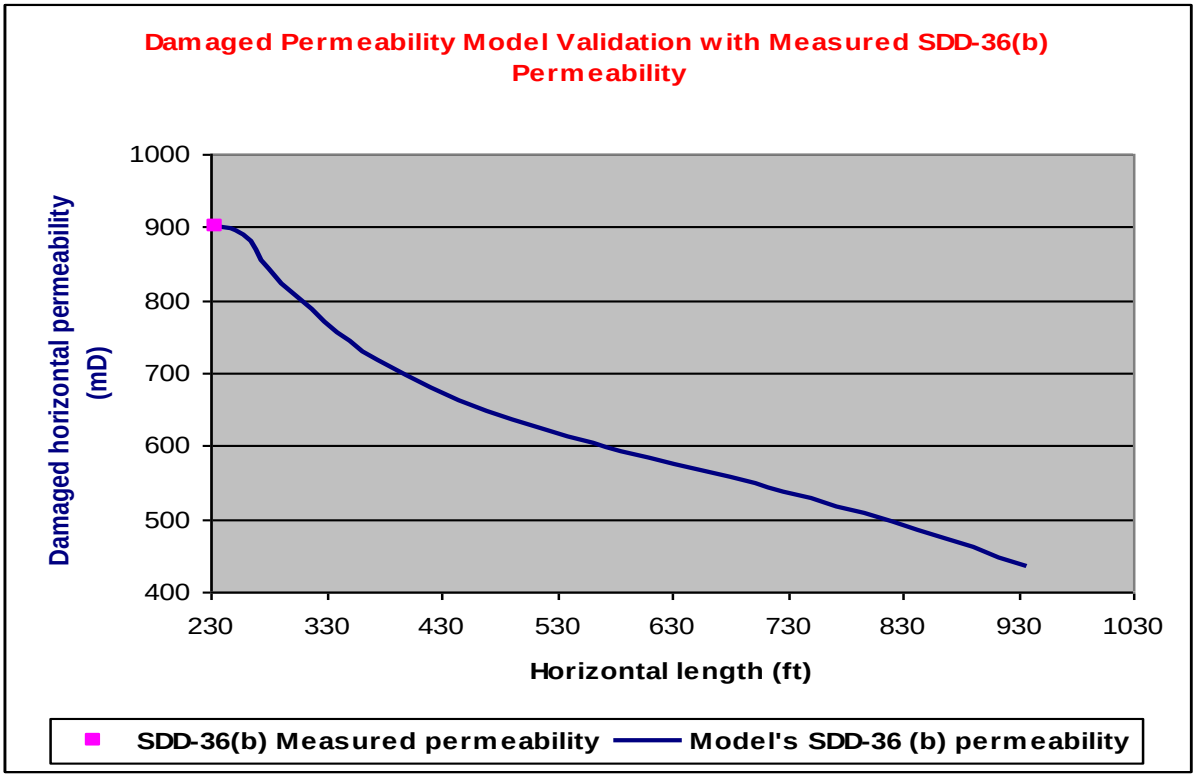

Figure 6.24: Field measured permeability vs. model's distribution of permeabilities

Also to justify an economic decision to go for a horizontal sidetrack or not, impacts of lateral length, and of k_v/k_h ratio on PIF at each L_h were analysed. It was decided that unless the PIF value was about 2, sidetracking a vertical well would not be considered economical. Since the lateral length L_h as well as k_v/k_h values are directly proportional to the horizontal production rate then for each lateral length and k_v/k_h ratio corresponding PIF was calculated to decide on economic length L_h. Table 6.28 shows calculated PIF values. Based on the results shown in table 6.28, it was decided that for the horizontal sidetrack to be economical, a minimum lateral length of 328 ft or more should be drilled. This length corresponded with PIF $\approx$ 2.

Table 6.28: Sensitivities of k_v/k_h and L_h on Production Improvement Factor (PIF)

Lateral length (ft)	PIF if k_v/k_h =0.3	PIF if k_v/k_h =0.2	PIF if k_v/k_h =0.1
33	0.833269	0.762282	0.638701
66	1.138831	1.070695	0.942608
164	1.620288	1.563325	1.447728
328	2.10122	2.052722	1.950475
656	2.797813	2.754487	2.660899

Table 6.28 clearly shows that the longer the horizontal length, L_h, the greater the PIF value. In other words, using such an analysis, the economic lateral length can be directly determined. In this case, 328ft which corresponds to PIF = 2 almost in all 3 k_v/k_h scenarios. Hence 328ft was the minimum lateral length to be drilled in order to justify sidetracking the vertical well, since that meant the horizontal well production expectation fulfilled the minimum production requirement over and above the vertical well productivity expectation. Table 6.29 summarizes all percentage errors observed when field practise analysis results were compared to the developed model results.

Table 6.29: Error Percentages: Developed Model Results vs. Field Practice Results

Validation No.	Analysis Used	Well type	Producer / Injector	Error %
1	Pressure build-up survey	Any, horizontal or vertical	Oil producer	17.5
2	Pressure build-up survey	Any, horizontal or vertical	Oil producer	4.32
3	Pressure build-up survey	Any, horizontal or vertical	Oil producer	13.19
4	Pressure drawdown survey	Any, horizontal or vertical	Oil producer	20.0
5	Pressure fall-off survey	Any, horizontal or vertical	Water injector	3.5
6	Pressure build-up survey	Any, horizontal or vertical	Gas producer	16.1
7	Pressure build-up survey	Any, horizontal or vertical	Gas producer	52.9
8	Pressure build-up survey	Any, horizontal or vertical	Gas producer	42.2
9	Horizontal inflow	Horizontal	Oil producer	20.3
10	Vertical inflow	Vertical	Oil producer	21.0

In areas where substantial differences were observed, suggestions for further work to reduce the uncertainties are given in chapter 8.

Research discussions, conclusions and recommendations are given in chapter 7.

Chapter 7

DISCUSSIONS, CONCLUSIONS AND RECOMMENDATIONS

7.1 Discussions

This research work resulted in an overall fulfilment of the main objectives defined at the beginning of this thesis (section 1.2), considering the achievements obtained as explained in the preceding chapters. Areas where expectations could not be fully achieved for reasons outlined in the text are explained in this chapter with recommendations on how to improve future investigations of those areas for better results achievements. As far as particle analysis is concerned, figure 3.7 demonstrates a unique feature in this study. Despite the simultaneous liquid and solid particle mixture flow complexity, instantaneous particle velocities were exclusively being measured. This makes the dynamic flow analysis more comprehensive compared to today‘s conventional laboratory approaches since in a core laboratory analysis, the best that could be achieved are the fines injection velocities before mixing with liquid while when a fines-liquid mixture moves, there is no facility to measure separately solid velocity from liquid velocity during the motion whereas in this study that was possible. Unfortunately the industry has not been successful in properly identifying the true nature, magnitude and mechanism of the problem. For example core laboratory experiments which are the major particle risk analysis methods, do not involve hydrocarbon gas due to safety reasons and also do not incorporate detailed hydrocarbon fluid-and-particle flow studies at reservoir conditions. Yet the experimental results are used in reservoir simulators to simulate reservoir production prediction. Meanwhile, the reservoir simulators are not designed to analyse particles interaction with hydrocarbon rock or fluid. Hence impact of fines particles

on pressure or permeability is not possible as far as existing simulation capability is concerned.

This research ended with several important results which are discussed in this section.

Having carried out hundreds of sensitivities and scenarios in the study of migrating fines particles and their impacts on hydrocarbon production determined by permeability magnitudes in the reservoirs, all major permeability trends were studied thoroughly. For example, pressure drop profiles in a high permeability (2000 mD) scenario due to 10 microns (figure 3.31) differ from the pressure drop patterns revealed in a comparatively lower (1000 mD) scenario (figure 3.17). When fluid type impact particularly on pressure drop was analysed for each grain size, different profiles were revealed. Details of pressure drops caused by particle sizes 10 μm, 50 μm, 100 μm, 150 μm and 200 μm, flowing in both multiphase and liquid media, through both 1000 mD and 2000 mD absolute permeability rocks as shown in figures 3.32, 3.34, 3.36, 3.38 and 3.40 are quite distinct from one another. The pressure drop patterns resulted from simulations of those particles also showed that in the case of less permeable drainage, the pressure drop ends in lower values while in more permeable environment, the draw down ends up with higher magnitudes. Current laboratory analyses which do not involve true multiphase experiments (which do not use hydrocarbon gas), result in pressure drop predictions that are different from the pressure drop results in presence of gas in the liquid. Hence high uncertainty exists in the production prediction. This in turn might end up with erroneous reservoir production prediction whose impact may affect field development projects. As such errors associated with pressure drop predictions such as those resulted in gas-free analysis may affect investment and may jeopardize proper reservoir management.

To minimise uncertainties and to have a better understanding of fines particles impact on production, in this research pressure drops in high permeability sands were thoroughly studied and eventually comprehensive particle-damaged permeability models were developed for multiphase and liquid flow as explained in chapter 5. The models were tested and validated using several real field practices and field data with reasonable accuracy as demonstrated in chapter 6. As shown in the chapter, testing was done using non simulated data whereas validations were carried out using field data and field practices explained in sections 6.1.2 to 6.2.11. Ten conventional field practices using actual field well data were used to validate the developed models. The field practices involved standard oil field ~~-p~~ressure build-up", ~~-p~~ressure drawdown" and ~~-p~~ressure fall-off" surveys whose theories are explained in chapter 2. The testing and validation outcomes as demonstrated in chapter 6 suggest that the developed models are robust and are with acceptable accuracy. In few areas where large error margins were revealed, the models are not relevant e.g. when the multiphase model was compared with dry gas analysis. In this case the validation was verified as to investigate how far off the model will be. The fact that these particle-damaged permeability models do not exist; this research work contributed new additions to permeability knowledge. In addition incorporation of the models into a reservoir simulator to further minimise existing uncertainties in dynamic reservoir studies is another contribution to the current knowledge.

The oil and gas industry suffers significant production losses due to impairment of unconsolidated sandstone reservoirs caused by fine particles in multiphase flow within the reservoir as well as particles injected through the wellbore into the reservoir pore structures. As a result, reductions in oil and gas production as well as loss of well integrity due to

particle erosion occur. As such, with an objective of further reduction of particle migration risks on production, this research demonstrated the following:

The ability to carry out hydrocarbon simulation in a complex mixture of multiphase fluid and fines particles flowing together through porous media. Hence a better way to study hydrocarbon and fines flow and thus better production and prediction performances can be achieved.

Step-wise analysis of quantifying fines damage mechanisms were demonstrated in this research covering multiple sensitivities of rock and fluid properties to hydrocarbon reservoir scale. Today, neither experimental work nor numerical reservoir simulators have such unique capabilities.

Procedures and methodologies of how to create an integrated particle analyzing software package which incorporates fines grains flow simulator into hydrocarbon reservoir performance prediction simulator are among the research‘s major outcomes. So far no evidence exists on such attempts elsewhere.

While core laboratory analyses are limited to small core sample plugs with limited particle sensitivities analysis, this research work resulted in reservoir-wide study of particles, gas, liquid and major rock and fluids properties. Unfortunately, despite the fact that laboratory core samples are too small to represent the entire reservoir extent, their results are nevertheless scaled-up to the entire reservoir span. This renders core-based reservoir analysis results uncertain as far as risk assessment is concerned. More explanations on the limitations of reservoir simulators and core laboratory experiments are given in chapters 2, 3 and 5.

Therefore this research was carried out beyond the limitations currently faced by conventional laboratory analyses of core-flood experiments and reservoir simulations.

The study ended up with two developed fines particle-damaged permeability models. One model for multiphase granular flow and the other model for liquid granular flow. These are outlined in section 7.2 along with results comparisons between field practice and the model outcomes.

More importantly, the research outcomes helped in minimising existing uncertainties in quantifying the impact of fines particles on oil, water and gas production and prediction.

The research is concluded with several important outcomes. The following are conclusions highlighting the major achievements.

7.2 Conclusions

7.2.1 Damaged Permeability Models Development for 1000 mD Rock

Particle-damaged permeability models for liquid and multiphase were developed, tested and validated using field data. The following is the developed model for liquid conditions whose details are given in chapter 5 section 5.3.1:

$$\sum_{i=1}^{i=n} k_{di}(G_F) = \sum_{i=1}^{i=n} \left\{ \frac{\{-1*141.2(\mu)(\mathrm{B})(\mathrm{q})*(\ln(r_{ei}) - \ln(\mathrm{r_w}) + S - 3/4)\}}{\left\{0.0005(r_{ei}^{\,2}) - 3.0693(r_{ei}) - 140.42\right\} - \left\{\{(0.0003\,(r_{ei}^{\,2}) - 1.3426(r_{ei}) - 25.87)\}\,\frac{\{(100-(G_F-10))\}}{100}\right\}} \left\{\frac{1}{h}\right\} \right\}$$

This model's outputs and their comparisons to the CFD simulation results are shown in figure 7.1. The model can be used to calculate particle-damaged permeability in a porous medium in which various particle grain sizes flow in the hydrocarbon liquid including sizes beyond those simulated by the CFD as explained in section 5.3.1 and as shown in figure 7.2. The model was a result of studies of so many sensitivities and scenarios as explained in the preceding chapters whose outcomes were then combined, evaluated, tested and validated

using ten different well data and actual field analyses. The model's output revealed comparable output during validations using real data from several wells in various fields covering oil producers, water injectors and gas producers.

Distributions of damaged permeability curves per reservoir lateral length per particle size, were plotted as shown in figure 7.1.

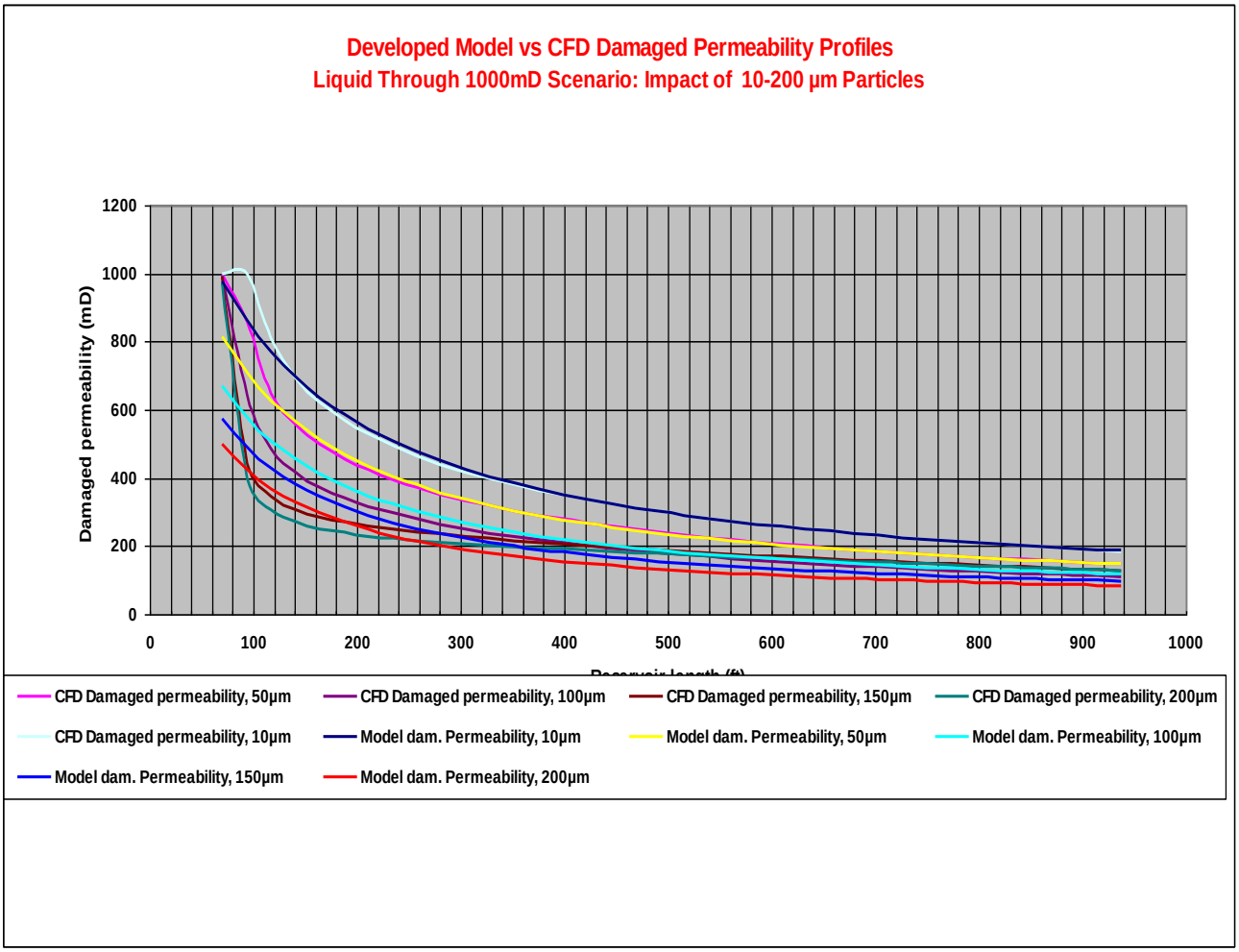

Figure 7.1: Model matching CFD Damaged Permeability profiles in a 1000 mD liquid scenario

Figure 7.2 shows the model's output of damaged permeability profiles across the simulated reservoir showing impacts of various non-simulated fines grain sizes on the initial absolute permeabilities. The grain sizes on the figure were not simulated, but the results reflect similar

profiles when grain size very close to the simulated ones were compared e.g. 55µm profile vs. 50 µm, 5 µm vs. 10 µm and so forth.

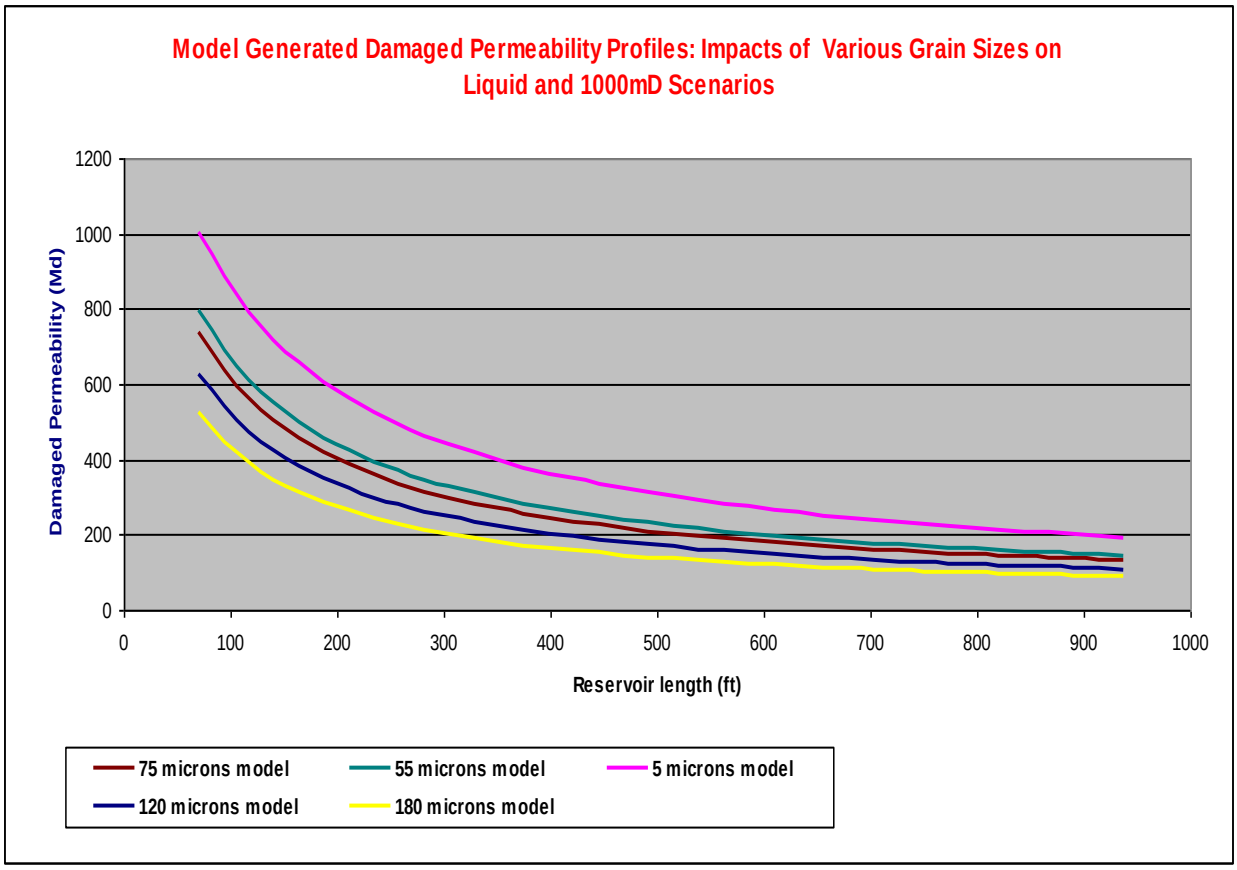

Figure 7.2: Model generated damaged permeability profiles of non-simulated grain sizes

The CFD drawdown pressure profiles were used in the Darcy equation (chapter 2, section 2.91) to calculate the corresponding absolute permeability (k_{abs}) as a function of grain size. The second developed model was for the scenario which involved multiphase sensitivities where gas fluid was added into the liquid keeping the rest of the parameters unchanged. In this case the developed damaged permeability per lateral reservoir length as a function of fines grain size in multiphase conditions as explained in chapter 5 section 5.4 is as follows:

$$\sum_{i=1}^{i=n} k_{di}(G_f) = \sum_{i=1}^{i=n} \left\{ \frac{\{-1*141.2(\mu)(B)(q)*(\ln(r_{ei}) - \ln(r_w) + S - 3/4)\}}{\{0.0007(r_{ei}^{\,2}) - 2.9365(r_{ei}) - 166.92\} - \left\{ \{(0.0004\,(r_{ei}^{\,2}) - 1.2916(r_{ei}) - 35.88)\} \dfrac{\{(100-(G_f-10))\}}{100} \right\}} \left\{ \frac{1}{h} \right\} \right\}$$

Figure 7.3 shows model results matching the CFD simulation results of particle-damaged permeabilities. Various particles grain sizes ranging between 10 and 200µm flowing in a multiphase scenario were simulated.

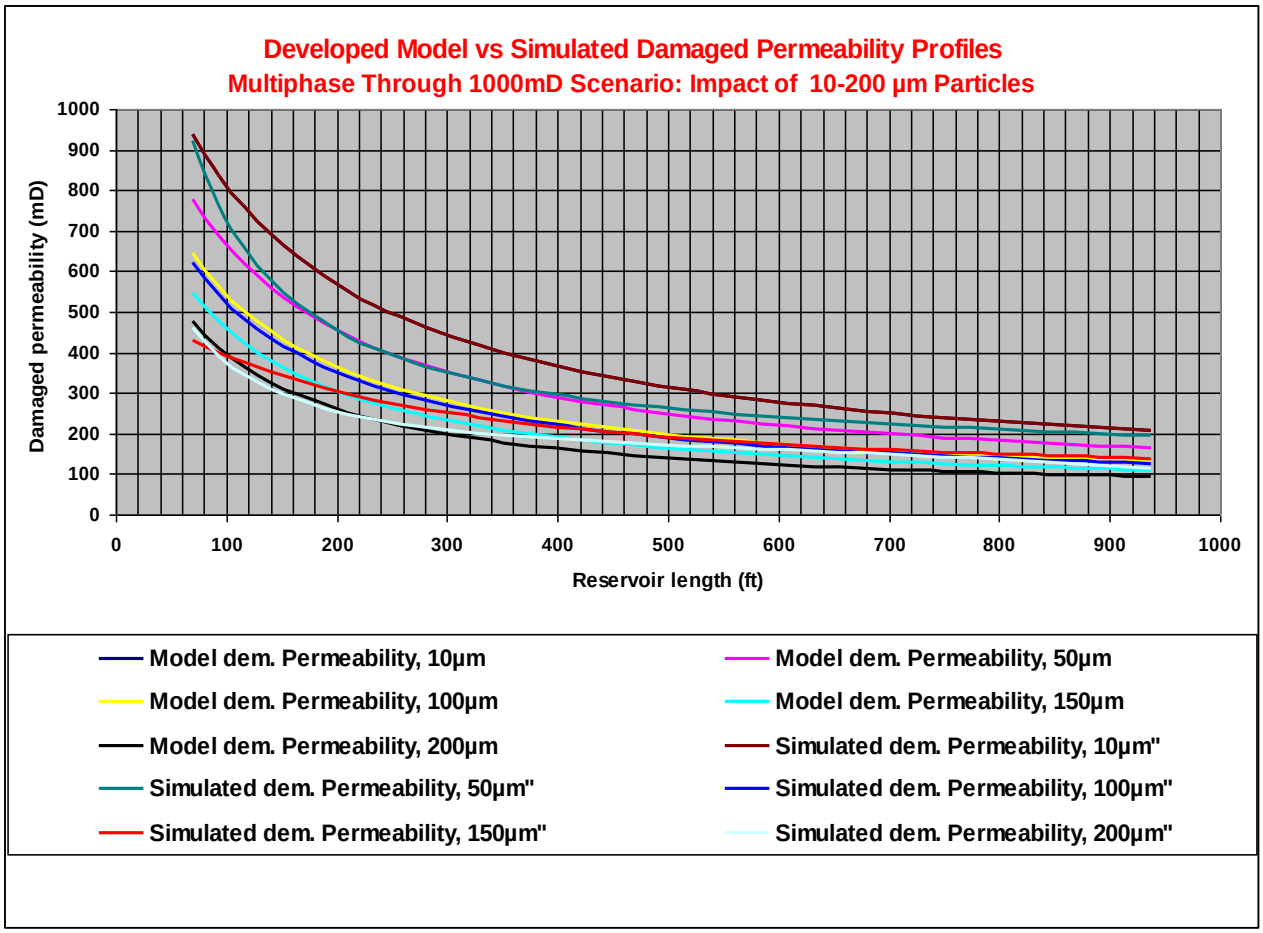

Figure 7.3: Matching CFD damaged permeability profiles in a 1000mD multiphase scenario

When the developed model was tested using grain sizes other than those simulated by the CFD, it revealed acceptable results.

Figure 7.4 shows the model output of damaged permeability profiles across the simulated reservoir model showing impacts of various fines grain sizes on the initial absolute permeabilities. The grain sizes in the figure were never simulated, but the results reflected similar profiles to the simulated ones. For details refer to section 5.4.

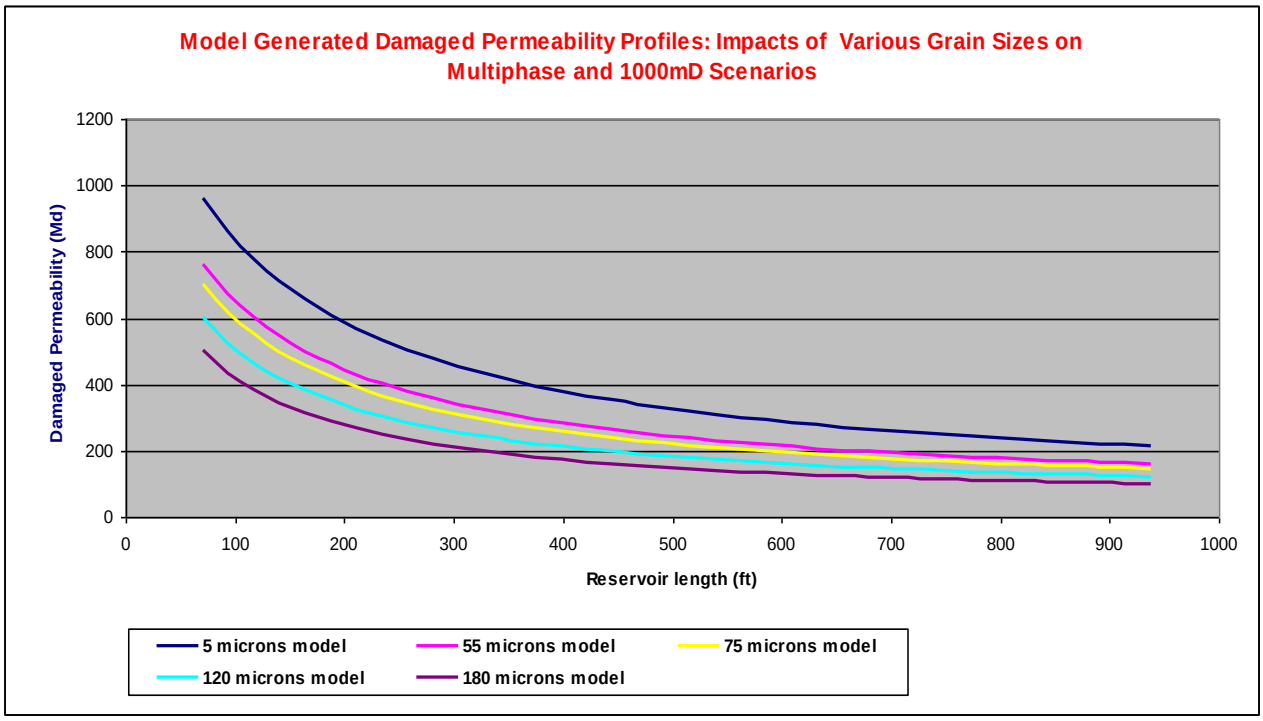

Figure 7.4: Multiphase model generated damaged permeabilities of un-simulated grain sizes

Model validations using ten different well pressure survey analyses were carried out as explained in chapter 6 sections 6.2.3 to 6.2.11. Figures 7.5 and 7.6 summarize results and comparisons of model's output with ten actual field analyses. While each survey resulted in a single permeability value according to field practice, the model calculated an array of permeabilities for each survey using the same pressure survey data.

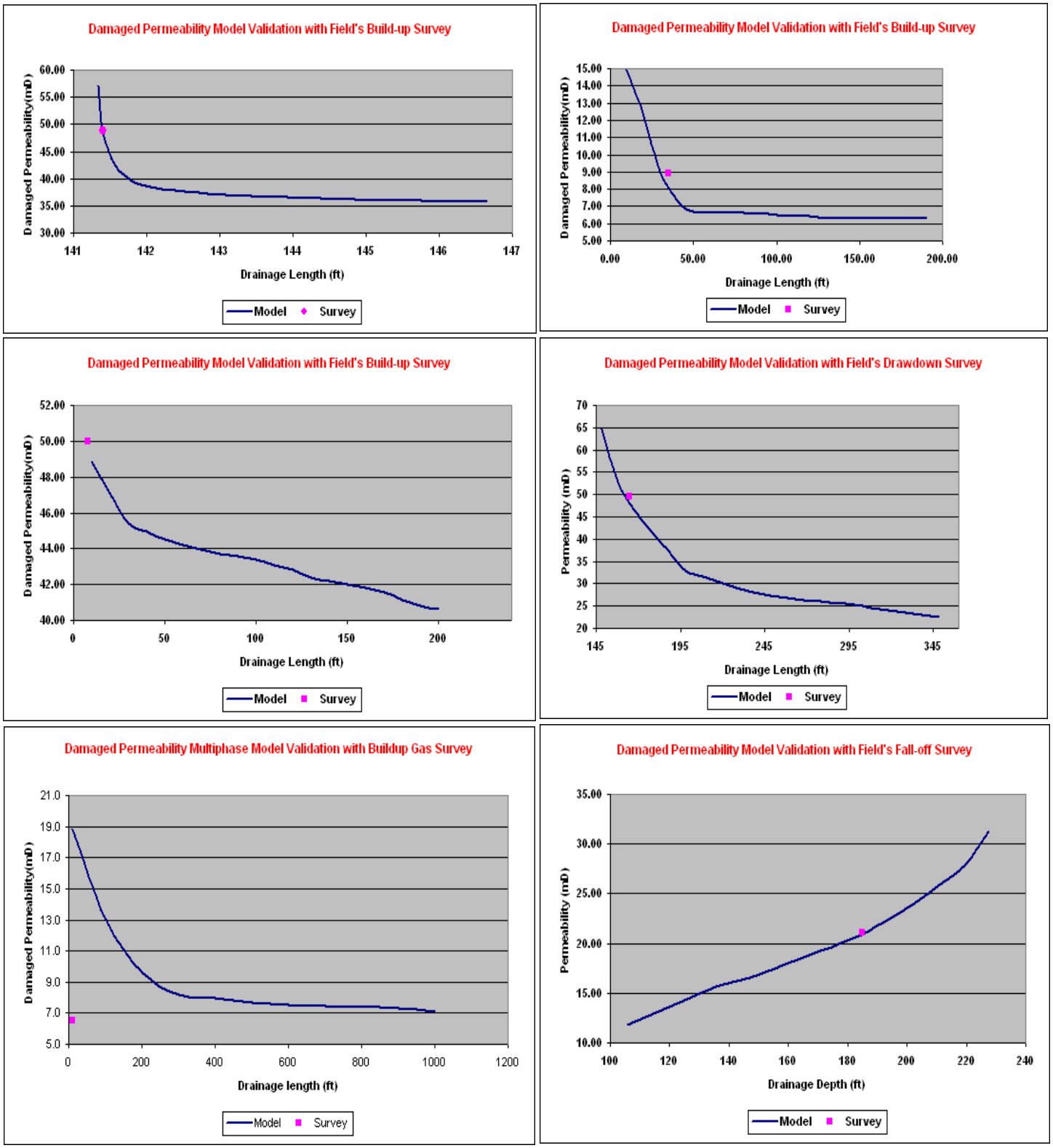

Figure 7.5: Model validation results using real field pressure survey data

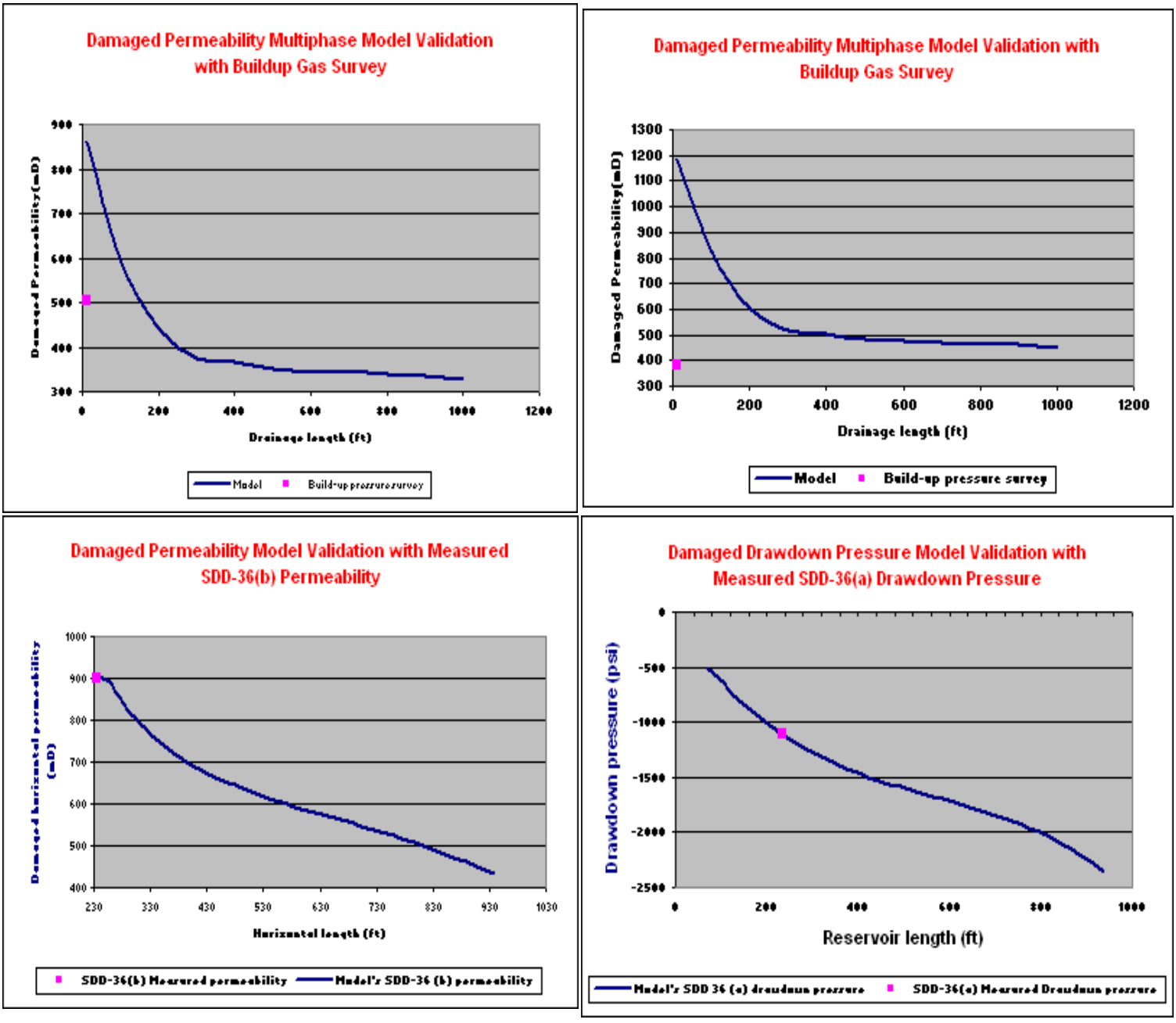

Figure 7.6: Model validation results using real field pressure survey data

As shown in table 6.29, reasonable % errors were revealed when results of ten different field‘s pressure build-up surveys, pressure drawdown surveys and fall-off survey were compared to the model‘s pressure and permeability results. However, of the three gas wells survey results compared, two of them revealed quite different results compared to the developed model results, reason being the multiphase conditions used in developing the model included a mixture of oil, water and gas while the field surveys compared were from a purely dry gas fluid analysis. It is very difficult to separate gas from condensate oil and water mixture at high pressure when flowing inside the reservoir. Another reason for the large difference between the multiphase model‘s result and the gas well survey result is given below in the model‘s assumption number six.

For the oil wells and water injection well, differences between the model results and field results could be due to assumptions used in the CFD which are summarised as follows:

1. The CFD modelling includes grain shape roundness of all
sizes whereas in the field, various shape sizes exist.

2. While in the field combinations of grain sizes flow together, in the CFD, it is assumed that one uniform particle size and shape flow at a time.

3. Temperature variations are assumed negligible in the CFD due to vertical depths being similar along the horizontal reservoir span hence similar geothermal gradient, while in the field temperature variations may occur even along the same reservoir horizon.

4. Fluid viscosity as a function of temperature may change in the field while in the simulation the viscosity variations may not occur since geothermal gradient is

considered the same at constant horizontal reservoir level having same corresponding vertical depth.

5. Assumptions related to the chemistry of the fluids may differ from the actual reservoir chemical reactions. For example water chloride content (salinity) changes may happen in the field whereas is constant in the model. Also chemical precipitates such as Ca2CO3, BaSO4, FeSO4, are possible in hydrocarbon reservoirs but are too complex to model.

6. Since this research focussed on high permeability reservoir which is usually associated with high production hence high reservoir pressures, in such reservoir conditions, gas is normally disolved in liquid solution where the pressure is above the bubble point. Only when the pressure reduces below the bubble point then gas is released out of solution and that can be away from the reservoir above the well. Bubble point pressure is the pressure at which the first bubble breaks out of solution. Based on that, CFD pressure simulations were carried out as part of multiphase flow as a mixture of oil, water, gas and particles. Since the presence of liquids inhibits dry gas effects on pressure drawdown and on permeability, that is why the three gas well validations revealed large error margins as shown in table 6.29. Hence one of the research suggestions for further work is to carryout simulations of dry gas migrated particles and their impacts on permeabilities at reservoir levels.

To further minimise errors caused by other factors, suggestions for further work are given in chapter 8. Overall research recommendations are proposed in section 7.3.

7.3 Recommendations

Having analysed particle impacts on pore structures and how to model resultant particle-damaged permeabilities, it is recommended to incorporate the resultant models into the 3D reservoir simulators substituting core sample permeability inputs and comparing results of this method with ongoing methods in terms of measured field production data. Hence, as far as reservoir performance prediction simulation is concerned, it is recommended not to use fixed constant permeability inputs or linear profiles in the reservoir simulator as that can cause unrealistic reservoir performance predictions. This is due to the fact that reservoirs are very heterogeneous with complex flow of multiphase fluid and fines particle mixtures. Despite the fact that presence of fines particles do affect permeability, today‘s reservoir simulators do not analyse particle impact on production prediction. Hence, it is time to stop the ongoing use of well-bore determined permeability which not only is assumed to represent the entire reservoir but also assumed to remain constant during the production phase regardless of fines migration effects. Degradation of permeability due to the particles flow with reservoir fluids across the porous medium has been demonstrated in this research work, hence mapping of such particle-damaged permeability across the reservoir is essential to minimise uncertainties. In this respect, it is recommended to incorporate a module which will compute fines effects on permeability and provide damaged permeability trends across the drainage areas which then become input to reservoir simulators for production performance predictions. In addition to these recommendations, chapter 8 focuses on suggestions for further work to be done to further improve the understanding of fines migration mechanisms in high permeability sands and their impacts on production and injection performances in

order to further minimise the uncertainties associated with particles influences occurring in the hydrocarbon reservoirs. .

Chapter 8

SUGGESTIONS FOR FURTHER WORK

It is suggested to carry out dry gas and solid particle CFD simulations to investigate dry gas impact on pressure drawdown and hence permeability at reservoir pressures below bubble point pressures. Dry gas impact in absence of liquid at reservoir conditions where the pressure is above the bubble point, is not easy to analyse since gas is usually disolved in liquid at above bubble point reservoir pressures. However, below that pressure gas breaks out of solution and moves freely and in the process may flow with particles.

To further develop this research work, it is suggested to study fines migrations phenomena and fines particle impacts to production and injection using a group of real rock pore distribution networks from one field as opposed to a single core mesh structure. That can be obtained by scanning real core plug samples or thin-sections from the same field then transferring the pore structure distributions from several samples into CFD via an irregular mesh generator package such as Gambit or others. Meanwhile it is also suggested that the same plug samples be analysed in special core lab analyses (SCAL) to determine all petrophysical parameters and then to compare the SCAL results with CFD outcomes. Then both results can be used separately in reservoir simulations. Outcomes of the simulations should be compared with actual well‘s production performance to determine which method resulted in a more realistic performance closer to the measured well‘s performance.

Also suggested is to carry out simulation sensitivities of multiple particle sizes and to model their impacts on production. The reason being various sandstone reservoirs contain multiple particle sizes which exist in each well.

In addition, it is suggested to develop a comprehensive all-in-one granular 3D reservoir simulator which can perform all particle and multiphase analyses and simulate all possible impacts on reservoir production and prediction performances. So far neither a commercial nor an academic simulator of such capability exists.

It is also suggested to investigate and carry out similar studies in unconventional operations such as enhanced oil recovery (EOR) practices involving miscible injected fluids, steam injection, very heavy oil (low ^{o}API grades) extraction, acid stimulation and others. In that way the impact of particles on reservoir performance can be quantified in any reservoir fluid type, hydrocarbon production, steam injection, as well as other EOR techniques.

Finally it is suggested to establish more comprehensive fines grain size and pore size downhole sensors which can more accurately measure downhole pore and particle sizes directly at the reservoir level and reservoir conditions. Sensors to be similar to or better than Scanning Electron Microscope (SEM) or Back-Scattered Electron (BSE) or at least Laser Particle Size Analyser (LPSA).

If the above suggestions are incorporated in further work, significant reductions in uncertainties are expected. However, due to the complex nature of the subject, even after that, additional investigations will be required and such a process is suggested to be continued.

References

1 Beard, D.C., and Weyl, P.K. *Influence of texture on porosity and permeability of unconsolidated sand*, 1973, AAPG Bulletin, vol. 57, no. 2, p. 349-369.

2 Krumbein, W.C., and Sloss, L. L. *Stratigraphy and Sedimentation*, 1963, 2nd edition Freeman publication.

3 Brown, R.B. *Soil and Water Science,* 2003, Institute of Agricultural Sciences, University of Florida.

4 Colmenares, F., Padron, A., Maraven, S. and Bennaceur, K. *Evaluation of Treatments for Control of Fines Migration in the Ceuta Field in Venezuela*, 1997, SPE Paper No. 38596.

5 Civans, F. *Predictability of Porosity and Permeability Alterations by Geochemical and Geomechanical Rock and Fluid Interactions*, 2000, SPE Paper No. 58746.

6 Prammer, M., Drack, E., Bouton, J., Gardner, J., Coates, G. and Chandler, R. *Measurements of Clay-Bound Water and Total Porosity by Magnetic Resonance Logging,* 1996, SPE Paper No. 36522.

7 Sachan, A. and Penumadu, D. *Identification of Microfabric of Kaolinite Clay Mineral Using X-ray Diffraction Technique*, 2007, Geotechnical and Geological Engineering, Springer Netherlands.

8 Durand, C. and Rosenberg, E. *Fluid distribution in kaolinite- or illite-bearing cores: Cryo-SEM observations versus bulk measurements*, 1996, Institut Francais du Petrole, SCA Conference Paper Number 9627.

9 Byrne, M.T., Spark, I.S.C. and Patey, I.T.M. *A Laboratory Drilling Mud Overbalance Formation Damage Study Utilising Cryogenic SEM Techniques,* 2000, SPE Paper No. 58738.

10 Recham, R. *Super-Critical Rate Based on Economic Recovery in Water and Gas Coning by Using Vertical and Horizontal Well Performance*, 2001, SPE Paper No. 71820.

11 Beard, D.C. and Weyl, P. K. *The influence of Texture on Porosity and Permeability of Unconsolidated Sand*, 1973, Bull. Am. Ass. Petrol. Geol. 57, p.p. 349-369.

12 Pietro, P., and Gijs, O. *Acoustic Removal of Colloidal Particles From Berea Sandstone,* 2004, SPE Paper No. 86490.

13 Bauder, V. *Reservoir permeability and porosity in the House Creek field: Sussex "b" sandstone heterogeneity,* 1981, U. S. Geological Survey Digital Data Series DDS-33.

14 Tillman, R.W., and Martinsen, R.S. *Sedimentologic model and production characteristics of Hartzog Draw field, Wyoming*, 1987, Society of Economic Paleontologists and Mineralogists Special Publication No. 40, p.p. 15-112.

15 Vásquez, H., Sánchez, D. and Yánez, R.L. *The Diagnosis, Well Damage Evaluation and Critical Drawdown Calculations of Sand Production Problems in the Ceuta Field, Lake Maracaibo, Venezuela,*1999 SPE Paper No. 54011.

16 Scheldt, T. and Havmøller, O. *Quantifying the effect of waterbreakthrough on sand strength and sand production*, 2006, Oil & Energy.

17 Wenrong, M., Shihong, S., Tianhua, L., Wenzhong, L. and Guoheng, H. *Pore and throat network model and its application to the optimal selection of temporary plugging particles*, 1996, International symposium on formation damage control.

18 Aitken, J.F., Millson, J. A., Fryberger, S.G., Rovira, A., Skaloud, D., Al-Shuaily, H., Al-Habsy, A., Al-Harthy, M., Ugwu, C., Singh, B.N. and Vaddey, S. *The Barik Sandstone Member, Northern Oman: Stratigraphic Traps and Review of a Tight Gas Play,* 2008, GEO Middle East Conference and Exhibition.

19 Poynton, N., Tidswell, R., and Steele, J. *Squeezing Aqueous Based Scale Inhibitors into a Water Sensitive Reservoir Development of a Squeeze Strategy*, 2000, SPE Paper No. 60219.

20 Recham, R. *Super-Critical Rate Based on Economic Recovery in Water and Gas Coning by Using Vertical and Horizontal Well Performance*, 2001, SPE Paper No. 71820.

21 Schechter, R.S. *Oil Well Stimulation,* 1992, Englewood Cliffs, Prentice Hall.

22 Wagner, M., Webb, T., Maharaj, M., Twynam, A., Green, T., Salamat, G. and Parlar, M. *Horizontal Drilling and Openhole Gravel Packing With Oil-Based Fluids—An Industry Milestone*, 2006, SPE Paper No. 87648-PA.

23 Rahman, S., Aziz, A. and Hong, C. *Prediction of Critical Condition for Fines Migration in Petroleum Reservoirs*, 1994 SPE Paper No. 28760.

24 Nguyen, P. D., Ingram, S. R. and Gutierrez, M. *Maximizing Well Productivity Through Water and Sand Management: A Combined Treatment*, 2007, SPE Paper No. 106592-MS.

25 Smith, C.R., Tracy, G.W. and Farrar, R.L. *Applied Reservoir Engineering*, OGCI. 1992. Chp.13. p.3.

26 Van Everdingen, A.F., and Hurts, W. *The application of Laplace transformation in flow problems in reservoirs,* 1946, Trans. AIME, 186, p.p. 305-324.

27 Barenblat, G.I. and Entoy, V.M. *Theory of Fluid Flows Through Natural Rocks*, 1990, Kluwer.

28 Geilikman, M.B., Dria, D.E., Stewart, D.R. and Wong, G.K. *Bean-up Guidelines for Sand-Control Completions*, 2005, SPE Paper No. 95870.

29 Moreci, M. *Beyond Propaganda: Oil giant BP greenwashes Alberta tar sands,* 2006, GCM.

30 Amory, M.E. *Sand Prediction*, 1990, The Hague: Shell International. p.p. 5 – 25.

31 Duey, R. *Marathon scores big with risky move,* 2004, Hart Energy Publishing.

32 McPhee, C., Farrow, C. and McCurdy, P. *Challenging Convention in Sand Control: Southern North Sea Examples*, 2006, SPE Paper No. 98110-MS.

33 Brenner, B. *3-D Reservoir Characterization of the House Creek Oil Field, Powder River Basin, Wyoming,* 1978, V1.00, U. S. Geological Survey Digital Data Series Dds-33.

34 Nagy, V., and Vas, L. M. *Pore Characteristic Determination with Mercury Porosimetry in Polyester Staple Yarns,* 2005, Budapest University of Technology and Economics.

35 Jena, A. and Gupta, K. *Liquid Extrusion Techniques For Pore Structure Evaluation of Nonwovens,* 2003, Porous Materials, Inc., International Nonwovens Journal, p.p. 45-53.

36 Dullien F. A. L. *Porous media: fluid transport and pore structure*, 1992, 2nd ed. San Diego: Academic Press.

37 Macdonald M. J., Chao-Feng, C., Guilloit, P. P. and Ng, K. M. *A generalized Blake-Kozeny equation for multisized spherical particles*, 1991, Univ. Massachusetts, dep. chemical engineering, vol. 37, no10, p.p. 1583-1588.
38 Coberly, C.J. and Wangner E.M. *Some Considerations in the Selection and Installation of Gravelpack for Oil Well,* 1938, API Tech., Paper No. 960.
39 Carman, P.C. *Fluid-flow through granular beds,* 1973, Trans. Inst. Chem. Eng., Vol. 15, p.p. 150-166.
40 Carman, P. C. and Kozeny, P. C. *Fundamental Principles of Industrial Filtration*,1938, Trans. Institute of Chemical Engineers, vol. 16. p.p. 168 -188.
41 Cargnel, R.D., Luzardo, J. P. *Particle Size Distribution Selection of CaC03 Drill-In Fluids: Theory and Applications,* 1999, SPE Paper No. 53937.
42 Pautz, J. F. and Crocker, M. E. *Relating Water Quality and Formation Permeability to Loss of Injectivity*, 1989, SPE Paper No. 18888
43 Prince, L. R. and Henry II, W. A. *Measurement of Pore Size And Porosity,*1972, American Standard Inc. NY.
44 Allen, T., *Particle Size Measurement*, 1968, Chapman and Hall, London.
45 Oyeneyin, M.B., Bigno, Y. and Peden, J. M. *Investigations of Pore blocking mechanisms in gravel packs in the management and control of fines migration.* 1994. SPE Paper No. 27342.
46 Kaufmann, J. *Experimental identification of damage mechanisms in cementitious porous materials on phase transition of pore solution under deicing salt attack*, 2000, Swiss federal laboratories for materials testing and research, , vol. no 248, p.187.
47 Bennion, D. B. *Formation Damage in Production and Injection Wells*, 2000, Hycal Energy Research Laboratories.
48 Bergosh, J. L., Wigglns, R. B., Ennlss, D. O. and Jones, A.H. *Mechanisms Of Formation Damage In Matrix Permeability Geothermal Wells*, 1981,Terra Tek Inc.
49 Abrams, A. *Mud Design to Minimize Rock Impairment Due to Particle Invasion*, 1977, Journal of Petroleum Technology, p.p. 586-592.
50 Van Velzen, J. F. G. and Leerlooijer, K. *Impairement of a water injection well by suspended solids: Testing and prediction*, 1992, SPE Paper No. 23822.
51 Pautz, J. F. and Crocker, M. E. *Relating Water Quality and Formation Permeability to Loss of Injectivity,* 1989, SPE Paper No. 18888.
52 Zhang, N. S., Somerville, J. M. and Todd, A. C. *An Experimental Investigation of The Formation Damage Caused by Produced Oily Water Injection*, 1993, SPE Paper No. 26702.
53 Economides, M. J., Hill, A.D. and Ehlig-Economides, C. *Petroleum Production Systems: Formation Damage Mechanism*, 1994, Prentice Hall. p.p. 106-107.
54 Patchett, J.G. and Coalson, E.B. *The determination of porosity in sandstone and shaly sandstone, part 2: effects of complex mineralogy and hydrocarbons*,1982, 23rd Annual SPWLA Logging Symposium.
55 Karacan, C. O., Grader, A. S. and Halleck, P. M. *Mapping of Permeability Damage Around Perforation Tunnels*, 2001, Pennsylvania State University.
56 Millhone, R.S. *Completion Fluids –Maximizing Productivity,* 1982, SPE Paper No. 10030.

57 Suryanarayana, P.V., Wu, Z., Ramalho, J. and Himes, R. *Dynamic Modeling of Invasion Damage and Impact on Production in Horizontal Well*, 2005, SPE Paper No. 95861
58 Economides, M. J. *A Practical Companion to Reservoir Stimulation,* 1992, Elsevier, Amsterdam.
59 Economides, M. J. *A Practical Companion to Reservoir Stimulation*, 1992, Elsevier, Amsterdam.
60 Barkman, J. H. and Davidson, D. H. *Measuring Water Quality and Predicting Well Impairment*. Journal of Petroleum Technology, July 1972, pp. 865-873.
61 Gruesbeck, C. and Collins, R. E. *Partic1e Transport Through Perforations*. Soc. Petrol. Engineer. Journal., 1982, p.p.857-865.
62 Wojtanowicz, A., Krilov, K., Z. and Langlinais, J. P. *Study on The Effect of Pore Blocking Mechanisms on Formation Damage*, 1987, SPE Paper No. 16233.
63 Donaldson, E. C., Baker, B. A. *Particle Transport in Sandstone*, 1977, SPE Paper No. 6905.
64 Vetter, O. T., Kandarpa, V., Stratton, M. and Veith, E. *Particle Invasion Into Porous Medium and Related Injectivity Problems*, 1987, SPE Paper No. 16255.
65 Oyeneyin, M. B., Pedden, J.M., Hosseini, Ali and Ren, G. *Factors to Consider in the Effective Management and Control of Fines in High Permeability Sands*, 1995, SPE Paper No. 30112.
66 Tague J.R. *Overcoming Formation Damage in Heavy Oil Fields: A Comprehensive Approach*, 2000, SPE 62546. p.p. 2-3.
67 Amory, M.E. *Sand Control: Why, When and Which Type?* 1990, The Hague: Shell International. p.p. 25 – 33.
68 Hartmann, D. J., Edward A. B, and Coalson E. *Predicting Sandstone Reservoir System Quality and Example of Petrophysical Evaluation*, 1999, Treatise of Petroleum Geology: Handbook of Petroleum Geology.
69 Wilson, M.D. *Reservoir Quality Assessment and Prediction in Clastic Rocks,* 1994, SEPM Short Course 30, p.p. 183-208.
70 Sneider, R.M., and King, H.R. *Integrated rock-log calibration in the Elmworth field, Alberta, Canada,* 1984, AAPG Memoir 38, p. 205-214
71 Nasr-El-Din, H. A. *Formation damage induced by chemical treatments : Case histories*, 2005, Saudi Aramco R&D, Journal of energy resources technology, vol. 127, no 3, p.p. 214-224
72 Ferguson S. E., Moyes P. B. *Preventing fluid losses in ESP well completions : Avoid formation damage and improve pump life,* 1997, Asia Pacific oil & gas conference & exhibition, ETATS-UNIS, p.p. 225-233.
73 Churcher, P. L., Yurkiw, F. J., Bietz, R. F. and Bennion, D. B. *Properly designed underbalanced drilling fluids can limit formation damages,* 1996, Oil and Gas Journal, p.p. 50-55.
74 Mason, D., Evans M., Ekamba, B. and Jones, C. *Long-Term Performance of Sand-Control Completions in the Mokoko-Abana Field, Cameroon,* 2007, SPE No. 111005-PA.
75 Amory, M.E. *Sand Prediction*. 1990, The Hague: Shell International. p.p. 5 – 25.

76 McKay, G., Bennett, C. and Gilchrist J.M. *High Angle OHGP's in Sand/Shale Sequences: A Case History Using a Formation Drill-In Fluid,* 2000, SPE Paper No. 58731 .
77 Bennett, C., Gilchrist, J.M., Piton, E., Burton, R.C., Hodge, R.M., Troncoso, J., Ali, S.A., Dickerson, R., Price-Smith, C. and Parlar M. *Design Methodology for Selection of Horizontal Open-Hole Sand Control Completions Supported by Field Case Histories,* 2003, SPE Paper No. 85504
78 Mujaini, R. and Stevenson, E. *Well Impairment Management Strategy for PDO*. Muscat: PDO Printing Press, 2001. p.p. 8-17.
79 Amory, M.E. *Sand Prediction*. The Hague: Shell International. 1990.
80 McFadyen, K. *Rock mechanical tests for sand influx prediction,*1990, Sand control, SIPM, p.p. 53-56.
81 Wildg, A. *Research on the prediction and detection of sand production – Final report,*1980, vol. 1., EP 51935, SIPM.
82 Okorie, E. *Sand Control Review: Santa Barbara field development*, 2003, SPDC.
83 Van Den Hoek, P. J., Hertogh, G. M. and Kooijman, A. P. *A new Concept of Sand Production Prediction: Theory and Laboratory Experiments,* 1996, SPE Paper No. 35418.
84 Amory, M.E. *Sand Prediction*. The Hague: Shell International. 1990. p.p. 6 – 40.
85 Oyeneyin, B.M. and Faga, A.T. *Formation-Grain-Size Prediction Whilst Drilling: A Key Factor in Intelligent Sand Control Completions,* 1999, SPE Paper No. 56626.
86 Faga, A.T. and Oyeneyin, B.M. *Effects of Diagenesis on Neural-Network Grain-size Prediction,* 2000, SPE Paper No. 60305.
87 Dake, L.P. *Darcy's Law Applications*. Fundamentals of reservoir engineering, 1978, Elsevier SPC, p.p. 116-120.
88 Dake, L.P. *Oil Well Testing*. Fundamentals of reservoir engineering, 1978. Elsevier SPC, p.p. 166-170.
89 Al Mufarji, S.S. *Optimum Production Management,* AL ABRAJ Newsletter (Magazine), 2005, Issue 9, April-June. p. 3.
90 Dake, L.P. *The Mathew, Brons, Hazebroek Pressure Buildup Theory*. Fundamentals of reservoir engineering, 1978. Elsevier SPC, p.p. 179 -201.
91 Beggs, H.D., *Gas reservoir Performance, Transient Tests*, 1985, Gas Production Operations. OGCI Publications, p.p. 70 – 76.
92 Joshi, S.D. *Augmentation of well Productivity Using Slanted and Horizontal Wells,* 1986, SPE 15375.
93 Babu, D.K. and Odeh, A.S. *Productivity of a Horizontal Well*, 1989 SPE Res. Eng., p.p. 417 – 421.
94 Fluent Inc. Fluent 4.5. *Eulerian Multiphase Enhancements*, *chapter 3*., Lebanon (USA): Fluent Inc. Press. 1999.
95 Fluent Inc. Fluent 4.4 *User's Guide: Chapter 1*. Lebanon (USA): Fluent Inc. Press. 1997. p. 1.
96 Fluent Inc. Introduction to Fluent 4.4 *User's Guide: Chapter 1*. Lebanon (USA): Fluent Inc. Press. 1997. p. 2.
97 Fluent Inc. *Program Structure: Chapter 1.* Lebanon (USA): Fluent Inc. Press. 1997. p. 5.

98 Fluent Inc. Fluent 4.4 *User's Guide: Chapter 19*. Lebanon (USA): Fluent Inc. Press. 1997.
99 Fluent Inc. Fluent 4.4 *User's Guide: Chapter 14*. Lebanon (USA): Fluent Inc. Press. 1997.
100 Etter, D.M. and Kuncicky, D.C. *Introduction to MATLAB for Engineers and Scientists,* 1966, Prentice Hall. The MathWorks Inc.

101 Mason, D., Evans M., Pena, C.M., Cameron, J. and Jones, C. *A Comparison of Performance of Recent Sand Control Completions in the Makoko Abana field Offshore Cameroon*, 2005, SPE paper No. 94651.
102 Fluent Inc. Fluent 4.4. *Chapter 6: Porous media modeling* ., Lebanon (USA): Fluent Inc. Press. 1997.p.p. 179-183.
103 Fluent Inc. Fluent 4.5. *Chapter 3: Wall Boundary conditions for Solid Velocity*., Lebanon (USA): Fluent Inc. Press. 1998.p.p. 11-12.
104 Fluent Inc. Fluent 4.0. *Chapter 11: Particle Trajectory Calculations*., Lebanon (USA): Fluent Inc. Press. 1997.p.p. 5.
105 Fluent Inc. Fluent 4.0. *Chapter 11: Particle Trajectory Calculations*., Lebanon (USA): Fluent Inc. Press. 1997.p.p. 7.
106 Fluent Inc. Fluent 4.0. *Chapter 11: Calculation Procedures for the Dispersed Phase*., Lebanon (USA): Fluent Inc. Press. 1997.p.p. 92 - 124.
107 Fluent Inc. Fluent 4.4. *Chapter 3: Fluid Molecular Viscosity*., Lebanon (USA): Fluent Inc. Press. 1998. p. 25.
108 Jones A., Mujaini, R. and Stevenson, E.. *Well Impairment Management Strategy for PDO*, 2001, PDO Printing Press, p.p. 10 – 25.
109 Ismail, I. and Babu, J. *Analysis Of Formation Damage Caused By Oil-Basedmud On Berea Sandstone Using SEM*, 2004, Journal of Technology, 4, p.p. 65-76.
110 Amory, M.E. *Sand Control: Why, When and Which Type?* The Hague: Shell International, 1990. p.p. 25 – 33.
111 Al Mufarji, S.S., Oyeneyin, M.B. and Jihan, S. *Optimizing Production from Fractured Damaged Reservoirs*, 2004, SPE Paper No. 91971
112 Al Mufarji, S.S., Oyeneyin, M.B. and Jihan, S. *Optimal Production Management in Unconsolidated Mature Sandstone Environments*, 2005, SPE Paper No. 91987
113 Dake, L.P. *Two phase flow: Effective and Relative Permeabilities*. Fundamentals of reservoir engineering, 1978. Elsevier SPC, p.p. 121-124.
114 Smith, C.R., Tracy, G.W. and Farrar, R.L. *Applied Reservoir Engineering*, OGCI. 1992. Chp.12. p.2-4.
115 Al Mufarji, S.S. *Fines migration & Solid intrusion Effects on Reservoir Permeability & Formation Damage*, 2004, Poster presentation in Mature Reservoirs SPE Forum-Muscat.
116 Koninklijke/Shell. *Simulation of Fractured Reservoirs: MoReS Technical Reference Manual*. Rijswijk,1992 SIPM.
117 Koninklijke/Shell. *MoReS Technical Reference Manual*,1992, Rijswijk, SIPM.
118 Shell SIPM. *MoReS Online Users Manual: General Description of MoReS*, 1997, Rijswijk, SIPM.

119 Shell SIPM. *Aquifer Models: MoReS Reservoir Simulator*, 1992, Rijswijk, SIPM.
120 Shell SIPM. *Physical Processes in a Fractured Reservoir Dual Continuum Approach*, 1993, Rijswijk SIPM.
121 Smith, C.R., Tracy, G.W. and Farrar, R.L. *Applied Reservoir Engineering*, 1992, OGCI. Chp.16. p.19-22.

Appendix A-1: Fluent's CFD commercial applications in various industries

According to FLUENT Inc., –Almost every industry that involves advanced engineering uses CFD. Its use is rapidly expanding, and more engineers use Fluent's CFD software worldwide than any other technology".

A-1.1 Applications in the Oil & Gas industry

Downhole Analysis

Drilling

Emission Control

Gas Dispersion/Accumulation

Hazard Assessment

Multiphase Flows

Pipeline Flow Analysis

PWFD Performance

Reaction

Seals

Separation

Sub-sea Safety

Valves

A-1.2 Fluent's CFD applications in other industries

AEROSPACE

APPLIANCES

AUTOMOTIVE

BIOMEDICAL

CHEMICAL PROCESS

HVAC&R

GLASS

MIXING

POWER GENERATION

SEMICONDUCTOR

TURBOMACHINERY

Advances in Fluent CFD

Special physics are available if one of the fluids is granular such as solid fines particles. In many cases, the more economical mixture model can be used for granular and non-granular mixtures as well. Three-phase mixtures (liquid, granular, and gas) can be modeled, so simulations of slurry bubble columns and trickle bed reactors are now possible. Heat and mass transfer between phases can take place, making homogeneous and heterogeneous reactions possible. Several other multiphase models are also standard in FLUENT. For some multiphase applications, such as spray dryers, coal furnaces, and liquid fuel sprays, the discrete phase model (DPM) can be used. Injections of particles, bubbles, or droplets can undergo heat, mass, and momentum transfer with the background fluid. The volume of fluid model is available for free surface flows, such as ocean waves, where the prediction of the interface is of interest. The cavitation model has proven useful for modeling hydrofoils, pumps, and fuel injectors. Boiling can be implemented though readily available user-defined functions.

Appendix A-2: Summary of MoReS features

1. Several types of one, two and three dimensional grids can be defined, or imported from ~~"in~~clude" files such as: GEOCAP, SPIDER, FloGrid, GRID100 or Gridder:

a) Generalised corner point grids, in which every grid block has eight arbitrary corner points.

b) Top map grids, in which an arbitrary XY-map of the top-horizon is repeated through all layers.

c) Box grids, in which the spacing along each of the X,Y,Z axes independently is repeated throughout the grid.

d) Radial grids, a box grid in which the Y-axis is replaced by an angle around a well bore.

e) Fully unstructured grids can be imported from FloGrid together with associated properties (but does not rigorously support all other MoReS features yet)

2. Special connections are supported in all grids, allowing for flow between grid blocks that are not topologically connected (e.g. for modelling faults, pinch out layers)

3. Nested local grid refinements (e.g. for advanced well test simulations)

4. Void blocks are supported in all grids.

5. An unlimited number of different regions in the grid for area dependent initialisation, modelling of rock and fluid properties, and calculating of aggregate data.

6. Two- and three-phase relative permeability, capillary pressure and surface tension modelling with hysteresis.

7. Segregated and diffuse flow.

8. Several PVT modelling options:

- single phase

- two-phase water-oil, water-gas and gas-oil

- three phase black oil, volatile oil, MoReS-PX

- multi-phase polymer floods, slug flows

- multi-phase equation of state (Peng-Robinson, …)

- multi-phase thermal and iso-thermal

- K-values

- single-tracer PVT-tracking

Data can be imported from Libra and in Eclipse format.

9. Dual porosity modelling with gravity drainage, gravity imbibition, incorporating a forward discretisation of the flow equations.

10. Pressure/Saturation initialisation, hydro-static initialisation, composition vs. height.

11. Region based total fluids and mobile fluids in place computations.

12. Static and dynamic pseudos calculation and application.

13. Chemical reactions (e.g. for reservoir souring)

14. Passive dye tracers on components and phases (e.g. for underground storage studies, gas cycling)

15. Pressure and flux boundary conditions for sector modelling.

16. Vertical, inclined, horizontal and multi-lateral wells, with per interval production/injection reporting. Symmetry wells.

17. Peaceman inflow modelling as well as K,dH from PI

Skin friction, well-bore storage modelling, cross-interval flow, down-hole chokes, smart well functions.

18. Various types of lift tables, which can be imported from WePS and VFP.

19. Pressure and rate constraints on wells, advanced well control depending on flow ratios.

20. History matching option honouring well status or interpolating cumulative rates.

21. Lumping and de-lumping well rates at the tubing head, allowing multiple reservoirs with different fluid characterisations to deliver in a single network of surface facilities.

22. Surface network facilities with gathering stations, separators, distributors, under-water manifolds, trunk lines.

23. Heuristic and Simplex linear programming optimisation of surface networks, automatically driving well control.

24. Advanced time-step control and recurrent data handling with the use of monitors.

25. Fully implicit solver with CG and ORTHOMIN preconditioning. Multi-grid option, domain decomposition, parallel option. Adaptive Implicit solver planned for 2002.

26. Powerful and flexible FrontEnd data management, data processing and Graphical User Interface.

27. Intimate link with IMath providing advanced control over multiple scenario management, well test simulation, history matching, integrated static and dynamic modelling and corporate field management.

28. Bi-directional link with Reduce++, providing dynamic up scaling.

29. Link with the PDS data store through TIES, for import of well deviation data, production data etc.

30. Eclipse models can be imported, converting automatically reservoir architecture, initialisation data and PVT data.

Appendix A-3: Collaboration establishment

Shell U.K. Limited

14 October 1998

Director of Studies
The Robert Gordon University
Mechanical & Offshore Engineering Department
ABERDEEN

For the attention of Dr. M.B. Oyeneyin

Switchboard

Sender's Direct Line Information
Tel 817635

Fax 817700
e-mail

Dear Sir

COLLABORATION ESTABLISHMENT

Research in "Modeling Fines Migration in High Permeability Sands" undertaken by our staff Said S. Al-Mufarji working for North Cormorant field, is of interest to the Shell UK Exploration and Production. Shell is willing to support this research by allowing Said to use Shell's proprietary reservoir modelling and sand analysis softwares. He may also use some field data. While results of these data can be shared, the algorithms in these models will remain confidential to Shell. Apart from that there is no obligation from Shell to provide any further facilities.

Yours faithfully

W.G. Townsley
Development Asset Team Leader: North Cormorant/Eider

Appendix A-4: MATLAB software used in trends matching

In order to closely study the trends of the particle-damage permeability profiles, a software called MATLAB (100) described in chapter 3 was used. Hence the CFD-generated pressure drops from which permeability profiles were calculated, were analysed using MATLAB as explained below. MATLAB is often used in the studies of graphical curve trends in order to extrapolate future predictions.

MATLAB software was employed to match and predict simulation output curves generated by the Computational Fluid Dynamics (CFD) package. It was used due to its comprehensive data analysis capability which can be used for building custom graphical user interfaces as well as functions for integrating MATLAB based algorithms with other applications for trends analyses. In addition, MATLAB software can be used to provide detailed mechanistic and predictive models from complex trends using analyses such as 1) Linear Regression Line, 2) Power Equation, 3) Saturation Growth, and 4) Fitting Multiple Regression.

Simple forms of corresponding MATLAB correlations are as follows:

$Y = -0.2937X + 1001.3201$ ***Fitting Linear Regression Line*** *………………………… (1)*

$Y = 6084.374X^{-0.3262}$ ***Fitting Power Equation*** *………………………………………………(2)*

$Y = 551.5759\left\lfloor \dfrac{X}{-95.6828 + X} \right\rfloor$ ***Fitting Saturation Growth*** *……………………………(3)*

$Y = 1062.9786 - 0.4506X + 0.0001X^2$ ***Fitting Multiple (Parabola) Regression****….(4)*

These equations are from the CFD data and were used to draw graphs shown below in figures 1 and 2. As shown in figures, the best correlation was the ―Fitting Multiple Regression" which was used to determine matching trends for various grain sizes (10 – 200 µm) and

permeabilities of 1000 mD and 2000 mD. From the matching correlation, universal model was developed. Below are examples of the scenarios analysed. This page and the next one are not well presented – whole pages are muddled.

The last matching technique (equation 4) as shown in figure A.1 provided almost a perfect fit. In figure 1, the blue curves are the simulation results data for a 10 microns grain diameter flowing in a liquid medium through a 1000 mD sand-face absolute permeability rock. Red plots are MATLAB matching trends (100).

Impact of 10 µm fines particles on permeability: 1000 mD scenario

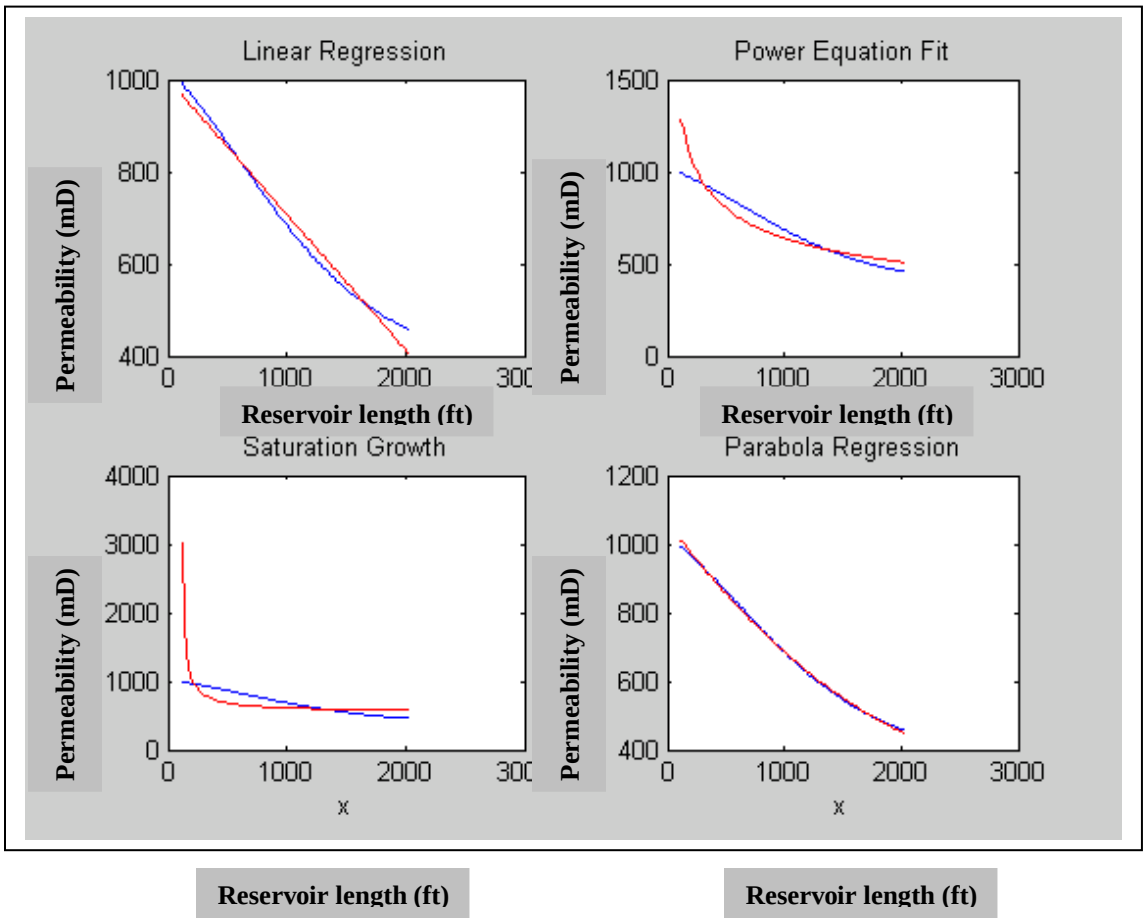

Figure A.1: Fitting 10 µm, 1000 mD liquid scenario CFD results using MATLAB

Based on matching performance, parabola regression was selected and was the basis for sensitivity profile matching. From the resultant matching correlation which was further analyzed, and per the analysis explained in chapter 5, a model was developed The correlation was further analysed to studying impact of all fines particle sizes (10 – 200 μm) on permeability. As shown in chapter 5, several analyses were carried out in the process of developing the particle-damaged permeability model in the liquid scenario. Each grain size revealed its own distinct permeability curve along the reservoir model.

Figure A.2 shows profile matching for a 10 μm fines grain size sensitivity in a multiphase medium as well as in a liquid medium for both 1000 mD and 2000 mD rock scenarios. In the figure, the y axis represents permeability in mD and the x axis represents reservoir length in feet.

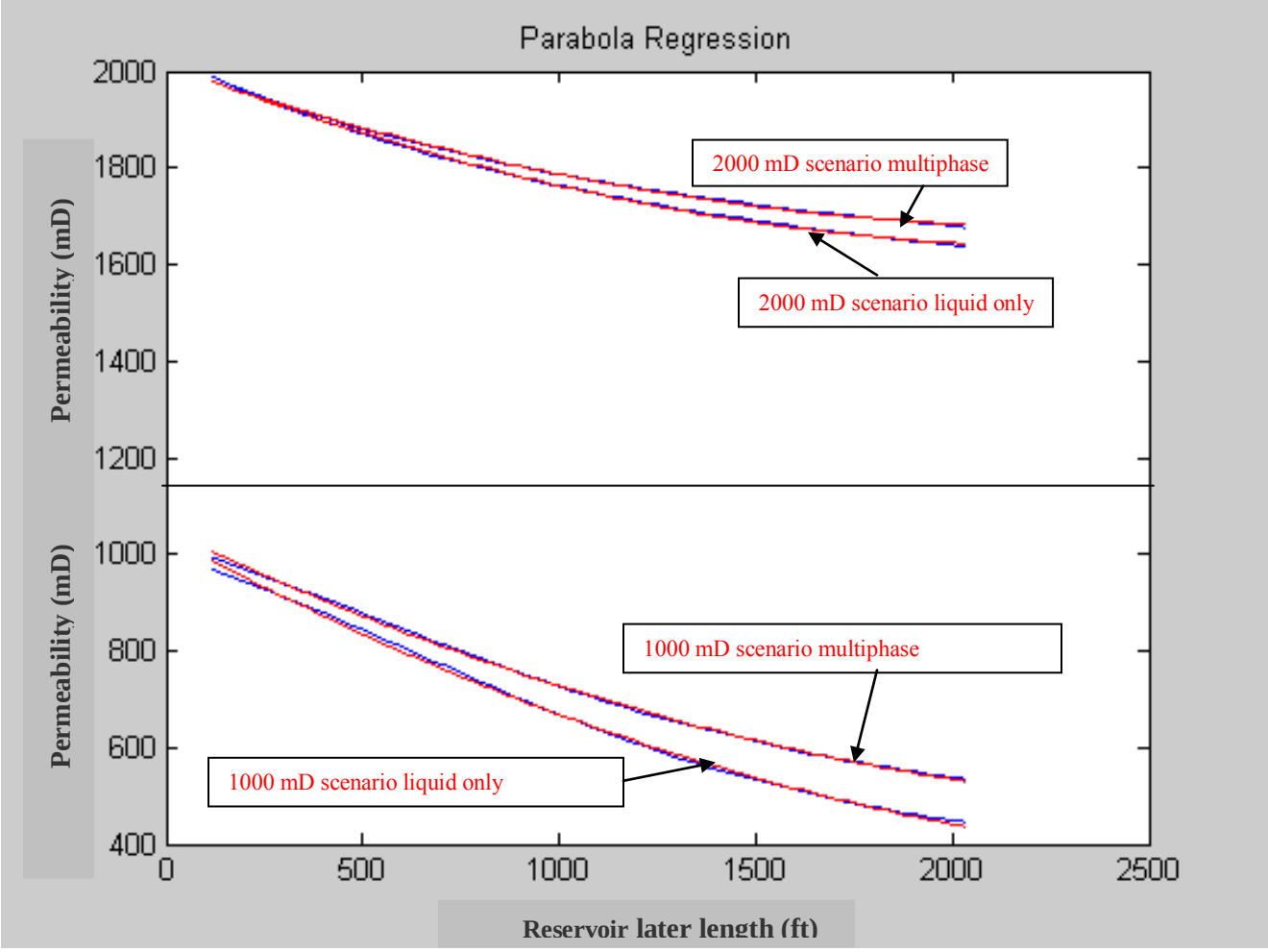

Figure A.2: Parabola regression matching of 10 µm fines grain and various sensitivities

Appendix A-5: Simulation results of crude and fines flow at each water cut

Parameter	Average Velocity (m/s)	Std deviation	No of cells in the grid penetrated	Water cut (%)
Crude	0.210753	0.312263	1204	20
Fines particles	0.066384	0.217451	1797	
Crude	0.210827	0.312308	1204	30
Fines particles	0.071069	0.221385	1784	
Crude	0.2108015	0.3122935	1204	31
Fines particles	0.0690604	0.2195275	1791	
Crude	0.2107096	0.3122256	1204	33
Fines particles	0.0645439	0.2155885	1801	
Crude	0.2106664	0.3121862	1204	34
Fines particles	0.0628911	0.2134588	1806	
Crude	0.2080938	0.3136346	1204	40
Fines particles	0.0732604	0.2233658	1767	
Crude	0.2094555	0.3129885	1204	41
Fines particles	0.0733215	0.2234972	1767	
Crude	0.2122985	0.3116246	1204	42
Fines particles	0.0734428	0.2237285	1767	
Crude	0.2137662	0.3109141	1193	43
Fines particles	0.0735035	0.2238435	1767	
Crude	0.2145085	0.3105539	1024	44
Fines particles	0.0735333	0.2239085	1767	
Crude	0.103126	0.1539326	1203	50
Fines particles	0.0299547	0.1039625	1829	
Crude	0.0509811	0.0764658	1203	51
Fines particles	0.0123294	0.0484899	1862	
Crude	0.0250237	0.0382822	1203	52
Fines particles	0.0052655	0.0228178	1891	
Crude	0.0124576	0.0191439	1202	53
Fines particles	0.0022011	0.0109192	1921	
Crude	0.0062609	0.0096217	1204	54
Fines particles	0.0009461	0.0048914	1921	
Crude	0.2368296	0.2995866	1153	60
Fines particles	0.0675055	0.2194006	1797	
Crude	0.2310065	0.3023753	1132	61
Fines particles	0.0680367	0.2195758	1794	
Crude	0.2282462	0.3037118	1136	62
Fines particles	0.0683715	0.2197148	1793	
Crude	0.2251216	0.3052355	1114	63
Fines particles	0.0688214	0.2199295	1792	

Appendix A-5…cont

Crude	0.221558	0.3069871	1134	64
Fines particles	0.0694642	0.2203087	1791	
Crude	0.2108545	0.3123305	1203	80
Fines particles	0.0733862	0.2236168	1767	
Crude	0.2108525	0.3123302	1203	81
Fines particles	0.0733856	0.223616	1767	
Crude	0.2108521	0.3123295	1203	82
Fines particles	0.0733851	0.2236154	1767	
Crude	0.2108529	0.3123281	1203	83
Fines particles	0.0733848	0.2236149	1767	
Crude	0.2108534	0.3123268	1203	84
Fines particles	0.0733845	0.2236145	1767	
Crude	0.2109316	0.3127686	1204	90
Fines particles	0.0735521	0.2240859	1767	
Crude	0.210893	0.3125584	1204	91
Fines particles	0.0734723	0.2238691	1767	
Crude	0.2108603	0.3123553	1204	92
Fines particles	0.0733959	0.2236456	1767	
Crude	0.2108328	0.312158	1203	93
Fines particles	0.0733216	0.2234451	1767	
Crude	0.2108105	0.3119672	1203	94
Fines particles	0.0732499	0.2232369	1767	
Crude	0.2107934	0.3117812	1203	95
Fines particles	0.0731843	0.2230507	1767	
Crude	0.2107804	0.3116017	1203	96
Fines particles	0.0731172	0.222869	1767	
Crude	0.2107722	0.3114259	1203	97
Fines particles	0.0730551	0.2226936	1767	
Crude	0.2107679	0.3112547	1203	98
Fines particles	0.0729939	0.2225104	1767	
Crude	0.2107683	0.3110876	1203	99
Fines particles	0.0729367	0.222347	1767	
Crude	0.2107721	0.3109243	1203	100
Fines particles	0.0728822	0.2221885	1767	

Reservoir	Pressure (psi)	Pressure (psi)	Pressure (psi)	Pressure (psi)	Pressure (psi)	Pressure (psi)	Pressure (psi)	Pressure (psi)	Pressure (psi)	Pressure (psi)
Length (ft)	Multiphase 10µm	Liquid 10µm	Multiphase 50µm	Liquid 50µm	Multiphase 100µm	Liquid 100µm	Multiphase 150µm	Liquid 150µm	Multiphase 200µm	Liquid 200µm
113.0	-1153.5	-1212.5	-1036.5	-1088.2	-1026.4	-1077.2	-1024.4	-1075.1	-1023.7	-1074.3
140.6	-1172.2	-1251.4	-1056.0	-1126.9	-1046.1	-1116.0	-1044.1	-1113.9	-1043.4	-1113.1
164.0	-1162.6	-1252.5	-1049.4	-1130.6	-1039.7	-1120.1	-1037.8	-1118.0	-1037.2	-1117.3
187.5	-1147.0	-1243.3	-1037.0	-1124.6	-1027.7	-1114.4	-1025.9	-1112.4	-1025.2	-1111.7
210.9	-1130.8	-1231.9	-1024.1	-1116.4	-1015.1	-1106.5	-1013.3	-1104.6	-1012.7	-1103.9
234.3	-1115.2	-1220.6	-1011.7	-1108.3	-1003.0	-1098.7	-1001.3	-1096.9	-1000.7	-1096.2
257.8	-1100.4	-1210.0	-1000.0	-1100.7	-991.6	-1091.5	-989.9	-1089.7	-989.4	-1089.0
281.2	-1086.5	-1200.1	-989.1	-1093.9	-981.0	-1084.9	-979.4	-1083.2	-978.8	-1082.5
:	:	:	:	:	:	:	:	:	:	:
:	:	:	:	:	:	:	:	:	:	:
468.7	-1005.9	-1150.0	-929.7	-1065.4	-923.6	-1058.5	-922.4	-1057.2	-922.0	-1056.7
492.1	-999.6	-1147.4	-925.8	-1065.2	-919.9	-1058.5	-918.7	-1057.2	-918.3	-1056.8
515.6	-994.2	-1145.7	-922.6	-1065.8	-916.9	-1059.3	-915.8	-1058.1	-915.4	-1057.6
539.0	-989.6	-1144.7	-920.3	-1067.1	-914.8	-1060.9	-913.7	-1059.6	-913.3	-1059.2
562.4	-985.9	-1144.6	-918.7	-1069.2	-913.4	-1063.2	-912.3	-1062.0	-911.9	-1061.6
585.9	-983.0	-1145.3	-917.9	-1072.1	-912.7	-1066.2	-911.7	-1065.1	-911.3	-1064.7
:	:	:	:	:	:	:	:	:	:	:
:	:	:	:	:	:	:	:	:	:	:
937.4	-1043.4	-1260.5	-1003.3	-1213.9	-1000.4	-1210.4	-999.7	-1209.6	-999.5	-1209.4
960.8	-1054.7	-1275.6	-1015.9	-1230.4	-1013.1	-1227.0	-1012.4	-1226.3	-1012.2	-1226.0
984.3	-1066.9	-1291.6	-1029.4	-1247.9	-1026.6	-1244.5	-1026.1	-1243.8	-1025.8	-1243.6
1007.7	-1080.1	-1308.6	-1043.8	-1266.2	-1041.2	-1263.0	-1040.6	-1262.4	-1040.4	-1262.2
:	:	:	:	:	:	:	:	:	:	:
:	:	:	:	:	:	:	:	:	:	:
1710.7	-2017.8	-2379.3	-2006.8	-2365.9	-2006.2	-2364.8	-2005.8	-2364.5	-2005.8	-2364.5
1734.2	-2071.4	-2437.9	-2061.0	-2425.2	-2060.4	-2424.1	-2060.0	-2423.8	-2060.0	-2423.8
1757.6	-2126.8	-2498.3	-2117.0	-2486.3	-2116.4	-2485.2	-2116.0	-2484.9	-2116.0	-2484.9
:	:	:	:	:	:	:	:	:	:	:
:	:	:	:	:	:	:	:	:	:	:
1921.6	-2569.2	-2975.7	-2563.0	-2968.2	-2562.7	-2967.3	-2562.3	-2967.1	-2562.3	-2967.1
1945.1	-2640.7	-3052.2	-2635.0	-3045.3	-2634.8	-3044.5	-2634.3	-3044.3	-2634.4	-3044.3
1968.5	-2714.5	-3131.0	-2709.3	-3124.7	-2709.1	-3123.9	-2708.6	-3123.7	-2708.7	-3123.7
1991.9	-2790.6	-3212.0	-2785.8	-3206.3	-2785.7	-3205.6	-2785.2	-3205.4	-2785.3	-3205.4
2015.4	-2869.0	-3295.4	-2864.7	-3290.3	-2864.6	-3289.6	-2864.2	-3289.4	-2864.3	-3289.5

Appendix A-6.1: Multiphase-liquid pressure drops due to particles through 2D rock

Reservoir	Pressure (psi)	Pressure (psi)	Pressure (psi)	Pressure (psi)	Pressure (psi)	Pressure (psi)	Pressure (psi)	Pressure (psi)	Pressure (psi)	Pressure (psi)
Length (ft)	Multiphase 10μm	Liquid 10μm	Multiphase 50μm	Liquid 50μm	Multiphase 100μm	Liquid 100μm	Multiphase 150μm	Liquid 150μm	Multiphase 200μm	Liquid 200μm
117.2	-770.1	-788.7	-708.6	-733.1	-702.1	-726.8	-700.8	-725.6	-700.4	-725.2
140.6	-874.6	-907.0	-814.6	-854.5	-808.1	-848.4	-806.9	-847.1	-806.4	-846.7
164.0	-945.8	-992.0	-888.3	-943.4	-882.1	-937.6	-880.9	-936.4	-880.4	-936.0
187.5	-999.0	-1058.6	-943.8	-1013.3	-937.8	-1007.7	-936.6	-1006.6	-936.1	-1006.2
210.9	-1041.3	-1113.7	-988.0	-1070.8	-982.1	-1065.4	-980.9	-1064.3	-980.5	-1064.0
:	:	:	:	:	:	:	:	:	:	:
281.2	-1136.9	-1242.4	-1087.3	-1203.8	-1081.8	-1198.8	-1080.7	-1197.8	-1080.3	-1197.4
304.6	-1164.2	-1279.0	-1115.4	-1241.2	-1110.1	-1236.3	-1109.0	-1235.3	-1108.6	-1235.0
328.1	-1190.5	-1314.1	-1142.6	-1277.0	-1137.4	-1272.2	-1136.3	-1271.3	-1135.9	-1270.9
351.5	-1216.5	-1348.3	-1169.4	-1311.8	-1164.3	-1307.2	-1163.2	-1306.2	-1162.8	-1305.9
375.0	-1242.4	-1382.1	-1196.0	-1346.1	-1191.0	-1341.5	-1190.0	-1340.6	-1189.6	-1340.3
398.4	-1268.3	-1415.6	-1222.7	-1380.1	-1217.8	-1375.7	-1216.8	-1374.8	-1216.4	-1374.4
421.8	-1294.4	-1449.0	-1249.6	-1414.1	-1244.7	-1409.7	-1243.7	-1408.8	-1243.4	-1408.5
:	:	:	:	:	:	:	:	:	:	:
890.5	-1890.9	-2181.8	-1859.8	-2156.5	-1856.7	-2153.6	-1856.0	-2153.0	-1855.7	-2152.7
913.9	-1925.2	-2222.7	-1894.8	-2197.8	-1891.8	-2195.0	-1891.1	-2194.5	-1890.8	-2194.2
937.4	-1960.1	-2264.0	-1930.3	-2239.7	-1927.4	-2236.9	-1926.6	-2236.4	-1926.4	-2236.1
960.8	-1995.5	-2305.9	-1966.3	-2282.0	-1963.4	-2279.3	-1962.7	-2278.8	-1962.5	-2278.5
984.3	-2031.4	-2348.2	-2002.9	-2324.8	-2000.1	-2322.2	-1999.3	-2321.7	-1999.1	-2321.4
1007.7	-2067.8	-2391.1	-2039.9	-2368.1	-2037.2	-2365.6	-2036.5	-2365.1	-2036.3	-2364.8
:	:	:	:	:	:	:	:	:	:	:
1171.7	-2338.7	-2706.1	-2314.9	-2686.3	-2312.6	-2684.2	-2312.0	-2683.8	-2311.8	-2683.5
1195.2	-2379.8	-2753.3	-2356.6	-2734.0	-2354.4	-2732.0	-2353.7	-2731.5	-2353.6	-2731.3
1218.6	-2421.4	-2801.2	-2398.8	-2782.3	-2396.7	-2780.3	-2396.1	-2779.9	-2395.9	-2779.6
1242.0	-2463.8	-2849.6	-2441.7	-2831.2	-2439.6	-2829.3	-2439.0	-2828.9	-2438.9	-2828.6
1265.5	-2506.8	-2898.7	-2485.3	-2880.7	-2483.2	-2878.9	-2482.6	-2878.5	-2482.5	-2878.2
1288.9	-2550.4	-2948.4	-2529.5	-2930.8	-2527.5	-2929.1	-2526.9	-2928.7	-2526.7	-2928.4
1312.3	-2594.7	-2998.7	-2574.3	-2981.6	-2572.4	-2979.9	-2571.8	-2979.5	-2571.7	-2979.2
:	:	:	:	:	:	:	:	:	:	:
1499.8	-2974.7	-3425.5	-2958.6	-3411.9	-2957.2	-3410.6	-2956.6	-3410.3	-2956.5	-3410.1
1523.3	-3025.5	-3482.1	-3010.0	-3468.9	-3008.6	-3467.6	-3008.1	-3467.4	-3008.0	-3467.1
1546.7	-3077.2	-3539.4	-3062.2	-3526.6	-3060.9	-3525.4	-3060.3	-3525.2	-3060.2	-3524.9
1570.1	-3129.7	-3597.4	-3115.2	-3585.1	-3113.9	-3584.0	-3113.4	-3583.7	-3113.3	-3583.4
1593.6	-3182.9	-3656.2	-3169.0	-3644.3	-3167.8	-3643.2	-3167.2	-3643.0	-3167.1	-3642.7
1617.0	-3237.1	-3715.8	-3223.6	-3704.3	-3222.5	-3703.3	-3221.9	-3703.1	-3221.8	-3702.8
:	:	:	:	:	:	:	:	:	:	:
1804.5	-3701.2	-4221.0	-3691.9	-4212.9	-3691.1	-4212.3	-3690.6	-4212.2	-3690.5	-4211.8
1827.9	-3763.2	-4287.2	-3754.3	-4279.5	-3753.6	-4279.0	-3753.1	-4278.9	-3753.1	-4278.5
1851.3	-3826.0	-4353.7	-3817.6	-4346.4	-3817.0	-4345.9	-3816.4	-4345.8	-3816.4	-4345.5
1874.8	-3889.3	-4419.9	-3881.5	-4413.0	-3880.9	-4412.6	-3880.3	-4412.5	-3880.3	-4412.1
1898.2	-3953.0	-4485.1	-3945.6	-4478.7	-3945.1	-4478.3	-3944.5	-4478.2	-3944.5	-4477.9
:	:	:	:	:	:	:	:	:	:	:
2015.4	-4237.7	-4729.9	-4232.7	-4725.5	-4232.4	-4725.4	-4231.9	-4725.4	-4231.9	-4725.0
2038.8	-4267.0	-4732.9	-4262.5	-4728.9	-4262.3	-4728.8	-4261.8	-4728.8	-4261.7	-4728.4

Appendix A-7: Particle-damaged permeability model in liquid flow

Reservoir Length (ft)	10 μm Permeability (mD)	50 μm Permeability (mD)	100 μm Permeability (mD)	150 μm Permeability (mD)	200 μm Permeability (mD)
70	999	997	992	988	972
94	998	860	645	441	397
117	809	647	485	345	307
141	694	555	417	307	271
164	622	498	374	285	252
187	570	456	342	270	239
211	529	423	317	259	230
234	494	395	297	249	222
258	465	372	279	241	216
281	440	352	264	234	211
305	417	334	251	228	207
328	398	318	239	222	203
352	380	304	228	217	199
375	364	291	218	211	195
398	349	279	209	206	191
422	335	268	201	202	188
445	323	258	194	197	184
469	311	249	187	193	181
492	301	241	181	188	178
516	291	233	175	184	175
539	282	225	169	180	172
562	273	218	164	176	169
586	265	212	159	173	166
609	257	206	154	169	163
633	250	200	150	166	160
656	243	195	146	162	157
680	237	190	142	159	155
703	231	185	139	156	152
726	225	180	135	153	149
750	220	176	132	150	147
773	214	172	129	147	144
797	209	168	126	144	142
820	205	164	123	141	140
844	200	160	120	139	137
867	196	157	118	136	135
891	192	153	115	133	133
914	188	150	113	131	131
937	184	147	110	129	128

Appendix A-7.1: Damaged permeability model in multiphase, 1000 mD rock

Reservoir length (ft)	10 µm Permeability (mD)	50 µm Permeability (mD)	100 µm Permeability (mD)	150 µm Permeability (mD)	200 µm Permeability (mD)
70	999	995	986	978	964
94	998	874	655	464	397
117	810	648	486	362	309
141	691	553	415	322	275
164	620	496	372	298	256
187	569	455	342	282	243
211	530	424	318	270	234
234	498	399	299	260	226
258	471	377	283	251	220
281	448	359	269	244	215
305	428	343	257	237	210
328	410	328	246	230	206
352	394	315	236	225	202
375	379	303	228	219	198
398	366	293	219	214	194
422	353	283	212	208	191
445	342	273	205	204	187
469	331	265	199	199	184
492	321	257	193	194	180
516	312	249	187	190	177
539	303	242	182	186	174
562	294	236	177	182	171
586	287	229	172	178	168
609	279	224	168	174	165
633	272	218	164	170	162
656	266	213	160	167	159
680	259	208	156	163	156
703	253	203	152	160	154
726	248	198	149	157	151
750	242	194	145	154	148
773	237	190	142	151	146
797	232	186	139	148	143
820	227	182	137	145	141
844	223	178	134	142	139
867	218	175	131	140	136
891	214	171	129	137	134
914	210	168	126	134	132
937	206	165	124	132	130